EXPLORING THE POSSIBILITIES OF EXTENDING THE APPLICATION OF PCBN CUTTING TOOLS TO THE MACHINING OF ADI THROUGH THE UNDERSTANDING OF WEAR MECHANISMS

Kambuyi Katuku

A thesis submitted to the Faculty of Engineering and the Built Environment, University of the Witwatersrand, Johannesburg, in fulfilment of the requirements for the degree of Doctor of Philosophy in Metallurgy and Materials Engineering

Johannesburg, 2010

DECLARATION

I declare that this thesis is my own, unaided work. It is being submitted for the Degree of Doctor of Philosophy in Metallurgy and Materials Engineering at the University of the Witwatersrand, Johannesburg. It has not been submitted before for any degree or examination to any other University.

……………………………………………….

(Signature of Candidate)

……………….………….day of …………………..year……………..

ABSTRACT

Experimental studies of wear, cutting forces and chip characteristics when dry turning ASTM Grade 2 ADI with cBN-TiC cutting tools under finishing conditions were carried out. A depth of cut of 0.2 mm, a feed of 0.05 mm/rev and cutting speeds ranging from 50 to 800 m/min were used. Oxidation experiments of the cBN-TiC cutting tools were carried out in the temperature range 500-1110 °C for a constant dwell time of 60 min. Static interaction experiments were done with ADI/cBN-TiC/ADI and Si/cBN-TiC/Si sandwiches in the temperature range 1000-1100 °C under argon for a constant dwell time of 60 min and a pressure of 200 MPa.

An X-ray diffractometer, optical, scanning and transmission electron microscopes as well as an energy dispersive spectroscope (EDS) were appropriately used for characterization of ADI workpieces, PcBN cutting tools, chips, wear scars on PcBN cutting tools, scale on PcBN cutting tools after oxidation experiments and interaction interfaces after static interaction experiments.

Flank wear and crater wear were the main wear modes within the range of cutting speeds investigated. At cutting speeds greater than 150 m/min, shear localization within the primary and secondary shear zones of chips was the key-process that controlled the wear rate indirectly, the static cutting forces and the dynamic cutting forces. Cutting speeds between 150 and 500 m/min were found to be optimum for the production of workpieces with acceptable cutting tool life, flank wear rate and lower dynamic cutting forces. Adhesion and adhesion induced abrasion were the main wear mechanisms at cutting speeds less than 150 m/min. Abrasion and wear by thermally activated diffusion and oxidation / chemical reaction wear were the main wear mechanisms at cutting speeds greater than 150 m/min.

At cutting speeds greater than 150 m/min, the superficial melting of the BUL on the chip underside produced a lubricating film that maintained more or less constant tribological conditions at the tool-chip interface, thus reducing shear localization in the secondary shear zone of chips. This lubricating film also played a role in the reduction of the tool-chip contact length, the increase of the shear angle and, consequently in the reduction in average chip thickness.

The BUL on the crater wear scar was a sandwich of approximately 3 layers: a very thin C rich layer, an intermediate layer containing mainly Si, Mg, and O, slight amounts of B, C and N and very low amounts of Al and Ti as well as a Fe layer in preferential contact with the TiC binder. It became apparent that clues of diffusion wear should be sought in the BUL on the wear scars rather than in the secondary shear zone of chips.

Constituents in the BUL on contact zones and non-contact zones of the tools were the products of thermally activated chemical reactions between constituents of the cutting tool, constituents of ADI (particularly Mg and Si) and atmospheric O_2. Accordingly, the superficial melting of the BUL increased the wear rate of cBN-TiC cutting tools for cutting speeds greater than 150 m/min.

Although a minor phase in cBN-TiC cutting tools, TiB_2 emerged as a critical phase with regard to their wear behaviour. Its thermally activated dissolution in Fe and its thermally activated reactions with O_2 or O_2 and Mg as well as its thermally induced cracks might be expected to have synergistic effects on cBN grain pull-out and thus on the wear rate.

Blistering and cracking of the non-contact zones of cBN-TiC cutting tools characterized the oxidation behaviour of cBN-TiC cutting tools. The cBN-TiC cutting tool material is not oxidation-resistant in air above 550 °C and the scale that formed on cBN-TiC cutting tools is not able to provide effective protection against oxidation. The TiC binder of the cutting tool material showed extensive oxidation, producing brittle titanium oxide crystallites.

Oxidation experiments on cBN-TiC cutting tools showed that oxidation involved intense outward diffusion of elements such as Ti and Al. In addition to the grain coarsening of TiO_2 and increased segregation of Al_2O_3 in the outer scale layer, it was clear that the formation and evaporation of B_2O_3 affected the morphology of the inner oxygen-affected zone significantly in terms of porosity. Mutual dissolution or reaction between B_2O_3 and TiO_2 which could be expected to reduce such porosity was not evident. The same was true for TiO_2 and Al_2O_3.

From the static interaction experiments, strong indications of diffusion of Fe in the TiC binder as well as reprecipitation of Fe in TiC were evident. Strong indications of dissolution of TiC and diffusion of Ti and C as well as reprecipitation of TiC in Fe were also evident. The reprecipitation in Fe of this C in the form of Fe_3C or Ti(C,N) is evidence of depletion in Si of the ADI close to the interface and thus evidence of diffusion of Si towards the cBN-TiC side. The evidence of diffusion of N in Fe and its reprecipitation in the form of Ti(C,N) is a strong indication of the dissolution of N-bearing phases such as Ti(C,N), AlN and BN in the cBN-TiC cutting tool material. Strong indications of diffusion of Si in the TiC binder as well as its reprecipitation as Si_xC or $TiSi_{4-x}$ were evident. All this correlates with the penetration of Si and Fe observed approximately 0.5 µm below the crater scar of the cBN-TiC cutting tools, at the boundaries between cBN grains and the TiC binder.

The diffusion of Si in the TiC binder and its eventual reprecipitation as Si_xC or $TiSi_{4-x}$ give an indication of how the degradation of the wear resistance of the cBN-TiC cutting tool can occur during the machining of ADI. The same applies to the diffusion of Fe in the TiC binder.

The strong evidence of interaction of Si, Fe and TiC obtained from the static interaction couples clearly indicates that during the machining of ADI with cBN-TiC cutting tools, bonding of ADI to the tool occurs preferentially through the TiC binder. Indication is also given of how the depletion in Si of the ADI can occur at the tool-chip and tool-workpiece interfaces.

The knowledge generated in this work should contribute towards improved design and processing of PcBN cutting tools for use in the machining of ADI.

To Charlotte, Tania, Eliana, Elsa and Manoah

ACKNOWLEDGEMENTS

My deepest gratitude goes to my supervisors, Prof. Andreas Koursaris and Prof. Iakovos Sigalas for their strong and endless support, fruitful discussions and patience. This thesis has benefited greatly from their direction, perceptive criticism and experience.

I am grateful to Prof. Mani Subramanian and Dr Matthias Herrmann for fruitful discussions. I am also grateful to Prof. Jan Neetheling, Dr Frick Kock and Mr Johan Westraad for their valuable help in transmission electron microscopy investigations.

I give my special thanks to the personnel of the Research Department of Element Six, South Africa. Their insights have had a tremendous influence on the direction of this investigation. It was an enormous pleasure to meet such sharp fellows.

My thanks go to all my elders, colleagues and friends who provided support while working on this research. Whether their support was in inspiration, advice, technical matters, consultation or simply a helping hand, it was a superb experience.

I would also like to take advantage of this opportunity to thank the staff and students of the School of Chemical and Metallurgical Engineering for their contributions to this research project.

Thanks to Element Six, South Africa who showed a lot of interest in this research and provided me with laboratory facilities and materials for experimental work without which this work would not have been possible.

I am indebted to the DST/NRF Centre of Excellence in Strong Materials, University of the Witwatersrand, Johannesburg, for partially funding this research and for awarding me a scholarship.

Any opinions, findings and conclusions or recommendations are those of the author and do not necessarily reflect the views of Element Six, South Africa or the NRF/DST Centre of Excellence in Strong Materials, University of the Witwatersrand, Johannesburg.

Finally, I take this opportunity to express my gratitude to my family for unfailing encouragement and support. Special thanks to my parents Marcel and Gertrude - I cannot find appropriate words to convey my sense of gratitude for their support throughout my life.

CONTENTS

LIST OF FIGURES

LIST OF TABLES

LIST OF ABBREVIATONS

Austempered Ductile Iron	ADI
Backscattered electron	BSE
Built Up Edge	BUE
Built Up Layer	BUL
Cubic Boron Nitride	cBN
Carbon Equivalent	CE
Compacted Graphite Iron	CGI
Computer Numerical Controlled	CNC
Differential Thermal Analysis	DTA
Electronic Discharge Machine	EDM
Energy Dispersive Spectroscope	EDS
Energy Dispersive X-ray Spectroscopy	EDX
Electron Probe Micro-Analyser	EPMA
Focused Ion Beam	FIB
Hexagonal Boron Nitride	hBN
High-Speed Steels	HSS
Polycrystalline Cubic Boron Nitride	PcBN
Polycrystalline Compact Diamond	PCD
Peripheral Component Interconnect	PCI
Regression Coefficient	R^2
Rhombohedral Boron Nitride	rBN
Selected Area Diffraction Pattern	SADP
Secondary electron	SE
Scanning Electron Microscope	SEM
Scanning Transmission Electron Microscope	STEM
Transmission Electron Microscope	TEM
Thermogravimetry Analysis	TGA
Wurtzitic Boron Nitride	wBN
X-Ray Diffraction	XRD

1 INTRODUCTION

1.1 GENERAL BACKGROUND AND JUSTIFICATION OF THE RESEARCH

The automotive industry, which is extremely competitive, is interested in austempered ductile iron (ADI) because it offers properties similar to those of heat-treated alloy steels. These include high strength, high hardness, excellent toughness, high ductility, good fatigue properties and useful wear characteristics at lower cost and reduced weight.

Because of these properties, ADI is difficult to machine in the austempered condition. Cutting tools for machining ADI should posses high hot hardness and strength, excellent hot chemical resistance as well as high toughness. Such cutting tools are ideal and do not, strictly speaking, exist at present in the field of cutting tools. However, they are the purpose of continuous research in the field.

Research in machining has consistently aimed at higher cutting speeds, taking advantage of the latest advances in cutting tool materials, coating technologies, inclusion-engineered workpieces and computer interfaced machine-tools (1).

As a consequence, there is strong interest in extending the application of polycrystalline cubic boron nitride (PcBN) cutting tools beyond the traditional machining of hardened steels, flake graphite cast irons and steels produced by powder metallurgy (2,3). Indeed, PcBN cutting tools appear to be an alternative for the machining of ADI at high cutting speeds (high temperatures). At these high cutting speeds, cemented carbide cutting tools do not maintain hardness, and Al_2O_3-based ceramic cutting tools do not offer adequate fracture toughness and transverse rupture strength (4).

In the published literature, very few research papers deal with the machining of ADI with PcBN cutting tools (5). The aim of this work was to explore the possibilities of extending the application of PcBN cutting tools to the machining of ADI through an in-depth understanding of the wear mechanisms, particularly with regard to the recent improvements in the PcBN cutting tool processing technology.

1.2 PROBLEM STATEMENT AND SIGNIFICANCE OF THE RESEARCH

Despite the huge number of papers and research dedicated to ADI, which was developed during the early 1960's, it could to some extent still be considered as a new material (6) for which, in particular, a thorough knowledge of machining of ADI is still needed to support a number of its potential applications (7). ADI components are usually rough machined before austempering and finish machined after this heat-treatment.

Machining of ADI in its austempered condition is highly desirable because it can yield the tight tolerances and surface finishes generally required (8), save machining time and thus reduce costs (9). In addition, it can induce significant compressive stresses in the machined surfaces, thus improving the bending-fatigue strength (10).

Failure of cutting tools, generally takes place by wear which involves a number of physical, chemical, mechanical and metallurgical processes. These processes interact at the high temperatures reached during the cutting operation at high cutting speeds.

In this connection, the cutting tool industry is interested in a fundamental understanding of the interactions involved in the wear of PcBN cutting tools when machining ADI. Although these interactions are extremely complex, their understanding is the very resource that can effectively assist the cutting tool industry in the development and production of specific PcBN cutting tools for the efficient machining of ADI.

In other words, the deeper fundamental understanding of the failure mechanisms of the PcBN cutting tools when machining ADI will generate a phenomenological model that may be expected to point out optimum machining parameters and some properties (structures) to be considered in the design of competitive PcBN cutting tool materials.

1.3 PROPOSED SOLUTIONS

In order to acquire an in-depth understanding of the wear mechanisms involved, it is required to investigate the complex wear environment wherein machining of ADI with PcBN cutting tools takes place. Such machining experiments consist of assessing and understanding the performance of PcBN cutting tools when machining ADI. At the same time they afford an assessment of the machinability of ADI with PcBN cutting tools and the establishment of a body of knowledge on the machining of ADI with PcBN cutting tools.

In itself, machining is a dynamic process that occurs on a very small surface area of the cutting tool, which increases the complexity of a failure analysis of the tool. Static tests on PcBN cutting tools and ADI (static interaction couples) can allow simulation and easy understanding of some critical wear mechanisms involved in the failure of cutting tools during machining, particularly those related to the chemical matching (11) of cutting tool, workpiece and environment at high temperatures. Static tests should aid the understanding of tool wear.

1.4 STATEMENT OF BASIC CONCEPTS

The basic concepts involved in this research are: cutting speed, flank wear and flank wear rate, crater wear and crater wear rate, tool life, cutting length to end of tool life, “ratio of volume of metal removed per unit flank wear”, static and dynamic cutting forces, effective friction coefficient, chip characteristics, shear localization, wear mechanisms, tribo-transfer layers, oxidation behaviour and, physical and chemical interactions.

1.5 OBJECTIVES OF THE RESEARCH

In light of the experimental work described later, this research was expected to produce the following outputs, in the context of machining ADI with PcBN cutting tools:

1. Description of the effect of cutting speed on the wear performance of PcBN cutting tools
2. Description of the effect of cutting speed on static and dynamic cutting forces
3. Description of the effect of cutting speed on the effective friction coefficient at the crater wear scar of the PcBN cutting tools
4. Description of the effect of cutting speed on chip characteristics, particularly the microstructure in the flow zone

   The microstructure of adiabatic shear bands in the primary and secondary shear zones of the chips, particularly at high cutting speeds, and the role played by these adiabatic shear bands in the wear process of PcBN cutting tools are of particular importance at this time.
5. Description of the effect of cutting speed on the wear mechanisms acting on the PcBN cutting tools
6. Description of the tribo-transfer layers that build up on the wear scar of PcBN cutting tools during machining as well as the role played by these layers in the process of wear of PcBN cutting tools
7. Description of the oxidation behaviour of PcBN cutting tools

8. Description of the interactions involved in diffusion couples of ADI and PcBN cutting tools at elevated temperatures and under uniaxial pressure
   Such interactions would produce insights into the fundamental understanding of the adhesion wear mechanism and the interaction between the chip (tribo-transfer layer) and the PcBN cutting tools during the machining process.

1.6 SCOPE OF THE RESEARCH

The PcBN cutting tools used in this research were essentially cBN-TiC cutting tools. The austempered ductile iron used was the ASTM Grade 2 material. The machining operation used was dry turning under finish conditions. The machining parameters used were: rake angle –26°, clearance angle 6°, approach angle 45°, depth of cut 0.2 mm, feed 0.5 mm/rev and cutting speed in the range 50-800 m/min.

The oxidation experiments of the cBN-TiC cutting tools were isothermal. The range of temperature was 500-1110 °C and the dwell time was constant at 60 min.

The static interaction experiments involved the combinations ADI/cBN-TiC/ADI and Si/cBN-TiC/Si. The range of temperatures was 1000-1100 °C and the dwell time was constant at 60 min. The pressure on these couples was constant at 200 MPa. The atmosphere was kept inert by using argon.

1.7 METHODS AND TECHNIQUES

The approach used in the present research was essentially experimental. Machining experiments were conducted on a CNC lathe in order to collect quantitative and qualitative data for the measurement of the performance of PcBN cutting tools when machining ADI.

Naturally, the machining experiments that underlie the data collection were preceded by the characterization of ADI workpieces and PcBN cutting tools. A hardness tester and a microhardness tester were used for the characterization of the ADI workpieces and chips.

A triaxial dynamometer mounted on the lathe turret and coupled to a multi-channel amplifier was used for the measurement of cutting forces. A TGA-DTA thermo-balance and a muffle furnace were used for the oxidation experiments of PcBN cutting tools. A hot uniaxial press was used for the static interaction experiments.

An X-ray diffractometer, optical, scanning and transmission electron microscopes as well as an energy dispersive spectroscope (EDS) were appropriately used for characterization of ADI workpieces, PcBN cutting tools, chips, wear scars on PcBN cutting tools, scale on PcBN cutting tools after oxidation experiments and interaction interfaces after static interaction experiments.

The worn cutting tool samples for transmission electron microscopy were prepared by use of focused ion beam (FIB). Most of the above equipment was computer controlled using specific software.

1.8 LAYOUT OF THE THESIS

Chapter 1 is dedicated to the introduction. Chapter 2 is dedicated to the literature review. This literature review adapts the approach used in the research and deals with the fundamentals of metal cutting, PcBN cutting tool materials, cutting tool wear mechanisms, ADI, and the state of the art on the machinability of ADI. Chapter 3 sketches the structure of the experimental work to be carried out in order to meet the objectives drawn up. The experimental procedures, i.e. the methodologies and major equipment used for the investigations are outlined in Chapter 4. Chapters 5 and 6 present respectively the results and the discussion of results. Conclusions and recommendations of this project are dealt with in Chapter 7.

2 LITERATURE REVIEW

2.1 FUNDAMENTALS OF METAL CUTTING

2.1.1 Introduction

Machining is a manufacturing process based on removing of unwanted material from a workpiece in the form of relatively thin layers called chips. If the workpiece is a metallic material, the process is often called metal cutting (12,13).

Metal cutting operations provide high accuracy relative to most other shaping processes. Therefore, metal cutting is often selected when tolerances are close. Turning, drilling, and milling are the principal metal cutting processes (14).

The fundamental mechanism involved in metal cutting is that of a localized shear deformation on the work material immediately ahead of the cutting edge of the tool. The relative motion between the cutting tool and workpiece induces a primary shear deformation, which forms the chip. The chip then passes over the rake face of the cutting tool and receives through shearing and sliding, a secondary shear deformation (15).

Dislocation slip is the predominant mode of plastic deformation. Twinning is generally negligible, except in Ni-based alloys which are characterized by an FCC crystal structure and high hot strength (16).

Plastic deformations in the primary and secondary shear zones have a mutual dependence. The deformation in the secondary shear zone is influenced by the phenomena in the primary shear zone. The shear plane angle in the primary shear zone is also directly influenced by the deformation and friction at the tool-chip interface. The shear plane angle influences the strain and heat generation in the primary shear zone (15).

A relatively large amount of energy is required to form the chip and to move it across the rake face of the cutting tool. The formation of new surfaces, namely the machined surface and the under surface of chips, also requires energy. However, the latter energy is an insignificant proportion of that required to deform plastically the whole of the metal removed (13).

A wide variety of inputs and outputs (Figure 2.1) is involved in the metal cutting process, thus making it very complex.

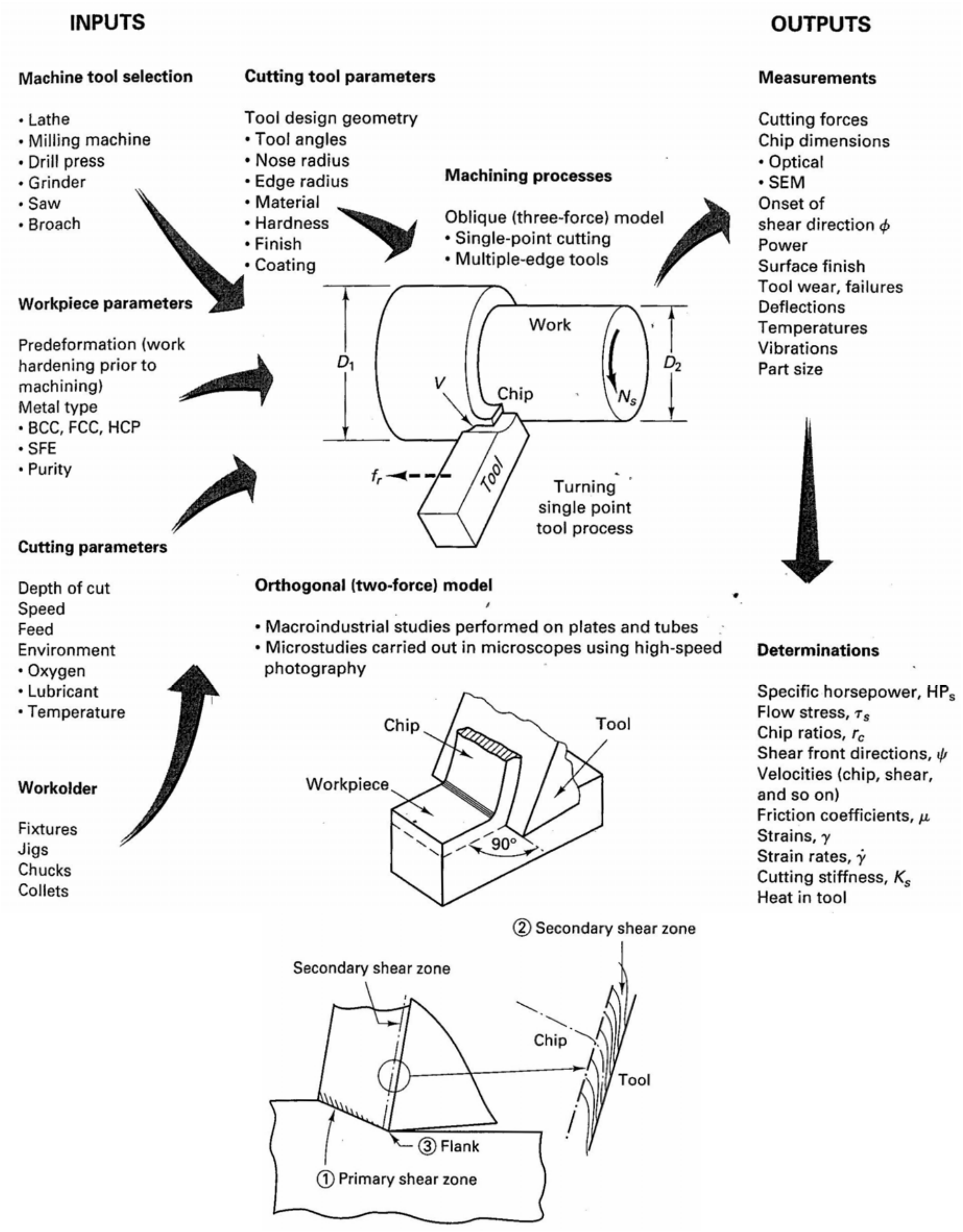

Figure 2.1: Fundamental inputs and outputs to metal cutting process (12)

2.1.2 Chips and cutting models

In the analysis of the metal cutting process, detailed knowledge of chip formation plays a key-role in the understanding of cutting tool performance, rate of metal removal as well as accuracy and condition of the machined surface. The cross-section of chips and their thickness are particularly of great importance in the analysis of the cutting process (13).

Most industrial machining operations take place within the oblique geometry (3-D). However, the analysis and modelling of metal cutting process is significantly simplified within the orthogonal geometry (2-D), particularly for chip formation. In this connection, quick stop devices used with orthogonal cutting are very useful (13). Orthogonal cutting can be obtained in practice by end machining a tube wall or by machining a plate (Figure 2.1).

2.1.3 Essential features of metal cutting

2.1.3.1 Primary shear zone

The primary shear zone evolves out of a radial compression zone that travels ahead of the shear process as the cutting tool passes over the workpiece (Figure 2.2). The plastic compression generates dense dislocation tangles and networks in annealed work materials to such an extent that when the consecutive work-hardened material reaches the cutting tool, it shears in the direction of the free surface (15).

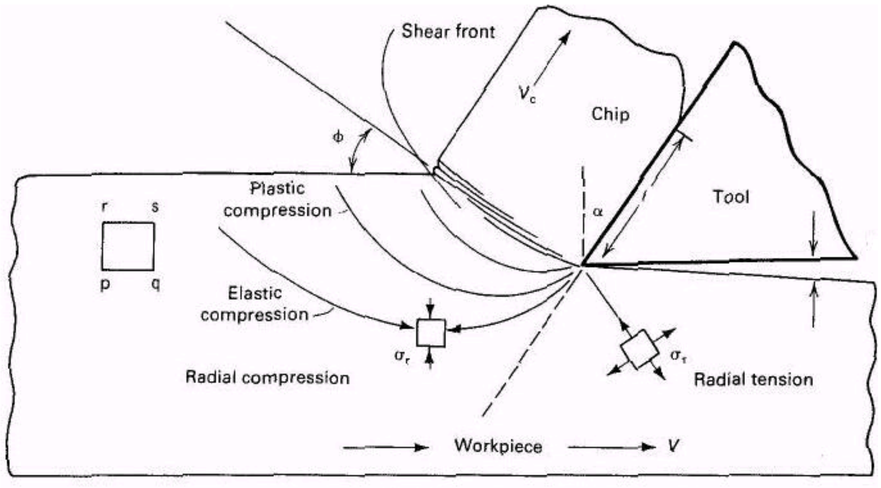

Figure 2.2: Development of the shear front lamella structure in the primary shear zone (15)

Evidence of various methods indicates consistently that shear strain in the primary shear zone takes place in a finite narrow volume of work material, the shape of which varies with the work material and cutting conditions. Most evidence indicates that the average thickness of the primary zone is on the order of one tenth of the chip thickness (13,17).

Very high values of shear strain (typically two to five) and exceptionally high values of shear strain rates (typically from 10^3 to 10^5 s^{-1} with local variations as high as 10^7 s^{-1}) occur within the primary shear zone (13,15,18,19).

Strains in the primary shear zone are sufficient to produce saturation strain hardening. Most metals also exhibit strain rate hardening, especially at strain rates over 10^4 s^{-1}. Generally, a dislocation drag mechanism sets in from a strain rate of 10^4 s^{-1} and triggers a rapid rise in shear stress (13,20).

The primary shear zone can sometimes extend into the workpiece below the cutting edge, having a major influence on the quality of the machined surface, particularly in terms of residual stresses. The thickness of the deformed layer on the workpiece is very variable (13,17,21).

2.1.3.2 Adiabatic shear front-lamella structure

Considering the very high strain and extremely high strain-rate characteristics of metal cutting, shear instability conditions are attained in the primary shear zone (22). In connection with the fundamentals behind the shear instability phenomenon, Zener and Hollomon (23) proposed that when the decrement in flow stress due to thermal softening overtakes the increment in flow stress due to strain hardening, plastic deformation becomes unstable and homogeneous deformation gives way to a localised band-like deformation to form adiabatic or thermoplastic shear bands (22). Very high temperatures are generated in adiabatic shear bands and the temperature cycle is very short, usually in the order of ms (13,15).

At such high temperatures, very high strain and exceptionally high strain rates, a steep decrement of flow stress due to thermal softening occur either through recovery processes or phase transformation (13,24).

Therefore, the primary shear process is essentially a discontinuous series of adiabatic shear fronts that produce a lamellar microstructure in chips, irrespective of metallic work material and cutting parameters. Adiabatic shear fronts are produced by the activation of many dislocations travelling in waves from the cutting tool edge to the free surface (15).

Individual adiabatic shear fronts coalesce into narrow shear bands (Figure 2.2). The lamella represents heavily deformed material that has been segmented by the adiabatic shear fronts. Shear bands are very narrow (20 to 200 nm) compared to lamella (2 to 4 μm) (15,20).

2.1.3.3 Chip curl

In all metal cutting operations, chips develop a curvature as they leave the workpiece surface. Among the possible factors contributing to the phenomenon are the distribution of stresses in the primary and secondary shear zones, thermal effects, work-hardening characteristics of the work material, and the geometry of the rake face of the cutting tool (17,21).

Generally, the chip becomes curlier as the depth of cut decreases. This increases the rake angle, and decreases friction at the tool-chip interface. Lubricants as well as inclusions or various types of inhomogeneities in the work material also influence chip curl (21).

2.1.3.5 Tool-chip-interface

The movement of chips and workpiece across the faces and around the edge of the cutting tool is essential for the understanding of chip formation and performance of cutting tools (13,25). For instance, the tribology at the tool-chip interface influences the deformation in the primary shear zone, built up edge (BUE) formation, cutting forces and cutting temperatures (17).

Evidence from detailed metallographic characterisation of worn cutting tools, quick-stop sections and chips, shows that full sliding contact at the interface is impossible under most cutting conditions. This evidence reveals that adhering work material penetrates both major and minor irregularities in the cutting tool surface close to the cutting edge, producing a strong mechanical-interlocking and or metallic bonding, characteristic of seizure. Freshly generated, cut metallic surfaces are atomically clean and exceptionally active chemically to the extent that they bond very readily to other metal surfaces (13,17,26).

Sticking friction or seizure occurs at the interface near the cutting tool edge and sliding friction takes place beyond the sticking region (Figure 2.3). Seizure also occurs on the flank face, particularly close to the cutting edge (13).

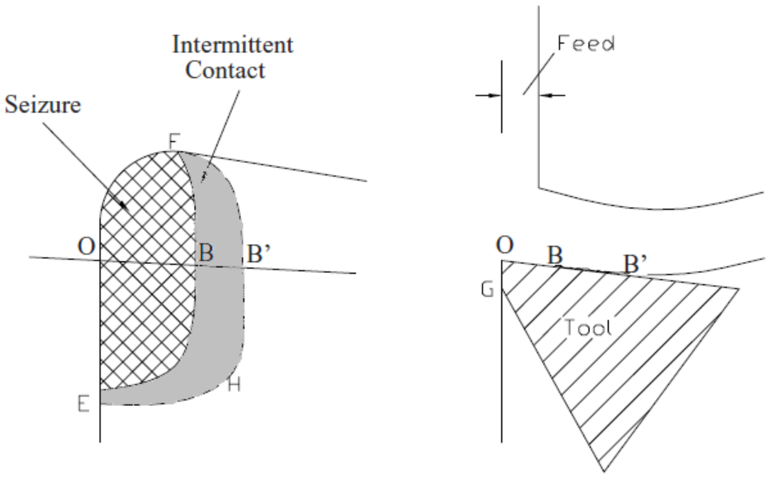

Figure 2.3: Areas of seizure and intermittent contact on cutting tool (13)

It has been demonstrated that at very low cutting speeds (a few cm/min), almost full sliding contact occurs particularly at the tool-chip interface. At these cutting speeds, sliding friction is remarkably promoted by the use of active lubricants (13,17).

The effective friction coefficient μ_e represents a simplest way to characterize the tool-chip friction. In metal cutting, μ_e is usually larger than friction coefficients measured in conventional sliding friction tests. Values above 1.0 are not unusual (13,17).

μ_e usually increases with rake angle (27) and also varies with cutting speed and often reaches a maximum over a narrow range of cutting speeds. In this range, the chip adheres strongly to the cutting tool and may form a BUE. However, μ_e does not provide information on the distribution of stresses and strains across the tool-chip interface (17).

2.1.3.6 Chip flow under conditions of seizure: flow zone or secondary shear zone (13)

The shear strain resulting from seizure is confined to a thin region, usually called flow zone, which may lie immediately adjacent to the interface or at some distance from it. There is no sharp line separating the flow-zone from the bulk of the chip, but a gradual blending in.

In general the flow-zone is very thin compared with the bulk of the chip - commonly of the order of 5% of the chip thickness. The thickness of the flow zone varies considerably with the work material, from more than 100 μm to less than 12 μm. This thickness must depend on the flow stress at the tool-chip interface which, in turn, is temperature, strain and strain-rate dependent. It tends to be thicker at low cutting speeds, but does not vary greatly with the feed. At present, little is known about the influence of factors such as work material, cutting tool geometry, or cutting tool material on the flow-zone thickness. Strain rate within the flow zone is on the order of 10^4 s^{-1}. In high speed machining operations, the flow zone is a thermoplastic shear band.

The flow zone is not a transient structure. It is a body of work material trapped at the cutting tool surface and maintaining its integrity for the duration of a cutting operation. Thus, since the bottom of the flow-zone remained anchored to the cutting tool surface, the material in that part very close to the cutting tool surface continues to be subjected to strain. Normal structural features of the work material such as grain boundaries and plastic inclusions either completely transform within the flow-zone or are drawn out so nearly parallel to the cutting tool surface.

Basically, the amount of strain within the flow-zone is very large, on the order of 100 or greater, i.e. several orders of magnitude greater than on the primary shear zone.

Examination of flow zones with a transmission electron microscope (TEM) shows that the main feature for all alloys so far investigated is a structure consisting of equiaxed grains of very small size (e.g. 0.1 to 1.0 μm) with few dislocations. Such a microstructure appears to be the result of recovery or recrystallization during the very short time when the work material is overwrought and heated as it passes over the contact area on the cutting tool.

2.1.3.7 Chip flow under conditions of seizure: built-up edge (BUE)

When cutting many engineering alloys with more than one phase in their microstructures(28) under cutting conditions for which temperature rise does not allow any recovery or recrystallization to occur at the chip underside, i.e. under conditions where the increment in flow stress due to strain hardening overtakes the decrement in flow stress due to thermal softening, layers of severely strain-hardened work material successively and gradually accumulate under conditions of seizure, forming a BUE (Figure 2.4) that adheres strongly to the cutting tool (13).

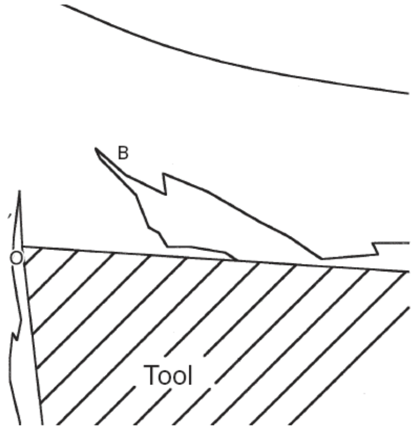

Figure 2.4: Form of BUE (13)

BUE most often arises when cutting soft metals, such as Al-based alloys (29). The tendency to form BUE is generally less with cold-worked work materials than annealed ones. Inclusions or other types of inhomogeneities in the work material reduce the tendency to form BUE (17,21).

There is no distinct line between a BUE and a flow-zone. Seizure between cutting tool and chip is a feature of both situations and every shade of transitional form between the two can be observed. BUE can be formed either with a continuous chip, for example when cutting steels, or even with a discontinuous chip, for example when cutting flake graphite cast irons. The cutting speed range within which a BUE sets in depends on the work material and feed. For instance, BUE forms at modest cutting speeds of up to 30 m/min when cutting medium carbon steels (13).

During the cutting operation, BUE is not a separate body of work material. The strain-hardened work material of the BUE does function as an extension to the cutting tool, displacing the chip from direct contact with the cutting tool, as shown in Figure 2.4 (13,15). BUE occurs in many shapes and sizes and it is not always possible to be certain whether or not it is present (21).

BUE is a transient structure persisting for ms. It sloughs off periodically as it becomes larger (13,15). Part of the broken BUE is carried away by the chip underside. The rest is randomly deposited on the machined surface. The process of BUE formation and destruction is repeated continuously during the cutting operation, unless measures are taken to eliminate it (21). Although BUE protects the cutting edge, its presence changes the cutting tool geometry (shear angle, etc.) causing instabilities in the chip formation process and damage to the machined surface (31,29). More insight on the formation mechanism of BUE is given further on in Section 2.3.3.2

BUE formation can be minimized or eliminated by using more positive rake angles, cutting tools with smooth surface finishes (< 5-10 μm), higher cutting speeds, small depths of cut, and active lubricants (29).

2.1.4 Fundamentals of orthogonal cutting

2.1.4.1 Introduction to mechanics of chip formation

The modelling and analysis of chip formation, i.e. attempts to devise equations which will predict quantitatively the behaviour of work materials during cutting from a knowledge of their properties, has been a continuing exercise over the past century (13). The essential features of the metal cutting process make its modelling a difficult task that continues to evolve over time (25).

The most difficult step in analysing the mechanics of chip formation is describing the stress-strain behaviour of the work material. Useful analyses must be based on realistic constitutive assumptions, and tests must be defined to estimate parameters in constitutive models (17).

2.1.4.2 Assumptions (Figure 2.5)

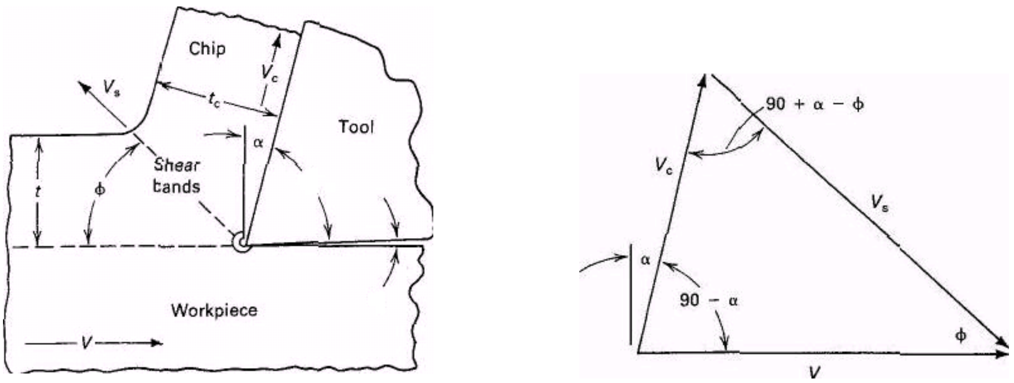

(a) Orthogonal model, **(b)** Velocity triangle

t, undeformed chip thickness (feed); t_c, chip thickness; Φ, shear plane angle; α, rake angle; V_s shear velocity; V_c, chip velocity; V, cutting speed

Figure 2.5: Schematic of orthogonal metal cutting mechanics (15)

A continuous chip is formed with no BUE, no corrugations at the topside and no curl. The primary shear zone is a plane. The deformation is idealized as a process of preferred slip planes. The cutting process is steady in time. The cutting tool is infinitely sharp, and no sliding friction between the flank face of the cutting tool and the workpiece occurs. In other words, forces on the flank face of the cutting tool are neglected. The work material is rigid-perfectly plastic, no side spread of chips occurs. Sliding friction takes place at the tool-chip interface. Stresses are uniformly distributed on the tool-chip interface (13,15,17).

2.1.4.3 Chip thickness ratio

The chip thickness ratio *r* (Figure 2.5) is expressed as (Equation 2.1):

$$r = \frac{t}{t_c} = \frac{V_c}{V} = \frac{\sin\phi}{\cos(\phi - \alpha)} \qquad \textbf{(2.1)}$$

With many ductile metals, the chip may be five times as thick as the undeformed chip thickness, or even more. Thus, it is important to emphasize that chip thickness ratio *r* will always be less than 1 and often in the range 0.2 - 0.5 (13).

Since chip thickness is greater than the undeformed chip thickness, the chip velocity V_c has to be lower than the cutting speed *V*. If the chip thickness ratio *r* is low, the shear plane angle *Φ* is small and the chip velocity is low (13,21).

2.1.4.4 Shear plane angle

The shear plane angle Φ has great significance in the mechanics of chip formation. It influences chip thickness, cutting forces and power requirements, heat and temperature determinations as well as vibration analyses associated with chip formation. Consequently, much attention has been focused on determining the relationships between the shear plane angle Φ, work material properties and cutting parameters (15,21).

Fundamentally, the shear plane angle Φ (Figure 2.5) is expressed as (Equation 2.2):

$$\phi = \arctan\left[\frac{r\cos\alpha}{1 - r\sin\alpha}\right] \tag{2.2}$$

The shear plane angle Φ can be measured statically by instantaneously interrupting the cutting operation through the use of quick-stop devices. Optical microscope and scanning electron microscope (SEM) are then used to observe the shear plane angle Φ (15).

The shear plane angle Φ can be computed dynamically during the cutting process if a reliable means of measuring chip velocity V_c can be found (Equations 2.1 and 2.2). Machining stages have been built that allow the cutting process to be performed inside a SEM and recorded at high-resolution for high-magnification examination of the deformation process (15).

2.1.4.7 Forces in orthogonal cutting: Merchant's circular force diagram

Merchant's circular force diagram (Figure 2.6) gives an analysis of the cutting forces involved in orthogonal cutting. Notwithstanding its weaknesses, Merchant's force circle remains an important milestone in metal cutting theory. Although there have been many attempts to update the model, change its boundary conditions and consider new material properties, it still remains a useful, direct way of appraising the power requirements and the shear plane angle. Usually cutting force F_c and feed force F_t are measured with dynamometers, whereas others forces (components or resultants) are derived analytically (13).

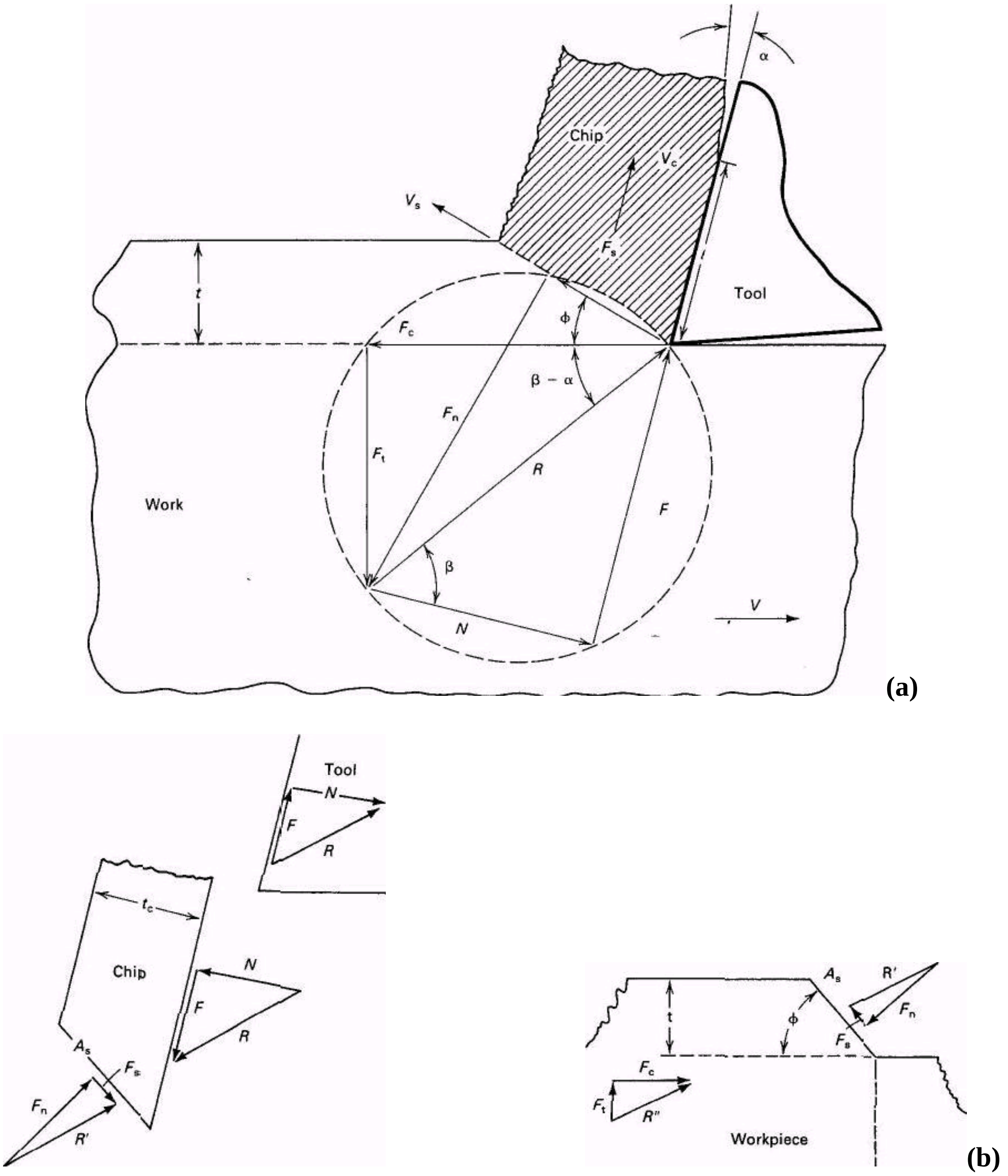

(a) Merchant's circular force diagram, **(b)** Chip free body diagram

t, undeformed chip thickness (feed); t_c, chip thickness; Φ, shear plane angle; β, friction angle, α, rake angle; V_s shear velocity; V_c, chip velocity; V, cutting speed; F, friction force; N, force normal to tool-chip interface; F_s, shear force; F_n, force normal to shear plane; F_c, cutting force; F_t, feed force; R, R',R", resultant force; l, contact length

Figure 2.6: Schematic of orthogonal metal cutting mechanics $^{(15)}$

The shear force F_s in the shear plane (Figure 2.6) is expressed as (Equation 2.3):

$$F_s = F_c \cos\phi - F_t \sin\phi \qquad \textbf{(2.3)}$$

The friction force *F* at the tool-chip interface (Figure 2.6) is expressed as (Equation 2.4):

$$F = F_c \sin\alpha + F_t \cos\alpha \qquad \textbf{(2.4)}$$

The force *N* normal to the tool-chip interface (Figure 2.6) is expressed as (Equation 2.5):

$$N = F_c \cos\alpha - F_t \sin\alpha \qquad \textbf{(2.5)}$$

The effective friction coefficient μ_e at the tool-chip interface (Figure 2.6) is expressed as (Equation 2.6):

$$\mu_e = \frac{F}{N} = \tan\beta \qquad \textbf{(2.6)}$$

The cutting force F_c (Figure 2.6) can be expressed as (Equation 2.7):

$$F_c = \frac{F_s \cos(\beta - \alpha)}{\cos(\phi + \beta - \alpha)} = \frac{tw\tau_s \cos(\beta - \alpha)}{\sin\phi \cos(\phi + \beta - \alpha)} \qquad \textbf{(2.7)}$$

where τ_s is the shear strength of the work material.

The feed force F_t (Figure 2.6) can be expressed as (Equation 2.8):

$$F_t = \frac{F_s \sin(\beta - \alpha)}{\cos(\phi + \beta - \alpha)} = \frac{tw\tau_s \sin(\beta - \alpha)}{\sin\phi \cos(\phi + \beta - \alpha)} \qquad \textbf{(2.8)}$$

where τ_s is the shear strength of the work material.

Differentiating the cutting force F_c (Equation 2.7) with respect to Φ gives (Equation 2.9):

$$\frac{dF_c}{d\phi} = \frac{tw\tau_s \cos(\beta - \alpha)\cos(2\phi + \beta - \alpha)}{\sin^2\phi \cos^2(\phi + \beta - \alpha)} \qquad \textbf{(2.9)}$$

By applying the assumption of minimum work (30), i.e. by considering $\frac{dF_c}{d\phi} = 0$, Merchant deduced that the shear plane angle should be (Equation 2.10):

$$\phi = 45° + \frac{\alpha}{2} - \frac{\beta}{2} \qquad \textbf{(2.10)}$$

An identical result is reached if it is assumed that the shear plane angle Φ assumes a value which maximizes the shear stress on the shear plane.

Stephenson and Agapiou (17) pointed out that in most cases the agreement between measured and predicted values of the shear angle Φ using various relationships is poor for a broad data set, except for some materials. These various predicted relationships are of value mainly because they provide physical insight and a convenient framework for interpreting experimental data, and not as accurate methods for predicting shear angle and cutting forces.

2.1.4.8 Stresses on the shear plane

Measurement of the cutting forces F_c and F_t and the chip thickness t_c (Figure 2.6) make it possible to explore the stresses involved in cutting. High shear and compressive stresses occur in the primary shear plane (13,25). The shear stress τ_s (Figure 2.6) required to form the chip is expressed as (Equation 2.11) (13,25):

$$\tau_s = \frac{(F_c \cos\phi - F_t \sin\phi)\sin\phi}{tw} \tag{2.11}$$

where w is the chip width (depth of cut) and t the undeformed chip thickness (feed).

The compressive stress σ_s on the shear plane (Figure 2.6) is expressed as (Equation 2.12) (13):

$$\sigma_s = \frac{(F_c \sin\phi + F_t \cos\phi)\sin\phi}{tw} \tag{2.12}$$

where w is the chip width (depth of cut) and t the undeformed chip thickness (feed).

The shear plane angle Φ is found to vary greatly under different conditions of cutting and thus do influence greatly cutting forces under conditions where the shear stress of the work material remains constant (13).

From the experimental data on primary shear zone shear stress (20), it emerges that the average remains relatively constant over a rather large range of cutting speeds (13). Thus, cutting forces (Equations 2.7 and 2.8) remain slightly constant when cutting speed increases. They increase in direct proportion to increments in feed and depth of cut (15).

2.1.4.9 Stress distributions on the rake face

High shear and compressive stresses occur on the rake face of the tool. The shear stress τ_f (Figure 2.6) at the tool-chip interface is estimated by (Equation 2.13) (25):

$$\tau_f = \frac{F_c \sin\alpha + F_t \cos\alpha}{wl} \tag{2.13}$$

where *w* is the chip width (depth of cut) and *l* the contact length.

The contact length *l* is always greater than the undeformed chip thickness *t*, and may be as much as ten times longer. It is usually uneven along the chip width (25).

The compressive stress σ_f (Figure 2.6) on the tool-chip interface is estimated by (Equation 2.14):

$$\sigma_f = \frac{(F_c \cos\alpha - F_t \sin\alpha)}{wl} \tag{2.14}$$

where *w* is the chip width (depth of cut) and *l* the contact length.

These stress models have been found to be useful approximations of the behaviour of chips as they slide over the cutting tool. However, experimental evidence of seizure at the tool-chip interface suggests that stresses are not uniformly distributed on the cutting tool rake face (Figure 2.7) (25).

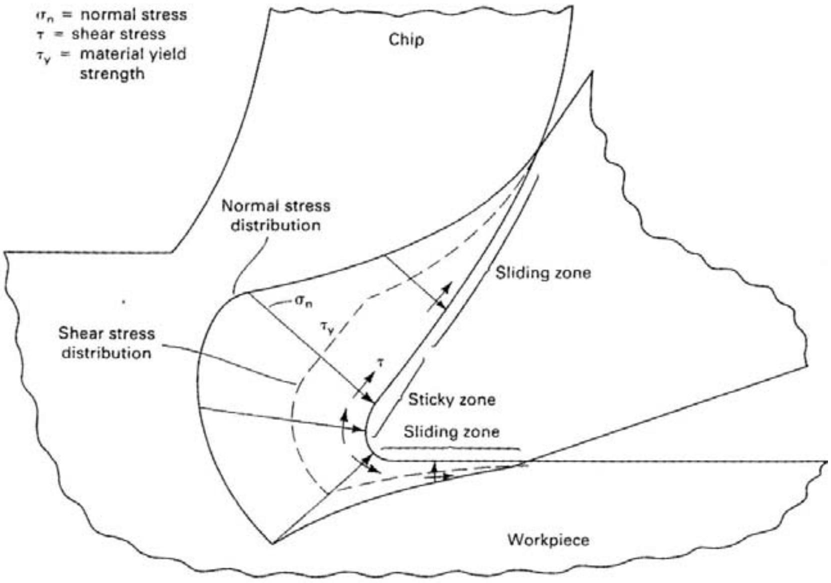

Figure 2.7: Model of stress distribution on the tool wear surfaces during cutting (31)

To sum up, although seizure and friction at the tool-chip interface is difficult to model, the contact length *l* is a most important parameter, having a very large influence on cutting forces, cutting tool life and many aspects of machinability (13,25).

2.1.5 Forces in metal cutting

When cutting many metals of commercial purity, the cutting forces are relatively high. This is particularly true for Fe, Ni, Cu and Al, among others. With these metals, the contact area on the rake face is very large, the shear plane angle is small and very thick, strong chips move away at low speeds. For these reasons, pure metals are particularly difficult to machine. However, few exceptions were reported. For instance, when cutting commercially pure Mg, Ti and Zr, the contact area on the rake face and cutting forces are much smaller and chips are thin. Solid solution strengthening a pure metal often reduces the related cutting forces, particularly at low cutting speeds, because the contact length on the rake face becomes shorter (13).

Cutting forces are also influenced by cutting tool geometry, particularly the rake angle (Equations 2.7 and 2.8). Increase in rake angle lowers cutting forces, but reduces the strength of the cutting tool edge and may lead to catastrophic fracture at a certain stage (13,15,17).

Cutting tool materials can also influence cutting forces. When one major type of cutting tool material is substituted for another, the forces may be altered considerably, even if the cutting conditions are kept constant. This is caused mainly by changes in the area of seizure (13) and in tool wear characteristics.

Cutting lubricants can, by penetrating from the periphery, act to restrict the seizure to a small region and thus greatly reduce cutting forces. They are most effective in doing this at very low cutting speeds and become largely ineffective in the high cutting speed range (13,32).

It is common experience when cutting most metals and alloys that beyond the range of cutting speeds corresponding to the formation of a BUE, cutting forces gradually decrease as cutting speed is increased. Such a decrease in cutting forces with cutting speed is partly due to a decrease in contact area and partly due to a decrease in flow stress due to thermal softening in the flow-zone as its temperature rises with increasing cutting speed (12,13,17).

In reality, the largest fall in cutting forces occurs in the low-to-medium cutting speed range, from about 30 to 200 m/min. For almost all metallic materials, over the cutting speed range from about 200 to 3000 m/min, cutting force curves flatten out and decrease by only 10-15%. This small decrease in mean cutting forces is a minor advantage. It is greatly outweighed by cutting tool wear hassles that arise from the imposed cutting force fluctuations that take place with the formation of shear-localized chips (13).

Cutting forces usually climb as the cutting tool is worn, the clearance angle is destroyed, and the contact area on the flank face is increased by flank wear (Figure 2.7) (13,17).

2.1.6 Heat in metal cutting

2.1.6.1 Introduction

Of the total energy involved in metal cutting operations, nearly all of it (~ 98%) is dissipated in the form of heat near the cutting edge of the tool which, in turn, particularly because of the very short time of heat dissipation, raises the temperature in the cutting zone. The remaining energy (~ 2%) is retained as strain energy in the chips (13,14).

Chips, work and cutting tool act as major heat sinks in metal cutting operations. Figure 2.8 shows the distribution of the heat generated to these three major sinks as a function of cutting speed which is the process parameter with the greatest influence on cutting temperatures. The cutting lubricant also acts as heat sink to the heat generated (12,21).

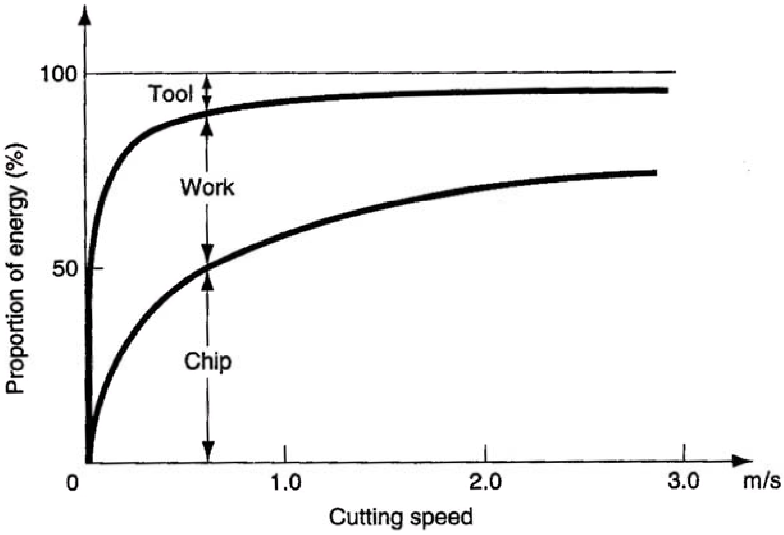

Figure 2.8: Typical distribution of total cutting energy between the cutting tool, the work and the chips as a function of cutting speed (14)

Since cutting forces generally do not vary strongly with cutting speed, increasing the cutting speed increases the rate of heat generation in the cutting zone. Increasing the feed also increases heat generation and cutting temperatures. For moderate ranges of these variables, the tool-chip interface temperature increases with the square root of the cutting speed but the third root of the feed (33). Other parameters which affect the cutting force, such as the depth of cut and the rake angle, also influence cutting temperatures (17,21).

Hardness, ductility, and strain hardening of work materials strongly influence cutting forces and cutting temperatures. Cutting temperatures are higher for harder work materials because cutting forces and heat generation increase. For work materials of similar hardness, cutting temperatures increase with ductility, since more ductile materials can absorb more energy through plastic deformation. For instance, at a cutting speed of ± 300 m/min, the tool-chip interface temperature is usually ± 750°C for brittle flake graphite cast iron with a hardness of 200 HB, and over ± 1000°C for ductile mild steel with a hardness of 200 HB (17,21).

High thermal conductivity and heat capacity of the work material generally decrease temperatures in the cutting zone. Similarly, high thermal conductivity and heat capacity of the cutting tool material and the type of lubricant used also reduces temperatures, although the effect for cutting tool material does not appear to be as marked as for the work material (17,21).

Temperatures in the primary shear zone influence the mechanical properties of the work material and thus the cutting forces. For this reason, most of the more complete analyses of the mechanics of chip formation use temperature-dependent constitutive models.

Peak tool-chip interface temperatures are influenced by the cutting tool shape (nose radius and wedge angle) (34). Increasing the nose radius reduces the peak temperature by reducing the maximum undeformed chip thickness (feed) and distributing frictional energy more evenly over the cutting edge. Reducing the wedge angle increases the peak temperature by reducing the space through which heat can diffuse from the cutting edge through the bulk of the tool (17).

It has to be mentioned that basically, cutting temperatures are difficult to measure or to model (analytically or with finite element methods). The same remains valid for temperature distribution in the cutting zones (13,17,35).

The limitations imposed by cutting temperatures in terms of thermally activated cutting tool wear mechanisms, cutting speed and feed, particularly in the machining of higher melting point metals and alloys such as steels, cast irons, etc. have been the stimulus to the advanced cutting tool material development of the last years. Problems remain however, and even with present day cutting tool materials, cutting speeds may be limited to 30 m/min or less when cutting for instance certain creep resistant alloys (13).

2.1.6.2 Heat in the primary shear zone, temperature of the chip bulk

The primary shear zone is the major heat source in metal cutting operations. As the cutting speed is raised, there is an increase in temperature, but the temperature of the bulk of the chip tends to become constant at high cutting speeds. Temper colour of chips which is caused by a thin layer of oxide on their surfaces, is the most obvious indication of their temperature

(Figure 2.9). For instance, when dry cutting steel at high cutting speed, chips are seen to change colour, usually to brown or blue, a few seconds after leaving the cutting tool (13).

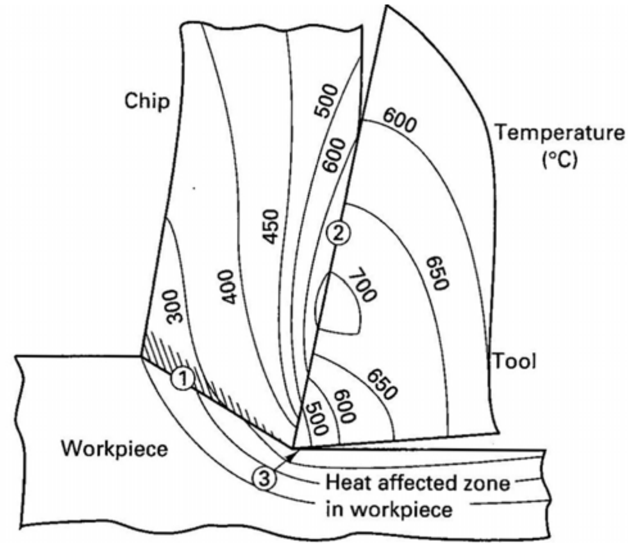

Figure 2.9: Typical temperature distribution in the cutting zone (12)

2.1.6.3 Heat at the tool-chip interface (13)

BUE and flow zone constitute the main heat sources raising the cutting tool temperature. The flow-zone material is continuously heated so that an increase in temperature can be expected away from the cutting tool edge. This is unlike from the bulk of the chip, which is heated only on the primary shear zone and no further as the chip flows over the tool.

Since the temperature in the flow-zone is higher than that of the bulk of the chip, there is a heat flow from the flow-zone into the bulk of the chip. After the chip leaves the rake face of the cutting tool, that part of the flow-zone which passes off on the under surface of the chip cools very rapidly to the temperature of the bulk of the chip, since cooling by metallic conduction is very efficient.

The conditions of heat loss from the flow-zone into the cutting tool are different from the latter because heat flows continuously into the same small volume of cutting tool material. A stable temperature gradient is built up within the cutting tool (Figure 2.9).

At very high cutting speeds, the tool-chip interface temperature does not vary with the square root of the cutting speed and the third root of the feed as indicated in Section 2.1.6.1, but rather approaches asymptotically the melting point of the work material. However, this view is in conflict with the concept of temperature saturation at the tool-chip interface suggested by Subramanian and co-workers (22).

2.1.6.4 Heat flow at the cutting tool flank face

Once the width of the flank wear scar increases by a long way (Figure 2.7), seizure often occurs at the tool-work interface. So, the flow zone in this region becomes a considerable heat source. Temperatures generated at the flank wear scar may be higher than on the rake face of the same cutting tool because the work material moves across this surface at the cutting speed of the operation, while the chip velocity over the rake face may be a half or a third of this cutting speed, or lower. Generation of high temperatures in this region is usually followed immediately by collapse of the cutting tool (13).

Temperatures on the flank face of the cutting tool affect the surface finish and surface integrity of the machined surface. Moderate levels of these temperatures induce residual stresses in the machined surface which, in turn, may cause surface damage such as tearing and cracking (13). High levels of these temperatures may leave a burned or hardened layer on the machined part, adversely affecting its properties such as fatigue life and corrosion resistance (17). They also cause dimensional changes in the part being machined, making it difficult to control dimensional accuracy and tolerances (21).

2.1.6.6 Measured temperature distribution in cutting tools

A typical temperature distribution in the cutting zone is shown in Figure 2.9. It shows that the maximum temperature is about halfway up the rake face of the cutting tool.

Figure 2.10 shows an example of temperature distributions respectively on the flank face and rake face of K3H carbide cutting tool used in the turning of AISI 52100 steel. It shows that temperature increases with cutting speed and that the highest temperature is almost 1100 °C.

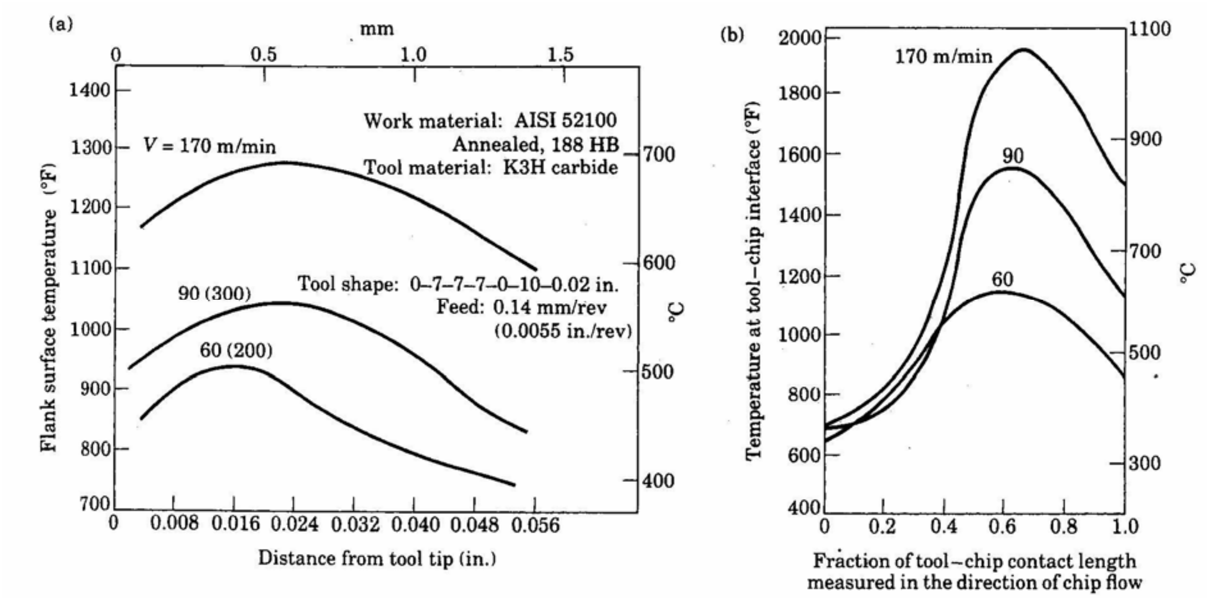

(a) Flank face temperature distribution, **(b)** Tool-chip interface temperature distribution

Figure 2.10: Temperatures developed in turning AISI 52100 steel (21)

2.1.7 Basic types of chips produced in metal-cutting

In metal cutting, the type of chips produced influence significantly the surface finish of the machined surface and the overall cutting operation in terms of tool life, vibrations and chatter (21). Basically, work material properties together with cutting parameters, i.e. dynamic flow stress behaviour of work materials with regard to strain, strain rate and temperature (13,22), control the whole chip formation process (15).

Indeed, work materials have different responses to very high strains, extremely high strain rates and high temperatures, characteristic of metal cutting, based on their properties (13) among which ductility plays a key-role. Such responses account for the variety of chips that can be formed.

All in all, significant deviations from the ideal model of continuous chip are observed in metal cutting. Many types of chips (Figures 2.11 and 2.12) can be produced. Of course, not all work materials exhibit all those basic types of chips (13).

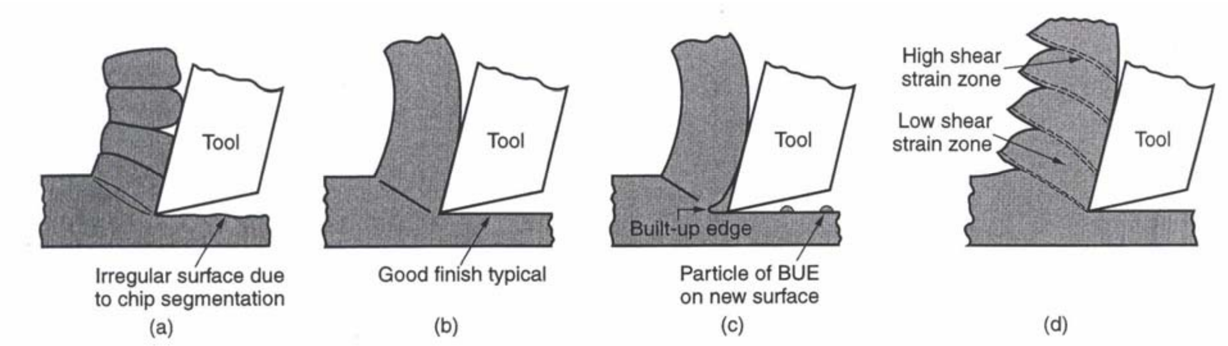

(a) discontinuous, **(b)** continuous, **(c)** continuous with BUE, **(d)** segmented or shear-localized

Figure 2.11: Basic types of chips produced in metal cutting (14)

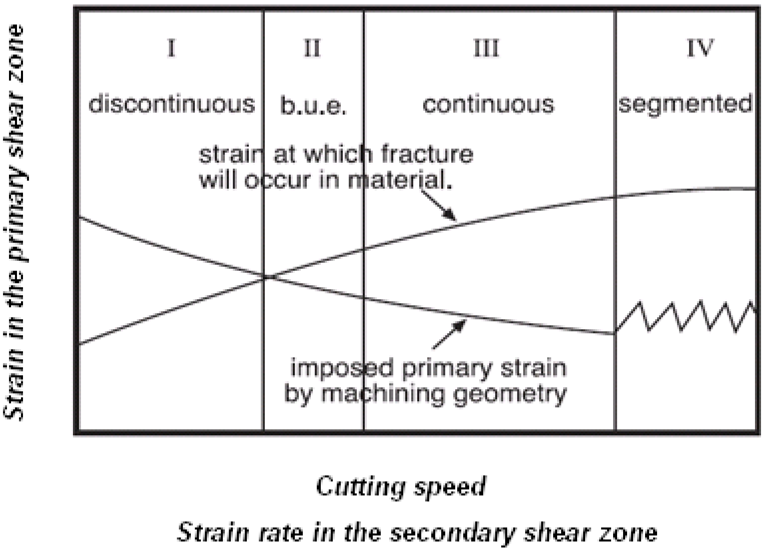

Figure 2.12: Basic types of chips produced in metal cutting: schematic variation of strain in the primary shear zone with cutting speed and hence strain rate in the secondary shear zone (13)

2.1.7.1 Discontinuous chips

Discontinuous chips (Figure 2.11 (a)) consist of segments that may be firmly or loosely attached to each other (21). As such, discontinuous chips have the practical advantage that they are easily cleared from the cutting area. Of course, continuous and discontinuous chips are not two sharply defined categories; every shade of gradation between the two types can be observed sometimes (13).

Discontinuous chips usually form when cutting heavily work hardened or inherently brittle materials such as flake graphite cast irons. Discontinuous chips form also when cutting relatively ductile materials at very low cutting speeds (Figure 2.12, Range I) (13,17,21).

Discontinuous chips form when cutting work materials with second phase particles. Indeed, second phase particles in the work material produce stress concentrations which promote crack nucleation and propagation in the primary shear zone (17,21).

Low or negative rake angles as well as lack of active lubricants favour the occurrence of seizure conditions at the tool-chip interface, then promoting discontinuous chip formation. The latter formation is supported by the cyclic occurrence of a stick-slip mechanism at the tool chip-interface (13,17,21).

Low stiffness of machine-tools increases the elastic strain energy stored in the system, especially at high feed, and promotes crack propagation and fracture in the primary shear zone (discontinuous chip formation). Large depths of cut also promote the formation of discontinuous chips (17,21).

Discontinuous chip formation leaves behind irregularities on the machined surface due to chip segmentation (Figure 2.11 (a)). Discontinuous chip formation is inherently unsteady and produces dynamic cutting forces. At low cutting speeds the dynamic cutting forces are significant, especially for low or negative rake angles (17,36).

2.1.7.2 Continuous chips

Continuous chips (Figure 2.11 (b)) form generally when cutting relatively highly ductile work materials such as conventional Al-based alloys and low carbon steels at relatively high cutting speeds and / or with high rake angles (13,14,21).

The elimination of the cold-welding conditions at the rake face, consecutive to relatively high cutting speeds (Figure 2.12, Range III), allows continuous chips to form under conditions where the primary shear zone strain is significantly less than the fracture strain. But still, there is seizure at the rake face (13). The plastic deformation of the work material takes place inside adiabatic shear bands within a narrow primary shear zone under conditions of shear instability. Continuous chips can form with a very narrow primary shear zone or a relatively large primary shear zone, particularly when cutting speeds or rake angles are relatively low (21).

In the opinion of Gekonde and Subramanian (37), continuous chips form under conditions where the critical strain for major microsoftening event in the primary shear zone is higher than that corresponding to the equilibrium shear angle.

Continuous chips have generally a long tool-chip contact length. As such, they undergo extensive plastic deformation in the secondary shear zone. Continuous chips are long. Often, they have a considerable strength and a characteristic curl. They may adopt many shapes (13).

Because of relatively high cutting temperatures, continuous chips form without any BUE. Instead, they may, because of seizure at the tool-chip interface, form with a flow zone, often very smooth. Continuous chips generally produce good surface finish. However, because of the difficulty of chip control, continuous chips are not always desirable (13,17,21).

2.1.7.3 BUE chips

BUE chips (Figure 2.11 (c)) are continuous chips which form under cutting conditions where a BUE sets in periodically on the cutting tool. BUE chips usually form when cutting many work materials at relatively low cutting speeds - particularly soft and ductile materials (17).

In this particular case, cold-welding occurs on the rake face because of the relatively low cutting speeds (Figure 2.12, Range II). Subsequent to the BUE formation, the increase in effective rake angle reduces the primary shear zone strain to such extent that the chip is continuous (13).

2.1.7.4 Shear-localized chips

Shear-localized chips (Figure 2.11 (d)) are semi-continuous chips consisting of individual segments that are slightly deformed and joined by exceptionally narrow bands that are heavily strained (21,38). Shear-localized chips generally form when cutting hardened steels, austenitic stainless steels, Ti-based alloys and Ni-based superalloys (13,17,21).

Shear-localized chips (Figure 2.12, Range IV) start forming from the cutting speed at which the shear plane angle starts oscillating between a maximum and a minimum in a periodic cycle. However, the precise physical event that triggers the onset of shear-localized chip formation at a critical threshold cutting speed is still the subject of investigations (13,26). From the research conducted so far, three theories emerged: the thermo-mechanical primary shear zone instability model (16), the secondary shear zone strain rate model (13) and quite recently the major microsoftening event model (22).

2.1.7.5 The thermomechanical primary shear zone instability model

This model considers that any event that causes catastrophic reduction of flow stress in the primary shear zone such as adiabatic shearing, inherent material weakness such as microcracks, inclusions, etc., is the root cause of shear localization. It is considered that the adiabatic shearing of a work material is inherent to its limited slip systems, high hardness and poor thermal properties. This model does not consider any possibility of occurrence of shear instability in the secondary shear zone.

2.1.7.6 The secondary shear zone strain rate model

Trent and Wright (13) pointed out that adiabatic shear bands form even during continuous chip formation. Therefore they consider that there is no reason for such adiabatic shear bands to become suddenly unstable and trigger shear localization in the primary shear zone as proposed by the thermomechanical primary shear zone instability model. Besides, when shear-localized chip formation is triggered the instantaneous shear plane angle suddenly decreases.

This model considers that shear-localized chips start forming at a cutting speed at which the effect of strain-rate in the secondary shear zone becomes important and can reintroduce a stick-slip mechanism at the tool-chip interface (13,39).

Strain hardening and strain rate hardening are thought to be the key-phenomena at the origin of the stick step of the stick-slip mechanism, i.e. the seizure at the tool-chip interface. Thermal softening is thought to be the key-phenomenon at the origin of the slip step of such mechanism.

2.1.7.7 The major microsoftening event model

Subramanian and co-workers (22) argue that the exceptionally steep decrease in flow stress that occurs in the primary shear zone from a critical threshold cutting speed and that is considered to be the root of shear-localized chip formation in the thermomechanical primary shear zone instability model, should be related not to a thermally activated dislocation motion mechanism, but on the contrary to the occurrence of a major microsoftening event.

In other words and as already mentioned in Section 2.1.3.2, thermal softening should be differentiated from dynamic softening which is a result of a major microstructural softening event such as dynamic recrystallization, phase transformation or geometrical softening (incompatibility of deformation between the matrix and second-phase particles).

Thus, when rotating towards the equilibrium position, the primary shear plane reaches the critical shear plane angle corresponding to one of the major microsoftening events (critical strain for dynamic recrystallization, temperature for phase transformation, or critical strain for fracture) before reaching the equilibrium shear plane angle (26).

In addition, Subramanian and co-workers (22) support and complete the secondary shear zone strain model by arguing that the occurrence of a major microsoftening event in the secondary shear zone which, follows from the occurrence of seizure, causes shear localization in the secondary shear zone.

Such shear localization triggers a decrease of the shear plane angle. In turn, such a decrease in shear plane angle triggers the occurrence of a major microsoftening event in the primary shear zone (shear localization in the primary shear zone).

2.1.8 Surface finish

Surface finish and dimensional accuracy of a machined part depend on many factors that can be grouped as geometric factors, work material factors, and vibration and machine tool factors (14).

2.1.8.1 Geometric factors

Geometric factors include the type of machining operation, cutting tool geometry, most importantly the cutting tool-nose radius and feed. The surface geometry that would result from these factors is referred to as the ideal surface finish (14).

Sharpness and integrity of the cutting edge are probably the most important issues to focus on (13). Thus, when assuming a sharp cutting tool edge, the effects of these geometric factors on the ideal surface finish are summarized in Figure 2.13. Large nose radius, small feed and small cutting-edge angle (ECEA) improve the surface finish. When tool wear becomes significant, especially nose radius wear, surface finish deteriorates compared to the ideal values (14).

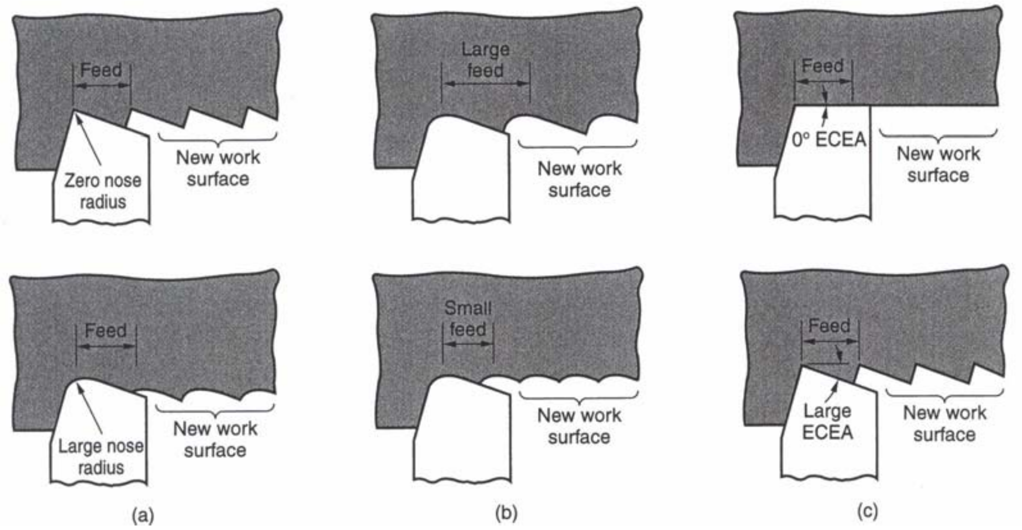

(a) effect of nose radius, **(b)** effect of feed, **(c)** effect of end cutting-edge angle (ECEA)

Figure 2.13: Effect of geometric factors on the ideal surface finish (single-point cutting tools) (14)

2.1.8.2 Work material factors

Achieving the ideal surface finish is not possible because of factors related to the work material and its interaction with the cutting tool. Essentially, these factors include the following (14):

- BUE effects

  BUE has the greatest influence on surface finish. The BUE damage is manifested in scuff marks, which deviate from the straight grooves that would result from normal machining, resulting in a rough surface finish (21). BUE changes the depth of cut (31).

- Damage to the machined surface caused by the chip curling back into the work
- Tearing of the work surface during chip formation

  Such tearing occurs when machining soft and ductile materials at low cutting speeds and low rake angles. As already mentioned in Section 2.1.3.1, during continuous chip formation, deformation may take place along a wide primary shear zone with curved boundaries (Figure 2.14). The lower curved boundary can settle below the machined surface, subjecting it to distortion and tearing (21).
- Cracks in the machined surface (when machining brittle materials)
- Friction between the flank wear scar and the machined surface (cf Section 2.1.6.4)

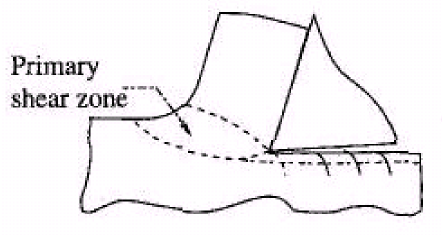

Figure 2.14: Continuous chip with large primary shear zone (21)

To sum-up, the characteristics of machined surfaces are greatly dependent on the flow patterns, stresses and temperatures at the all-important cutting tool edge (13). An increase in cutting speed or rake angle generally improves surface finish (14).

2.1.8.3 Vibration and machine tool factors

These factors include chatter or vibration in the machine or cutting tool, deflections in the fixturing and backlash in the feed mechanism. These factors adversely affect the surface finish and dimensional accuracy of the machined part by cyclically changing the dimensions of the cut. The course of action to take in this particular regard, especially in case of formation of discontinuous chips or shear-localized chips, comprises among others the reduction of cutting forces in particular through the reduction of feed and depth of the cut (14,21).

2.2 POLYCRYSTALLINE CUBIC BORON NITRIDE (PCBN) CUTTING TOOL MATERIALS

2.2.1 Introduction to cutting tool materials

Cutting tools must be made of materials capable of withstanding the high stresses and temperatures generated during chip formation. Essentially, the cutting ability of a material depends on the combination of its properties, the most important of these being: the hardness, the resistance to chipping (toughness), the abrasion wear resistance and the resistance to thermal softening (hot hardness) (40-42). The relative importance of these properties varies with the machining conditions (Figure 2.15). Basically, because of the enormous variety of cutting conditions of metals and alloys, a variety of cutting tool materials remains in use, and will continue to do so. No single cutting tool material exhibits all the desired properties of an ideal cutting tool material (42,43).

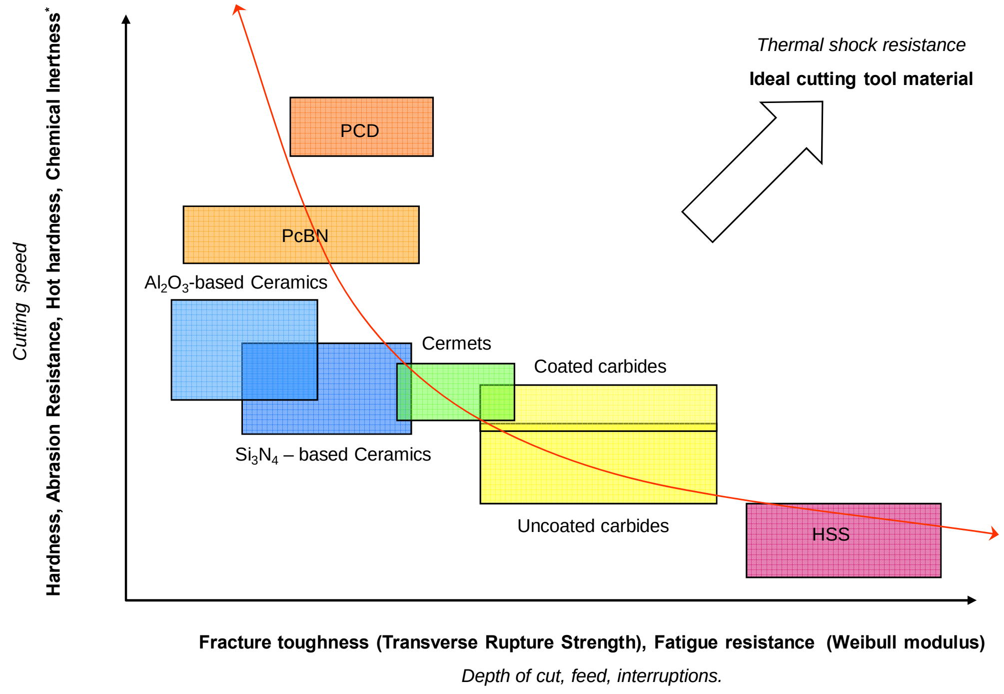

*The cutting speed and chemical inertness scale does not apply scrupulously.

Figure 2.15: Principal cutting tool material properties versus machining conditions (42,44,45)

A cutting tool that deforms or collapses for lack of strength is useless. High hardness generally gives increased tool life. However, the hardness must be balanced against the toughness required for the application. A cutting tool that lacks adequate ductility will fail prematurely. Strength and toughness are important during interrupted cuts and at high feed and depth of cut (40,41,44). Fracture toughness and fatigue resistance (Weibull modulus) determine allowable depths of cut and feeds (Figure 2.15) (42).

The abrasion wear resistance, the hot hardness and the chemical inertness are principally important as cutting speed increases. High speed machining requires a high initial hardness and a maximum resistance to thermal softening (40,44). As already mentioned in Section 2.1.6.1, hardness, abrasion wear resistance, hot hardness, chemical inertness as well as thermal conductivity determine the maximum cutting speed at which a cutting tool can be used (Figure 2.15) (42).

Theoretical and empirical relationships, usually produced from pin–on–disc measurements under constant load, have been derived relating abrasion wear resistance of a cutting tool material to its mechanical properties that reflect the difficulty of removing a chip of material from its surface (46,47). One such relationship applicable to relatively low fracture toughness cutting tool material is (Equation 2.15):

$$W_r = \frac{K_{Ic}^{\ 0.5}.H^{1.43}}{E^{0.8}} \qquad \textbf{(2.15)}$$

where W_r is the abrasion wear resistance figure of merit, K_{Ic} is the fracture toughness (MPa.m$^{1/2}$), E is the Young's modulus (GPa) and H is Knoop hardness (GPa) $^{(47)}$.

Thermal shock resistance is desired when high mechanical stresses, high cutting speeds, or cutting lubricants are involved. The literature mentioned more than one figures of merit for thermal shock resistance. One such figure of merit is (Equation 2.16):

$$Th_r = \frac{k.K_{Ic}}{E.\alpha} \qquad \textbf{(2.16)}$$

where Th_r is the thermal shock resistance figure of merit, K_{Ic} is the fracture toughness (MPa.m$^{1/2}$), E is the Young's modulus (GPa), k is the thermal conductivity (Wm^{-1}K^{-1}) and α is the thermal expansion coefficient (μm/m°K) $^{(44)}$.

2.2.2 Cubic boron nitride (cBN)

Boron nitride is a synthetic polymorph material. According to the pressure and temperature conditions (Figure 2.16), boron nitride can be typically found under four crystalline forms, namely cubic boron nitride (cBN), hexagonal boron nitride (hBN), rhombohedral boron nitride (rBN), and wurtzitic cubic boron nitride (wBN). cBN and wBN are the denser ultrahard forms of boron nitride $^{(48)}$.

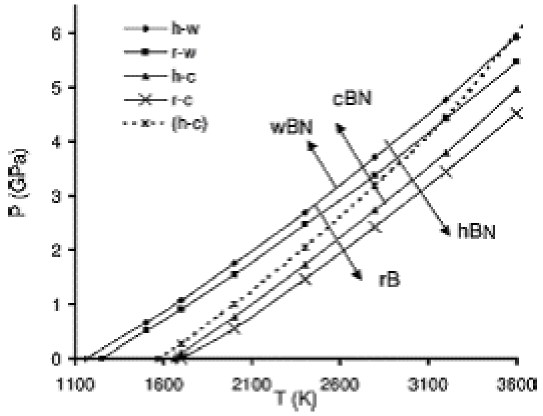

Figure 2.16: p-T phase diagram of boron nitride $^{(49)}$

Under standard conditions, cBN is the stable form of boron nitride and hBN its metastable form. Thermodynamic calculations show that cBN is stable up to 1000°C at atmospheric pressure. It was reported that the cBN- hBN phase transition occurs within a wide range of temperature (1000 - 1800°C) $^{(50)}$.

cBN has a zinc blende structure. This structure comprises two interpenetrating FCC lattices, one of B and another one of N. Bonding is principally covalent, with some ionic bonding present. cBN is the second hardest material after diamond. The hardness of cBN is anisotropic, with values ranging from 29.89 GPa in the [110] direction on the (001) plane to 43.12 GPa in the [100] direction, on the same plane (51).

cBN crystals are formed by conversion of hBN crystals using temperatures in the range 1400-1750 °C and pressure of the order of 5-8 GPa, usually under the presence of catalysts (52).

2.2.3 PcBN cutting tool materials

PcBN cutting tool materials are synthesized in the form of master blanks or substrate backed compact structures. The substrate material is typically a cemented metal carbide whose binder is Co, Ni, Fe or a mixture thereof (53).

The synthesis of PcBN cutting tool material consists of sintering randomly orientated cBN grains. Since cBN has predominantly covalent atomic bonding, sintering of highly pure cBN compacts is normally difficult and thus requires high temperature and ultra high pressure conditions for full densification (54). Therefore fully dense PcBN cutting tool materials are usually obtained by using sintering aids which function as catalysts or binders (47,55).

Composites or compounds of Group 4, 5 or 6 transition metals are most frequently used as binder phases in the synthesis of PcBN cutting tool materials. Among these particular compounds, TiN and TiC exhibit the highest chemical activity towards cBN (56,57). Hence, TiC with Al compounds, TiN with Al compounds, Al (AlB_2, AlN, α AlB_{12}), Co-W and Al compounds (58) are among binder phases that are often used in the synthesis of PcBN cutting tool materials.

The high temperature-ultra high pressure sintering of PcBN cutting tool materials is conducted typically at temperatures comprised in the range 1200-1600°C and pressures of the order of 5-7 GPa (52,58). Sintering time varies, typically being 3-120 min (53).

During this high temperature-ultra high pressure synthesis, chemical reactions between cBN grains and sintering aids occur, resulting in the formation of some new phases. The prediction of these new phases as well as the fundamental understanding of their mechanisms of formation is of critical importance in the selection of the appropriate binder phase or catalyst (57). Indeed, the performance of PcBN cutting tool materials is not solely dependent upon the bulk mechanical properties. Interactions of microstructural constituents of the tool and the work material can be vital to cutting tool performance (59).

The grade of PcBN cutting tool materials is determined by the cBN content, cBN grain size, grain size distribution, composition of the binder phase, and degree of sintering (47,58,60).

The range of cBN content in the different PcBN cutting tool materials varies in the range 40-90 vol. %. It comprises between 80-90 and 45-50 vol. % cBN respectively in high and low cBN content PcBN cutting tool materials.

PcBN cutting tool materials with high cBN content are typically sintered with a W-Co-Al based binder; a Ti-Al ceramic binder or a Al ceramic binder (52,55,58). Low cBN content PcBN cutting tool materials are typically sintered with a ceramic binder: TiC, TiN or a mixture thereof (56,57).

When the cBN content exceeds 80 vol. %, the contiguity of cBN (amount of cBN-to-cBN direct contacts) is considerable. During the sintering of such PcBN cutting tool materials, cBN grains form a skeletal structure. When the cBN content is lower, e.g. in the range 40-60 vol. %, the contiguity of cBN is limited (53,61).

When the cBN content in the PcBN cutting tool material is less than 70 vol. %, in order to prevent or reduce grain growth of the binder phase during the high temperature-ultra high pressure synthesis or even the use of PcBN cutting tool material, ultrafine powders of a secondary hard phase are purposely incorporated in the binder phase as grain growth inhibitors. Ceramic phases are suggested for this particular purpose. Examples of suitable ceramic hard phases are carbides, nitrides, borides and carbonitrides of a Group 4, 5 or 6 transition metal, Al_2O_3, and mixtures thereof (53,54).

Once produced, PcBN master blanks or PcBN substrate backed structures are then cut into smaller blanks before being ground to various shapes and sizes suitable for tipping different type of cutting tool. PcBN cutting tools are available in either layered or solid format (47,55).

2.2.4 Microstructure of PcBN cutting tool materials

Two of the many microstructures that can be produced in PcBN cutting tool material grades are shown in Figures 2.17 and 2.18. Figure 2.19 shows some of the sintering reaction products that can form in PcBN cutting tool materials. Due to the ultra high pressure applied during the synthesis of PcBN cutting tool materials, cBN grains exhibit high levels of plastic deformation in areas of cBN-cBN direct contact (62). Stresses and structural defects such as dislocations and twins (Figure 2.20) may be introduced in the cBN grains.

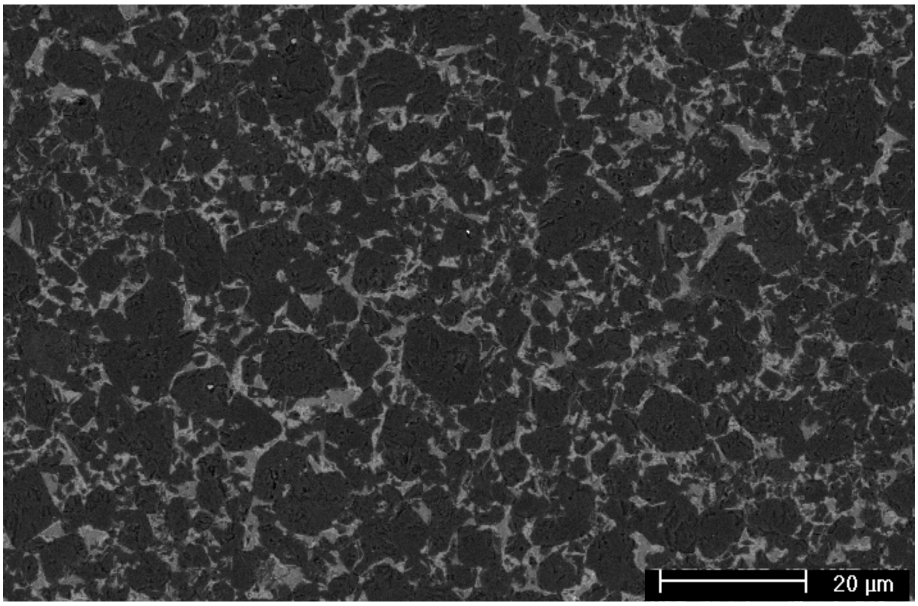

Dark phase, cBN; grey phases, AlB_2, AlN and probably AlB_{12}

Figure 2.17: High cBN content PcBN cutting tool material. SEM, BSE image (courtesy Element Six)

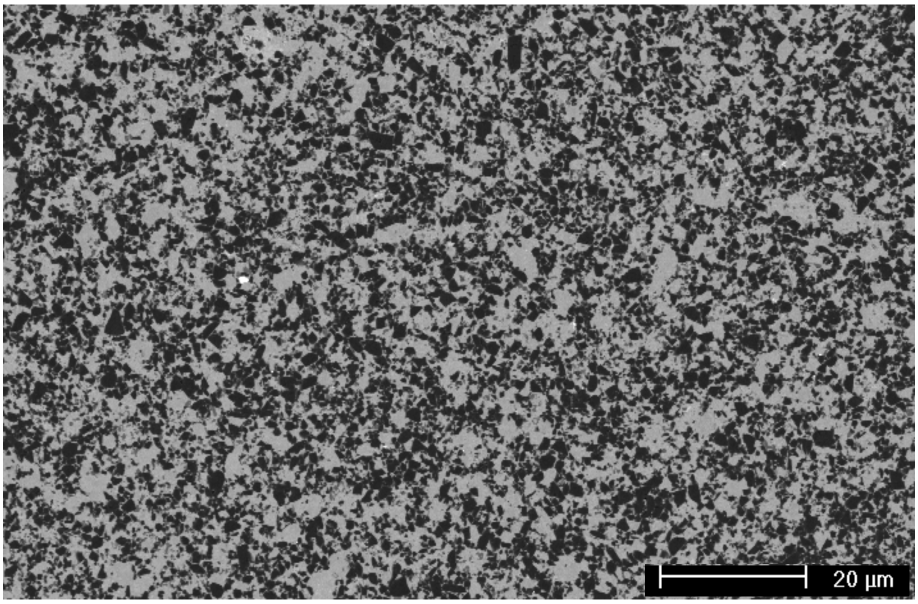

Dark phase, cBN; grey phase, TiC binder; white phase, W-bearing compounds

Figure 2.18: Low cBN content PcBN cutting tool material. SEM, BSE image (courtesy Element Six)

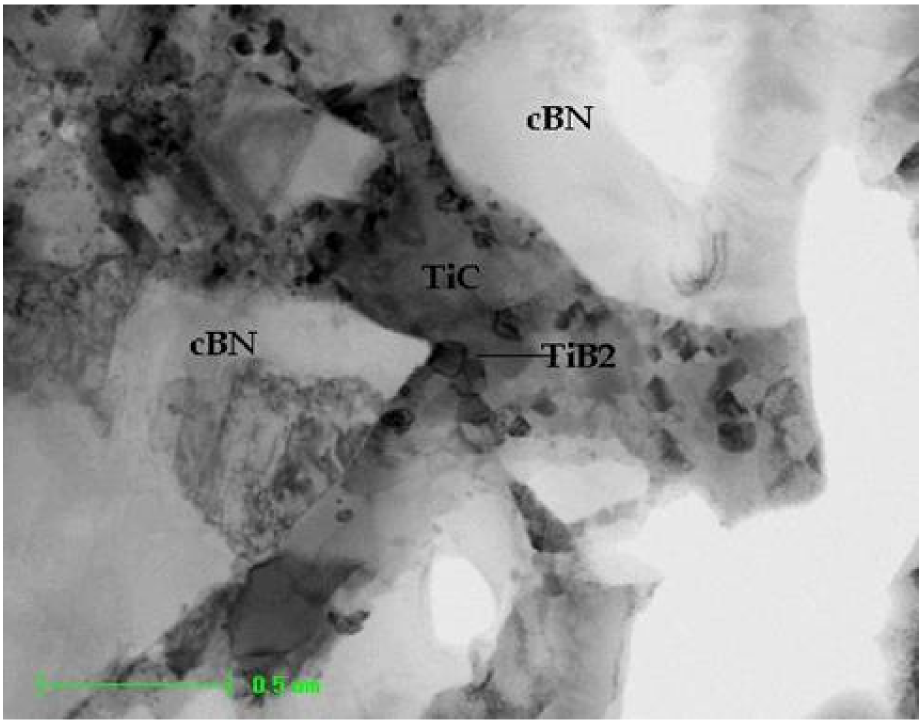

Figure 2.19: Interfaces cBN-TiC showing the formation of TiB_2 in a low PcBN cutting tool material. STEM, bright field image (courtesy Element Six)

Figure 2.20: Twins formed in cBN grains in PcBN cutting tool material. TEM, bright field image (57)

2.2.5 Thermal softening of PcBN cutting tool materials

The thermal softening of PcBN cutting tool material represents a limitation, particularly in high speed machining. Figure 2.21 shows an illustration of thermal softening of cBN, TiC and TiN single crystals. These curves give an indication of the expected thermal softening of cBN-TiC and cBN-TiN cutting tool materials.

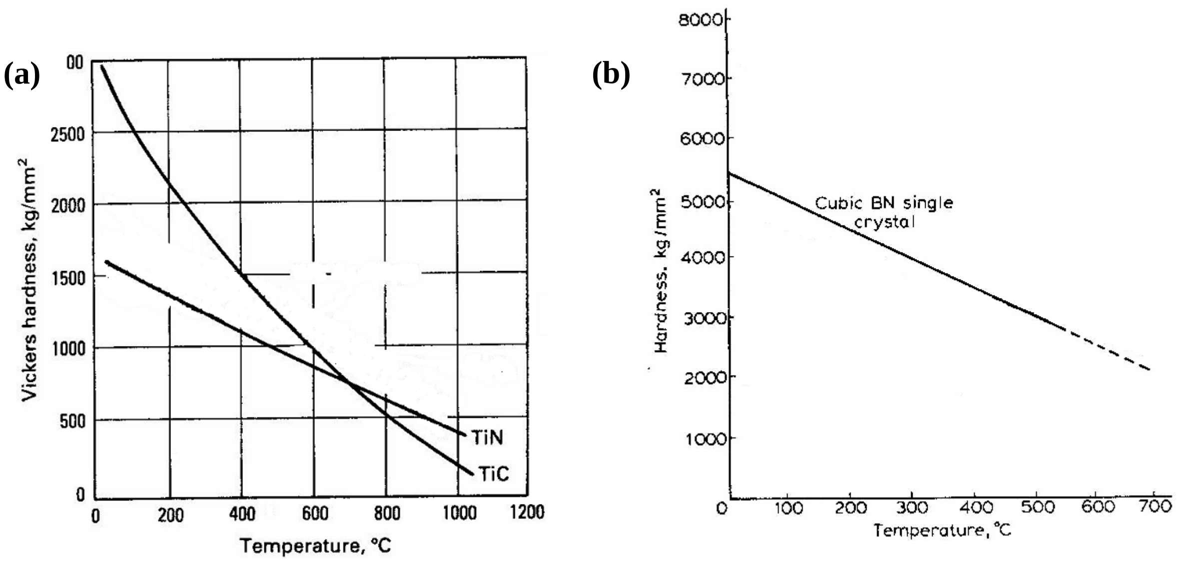

Figure 2.21: **(a)** Thermal softening of TiC and TiN single crystals (63)

(b) Thermal softening of cBN single crystals (64)

It was reported that annealing of PcBN cutting tools in vacuum induces thermal softening, probably by the reduction of dislocations and twins in cBN grains and / or grain growth in the binder phase (57). However, no evidence of cBN grain regrowth has been found so far.

The thermal softening of PcBN cutting tool materials appears to be mainly due to the onset of more and more active plastic deformation mechanisms that set in as temperature increases. Further work would be necessary to clarify the deformation mechanisms of composites like PcBN cutting tool materials (65).

The thermal softening of PcBN cutting tool materials may be followed by a thermally induced brittle-to-ductile transition. It was reported (58,65) that in cBN-TiC and cBN-TiN cutting tool materials, the flow stress decreases relatively rapidly as the temperature increases, with the brittle-to-ductile transition temperatures being identified as 794 °C, 782 °C, and 873 °C respectively for the 80, 50 and 45 wt% cBN content materials. These brittle-to-ductile transition temperatures would be very close to temperatures corresponding to change of plastic deformation mechanisms. Binder phase composition, cBN content (contiguity) and cBN grain size were found to play a considerable role in the thermal softening of PcBN cutting tool materials.

Although cBN is the stable form of boron nitride and hBN the metastable phase under standard conditions (50), catalytic cBN-hBN phase transition may be an additional source of superficial thermal degradation (softening) of PcBN cutting tool materials.

Sachdev et al. (66) investigated the cBN-hBN phase transition in the temperature range 25-1540 °C, under N_2 atmosphere with pressure in the range 0.3-1 bar, using cBN grains of different sizes and qualities. They found that the formation of hBN started preferentially at the surface of the cBN single crystals. They reported that the onset temperature of the cBN-hBN phase transition depended significantly on the cBN grain size: 900 ± 25 °C for cBN grains having a size in the range 0.75-1.5 μm, 1300 ± 25 °C for cBN grains having a size in the range 40-80 μm and 1500 ± 25 °C for cBN grains having a size in the range 600-1000 μm. They also pointed out that the presence of impurities could favour the lowering of the onset temperature of the cBN-hBN phase transition, particularly B_2O_3. Other factors would be the crystal morphology and catalysts.

2.2.6 Properties of PcBN cutting tool materials

It is not easy to generalize on physical, mechanical, and thermal properties as well as cutting performance of various PcBN cutting tool material grades because each manufacturer uses different catalyst / binder, particle size distribution, cBN content, etc. Besides, the manufacturers of cutting tool materials treat the compositions and properties of their grades as proprietary.

Generally, PcBN cutting tool materials have good (hot) hardness and good toughness. They exhibit exceptionally high values of thermal conductivity and low coefficient of friction in contact with various work materials. With regard to ceramic cutting tool materials, PcBN cutting tool materials have good abrasion resistance, impact resistance and thermal shock resistance (47,53,55,57).

An illustration of the physical, mechanical and thermal properties of PcBN cutting tool materials is given in Table 2.1.

Table 2.1: Physical, mechanical and thermal properties of PcBN cutting tool materials (47,52)

Property	**PcBN**	
	High cBN content	Low cBN content
Density (g cm^{-3})	3.12	4.28
Compressive strength (GPa)	3.8	3.55
Fracture toughness (MPa $m^{1/2}$)	7.2	3.82
Knoop hardness (GPa)	30.4	24.2
Young's modulus (GPa)	680	587
Modulus of rigidity (GPa)	279	284
Bulk modulus (GPa)	405	254
Poisson ratio	0.22	0.15
Thermal expansion coefficient (10^{-6} K^{-1})	4.9	4.70
Thermal conductivity at 20°C (Wm^{-1} K^{-1})	130	33.6

2.2.7 Applications of PcBN cutting tools

PcBN cutting tools are widely used for the machining of steels whose hardness is in the range 45-70 HRC such as cold-work tool steels, hot-work die steels, high tensile steels, high-speed steels, bearing steels, high Mn steels, case hardened steels and sintered irons. PcBN cutting tools are also used for the machining of Co, Fe, Ni, Cr-based hard facing alloys (> 35 HRC), hard cast irons such as white/chill cast irons (55 HRC), Ni-Cr cast irons (58 HRC) (47,55,60), etc.

In most of these work materials, the higher hardness is mainly achieved by two mechanisms, i.e. martensitic transformation hardening and carbide precipitation hardening. Thus, during the machining process, the heat generated at the cutting zone is expected to be enough to produce a cutting temperature in the range 700-800°C. This range of cutting temperature can favour the thermal softening of the work material in contact with the cutting tool by martensite tempering, carbide precipitate dissolution, etc. The relatively high hot hardness and chemical stability of PcBN cutting tools are thus exploited resulting in greater tool life (55,60).

The relatively high hardness and abrasion resistance of PcBN cutting tools are exploited in the machining of softer but very abrasive flake graphite cast irons whose hardness is in the range 200-280 HB, i.e. 16-29 HRC (55). It should be mentioned that excessive wear is sometimes reported when machining flake graphite cast irons having free ferrite content above 10 vol. % with PcBN cutting tools (42,47,52).

PcBN cutting tool materials are classified in roughing-grades and finishing-grades (47,52).

- Finish machining with depths of cut below 0.5 mm and typically 0.2 mm

  In order to induce the thermal softening of the work material, the relatively low heat generated during finish machining requires PcBN cutting tool materials with lower thermal conductivity. Low cBN content PcBN cutting tools which exhibit lower thermal conductivity and slightly reduced toughness are more advantageous in terms of wear resistance (55).

- Rough machining with depths of cut between 0.5 mm and 8 mm

  The intense heat generated during rough machining requires PcBN cutting tool materials with higher thermal conductivity. High cBN content PcBN cutting tools which exhibit higher thermal conductivity are more advantageous in terms of wear resistance (55).

Flake graphite cast irons are machined with PcBN cutting tools using cutting speeds in the range 500-2000 m/min. High cBN content PcBN cutting tools, with their high abrasion resistance, are normally the first choice for both rough and finish machining of these materials. Low cBN content PcBN cutting tools can sometimes offer a solution for the finish machining of flake graphite cast irons when the free ferrite content is greater than 10% or the cutting speed below 400 m/min (42,52).

Hard cast irons can be machined with PcBN cutting tools using cutting speeds in the range 50-250 m/min. For this purpose, high PcBN cutting tools are normally required for both finish and rough machining (42,47,52).

Cutting speed ranges for the machining of other materials with PcBN cutting tools are as follows (42,47,52): hard facing alloys, 50-250 m/min; hardened steels, 70-250 m/min; sintered irons 100-300 m/min.

2.3 CUTTING TOOL WEAR MECHANISMS

2.3.1 Introduction

Cutting tool wear is localized in specific areas where critical conditions of stress, strain, velocity and temperature exist and interact (31) (Figures 2.7 and 2.9). Cutting tool wear often occurs along the cutting edge as well as on adjacent rake and flank faces (Figure 2.22).

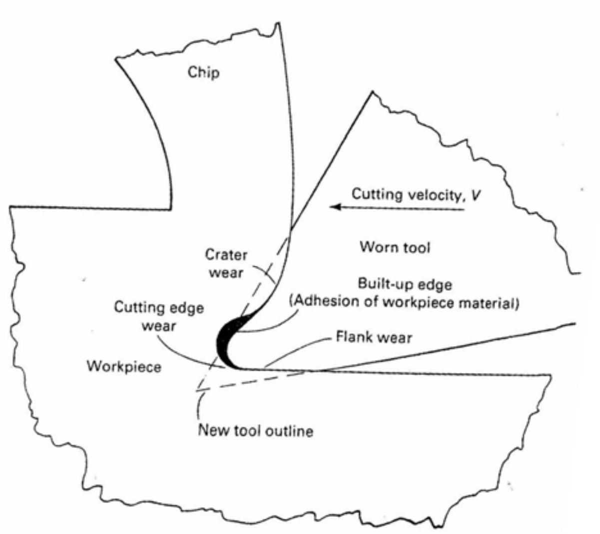

Figure 2.22: Typical wear surfaces (31)

Generally, cutting tool failure is classified according to the affected area of the cutting tool (failure modes) or the physical and or chemical mechanisms which produce it (failure mechanisms). Cutting tool failure modes are summarized in Figure 2.23. The failure mechanisms corresponding to these failure modes are summarized in Figure 2.24 (45,67). In essence, a failure mode is often not due to one individual failure mechanism, but is rather a result of a complex interaction of various failure mechanisms (31,45,68).

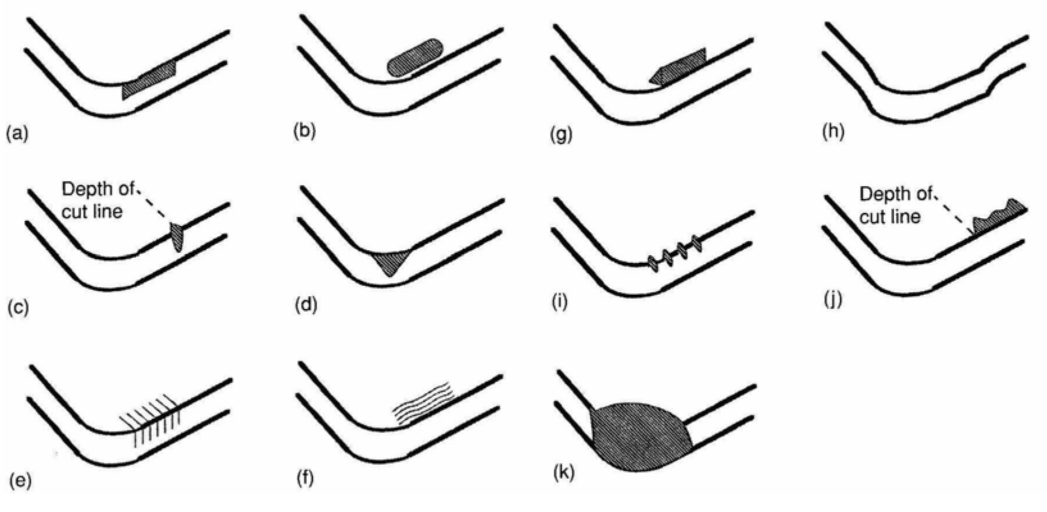

(a) flank wear, **(b)** crater wear, **(c)** notch wear, **(d)** nose radius wear, **(e)** thermal cracks, **(f)** mechanical cracks, **(g)** built-up edge, **(h)** gross plastic deformation, **(i)** edge chipping, **(j)** chip hammering, **(k)** catastrophic fracture

Figure 2.23: Cutting tool failure modes (29)

Failure modes	**Failure mechanisms**
Flank wear	Adhesion or attrition
Crater wear	Abrasion
Notch wear	Plastic flow
Nose radius wear	Creep
Thermal cracks	Surface destruction
Mechanical cracks	Fatigue
Built-up edge	Tribochemical reaction
Gross plastic deformation	
Edge chipping	
Chip hammering	
Catastrophic fracture	

Figure 2.24: Failure modes and failure mechanisms of cutting tools

Most of the physical and chemical processes involved in the failure mechanisms of cutting tools are thermally activated. Cutting temperature is an indirect parameter, depending globally on direct parameters which fundamentally play a key-role on the contact stresses and the relative velocities at the tool-workpiece and tool-chip interfaces (31,63). Therefore, the different tool failure mechanisms are often correlated to the cutting speed (Figure 2.25).

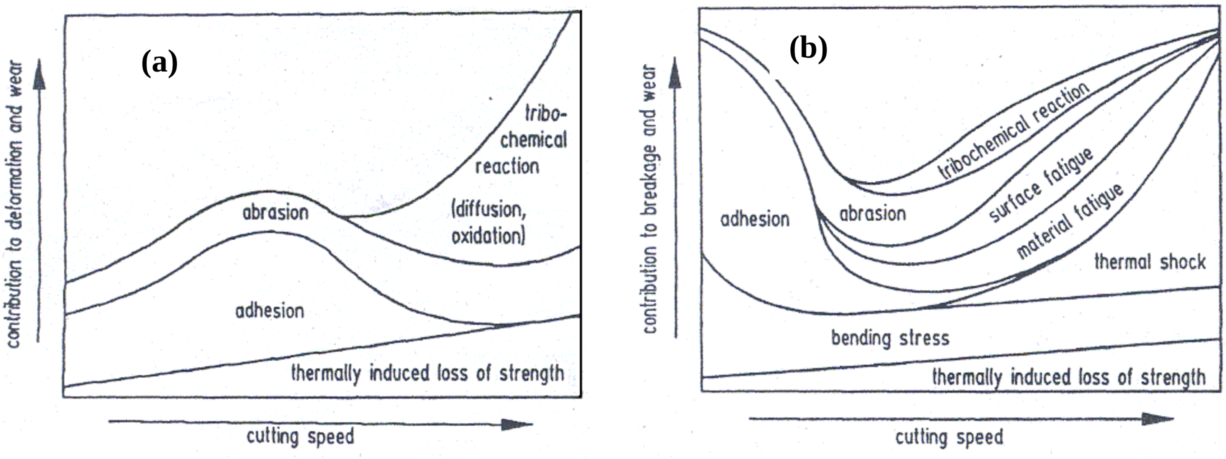

(a) continuous cutting **(b)** interrupted cutting

Figure 2.25: Failure mechanisms of cutting tools (45)

While in continuous cutting, the failure of the cutting tool is caused by thermal softening (thermally induced loss of strength), adhesion, abrasion and tribochemical reaction, in interrupted cutting, the failure of the cutting tool is caused by thermal softening, bending stress, adhesion, thermal shock, material fatigue, surface fatigue, abrasion and tribochemical reaction.

2.3.2 Main cutting tool wear modes

2.3.2.1 Flank wear

Along the flank face, relative motion between the cutting tool and workpiece, and high normal stresses produce flank wear (Figure 2.23 (a)). Flank wear most commonly results from abrasion of the cutting tool edge. The flank wear scar is generally of uniform width, but may be wider at either end (29). The extent of the flank wear scar is quantified by the average or maximum flank wear width V_{BC}. V_{BC} changes with cutting time as shown in Figure 2.26.

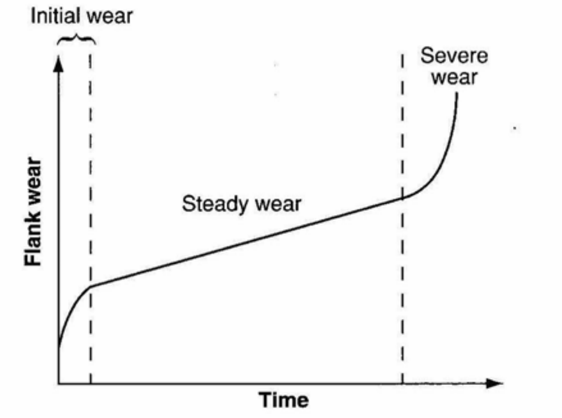

Figure 2.26: Variation of the flank wear V_{BC} with cutting time (29)

The cutting tool and the workpiece have surface irregularities in the form of asperities. At the tool-workpiece interface, asperities touch, creating tiny contact areas. Stresses and heat are intensified in these asperities, and partial removal may occur due to seizure accompanied by fracture of the asperities or melting in the asperities. As these asperities are removed, the initial surface roughness is altered and the contact area increases. If forces remain unchanged, stresses decrease and the active wear mechanisms change. This initial wear period creates a small visible wear surface (31).

After this initial wear period corresponding to the initial rounding of the cutting tool edge, flank wear increases slowly at a steady rate until a critical width is reached. Beyond this critical width, accelerated wear is triggered and wear becomes severe. Stresses and velocities on the enlarged surfaces cause the temperature to increase so that rapid diffusion / oxidation and local seizure or melting conditions occur, causing rapid deterioration of the cutting tool (31).

Flank wear can be minimized by increasing the abrasion and deformation resistance of the cutting tool material, and by coating the cutting tool (29).

2.3.2.2 Crater wear

Crater wear (Figure 2.23 (b)) is usually caused by chemical interaction between the cutting tool material and hot chips at the tool-chip interface and sometimes superficial plastic deformation under high stresses and chip motion. This chemical interaction may involve thermally activated diffusion, dissolution or chemical wear mechanisms (29,63).

The highest crater depth usually corresponds to the area at which the highest surface temperature occurs. The extent of crater wear scar is quantified by crater depth K_T. Crater wear depth increases with time in a manner similar to flank wear (29).

Edge wear (increase of the cutting edge radius) and crater wear alter the state of stress and strain in the cutting region, thereby altering cutting forces and the mechanics associated with the chip-formation process (31) (Figure 2.7). Moderate crater wear usually does not limit tool life. In fact, crater formation increases the effective rake angle of the tool and thus may reduce cutting forces (29).

A deep crater or a deep crater and wide flank wear decrease the wedge angle. This can weaken the cutting tool edge that may experience deformation, crumbling, chipping or even catastrophic fracture (31,29). Crater wear can be controlled by the reduction of cutting speed. The chemical stability of the cutting tool material or the coating material on the tool have a deciding influence on crater wear resistance (29,63).

2.3.3 Adhesion wear mechanism

2.3.3.1 Introduction

Adhesion wear is a mechanically activated wear mechanism which usually occurs and dominates at relatively low cutting speeds, especially in the case of cutting tools with negative rake angle that, enhances the probability of seizure (67). Adhesion wear is usually a dominating wear mechanism on the cutting edge, rake and flank faces of a cutting tool (29).

High pressure welding spots between the asperities of the cutting tool and the chip as well as between the cutting tool and the workpiece have two effects on wear processes. Firstly, an unstable friction coefficient and secondly a thick transfer layer of work material from the asperities. These thick transfer layers of work material often remain attached to the cutting edge, flank and rake faces of the cutting tool, eventually covering the wear tracks (69) and resulting in BUE formation in extreme cases (67).

Indeed, the combined action of microwelding and sliding motion causes severe plastic deformation of the asperities of the relatively ductile work material or surface cracking in the asperities of the relatively brittle cutting tool material (Figure 2.27), producing a sharply skewed worn asperity profile characteristic of adhesion wear.

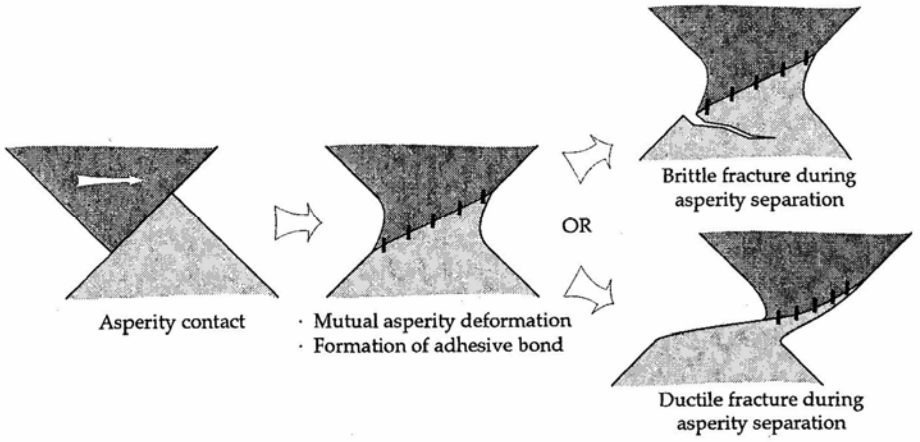

Figure 2.27: Model of deformation in adhesive asperity contact (70)

2.3.3.2 Characteristics features of adhesion wear

The formation of thick transfer layers of work material on the cutting tool surface is the characteristic feature that distinguishes adhesion wear from most other wear mechanisms (71). This formation is the result of strong adhesion between a clean cutting tool surface and clean work / chip underside surface, favoured by a mutual solubility or chemical interactions between the cutting tool and work materials (72). It is also the result of the lower plastic flow stress (ductility) of most work materials with regard to most cutting tool materials (73).

2.3.3.3 Formation of an adhesive transfer layer

The mechanism of shearing and cracking to form a transfer fragment (layer) in an adhesive contact between asperities is illustrated schematically in Figure 2.28. During the sliding process, a ductile asperity of work material deforms in the series of shear bands to accommodate the relative movement. When each shear band reaches a certain limit, due to strain-hardening and eventually lack of recovery or recrystallization, a crack is initiated or an existing crack progresses till a new shear band is formed. The crack extends across the asperity and ultimately a fragment detaches from the deformed asperity. The fragment of work material detached from one of the asperities remains attached to the cutting tool surface (71). Although the number of transfer fragments and the area covered by the transfer layer increase with load, the thickness of the transfer layer remains approximately constant.

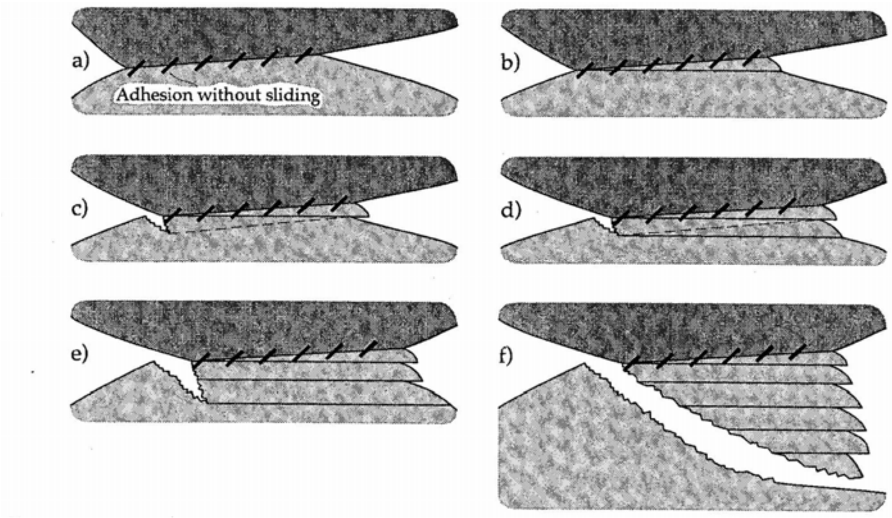

Figure 2.28: Schematic diagram of the formation of an adhesive transfer fragment (74)

2.3.3.4 Thin transfer layers

At relatively high cutting speeds, because of the high cutting temperatures, microwelds form between cutting tool and workpiece. Each shear band in the deformed asperities of work material is relatively far to reach a certain limit due to its dynamic recovery or recrystallization to such extent that no multiplication of shear bands or crack initiation are likely to occur as at low cutting speeds.

Thus, a very thin transfer layer spreads over the cutting tool, protecting the latter against adhesion wear and favouring a good surface finish of the machined workpiece. Nevertheless, the stability of this thin built-up layer (BUL) depends on its chemical interactions with the cutting tool substrate. It also depends on its resistance to abrasion.

2.3.3.5 Behaviour of thick transfer layers on cutting tools, mechanism of adhesion wear

The process of formation and break-up of thick transfer layers can periodically lift the chip or workpiece away from the cutting tool surface, causing fluctuations in the wear rate (71) and additional dynamic cutting forces.

Thick transfer layers are highly work-hardened and could probably produce, through a mechanism involving ploughing (Figure 2.29), severe damage (grooves) at the underside of chips or the machined surface (71).

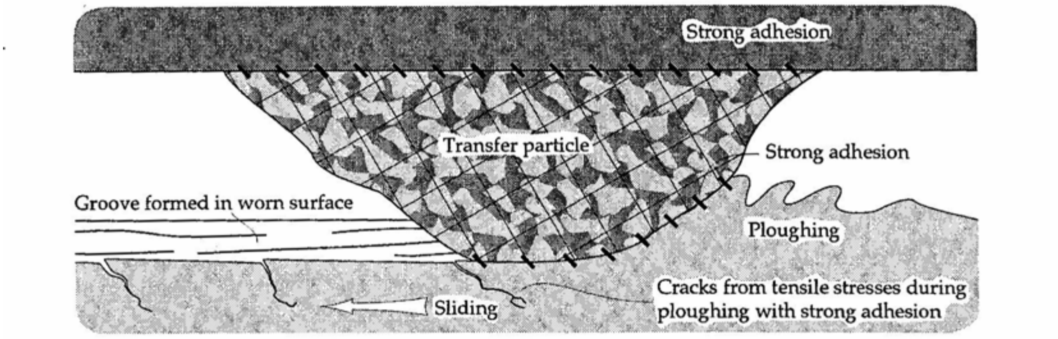

Figure 2.29: Mechanism of ploughing by transfer fragments (71)

Adhesion wear of cutting-tools involves attrition that is a mechanism in which, upon break-up of the adhesive tool-workpiece or tool-chip microwelds, individual grains or small aggregates of grains are pulled off the cutting tool surfaces and are carried away to the underside of chips or are torn away by the adherent workpiece (75,76). Therefore, wear scars produced by attrition are rough by contrast to usually smooth wear surfaces generated by tribochemical wear (75,77).

2.3.3.6 Adhesion wear of ceramic-like cutting tools

It was reported that in almost all ceramic-metal interactions under sliding or rolling contact, metal adheres to ceramic to form a transfer layer (78- 81). This feature should always be taken into account in the interpretation of wear results of ceramic-like cutting tools (73).

When machining relatively brittle work materials, the contacting asperities tend to break away cleanly with little deformation producing fewer wear fragments than when machining ductile work materials (82). Soft work materials such as brass and bronze usually generate thicker transfer layers (80,83) while steel and cast iron transfer layers are fragmentaric (80) (Figure 2.30). Therefore, the ductility of the work material has an undesirable effect of accentuating adhesion wear of ceramic-like cutting tools (45,84).

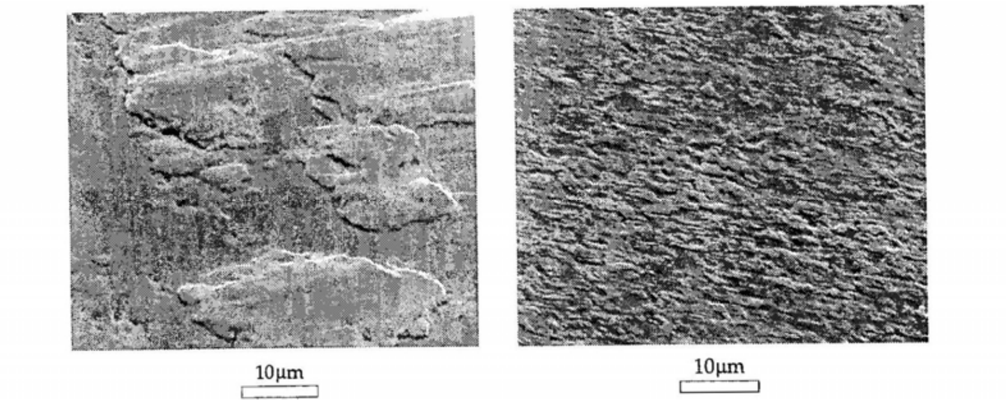

(a) soft metal (brass) **(b)** hard metal (cast iron)

Figure 2.30: Transfer layers onto ceramic surfaces at room temperature. SEM (73)

2.3.3.7 Control of adhesion wear: contaminants, oxide films, solutes and lubricants

Contaminants reduce significantly the extent of adhesion between the cutting tool and the workpiece / chip (81,85). In this regard, oxide films contribute to the reduction of adhesion wear. Surface oxidation of metals occurs rapidly even at low temperatures.

The rate at which oxidation proceeds is often limited only by the supply of O_2 until a critical thickness of 5 nm is reached (86). This indicates that under atmospheric pressure, oxide films, if removed, are reformed in just a few μs (71).

Work material solutes reduce adhesion wear to a lesser but still useful extent compared to surface oxidation. In fact, the relatively high cutting temperatures should promote the migration of solutes towards the surface (71). The application of lubricants can also control the extent of adhesion wear.

2.3.3.8 Adhesion wear rate, resistance to adhesion wear

Compared to abrasion wear, adhesion wear is characterized by a high wear rate because of its higher probability of generation of wear fragments (87) (Figure 2.28). Adhesion wear of a cutting tool can be expressed quantitatively by Equation 2.17 (88),

$$V = \frac{k_w F_n L_s}{H} \qquad \textbf{(2.17)}$$

where V is the volume of cutting tool material worn away, k_w is the wear coefficient, F_n is the force normal to the sliding interface, L_s is the distance slid, and H is the hardness of the tool.

The resistance of a cutting tool material to adhesion wear is likely to increase with hardness. However, if its surface finish is not free from imperfections and irregularities such as microcracks, scratches, dents etc., from which cracks can originate, this influence of high hardness on resistance to adhesion wear might not be effective. This influence of high hardness on resistance to adhesion wear would also not be effective if inter-grain bonding is weak (77).

Furthermore, the resistance of a cutting tool material to adhesion wear can be improved by reducing its grain size. It can also be improved, particularly on the flank face of a cutting tool (89), by inducing residual compressive stresses in the top layers during final lapping.

2.3.4 Abrasion wear mechanism (ductile and brittle)

2.3.4.1 Introduction

Abrasion wear is a mechanically activated wear mechanism that often controls cutting tool life at low to medium cutting speeds for continuous machining operations. Abrasion wear is usually a dominating wear mechanism on the flank face, it is also observed on the rake face, especially at lower cutting speeds (29,84,90).

Conditions of abrasion wear of a cutting tool are created by the sliding and or rolling of the workpiece on its flank face, the sliding of chips on its rake face, the cutting forces, the subsequent liberation of abrasive wear fragments from the workpiece, chips and its cutting edge as well the hard inclusions embedded in the workpiece and chips. In other words, abrasion wear is compounded by a number of parameters among which cutting speed, depth of cut, feed, workpiece and cutting tool microstructures are essential. As already mentioned in Section 2.2.1, hardness and fracture toughness of work and cutting tool materials play a major role in the abrasion wear of cutting tools.

2.3.4.2 Characteristic features of abrasion wear

Abrasion wear of cutting tools is characterized by the development of grooves and ridges on the flank and rake faces, often covered with work material transfer (built-up) layers (67). Smaller and more regular shaped wear patterns are indicative of abrasion wear mechanism. Abrasion wear is generally consistent and predictable.

High stresses generated at the tool-workpiece and tool-chip interfaces might cause many abrasion grooves and ridges on the rake and flank faces to show signs of plastic deformation (e.g. deformation and elongation in the direction of chip flow) (67).

2.3.4.3 Mechanisms of abrasion wear

The mechanisms of abrasion wear are hidden from sight by the cutting tool itself. Wear fragments or hard asperities may abrade and remove lumps of material from the cutting tool by microcutting, microfracture (particularly at the grain boundaries), pull-out of individual grains (91) or accelerated fatigue by repeated deformation as illustrated in Figure 2.31 (67,92).

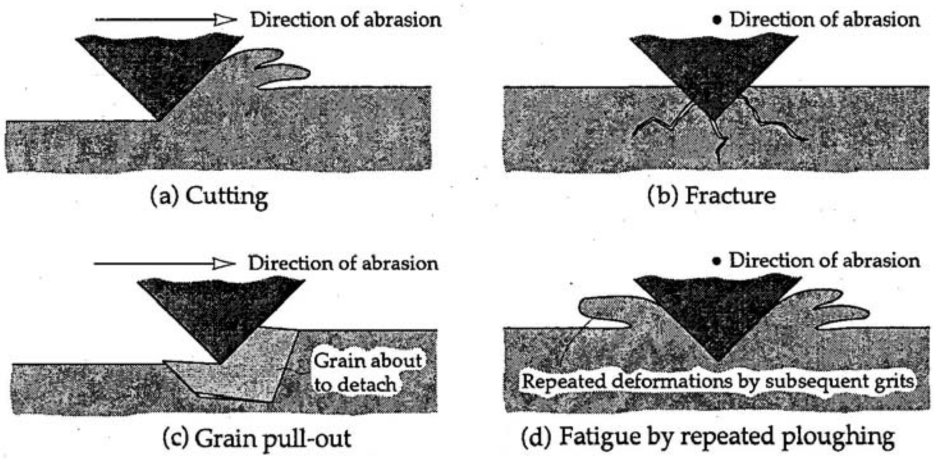

Figure 2.31: Mechanisms of abrasion wear: microcutting, fracture, grain pull-out and fatigue (92)

Microcutting and ploughing are more or less ductile forms of abrasion wear. Lubrication and multi-sharp edged wear fragments increase the rate of abrasion wear by microcutting or ploughing (92), whereas the hardness of the cutting tool should reduce this rate. Subsequently to microcutting and ploughing, substantial plastic deformation (93,94) might occur within the layers underneath the flank and rake faces of a worn cutting tool.

The repeated strains caused by wear fragments or hard asperities deforming an area on the flank or rake faces can also cause surface fatigue. Wear by repeated sideways displacement of material would be a relatively mild or slow form of abrasion wear since repeated deformations are necessary to produce a wear fragment (92).

Fracture and grain pull out are brittle forms of abrasion wear. When wear fragments or hard asperities move successively across the flank and rake faces of a relatively brittle cutting tool, they act as small indenters on these faces. The subsequent convergence of lateral and subsurface cracks from adjacent indentations can result in the release by fracture of lumps of cutting tool material (46). The presence of lateral cracks can also lead to intergranular fracture of the abrasion ridges on the flank face (95).

Brittle fracture-induced abrasion wear of relatively brittle cutting tool should be favoured by high loads acting on each wear fragment, sharp edges on wear fragments, as well as brittleness of the corresponding material (96). As already mentioned for resistance to adhesion wear in Section 2.3.3.8, surface finish and compressive residual stresses in the top layers of a cutting tool do also have an influence on the resistance to abrasion wear of relatively brittle tools.

Grain pull-out is a form of wear which is found in relatively brittle cutting tool materials. This mechanism of wear can become extremely rapid when inter-grain bonding is weak (97), and grain size is large (92).

2.3.4.5 Adhesion wear rate, resistance to abrasion wear

Abrasion wear of a cutting tool can also be expressed quantitatively by Equation 2.17 that expresses the adhesion wear of a cutting tool. Factors that have an influence on the abrasion wear resistance of a cutting tool material are nearly similar to factors that have an influence on the adhesion wear resistance of a cutting tool material (cf Sections 2.2.1, 2.3.3.8 and 2.3.4.2).

2.3.5 Fatigue wear mechanism

2.3.5.1 Introduction

Fatigue wear is a wear mechanism that generates wear fragments by fatigue propagated cracks. Fundamentally, fatigue wear derives from the nucleation and propagation of cracks in the region close to the cutting edge (98). As such, fatigue wear is strongly dependent on the fracture toughness of the cutting tool material.

Depending on whether the initiation and propagation of cracks is backed by mechanical stresses or simply by thermally induced stresses, fatigue wear is either mechanical fatigue wear or thermal fatigue wear. Depending on whether the initiation and propagation of cracks confines itself close to the top surface layers of the cutting tool or extends deeper in the bulk of the cutting tool, fatigue wear is either surface fatigue wear or material fatigue wear (45).

2.3.5.2 Surface crack initiated fatigue wear

During the machining process, contacts between asperities of the cutting tool and workpiece / chip, accompanied by very high local stresses, are repeated a large number of times (98).

A primary crack originates at the surface at some weak point (Figure 2.32). Adhesion and or high friction eventually widen the primary crack which then propagates downward along weak planes such as slip planes or dislocation pipes.

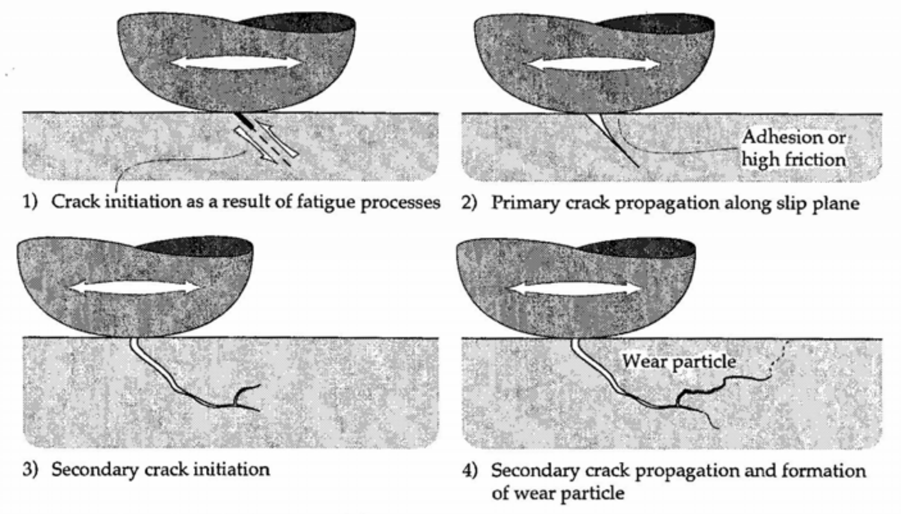

Figure 2.32: Schematic illustration of the mechanism of surface crack initiation and propagation (98)

Indeed, deformation induced due to sliding of workpiece or chips might eventually break down the original grain structure at the flank and rake faces of cutting tool to form dislocation pipes. The latter are probable regions for void formation and crack nucleation (99).

A secondary crack develops from the primary crack or alternatively the primary crack connects with an existing subsurface crack. When the developing crack reaches the surface again a wear fragment is released (100).

2.3.5.3 Subsurface crack initiated fatigue wear, delamination wear

A worn surface might remain quite smooth and lacking in obvious damage, while a few µm below the surface processes leading to the formation of wear fragment are taking place (101).

Under plastic deformation, pile-up of dislocations at grain boundaries, inclusions and other imperfections initiates voids a few µm below the worn surface of the cutting tool. These voids enlarge with further deformation since they act as traps for dislocations. They constitute a plentiful supply of crack initiators. All these factors favour the growth of a crack parallel to but beneath the worn surface (98).

At some unspecified point the crack finally turns upwards and a long thin lamellar fragment is released by delamination. Subsurface planar cracks are therefore the classic signs of delamination wear (98). Delamination wear is dependent on the level of friction (102). At high levels of friction, delamination does occur but is usually overshadowed by adhesion wear and work material transfer. At low levels of friction, subsurface shear forces are insufficient to support crack growth.

2.3.6 Tribochemical reaction wear mechanism

2.3.6.1 Introduction

Tribochemical reaction wear mechanism includes diffusion wear, dissolution wear, chemical wear and oxidation wear mechanisms. To some extent, the tribochemical reaction wear mechanism encompasses melt wear.

In the particular context of machining, tribochemical reaction wear depend globally on the cutting speed that controls preponderantly the cutting temperature. Therefore the cutting speed and the lifetime of the tribochemical reaction layers determine the tribochemical wear rate (103).

Abrasion can accelerate tribochemical reactions by the repeated removal of passivating tribochemical reaction films. When abrasion is more intense, tribochemical effects become insignificant, and when abrasion is less intense, tribochemical effects prevail (104). Severe tribochemical wear ultimately leads to cutting edge fracture.

2.3.6.2 Diffusion wear

Tribochemical reaction wear of cutting tools is a thermo-mechanically activated wear process that could involve a diffusion of elements of cutting tool material into the workpiece as well as chips. Elements of work material could diffuse into the cutting tool, eventually through the transfer layer, which results in the weakening of cutting tool faces by the degradation of mechanical properties and their subsequent wear through a mechanically activated process (29,105). Gradients of activities and particularly coefficients of diffusion of different elements under high cutting temperatures would control this diffusion process (106). The level of contact stresses between chips and rake face or workpiece and flank face is determinant in the control of diffusion wear. Lattice diffusion should compete with diffusion in short circuits such as grain boundaries, dislocations, twins, etc.

Diffusion wear is mainly associated with crater wear and, to some extent, with flank wear (67,84,106). This appears to correlate with the stress and temperature distribution around the cutting tool edge (Figures 2.7 and 2.9).

2.3.6.3 Dissolution wear

Tribochemical reaction wear of cutting tools is a thermo-mechanically activated wear process that could also involve dissolution of phases or compounds of cutting tool material into the workpiece as well as chips. Phases or compounds of work material could dissolve in the cutting tool, which results in the weakening of cutting tool faces by the degradation of mechanical properties and their subsequent wear through a mechanically activated process. Solubility products of different phases or compounds under high cutting temperatures would control this dissolution process. Deformation-induced dissolution could play a role in the sense that deformation can increase the specific area of reactants.

2.3.6.4 Chemical wear

Tribochemical reaction wear of cutting tools is a thermo-mechanically activated wear process that could also involve chemical reactions of elements or compounds of cutting tool material with elements or compounds of work material (transfer layer) which results in the formation of reaction products that could be compounds of lower strength, lower melting points (e.g. eutectics, glasses), etc.

Such reaction products are more susceptible to mechanically activated wear, e.g. abrasion or shearing (plastic deformation). They could be in a viscous state during the machining, in some cases forming stable layers of a glassy appearance (smooth and smeared surface) on the rake and flank faces (67,95,107). Such stable interfacial layers can protect the underlying cutting tool from excessive wear (107). In the case where reaction products form inside thermally activated cracks or other microcracks present on the flank and rake faces, specific volume and or thermal expansion coefficient mismatches can back a spalling wear process (67,108). Free energies of chemical reactions under high stresses and cutting temperatures would control this chemical reaction process (106).

Chemical wear produces both flank and crater wear, with flank wear dominating as the cutting speed is increased. Cutting edges that have large amounts of flank wear which are irregular in appearance would tend to indicate reactivity between the tool and the work material (109). Chemical wear scars are smooth compared to wear scars produced by other mechanisms and may appear to be deliberately ground in the tool (29).

2.3.6.5 Oxidation wear

Tribochemical reaction wear of cutting tools is a thermo-mechanically activated wear process that could also involve oxidation of elements or compounds of cutting tool material as well as elements or compounds of work material (transfer layer) by atmospheric O_2 which, results in the formation of brittle oxides that are subsequently removed by a mechanically activated wear process. Oxidation wear occurs most often occurs near the free surface of the workpiece, where the hot portion of the cutting tool in and around the tool-chip contact region is exposed to atmospheric O_2. Oxidation wear can be recognized from other wear mechanisms by the typical discoloration of the cutting tool material near the wear scar in the region close to the depth-of-cut line (29,84).

High cutting temperatures should promote rapid oxidation of the metallic transfer layers. The latter can be covered by a layer of superficial oxide (110,111). Tribo-oxidation of the metallic transfer layer is illustrated in Figure 2.33.

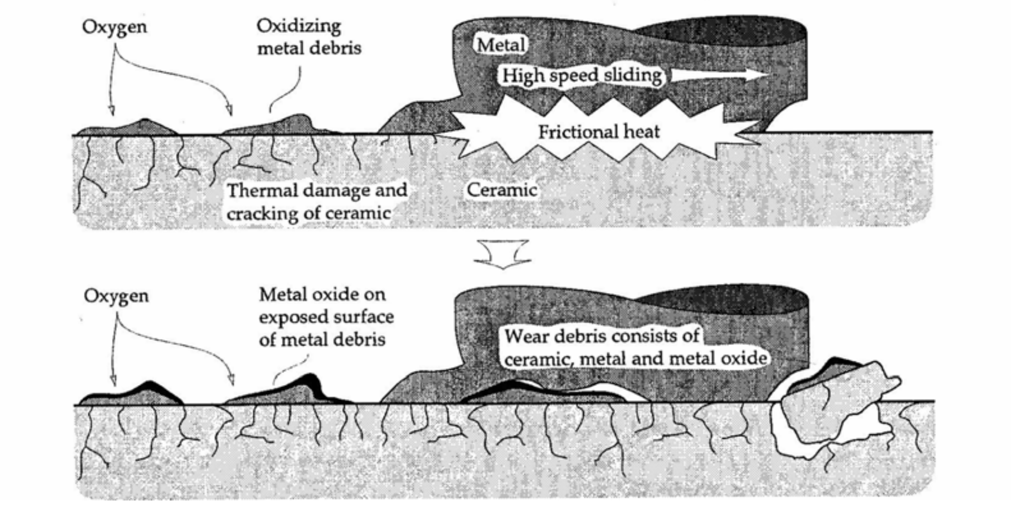

Figure 2.33: Tribo-oxidation of metallic transfer layers and thermal damage of ceramics (73)

In the case where different types of oxides form or are present, chemical reactions between these oxides can take place and result in the formation of complex oxides, generally spinels.

Oxidation of wear fragments or asperities may also result in the production of hard oxide fragments which increase abrasion wear (29,95,112).

Oxidation wear would initiate before diffusion wear and would then be overwhelmed by the latter with the increase in cutting speed (106,113). Free energies of oxidation under high cutting temperatures would control this process (106).

2.3.6.7 Adhesion and tribo chemical wear - friction coefficient

There might be a cutting speed that could realize a transition between dominant adhesion wear to dominant tribochemical wear. This transition would achieve a balance between adhesion wear and tribochemical wear and would correspond to a minimum wear rate.

During the machining process, inclusions embedded in the work material plastically deform but could remain chemically stable. These inclusions accumulate and get compacted into a glaze on the flank and rake faces of the cutting tool in the form of BULs. In some cases, this glaze of inclusions act as lubricant, thus reducing the extent of tribochemical wear processes through the reduction of temperatures and contact area on the rake.

Chemical reaction wear and oxidation wear share the surprising characteristic that a rapid wear rate is usually accompanied by a reduced coefficient of friction. This divergence between friction coefficient and wear rate is a very useful identifier of these wear processes.

2.4 AUSTEMPERED DUCTILE IRON

2.4.1 Introduction: Engineering cast irons

Engineering cast irons are Fe-C-Si alloys (Figure 2.34) that also contain small amounts of other elements such as Mn, P, S, etc. The matrix of engineering cast irons can be tuned through the chemical composition and cooling rate of the casting or an appropriate heat treatment. It could be ferritic, pearlitic, austenitic, martensitic, ausferritic or a mixture thereof. Graphite inclusions in engineering grey cast irons could be flake, compacted, spheroidal, or tempered.

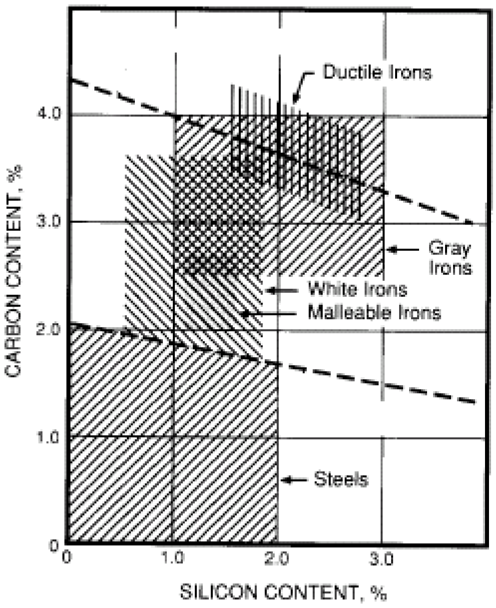

Figure 2.34: Approximate ranges of C and Si for steels and various engineering cast irons (114)

2.4.2 Austempered Ductile Iron (ADI)

2.4.2.1 Introduction

Austempered Ductile Iron (ADI) is an ausferritic spheroidal graphite cast iron. It is obtained by an austempering heat treatment of an almost eutectic ferritic-pearlitic spheroidal graphite cast iron. ADI is a versatile spheroidal graphite cast iron which offers the design engineer, the best combination of low cost, design flexibility, high strength-to-weight ratio and good toughness, exceptional wear resistance and fatigue strength (114,115).

For practical purposes, Gundlach et al. (116) suggested two principal classes of ADI:

- Class I: Harder ADI obtained at low austempering temperatures and exhibiting a lower ausferrite matrix and high strength and hardness (≥ 43 HRC).
- Class II: Softer ADI obtained at high austempering temperatures and exhibiting an upper ausferrite matrix and low hardness (26-38 HRC). Components in this material combine high ductility and toughness with high fatigue strength and wear resistance.

Many authors refer to three important international standard specifications, structured around these two classes and defining the minimum tensile properties: USA standards ASTM A897M-1990, British standards EN 1564-1995 and Japanese standards JIS G5503 (117,118). The ASTM A897M-1990 standard specification is the most stringent. This specification defines five ASTM standard grades:

- Grades 1 and 2: structured around Class II
  These grades are considered as structural grades of ADI.
- Grade 3, 4 and 5: structured around Class I
  Grades 4 and 5 are considered as wear grades, because of their high hardness.

2.4.2.2 Typical chemical composition of ADI

Nominally, ADI has the following chemical composition (6,114): Fe - 3.6 % C - 2.5 % Si - 0.5 % Mn - 0.05 % Mg. However, for a given quenching medium, selective alloying is required to avoid the formation of pearlite in heavier section size parts. For economic and metallurgical reasons, synergistic combinations of alloying elements are often used to achieve the desired hardenability in ADI (114). All things considered, selective alloying does not cause direct modification of the mechanical properties of ADI castings. Properties depend essentially on the austempering process. Selective alloying merely influences the heat treatment cycle and the austempering transformation, by changing the position and shape of the curves on temperature-time-transformation (TTT) and continuous cooling transformation (CCT) diagrams (114,119). The following ADI typical control range (Table 2.2) is successfully used industrially.

Table 2.2: Typical ADI composition in weight % (114)

C	Si	Mn	Cu	Ni	Mo *	Mg	Fe	CE **
3.7 ± 0.2	2.5 ± 0.2	0.20 ± 0.03	X ± 0.05 ≤ 0.8	X ± 0.10 ≤ 2.0	X ± 0.03 ≤ 0.25	0.05	Balance	4.5 ± 0.3

X = as required * only if required **CE = carbon equivalent = C + (Si + P)/3.

2.4.2.3 The heat treatment processing window

Depending on chemical composition and heat treatment parameters, the austempering reaction of ADI usually occurs in 2 stages in time sequence (118,120,121) (Figure 2.35):

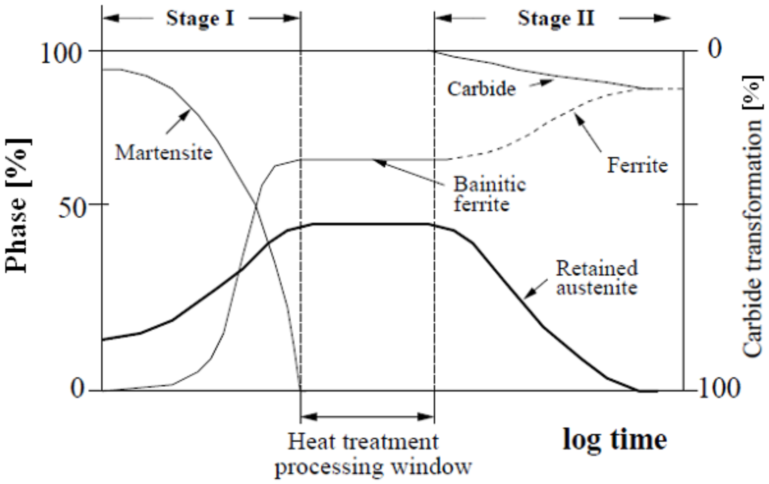

Figure 2.35: Schematic representation of the development of microstructure during austempering, together with an illustration of the "processing window" (122)

Stage I: $\gamma \rightarrow \alpha + \gamma_{hc}$

Acicular carbide-free ferrite α initially nucleates and grows by displacive transformation along the grain boundaries of prior austenite and in the vicinity of graphite nodules. With the growth of carbide-free acicular ferrite α, C diffuses from the ferrite to the surrounding austenite and leads to the formation of C-rich stabilized austenite γ_{hc} whose martensite start temperature (Ms) decreases. When this austenite is saturated with C, a metastable equilibrium is reached, and the Stage I reaction is complete (121,123,124). At this step, the high Si content hinders the formation of carbides.

The mixture of acicular ferrite and thermodynamically stabilized C-rich austenite is called ausferrite. It gives the material a good combination of toughness, strength and hardness, which make it very useful in engineering applications (123). Upper ausferrite forms at high austempering temperatures whereas lower ausferrite forms at low austempering temperatures.

Stage II: $\gamma_{hc} \rightarrow (\alpha + carbides) + \gamma_R$

Overtempering of C-rich stabilized austenite γ_{hc} produced in Stage I leads to its decomposition into acicular ferrite α and carbides, with some amounts of residual austenite γ_R. Overtempering should be avoided because it leads to reduced ductility, toughness and strength due the formation of carbides (119,121,123). Overtempering produces steel-like upper bainite at high austempering temperatures and steel-like lower bainite at low austempering temperatures.

The time interval between these 2 stages is a steady state period called the heat treatment processing window (Figure 2.35). During this time interval, only minor changes in the morphology and composition of the acicular ferrite and stabilised C-rich stabilized austenite take place (6,122,124).

The extent of this heat treatment processing window depends on many factors, including chemical composition, austempering and austenitizing temperatures (6,117) as well as solidification-induced chemical segregation. Alloying elements such as Ni, Mo and Cu enlarge the heat treatment processing window (125). In case of overlapping of the 2 stages, no heat treatment processing window exits and steel-like bainite forms in lieu of ausferrite.

2.4.2.4 Microstructures of ADI

Basically, ausferrite is the microstructure that optimises ADI ductility. Other phases and constituents involve martensite, carbides, steel-like bainite and pearlite, all of which tend to reduce the ductility of ADI. Since the inevitable solidification-induced chemical segregation does not allow having a uniform composition in the entire casting, it is difficult during normal austempering, to completely keep away from these phases and constituents.

2.4.2.5 Heat treatment of ADI

The typical heat treatment profile of ADI consists of the following steps (114,126).

- Heating of the casting to the austenitizing temperature (815–930 °C)
- Holding of the casting at the austenitizing temperature for a time (2-6 h)
- Quenching of the casting within a few seconds to the exact austempering temperature
- Austempering of the casting an optimum time (0.5-5 h)
- Cooling of the casting to room temperature

2.4.2.6 The austempering temperature of ADI

Austempering temperature is one of the major determinants of the mechanical properties of ADI castings. It influences the mechanical properties of ADI through the volume of retained austenite, the C content of the retained austenite as well as the morphology of ausferrite, especially the finesses of ferrite needles (127).

At high austempering temperatures, undercooling is low, thus giving a low nucleation rate of acicular ferrite. C diffusion being sped up by high temperatures, the resulting matrix microstructure is made up of coarse acicular ferrite and a large volume fraction of retained austenite (stringer-type morphology) (Figure 2.36 (a)) (121,128).

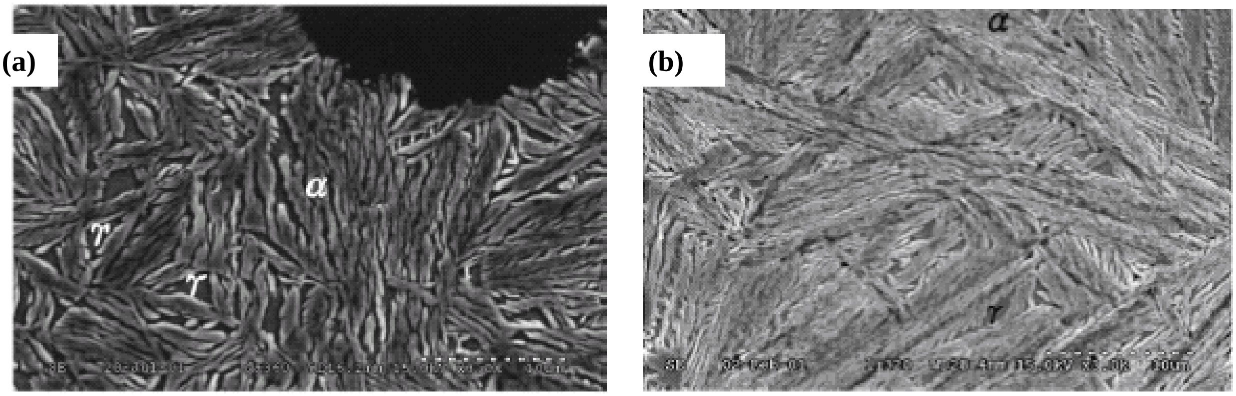

(α: ferrite, γ: island-like austenite)

(a) austempering at 360 °C for 2 hours **(b)** austempering at 320 °C for 2 hours

Figure 2.36: Typical matrix constituent of ADI microstructure. SEM (121)

By contrast, at low austempering temperatures, undercooling is relatively high, thus giving a high nucleation rate of acicular ferrite. C diffusion is slow resulting in reduced amount of retained austenite (Figure 2.36 (b)) (128). However, retained austenite is more stable when formed at lower temperatures because of the high C content (122,129).

The austempering temperature must be higher than the Ms temperature (114,130) except for ASTM Grade 5 ADI. All things considered, it varies in the range 230-450 °C (114,128,130). It is chosen according to the ADI grade required (Figure 2.37).

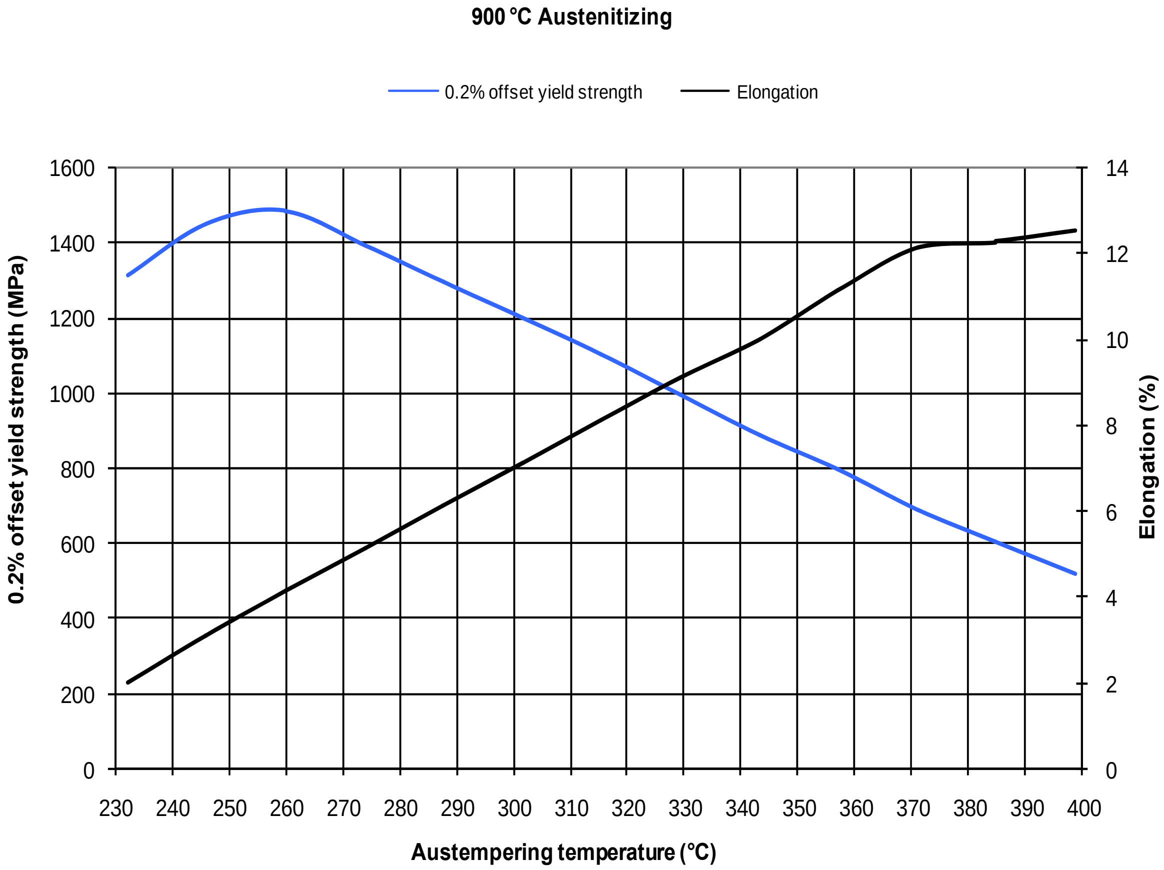

Figure 2.37: ADI yield strength and elongation versus austempering temperature (114)

To produce ADI with high strength and wear resistance, but low fracture toughness, austempering temperatures below 350 °C should be used to generate a matrix of lower ausferrite with less retained austenite (114,131).

To produce ADI with low strength and hardness but high elongation and fracture toughness (Figure 2.37), high austempering temperature (350-400°C) should be selected to generate a matrix of upper ausferrite with high amounts of retained austenite (20-40 vol. %) (114,132). ASTM Grade 1 and ASTM Grade 2 ADI would be typical of these conditions.

2.4.2.8 Strain-induced transformations in ADI

At room temperature, the metastable austenite can undergo martensitic transformation if the necessary activation energy is provided by straining (119,121,133). Islands of hard martensite formed by plastic deformation are mainly generated from the residual (island-like) austenite present in the microstructure. These islands of martensite can strongly influence the mechanical properties of ADI and enhance wear properties. Austempering temperature and austempering time (ADI grade) have a remarkable effect on the stability of residual austenite under deformation.

Alloying elements also have an influence on the stability of residual austenite during deformation. Chen et al. (123) reported that besides C, Mn and Mo have a very significant effect on the stability of austenite in ADI upon deformation. Ni seems to decrease the stability of austenite in ADI during deformation.

A minimum deformation would be required to cause a significant drop in the austenite content. In fact, Chen et al. (123) reported that, for an ADI containing 0.3 % Mn, 2.0 % Ni, austenitized at 880 °C for 2 hours and austempered at 370 °C for 2 hours, at least a deformation of about 10% was needed to cause a significant change in the austenite content and hardness. In ADI, plastic deformation may locally raise ausferrite temperature and then promote the C diffusion necessary to carry out the Stage II of austempering (121), especially for the stringer-type austenite which is rich in C.

2.4.2.7 Mechanical properties of ADI

The typical mechanical properties that one may observe in commercial ADI tailored around ASTM A897M-1990 specifications are illustrated in Table 2.3.

Table 2.3: Typical properties of ADI, ASTM A897 specifications (134)

ASTM 897 M	850-550-10	1050-700-07	1200-850-04	1400-1100-01	1600-1300-00
Typical properties	**Grade 1**	**Grade 2**	**Grade 3**	**Grade 4**	**Grade 5**
Monotonic (static) properties					
Tensile Strength (MPa)	966	1139	1311	1518	1656
Elongation %	11	10	7	5	3
Hardness Brinell HB	302	340	387	418	460
Reduction area (%)	10	9	6	4	2
Young's modulus (GPa)	159.3	157.9	156.5	155.1	153.8
Compressive strength (MPa)	1380	1650	1935	2275	2520
Shear strength (MPa)	870	1025	1180	1370	1490
Modulus of rigidity (MPa)	65.1	64	63.2	62.4	62.1
Poisson ratio	0.25	0.25	0.25	0.25	0.25
Strain hardening exponent n	0.143				
Dynamic properties					
Un-notched Charpy impact @ 21 °C (Joules)	120	120	93	80	53
Notched Charpy impact @ 21 °C (Joules)	12	10.6	9.3	8.6	8
Dynamic elastic modulus	170	168	167	165	164
Fracture toughness (MPa/m$^{1/2}$)	109	85	60	52	44
Strain hardening exponent n'	0.133	0.1376	0.1465	0.16	
Physical (intrinsic) properties					
Density	7.0965	7.0872	7.0779	7.0686	7.0593
Coefficient thermal expansion mm/mm/°C x 10^{-4}	14.6	14.3	14	13.8	13.5
Wear resistance A_{max} pin test, volume mm^3	10.9	10.8	10.6	10.3	9.8
Thermal conductivity (W/m°K)	22.1	21.8	21.5	21.2	20.9
Internal damping (log decr) x 0.0001	5.26	5.41	5.69	12.7	19.2

2.4.2.9 Applications of ADI

ADI has emerged as a major engineering material in recent years because of its excellent mechanical properties. Its structural grades as well as wear grades are being applied more broadly and have replaced some other alloys.

ADI often competes favourably with steel forgings, Al-alloys, and alloy steels for heavy-duty applications when reliability is an uncompromising requirement. It can also be used as an upgrade for standard grades of spheroidal graphite cast iron, and in some cases, as a replacement for Mn steel and Ni-hard cast iron for wear parts. With all these possibilities, ADI have found application in the following industries (6,114,115,133): heavy truck and bus, light auto and truck, pumps and compressors, construction and mining, miscellaneous manufacturing such as railroad, agriculture and defence, etc. For example, ADI is used in the manufacture of crankshafts, camshafts, bearing cups, clutch housings, transmission gears, connecting rods, train car wheels, suspension components and many other applications.

Basically, ADI austempered at temperatures in the range 325-400°C, this is to say, ASTM Grades 1 to 3, draw the most interest (7). However, reports of processing inconsistencies in the foundry and heat-treatment shops as well as machinability concerns and unknown costs have limited the use of ADI castings. This is particularly the case in high volume vehicle applications (130,135). Most ADI components, such as crankshafts, are subjected to extensive machining during manufacture. Good machinability is therefore highly desirable.

2.5 MACHINABILITY OF AUSTEMPERED DUCTILE IRON

2.5.1 Effect of microstructure on machinability of engineering grey cast irons

The machinability of engineering grey cast irons relates closely to their microstructure. Microstructures that increase either the hardness or the ductility of engineering grey cast irons reduce their machinability. Ductility appears to have a stronger effect on machinability compared to hardness (136).

The presence of graphite inclusions provides the free-machining characteristic of engineering grey cast irons, and the shape and amount of graphite inclusions establish the potential surface finish obtainable with a cutting process and the necessary cutting force (137).

Graphite inclusions and especially flake graphite inclusions, act to weaken engineering grey cast irons in the primary shear zone and initiate fracture. Graphite may extend an appreciable distance across the primary shear zone, thus reducing the cutting force. However, the shearing of grey cast irons in the primary and secondary zones would be different, particularly for flake graphite cast irons. Graphite might be expected to act as lubricant and to inhibit seizure at the tool-workpiece and tool-chip interfaces, but there is no evidence of this. A fine spray of graphite is produced during the machining of engineering grey cast irons (137,138). This dispersal of graphite and its subsequent lubrication effect could be less for spheroidal graphite cast irons for which graphite inclusions are often encased in ferrite shells (136).

Spheroidal graphite predisposes cast irons, particularly ferritic cast irons, to flank buildup and burr formation. This flank buildup causes high tool forces, high temperatures and poor surface finish. Flank built-up can be reduced or eliminated by decreasing the feed, using positive rake angles, increasing clearance angles, and by using a lubricant flood (136,138- 141).

Spheroidal graphite increases the ductility of cast irons and results in increased tool-chip contact lengths and higher cutting temperatures than those encountered in the machining of flake graphite cast irons (136).

Pearlite provides the best combination of machinability and wear resistance of cutting tools. When in thin plates in pearlite, carbide can be readily sheared, but when in larger particles, carbide is very detrimental to cutting tool life (137).

Ferritic grey cast irons are easier to machine than pearlitic grey cast irons. The moderate hardening effect of the dissolved Si in ferrite gives it a clean-cutting property. Yet, they may be subject to BUE formation (136).

In engineering grey cast irons, austenite is a relatively soft phase and is comparable to ferrite in machinability. However, the high propensity of austenite to strain hardening could bring some machinability concerns (137).

Thus, some have tried to produce austenite-free ADI using a special austempering (142) or a strong magnetic field (143) to eliminate austenite and improve the machinability of ADI at low cutting speeds. However, the resultant higher ferrite content might amplify BUE formation.

Tempered martensite is more machinable than martensite and sometimes even more machinable than pearlite of the same hardness. Acicular structures including ausferrite and bainite are generally of intermediate hardness and are a little less machinable than tempered martensite of the same hardness (137).

Generally, mixed-matrix structures in engineering grey cast irons result in cutting tool life intermediate between that of the individual constituents (137).

2.5.2 Cutting tool materials used for the machining of engineering grey cast irons

With the exception of PCD cutting tools, all cutting tools may be used to machine engineering grey cast irons. HSS cutting tools are often used for the machining of engineering grey cast irons. Cobalt containing HSS cutting tools are used for machining of grey cast irons with hardness higher than 200 HB (137).

Cemented carbide cutting tools are the most commonly used for machining engineering grey cast irons. Cermet cutting tools are used to turn and mill engineering grey cast irons. Both

Al_2O_3-based and Si_3N_4-based ceramic cutting tools are used to machine engineering grey cast irons. However, Si_3N_4-based cutting tools would not be used for the machining of spheroidal graphite cast irons because the cutting temperatures generated would exceed the softening temperature of the glassy phase in these tools resulting in rapid tool wear (136). The application of PcBN cutting tools for the machining of engineering cast irons is already exposed in Section 2.2.7.

2.5.3 State of the art in the machining of austempered ductile iron

2.5.3.1 Introduction

While ADI has attractive mechanical properties, it has some limitations. Its microstructure results in some machinability concerns. Its austenite is unstable and could, under certain conditions, transform to martensite during machining (144). Compared to other spheroidal graphite cast irons, the relatively high strength and hardness of ADI as well as the tendency of its ausferrite and residual austenite to strain harden lead to short chip-tool contact lengths and higher mechanical stresses on the cutting tool's edge (145- 149). The relatively high ductility of ADI favours its adhesion on the cutting tool, the formation of BUE at low cutting speeds and results in higher temperatures on the cutting tool's edge (47,145,149).

Because of higher mechanical stresses and higher temperatures on the cutting edge when machining ADI, cutting tools often suffer relatively high flank wear and crater wear compared to when machining hardened steels and other engineering grey cast irons. The severe crater scar that develops very close to the cutting edge exposes the latter to fracture damage (145,150). Of course, the higher cutting temperatures as well as the relatively low thermal diffusivity and short contact length of ADI could also expose the cutting edge to thermal softening (147).

Nevertheless, machining of ADI is highly desirable because it can yield the tight tolerances and surface finishes usually required (151), save machining time and reduce costs (145). In addition, it can induce significant compressive stresses in the machined surfaces, thus improving the bending-fatigue strength (152).

Cutting tools to machine ADI should possess high hot hardness and strength, resistance to chemical reactions at high temperatures as well as toughness. Such cutting tools are ideal and do not really exist at present. However, they are the purpose of continuous research undertaken in the field. Coating technology appears to be an alternative. Nowadays, coatings on cutting tools are being used to improve the tribological properties of cutting tools (45). Results show significant improvements in some cases, especially at relatively low cutting speeds. However, the issue of flaking of these coatings sometimes reduces performance. Thus, it is a matter of finding a compromise cutting tool material and or coating as well as optimum machining parameters. Let also mention that ion implantation as well as workpiece inclusion engineering are also undertaken these days to improve the performance of cutting tools by tuning the tribology at the tool-workpiece and tool-chip interfaces (153- 156).

As pointed out by Cakir et al. (7) and Seker et al. (157), it has to be mentioned that the amount of research conducted hitherto on the machinability of various grades of ADI is still very small. It has so far addressed few fundamental questions concerning the cutting performance and sometimes the wear mechanisms of various types of cutting tools under various machining conditions.

2.5.3.2 Investigation 1: machining of ADI with ceramic tools

Pashby et al. (150) investigated the wear of Al_2O_3, Al_2O_3-TiC, Al_2O_3-SiC_w, and Si_3N_4-Al_2O_3 ceramic cutting tools when dry turning ADI similar to ASTM Grade 2 under conditions close to light roughing (depth of cut: 2 mm; feed: 0.18 mm/rev; cutting speed: 100 – 450 m/min). They reported that flank wear was the main wear mode although tool fracture occurred at the highest speed. Si_3N_4-Al_2O_3 ceramic cutting tools suffered accelerated wear whereas Al_2O_3-SiC_w ceramic cutting tools significantly underperformed Al_2O_3 and Al_2O_3-TiC ceramic cutting tools under most conditions. Fracture damage on the tools' cutting edge and chemical interaction between tool and workpiece material were identified as important wear mechanisms in controlling tool life.

The characteristic grooved surface of the flank wear scar of these various ceramic cutting tools was thought to be the result of superficial plastic deformation and fracture. Moreover, in a situation where both stresses and temperatures were likely to be high, edge fracture might well contribute to the rapid initial flank wear by producing wear fragments that were carried down the flank face, thus producing self abrasion of the latter.

Chemical interaction of TiC with ADI was thought to accelerate flank wear of Al_2O_3-TiC ceramic cutting tools at higher cutting speeds. This interaction would expose the Al_2O_3 skeleton, allowing either removal of Al_2O_3 grains by an attrition mechanism or smearing of Al_2O_3 by plastic deformation. Fracture toughness anisotropy, thermal expansion mismatch and chemical interaction contributed to the extensive damage observed on the flank face of Al_2O_3-SiC_w ceramic cutting tools. Dissolution-diffusion, softening or weakening of the glassy phase in the Si_3N_4-Al_2O_3 ceramic cutting tools and thermal or chemical modification supported by atoms from the ADI might allow whole β' particles in the tools to be removed by an attrition type mechanism.

Smooth surfaces observed on the crater wear scars of Al_2O_3 ceramic cutting tools at cutting speed of 300 m/min were related to the fracture that followed the superficial plastic deformation. Rough surfaces observed on the crater wear scars of Al_2O_3-SiC_w ceramic cutting tools at cutting speed of 300 m/min were related to the fracture that followed the weakening of the Al_2O_3-SiC_w interfaces subsequent to thermal expansion mismatch and chemical interaction between SiC_w and ADI. Smooth surfaces also observed on the crater wear scar of Al_2O_3-SiC_w ceramic cutting tools were likely to be a combination of chemical interaction of SiC_w with ADI and superficial plastic deformation.

It appeared that the edge damage of Al_2O_3 ceramic cutting tools resulted from a microfracture mechanism caused by a combination of mechanically and thermally induced stresses, following the relative lack of fracture toughness and thermal conductivity and also the short tool-chip contact length. Widespread fracture occurred on the cutting edge of the Al_2O_3-SiC_w ceramic cutting tools showing both smooth and coarse areas. The edge fracture of Al_2O_3-TiC as well as Si_3N_4-Al_2O_3 ceramic cutting tools was nearly concealed by the action of chemical interactions.

2.5.3.3 Investigation 2: machining of ADI with cemented carbide and ceramic tools

Masuda et al. (158) investigated on the cutting performance and wear mechanism of P20 cemented carbide cutting tools, Al_2O_3-ZrO_2 (5 wt %), Al_2O_3-ZrO_2 (20 wt %), Al_2O_3-TiC (30 wt %), Al_2O_3-SiC_w-ZrO_2, Al_2O_3-SiC_w-TiC and Si_3N_4 ceramic cutting tools when dry turning ADI similar to ASTM Grade 1 under conditions close to light roughing (depth of cut: 1 mm; feed: 0.1 mm/rev; cutting speed: 50-400 m/min).

They reported that Al_2O_3-TiC (30 wt %) inserts had the longest life at a low cutting speed of about 100 m/min and less, and ZrO_2-toughened Al_2O_3 inserts had a longer tool life at about 250 m/min or more. Al_2O_3-SiC_w-ZrO_2 and Al_2O_3-SiC_w-TiC ceramic cutting tools exhibited flaking fracture at 250 m/min whereas Si_3N_4 ceramic cutting tools had no wear resistance at all. Cemented carbide inserts had longer life at very low cutting speeds. As cutting speed rose, the flank wear rate increased slightly for Al_2O_3-TiC (30 wt %) inserts. In contrast, it decreased for

ZrO_2-toughened Al_2O_3 inserts due to the monoclinic-to-tetragonal transformation of ZrO_2 at high cutting temperatures. This allotropic transformation leads to an increase in cutting tool hardness and was identified as the cause of the increased wear resistance and a change in tool life curves at 100 m/min.

2.5.3.4 Investigation 3: machining of ADI with ceramic tools

In order to elucidate the mechanism of poor machinability of ADI, Yamamoto et al. (145) investigated the turning of ADI similar to ASTM Grade 1 with Al_2O_3-SiC_w cutting tools under conditions close to light roughing (depth of cut: 1.5 mm; feed: 0.2 mm/rev; cutting speed: 6–300 m/min). Their results showed that at cutting speeds lower than 36 m/min, the residual austenite transformed to martensite in the chips as well as the damaged layer of the machined surface. This strain-induced transformation was responsible of the poor machinability of the ADI. At higher cutting speeds this strain-induced transformation occurred only in the damaged layer of the machined surface and not in the chips.

2.5.3.5 Investigation 4: machining of ADI with HSS tools

Seah and Sharma (159), conducted turning tests on ADI alloyed with Ni and similar to ASTM Grade 2 and ASTM Grade 3 using high Mo content HSS cutting tool, a depth of cut of 1 mm, a feed of 0.25 mm/rev and cutting speeds of 9.5 and 11.87 m/min. They determined the machinability based on material removal rate and power consumed. They found that power consumption increased progressively when machining ASTM Grades 2 and 3 ADI compared to when machining as cast material.

2.5.3.6 Investigation 5: machining of ADI with cemented carbide tools

Moncoda et al. (144) investigated the turning of ADI using a wide range of machining variables, such as cutting speed, feed, depth of cut, and lubrication and some cutting tool characteristics such as the carbide grade, rake angle, and coating. They reported that the higher the austempering temperature, the lower the machinability.

2.5.3.7 Investigation 6: machining of ADI with coated cemented carbide and ceramic tools

Wada et al. (160) investigated the wear of coated cemented carbide cutting tools, coated Al_2O_3 ceramic cutting tools and coated Si_3N_4 ceramic cutting tools in dry turning of ADI similar to ASTM Grade 2 under conditions close to light roughing (depth of cut: 1 mm; feed: 0.2 and

0.4 mm/rev; cutting speed: 30 – 400 m/min). They found that Ti(C,N)-Al_2O_3-TiN-coated P10 carbide inserts had the slowest flank wear rate compared to TiC-Al_2O_3-TiN-coated P20 and TiN-coated K10 carbide inserts. TiN-coated Al_2O_3 ceramic inserts had tool wear rates similar to Ti(C,N)-Al_2O_3-TiN-coated P10 carbide inserts. Abrasion wear was observed on the flank face of TiN-coated Al_2O_3 and TiN-Al_2O_3-TiN-coated Si_3N_4 ceramic inserts at relatively low cutting speeds. The flank wear of TiN-Al_2O_3-TiN-coated Si_3N_4 ceramic inserts increased rather slowly at the feed of 0.4 mm/rev. On the other hand, the TiN-coated Al_2O_3 ceramic inserts had a tendency to fracture easily at the feed of 0.4 mm/rev.

2.5.3.8 Investigation 7: machining of ADI with coated cemented carbide tools and ceramic tools

Klocke and Klöpper (148) investigated the turning of ADI similar to ASTM Grade 1 with coated cemented carbide cutting tools (Al_2O_3-coated K10, Ti(C,N)-coated K10, TiN-Al_2O_3-coated P15), Al_2O_3 and Si_3N_4 ceramic cutting tools using a depth of cut of 1 mm, a feed of 0.2 mm/rev, a cutting speed in the range 120-400 m/min under dry conditions as well as with lubricants. They pointed out that coated cemented carbide cutting tools could be successfully used at low cutting speeds. At high cutting speeds, the use of Al_2O_3 ceramic cutting tools was interesting. The performance of Si_3N_4 ceramic cutting tools was very poor. Cutting lubricants were very effective in the reduction of the flank and crater wear scars of cemented carbide tools, particularly at relatively high cutting speeds.

2.5.3.9 Investigation 8: machining of ADI with ceramic cutting tools

Goldberg et al (161) studied the dry interrupted facing of an ASTM Grade 3 ADI with Al_2O_3-TiC and Al_2O_3-SiC_w ceramic cutting tools under conditions close to light roughing (depth of cut: 2 mm; feed: 0.1-0.4 mm/rev; cutting speed: 425 m/min) and finishing (depth of cut: 0.5 mm, feed: 0.1-0.4 mm/rev; cutting speed: 700 m/min). Their results indicated that Al_2O_3-SiC_w ceramic inserts performed better than Al_2O_3-TiC ceramic inserts for rough interrupted facing as well as finish interrupted facing at high cutting speeds. The lack of overwhelming performance for Al_2O_3-TiC ceramic inserts in this very situation was linked to their poor thermal shock resistance. They reported that cutting tool wear was exclusively flank wear which was a direct consequence of adhesion - abrasion wear mechanism.

2.5.3.10 Investigation 9: machining of ADI with coated cemented carbide cutting tools

Cakir et al. (7) investigated the dry turning of ADI similar to ASTM Grade 1, ASTM Grade 2 and ASTM Grade 3-4 with coated cemented carbide tools under conditions close to light roughing (depth of cut: 1 mm; feed: 0.12 mm/rev; cutting speed: 96.7 m/min). They evaluated the machinability in terms of tool life, cutting forces and surface finish. ADI similar to ASTM Grade 1 appeared to cause the highest tool wear whereas ADI similar to ASTM Grade 3-4 appeared to cause the lowest tool wear. By reference to the as cast ductile iron, ADI similar to ASTM Grade 1 appeared to have the highest increase in the tangential cutting force (23%) whereas ADI similar to ASTM Grade 3-4 appeared to have the second highest increase (18%) in tangential cutting force. Surface roughness values varied between 1.35 and 2.17 µm. ADI similar to ASTM Grade 1 seemed to have the best surface quality. However these findings should be moderated because of the presence of martensite that was evident in these alloys.

2.5.3.11 Investigation 10: machining of ADI with cemented carbide cutting tools

Seker et al.(157) recently investigated the dry turning of ADI alloyed with various amounts of Cu and Ni for various austempering times and similar to ASTM Grade 2 ADI using M15/P15 cemented carbide tools under conditions close to light roughing (depth of cut: 1.5 mm; feed: 0.06 mm/rev; cutting speed: 113 m/min). They determined the machinability in terms of surface roughness and cutting forces. The surface roughness values of machined components approached those of ground as cast components. The cutting forces for the machined components were about 20 % higher then those of the as cast components.

2.5.3.12 Investigation 11: machining of ADI with ceramic cutting tools

Guo et al. (162) recently investigated the performance and wear mechanism of Al_2O_3-TiC ceramic cutting tools when dry turning ADI similar to ASTM Grade 3 under finishing conditions (depth of cut: 0.3 mm; feed: 0.16 mm/rev; cutting speed: 57, 89 and 141 m/min). They found that abrasion wear, adhesion wear, spreading wear, micro-chipping and fracture emerged as key-wear mechanisms.

2.5.3.13 Investigations 12-15: machining of ADI with PcBN cutting tools

Klocke and Klöpper(148) investigated the dry turning of ADI similar to ASTM Grade 1 with PcBN cutting tools under conditions close to light roughing (depth of cut: 1 mm; feed:

0.2 mm/rev; cutting speed: 160-400 m/min). Their results showed that the application of PcBN cutting tools was acceptable for cutting speeds in the range 160-200 m/min.

In an earlier investigation, Shintani et al. (163) reported that considering the surface roughness of machined components and tool life, cBN-TiC cutting tools performed better than Al_2O_3-TiC ceramic cutting tools for the machining of ADI similar to ASTM Grade 3 under finish machining conditions. Flank wear rate of cBN-TiC cutting tools was found to depend on cutting temperature. The optimum cutting temperature was found to be 827 °C. From the cutting temperature dependence of flank wear rate, wear behaviour of the cBN-TiC cutting tools was classified into two temperature regions. In the first region, a scratch mark was clearly observed on the wear surface of the tool due mainly to microspalling of cBN grains. In the second region, it was observed that tool wear was controlled by the falling-off of adhering particles from the cutting edge.

Kato et al. (164) investigated the wear performance of PcBN cutting tool in the turning of ADI similar to ASTM Grade 3 under finishing conditions (depth of cut: 0.2 mm; feed: 0.05 mm/rev; cutting speed: 40-300 m/min). They observed that from the standpoints of surface roughness of machined components and flank wear rate, the optimum cutting speed was 100 m/min at which the cutting temperature was 827 °C. They proposed that the cutting performance of PcBN cutting tools was controlled by the size and volume fraction of cBN grains as well as the thickness of the binder phase. PcBN cutting tools containing small-sized cBN grains exhibited excellent performance. The optimum combination of both cBN grain and binder phase was about 40 vol. % cBN in which the thickness of the binder phase was 3 µm. Cracking in the cBN grains by stress concentration emerged as key-wear mechanism.

The dependence of cutting performance upon size and volume fraction of cBN grains was also corroborated by Goldberg et al (161) in their study of the dry interrupted facing of an ASTM Grade 3 ADI with PcBN cutting tools. Their results indicated that low cBN content PcBN inserts were most suitable for dry finish interrupted facing at high cutting speeds, whilst high cBN content PcBN cutting tools adequately sustained dry rough interrupted facing.

2.5.4 Summary

In the limited literature published on ADI machinability, investigations were conducted essentially on ADI close to ASTM Grade 1, ASTM Grade 2 and ASTM Grade 3, using essentially turning and interrupted facing tests without and with lubricants.

2.5.4.1 Cutting tools tested so far

High Mo content HSS cutting tools have been tested. K-grade, P-grade and M-grade cemented carbide cutting tools have also been tested. Al_2O_3, Ti(C,N), TiN-Al_2O_3, Ti(C,N)-Al_2O_3-TiN, TiC-Al_2O_3-TiN and TiN coatings have been tested on these cemented carbide tools.

Al_2O_3-based ceramic cutting tools appeared to have been the most tested in the investigation of ADI machinability. Many types of second phases have been tested for these Al_2O_3-based ceramic cutting tools: TiC, ZrO_2, SiC_w individually or in combination. TiN coatings on these Al_2O_3-based ceramic cutting tools have also been tested.

Si_3N_4-based ceramic cutting tools have been tested, but to a lesser extent. TiN-Al_2O_3-TiN coatings on Si_3N_4-based ceramic cutting tools have also been tested.

PcBN cuttings tools have been tested to a lesser extent. Various types of binder have been tested for these PcBN cutting tools, particularly TiC binder.

2.5.4.2 Cutting parameters reported so far

So far, investigations were done in the following ranges of cutting parameters:

- HSS cutting tools, cutting speeds were in the range 9-12 m/min, depth of cut of 1 mm and feed of 0.25 mm/rev.
- Uncoated and coated cemented carbide cutting tools, cutting speeds varied in the range 30-200 m/min, depth of cut varied in the range 1-1.5 mm and feed varied in the range 0.06-0.4 mm/rev.
- Uncoated and coated Al_2O_3-based and Si_3N_4-based ceramic cutting tools, cutting speeds varied in the range 6-700 m/min, depth of cut varied in the range 0.3-2 mm and feed varied in the range 0.1-0.4 mm/rev.
- PcBN cutting tools, cutting speeds varied in the range 40-700 m/min, depth of cut varied in the range 0.2-2 mm and feed varied in the range 0.05-0.4 mm/rev.

2.5.4.3 Cutting performance reported so far

Depending on the type of ADI, depth of cut and feed, M-grade and P-grade cemented carbide cutting tools would be effective at cutting speeds up to about 100 m/min, whereas coated K-grade, P-grade and probably M-grade cemented carbide cutting tools would be effective at cutting speeds up to 160 m/min (148). In terms of tool wear and cutting forces, ASTM Grade 3

ADI would be the easiest to machine with cemented carbide cutting tools, followed by ASTM Grade 2 ADI and finally ASTM Grade 1 ADI. However, ASTM Grade 1 ADI would give the best surface quality, approaching those of ground as cast components. Al_2O_3, Ti(C,N), Ti(C,N)-Al_2O_3-TiN coatings appear to perform better than TiC-Al_2O_3-TiN, TiN and TiN-Al_2O_3 coatings. Cutting lubricants appear to be effective in the reduction of flank wear, particularly at relatively high cutting speeds.

Depending on the type of ADI, depth of cut and feed, Al_2O_3-based ceramic cutting materials would be effective at cutting speeds up to about 600 m/min. Al_2O_3-TiC (30 wt %) ceramic cutting tools would have the longest life at cutting speed of about 100 m/min and less, whereas ZrO_2-toughened Al_2O_3 inserts would have a longer tool life at cutting speed of about 250 m/min or more thanks to the monoclinic-to-tetragonal transformation of ZrO_2 that occurs at high cutting temperatures and leads to an increase in insert hardness. Al_2O_3-SiC_w ceramic cutting tools would be more suitable than Al_2O_3-TiC ceramic cutting tools in interrupted facing operations at cutting speeds above 400 m/min. When using Al_2O_3-based ceramic cutting tools to machine ADI, flank wear is found to be exclusively the main wear mode although catastrophic fracture could also occur at cutting speeds above 450 m/min. Adhesion wear, abrasion wear, chemical wear, micro-chipping and fracture damage on the tools' cutting edge emerge as key-wear mechanisms controlling tool life.

Si_3N_4-based ceramic cutting tools generally suffer rapid wear when machining ADI close to ASTM Grade 1 and ASTM Grade 2 at relatively low feed and might not be suggested for this application (152). Chemical wear, even at cutting speeds as low as 125 m/min, emerges as a key-wear mechanism controlling tool life.

However, the performance of TiN-Al_2O_3-TiN coated Si_3N_4-based ceramic cutting tools would be acceptable when machining ADI similar to ASTM Grade 2 at high feeds probably thanks to their relatively high cutting edge fracture resistance and the chemical stability brought about by the coating.

The application of PcBN cutting tools in the turning of ADI similar to ASTM Grade 1 would be acceptable for cutting speeds in the range 160-200 m/min.

When turning ADI similar to ASTM Grade 3 with cBN-TiC cutting tools under finish machining conditions, flank wear rate is dependent on cutting temperature. Cutting performance of PcBN cutting tools in this very situation appears to be controlled by the size and volume fraction of cBN grains as well as the thickness of the binder phase. Microspalling of cBN grains, falling-off of adhering particles from the cutting edge, and cracking in the cBN grains by stress concentration would emerge as key-wear mechanisms.

Low cBN content PcBN cutting tools appear to be suitable for dry finish interrupted facing of ASTM Grade 3 ADI at cutting speed of 700 m/min, whilst high cBN content PcBN cutting tools appear to adequately sustain dry rough interrupted facing of ASTM Grade 3 ADI at cutting speed of 425 m/min.

3 STRUCTURE OF THE EXPERIMENTAL WORK

3.1 BACKGROUND TO THE STRUCTURE OF THE EXPERIMENTAL WORK

From the literature review carried out, it appears that the outcome of machining experiments (wear tests) to conduct directly depends on the stress distribution in the cutting area, the temperature distribution in the cutting area and the chip formation mechanism as indicated in Figure 3.1. Such outcome indirectly depends on a very large number of variables related to the cutting tool, the material being cut and the cutting conditions as indicated in Figure 3.2. One way of gaining insight into the complex behaviour of PcBN cutting tools when machining ADI is to explore a relatively wide range of cutting speeds.

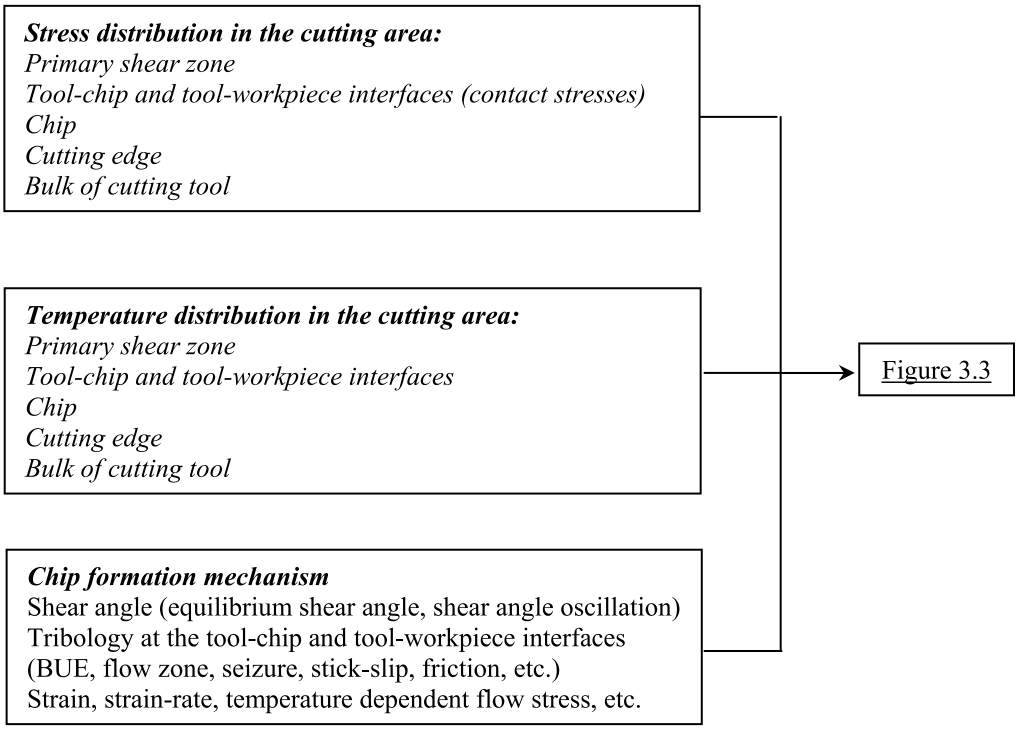

Figure 3.1: Factors affecting machinability directly

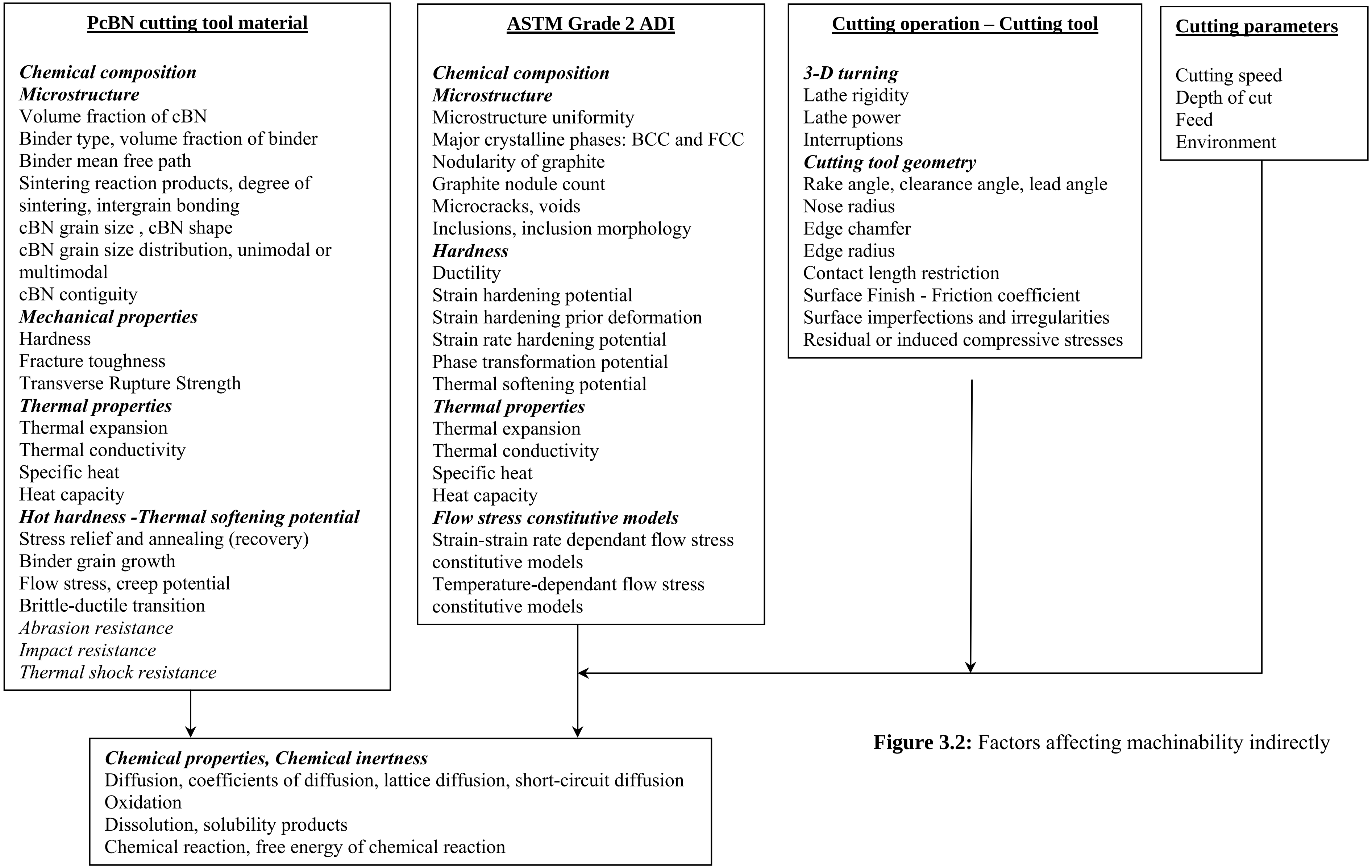

PcBN cutting tool material

Chemical composition
Microstructure
Volume fraction of cBN
Binder type, volume fraction of binder
Binder mean free path
Sintering reaction products, degree of sintering, intergrain bonding
cBN grain size , cBN shape
cBN grain size distribution, unimodal or multimodal
cBN contiguity
Mechanical properties
Hardness
Fracture toughness
Transverse Rupture Strength
Thermal properties
Thermal expansion
Thermal conductivity
Specific heat
Heat capacity
Hot hardness -Thermal softening potential
Stress relief and annealing (recovery)
Binder grain growth
Flow stress, creep potential
Brittle-ductile transition
Abrasion resistance
Impact resistance
Thermal shock resistance

ASTM Grade 2 ADI

Chemical composition
Microstructure
Microstructure uniformity
Major crystalline phases: BCC and FCC
Nodularity of graphite
Graphite nodule count
Microcracks, voids
Inclusions, inclusion morphology
Hardness
Ductility
Strain hardening potential
Strain hardening prior deformation
Strain rate hardening potential
Phase transformation potential
Thermal softening potential
Thermal properties
Thermal expansion
Thermal conductivity
Specific heat
Heat capacity
Flow stress constitutive models
Strain-strain rate dependant flow stress constitutive models
Temperature-dependant flow stress constitutive models

Cutting operation – Cutting tool

3-D turning
Lathe rigidity
Lathe power
Interruptions
Cutting tool geometry
Rake angle, clearance angle, lead angle
Nose radius
Edge chamfer
Edge radius
Contact length restriction
Surface Finish - Friction coefficient
Surface imperfections and irregularities
Residual or induced compressive stresses

Cutting parameters

Cutting speed
Depth of cut
Feed
Environment

Chemical properties, Chemical inertness
Diffusion, coefficients of diffusion, lattice diffusion, short-circuit diffusion
Oxidation
Dissolution, solubility products
Chemical reaction, free energy of chemical reaction

Figure 3.2: Factors affecting machinability indirectly

3.2 STRUCTURE OF THE EXPERIMENTAL WORK

The experimental work that conveys the objectives of the present research (cf Section 1.5) was structured around the flow chart represented in Figure 3.3 which, details the collection of data for the measurement of the performance of PcBN cutting tools when dry turning ASTM Grade 2 ADI under finishing conditions or the machinability of ASTM Grade 2 ADI with PcBN cutting tools under finishing conditions. This data collection bears on factors affecting directly as well as indirectly the machinability-performance (Figures 3.1 and 3.2).

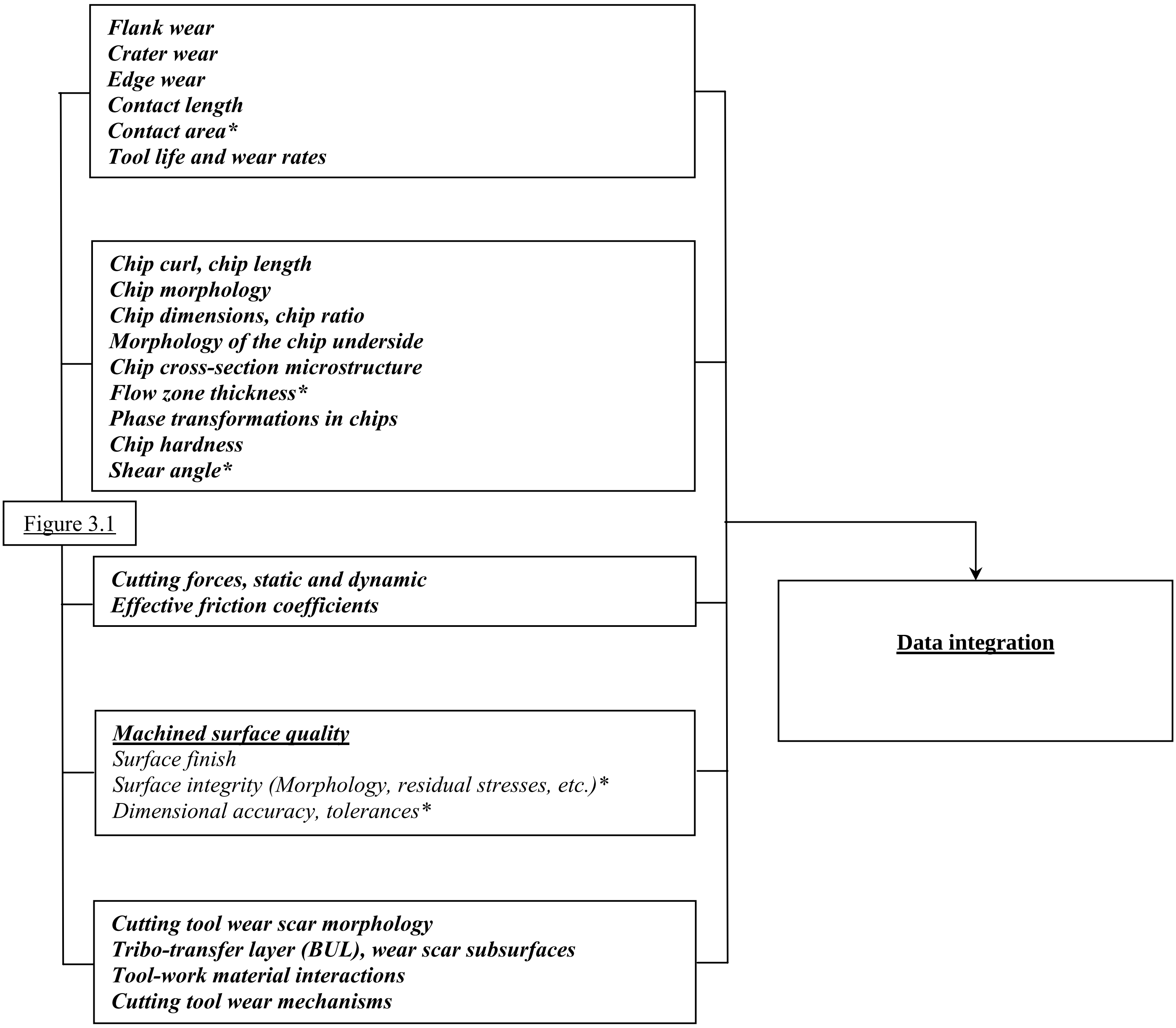

* = parameters that were not monitored

Figure 3.3: Data collection for machinability-performance measurement

Naturally, the dry turning experiments that underlied the data collection were preceded by the characterization of ASTM Grade 2 ADI workpieces and PcBN cutting tools. Oxidation experiments and static interaction experiments were conducted to give more insights on the cutting tool wear mechanisms. Chapter 4 will detail the experimental procedures followed to meet the objectives outlined in Section 1.5.

4 EXPERIMENTAL PROCEDURES

4.1 WORK MATERIAL AND CUTTING TOOLS: CHARACTERIZATION

ASTM Grade 2 ADI workpieces with chemical composition reported in Table 4.1 were used for the dry finish turning experiments. This composition yields a carbon equivalent of 4.323 % and a eutectic saturation of 1.021.

Table 4.1: Chemical composition of ASTM Grade 2 ADI workpieces in weight %

C	Si	Mn	P	S	Ni	Cu	Mg	Fe	CE*
3.51	2.61	0.19	0.016	0.009	0.002	0.62	0.044	Balance	4.385

***CE** is the carbon equivalent = C + (Si+P)/3

These workpieces were characterized in terms of their hardness and microstructure. Hardness tests were done on a ground surface. For the microstructural investigation, cutting, mounting (in Bakelite resin), grinding and polishing of samples were done by conventional metallographic techniques. The microstructure was first studied with an optical microscope followed by a more detailed examination in a SEM. X-ray diffraction (XRD) analyses were also carried out.

The etching reagents used were 3 % Nital and 4% Picral. An image analysis software was used for the characterization of the graphite nodules embedded in these workpieces.

Seco CBN100 PcBN cutting tools in the form of monolithic inserts were used for dry finish turning experiments. They contained about 50 % by volume of cBN, of about 2 µm in grain size and TiC binder, i.e. PcBN cutting tools used were cBN-TiC cutting tools (52).

These tools were investigated with a SEM in order to study their microstructure and with an X-ray diffractometer in order to determine particularly the sintering phases at the boundaries between the TiC binder and cBN grains, which are not easy to resolve with the SEM. The peak width at half maximum height (FWHM) was measured for low diffraction angles for appraising the peak broadening which, gives indication of grain size, lattice defects, stochiometry variation, residual stresses, etc. (165).

4.2 PRINCIPLES, METHODOLOGIES AND TECHNIQUES

4.2.1 Introduction

Dry finish turning experiments, chip characterization, worn cutting tool characterization, oxidation experiments and static interaction experiments constitute the cornerstones of the present research.

4.2.2 Dry turning experiments

The dry finish turning experiments were designed so as to investigate the wear (wear mode, wear mechanism, tool life, cutting length to end of tool life, "ratio of volume of metal removed per unit of flank wear", flank wear rate) of the PcBN cutting tools when machining ADI workpieces at various cutting speeds, according to the ISO Standard 3685-1977(E) for single point turning (166). In conformity with this standard, the wear criterion used for all the dry finish turning experiments was 300 μm of maximum flank wear. This wear criterion is critical to achieve dimensional accuracy and surface roughness required in finish machining.

The experimental setup used for this purpose is presented in Figure 4.1. After a cut corresponding to a certain cutting distance (cutting time), turning was stopped, the cutting insert removed from the toolholder and the flank wear and crater wear scar morphologies were assessed by means of microscopic examination on an optical microscope equipped with a camera. The maximum width of the flank wear scar was then measured. The insert was then carefully replaced in the toolholder, and the procedure repeated until the tool wear reached or exceeded the criterion.

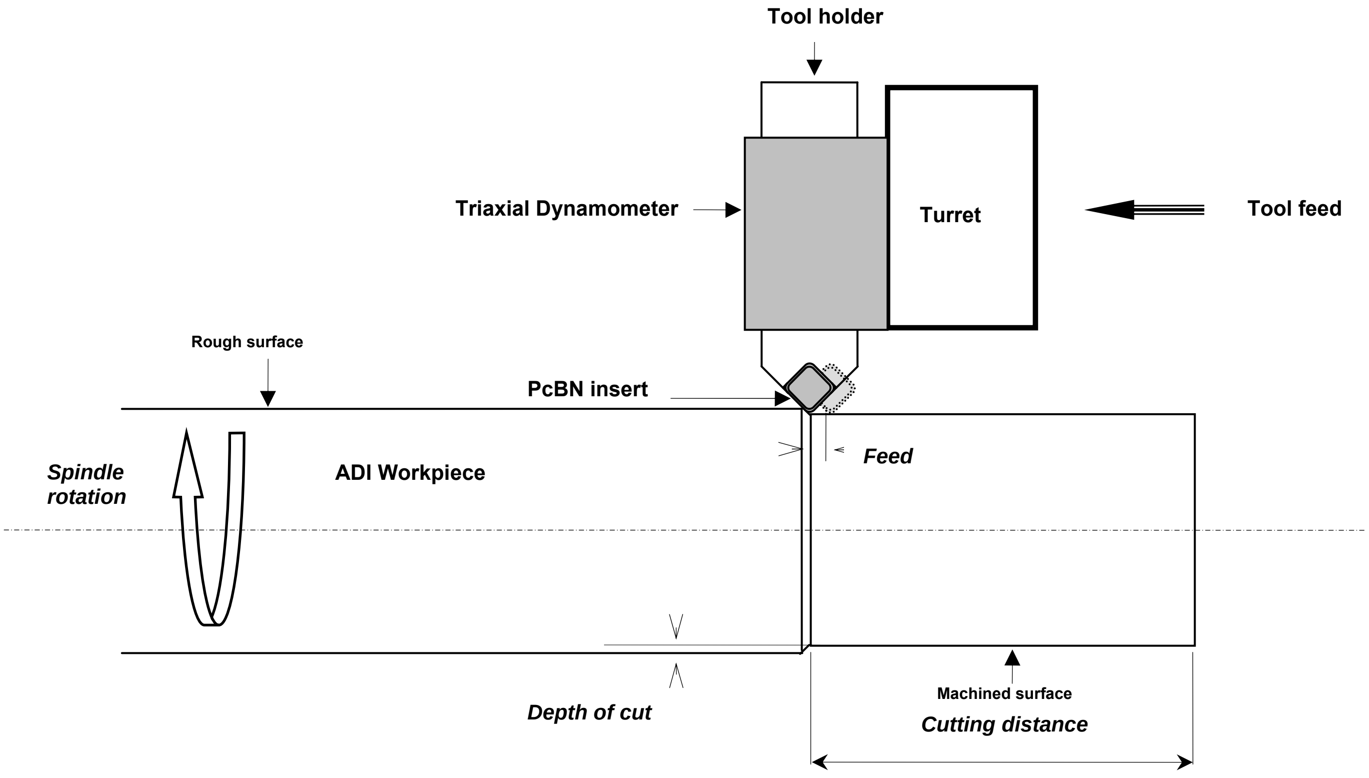

Figure 4.1: Experimental setup for dry turning experiments

The cutting time per cut t_i (s) was calculated from the initial diameter D (mm), cutting distance L (mm), cutting speed V (m/min) and feed f (mm/rev) by using Equation 4.1.

$$t_i = \frac{\pi DL}{1000Vf} \qquad \textbf{(4.1)}$$

The cutting time t (s) corresponding to a complete experiment was the cumulative time calculated from the total number of cuts i by using Equation 4.2.

$$t = \sum_i t_i \qquad \textbf{(4.2)}$$

The cutting length l_c (m) was calculated from the cutting speed V (m/min) and cutting time t (s) by using Equation 4.3.

$$l_c = \frac{Vt}{60} \qquad \textbf{(4.3)}$$

The metal removal rate MRR (cm^3/min) was calculated from the cutting speed V (m/min), feed f (mm/rev) and depth of cut d (mm) by using Equation 4.4.

$$MRR = Vfd \tag{4.4}$$

The volume of metal removed MR (cm^3) was calculated from the metal removal rate MRR (cm^3/min) and cutting time t (s) by using Equation 4.5.

$$MR = \frac{MRR.t}{60} \tag{4.5}$$

4.2.2.1 Cutting parameters

The index specification of Seco CBN100 PcBN cutting tools was SNGN 090312 S (nose radius 1.2 mm, honed, chamfer 0.1 mm x 20°). They were mounted on a toolholder described as CSDNN 2525M12C (Figure 4.2).

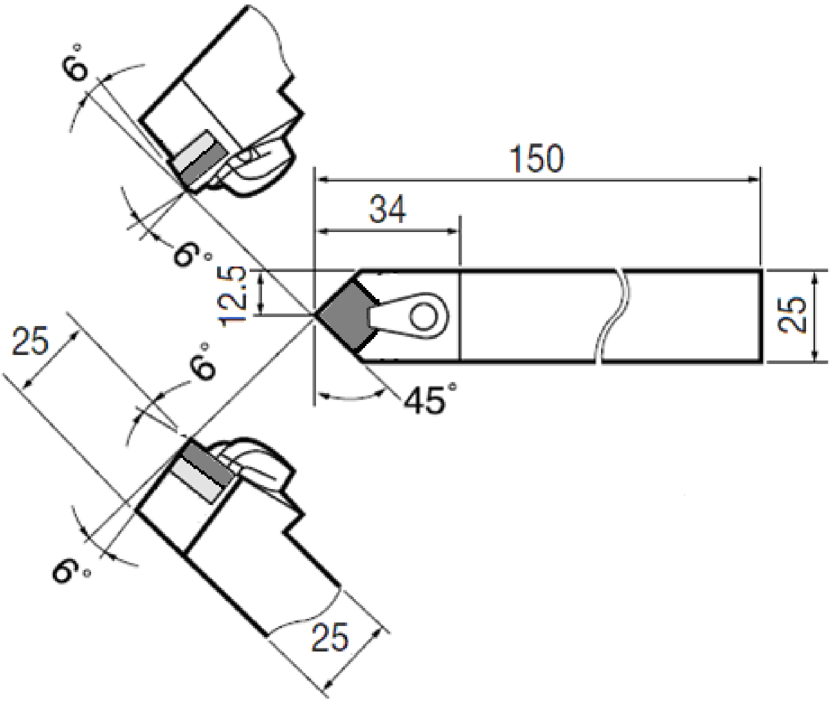

Figure 4.2: CSDNN 2525M12C toolholder

All the dry finish turning experiments were carried out using a depth of cut of 0.2 mm. The feed was constant at 0.05 mm/rev and cutting speeds ranged from 50 to 800 m/min. The depth of cut was similar in size to the tool chamfer (Figure 4.3).

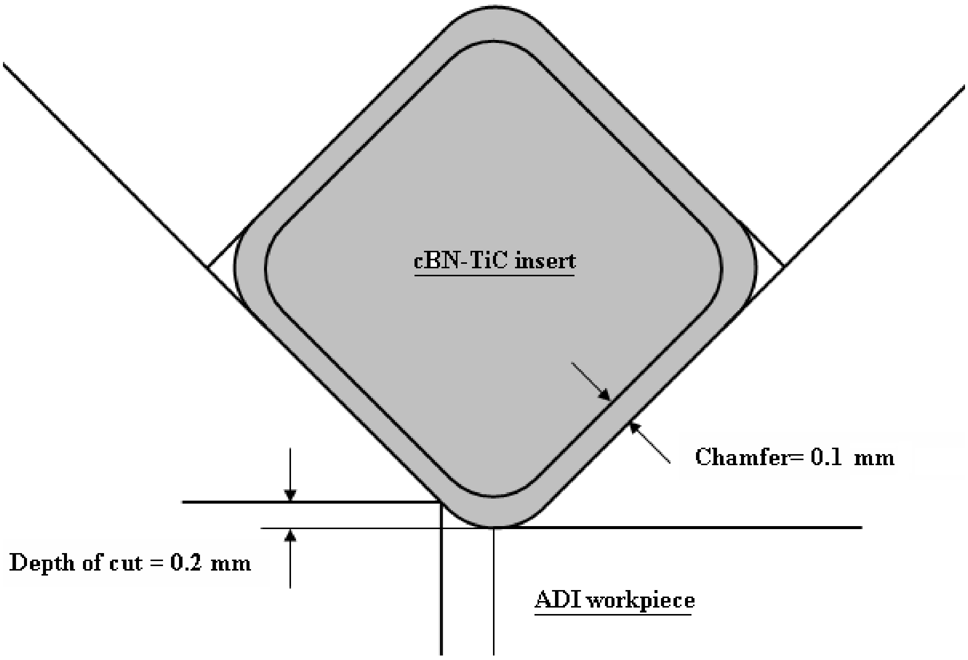

Figure 4.3: Depth of cut and edge chamfer

The combination of insert and toolholder resulted in a rake angle of -26°, a clearance angle of 6° and an approach angle of 45°. For such an assembly, the wear criterion of 300 µm of maximum flank wear used in this work corresponds to a cutting edge decline of 0.03 mm (60).

4.2.2.2 Temperature estimation

During the dry finish turning experiments, the temperature of chips was roughly estimated, for indication purposes, by temper colour in the dark.

4.2.2.3 Surface finish appraisal

After each cut, the surface finish of the machined surface was roughly appraised, for indication purposes, by visual and tactile examinations.

4.2.2.4 Wear curves

Plots of maximum flank wear V_{BC} (µm) against cutting time t (s) as well as plots of volume of flank wear per unit of engagement length V_α (μm^2) against cutting length l_c (m) were produced. The volume of flank wear per unit of engagement length V_α corresponding to the geometry of the cutting tools used in this research has been shown to be (167):

$$V_\alpha = 0.05\,(V_{BC})^2 \qquad \textbf{(4.6)}$$

Power regression was used to fit the plots of V_{BC} against t, to estimate the cutting tool life corresponding to the wear criterion and to determine the Taylor cutting tool life equation. The flank wear rate used in this research was the slope of the plot of V_α against l_c.

4.2.2.5 Cutting forces

A tri-axial piezoelectric dynamometer mounted on the lathe's turret (Figure 4.1) and coupled to a multi-channel amplifier was used for the measurement of cutting forces. These cutting forces (Figure 4.4) comprised the tangential force F_t (or simply cutting force F_c), the thrust force F_r (or radial force) and the axial force F_f (or feed force).

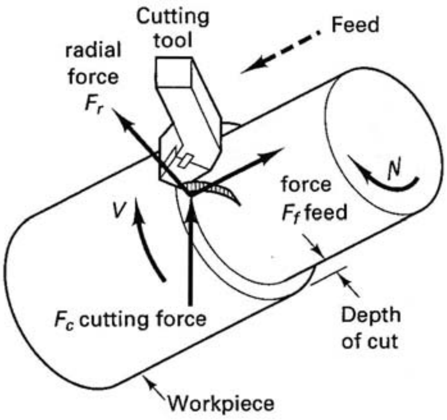

Figure 4.4: Cutting forces

The amplified cutting force signals (F_{ti}, F_{ri} and F_{fi}) were acquired and sampled at a sampling rate of 500 Hz per channel by using a data acquisition card coupled to a computer with the help of appropriate software.

The cutting force signals acquired were analysed so as to evaluate the static and dynamic cutting forces corresponding to a specific time. The static cutting forces were estimated as the average of the signals F_{ti}, F_{ri} and F_{fi} (Equations 4.7 to 4.9).

$$\bar{F}_t = \frac{1}{N}\sum_{i=1}^{N} F_{ti} \tag{4.7}$$

$$\bar{F}_r = \frac{1}{N}\sum_{i=1}^{N} F_{ri} \tag{4.8}$$

$$\bar{F}_f = \frac{1}{N}\sum_{i=1}^{N} F_{fi} \tag{4.9}$$

where N is the number of cutting force data recorded by the computer.

The dynamic cutting forces were estimated as the variation from the static cutting forces (168) (Equations 4.10 to 4.12).

$$F_{td} = \sqrt{\frac{\sum_{i=1}^{N} (F_{ti} - F'_{ti})^2}{N}} \quad \textbf{(4.10)}$$

$$F_{rd} = \sqrt{\frac{\sum_{i=1}^{N} (F_{ri} - F'_{ri})^2}{N}} \quad \textbf{(4.11)}$$

$$F_{fd} = \sqrt{\frac{\sum_{i=1}^{N} (F_{fi} - F'_{fi})^2}{N}} \quad \textbf{(4.12)}$$

where N is the number of cutting force data recorded by the computer; F_{ti}', F_{ri}' and F_{fi}' respectively the estimated values from linear regression of the tangential, thrust and feed cutting forces F_{ti}, F_{ri} and F_{fi}.

The force signals acquired were analysed for a cutting time of 1 s, i.e. a time presumably within the wear initiation period. This particular analysis was done in order to isolate the variations of cutting forces due to changes in cutting speed from variations of cutting forces due to cutting tool wear. Dynamic cutting forces were analysed to detect the influence of adhesion of chips on the rake face, chip segmentation, etc. on the cutting forces.

4.2.2.6 Effective friction coefficient

The effective friction coefficient μ_e was calculated from static cutting forces using Equation 4.13 derived from Figure 4.5.

$$\mu_e = \frac{\sqrt{(F_f)^2 + (F_r \cos 26° - F_t \cos 64°)^2}}{F_t \sin 64° + F_r \sin 26°} \quad \textbf{(4.13)}$$

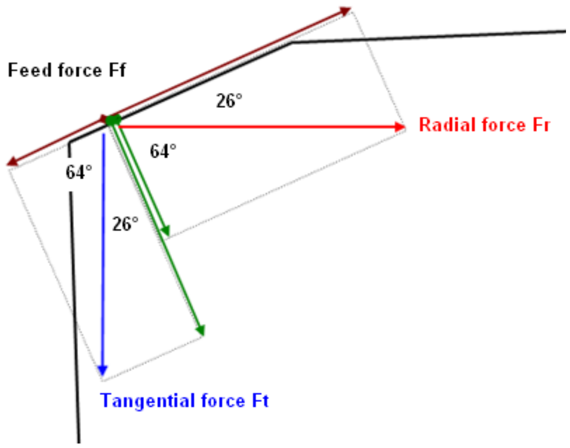

26°= - rake angle, **F_f** is perpendicular to the plane of the sheet

Figure 4.5: Components of cutting forces used to derive the effective friction coefficient

4.2.3 Chip characterization

Chips were collected after each cut and examined visually. Their underside and cross-section morphologies as well as their microstructure were investigated with an optical microscope and a SEM. The average chip thickness was measured to capture the mean level of material deformation involved in the chip formation process. The chip hardness was measured to assess the interplay between strain hardening and dynamic softening.

The microstructure of chips was extensively investigated in order to capture as much as possible the metallurgical aspects involved in the chip formation process and possible interactions with the cutting tool as these should affect wear mechanisms. In this regard, the secondary shear zone was of particular interest. Accordingly, TEM was used to examine the nanostructure of the primary and secondary shear zones of the chips.

The morphology of chips was particularly monitored to capture the cutting speed range at which the transition from continuous to shear-localized chip formation occurs. The morphology of the underside of chips was investigated to, among others, assess qualitatively the tribology at the tool-chip interface, particularly with regard to the temperature at this interface.

The underside morphologies of chips were investigated without any preparation. The average thickness of chips, cross-section morphology, microstructure and hardness were investigated after mounting in cold resin and metallographic preparation. The average chip thickness was measured using software for image analysis. Chip etching was carried out in 3 % Nital. Bright field optical microscopy and differential interference contrast (DIC) techniques were used on the optical microscope. The DIC technique was used to improve the contrast between the primary and secondary shear zones and the bulk of the chips. TEM samples were prepared by grinding, polishing and precision ion milling.

4.2.4 Worn cutting tool characterization

An optical microscope equipped with a camera was used to measure the width of the flank wear scar and to obtain optical micrographs of wear scars.

The worn cutting tools were also examined in the SEM at their wear initiation period as well as at the end of their life and energy dispersive X-ray spectroscopy (EDX) analyses were carried out to determine the nature of physical and chemical interactions taking place on the wear scars during machining. Backscattered electron (BSE) imaging was used to enhance contrast between different phases, whereas secondary electron (SE) imaging was used to show the topography of the surface.

The microstructure of the cross-section of selected worn cutting tools was investigated in detail by transmission electron microscopy. EDX analyses were extensively used to complete these investigations. Worn cutting tool samples for transmission electron microscopy were prepared with FIB using 30 kV Ga ions in a dual beam Nova FIB with in-situ “lift-out”.

TEM samples manufactured by the "lift-out" method provide a rapid means of preparing an electron transparent cross-section from a specific site of interest. Instead of beginning with a thin slice of material mounted on a grid, a relatively large bulk sample can be inserted directly into the FIB chamber and a specimen created straight from the bulk sample's surface.

The area of interest in the sample is coated first with a layer of platinum to protect the surface. Using a large beam current for fast ion milling, two trenches are milled on either side of the platinum that has been deposited above the area of interest.

The thin sample is ion polished on both sides to a thickness of between 120 and 50 nm. The final step, “lift-out” procedure involves the use of a glass needle and a micromanipulator to mount the thin sample on a TEM grid.

4.2.5 Oxidation experiments

The oxidation behaviour of cBN-TiC cutting tools was experimentally investigated in the temperature range 550-1100 °C in air by thermogravimetry under anisothermal conditions and isothermal conditions for 60 min.

The oxidation behaviour of cBN-TiC cutting tools was also experimentally investigated in the temperature range 900-1100 °C in still air by using a laboratory muffle furnace under isothermal conditions for 60 min.

4.2.5.1 Thermogravimetry thermal analyses of cBN-TiC cutting tools

Thermogravimetry analysis (TGA) was used primarily to determine the temperature at which significant oxidation of cBN-TiC cutting tools start taking place. It is also expected to retrieve information on oxidation kinetics.

As received Seco CBN100 PcBN cutting tools were crushed with a hydraulic press in order to get samples to suit the small crucible (diameter ~ 3 mm) of the TGA-DTA thermobalance. The small samples obtained were cleaned in acetone and ethanol to remove surface contaminations and then dried. TGA were done in a flowing air stream. Two categories of TGA were performed namely anisothermal and isothermal.

In the first category of experiments, cBN-TiC cutting tool samples were heated in the TGA-DTA thermobalance from room temperature up to 1100 °C at a rate of 5 °C/min and then immediately cooled to room temperature at the same rate in order to get an indication of characteristic temperatures.

In the second category of experiments, cBN-TiC cutting tool samples were heated from room temperature up to temperatures of 550, 900, 1000 and 1100 °C at a rate of 5 °C/min, then maintained at this specific temperature for 60 min, and finally cooled to room temperature at the same rate. A typical temperature profile used for isothermal TGA of cBN-TiC cutting tools is presented in Figure 4.6.

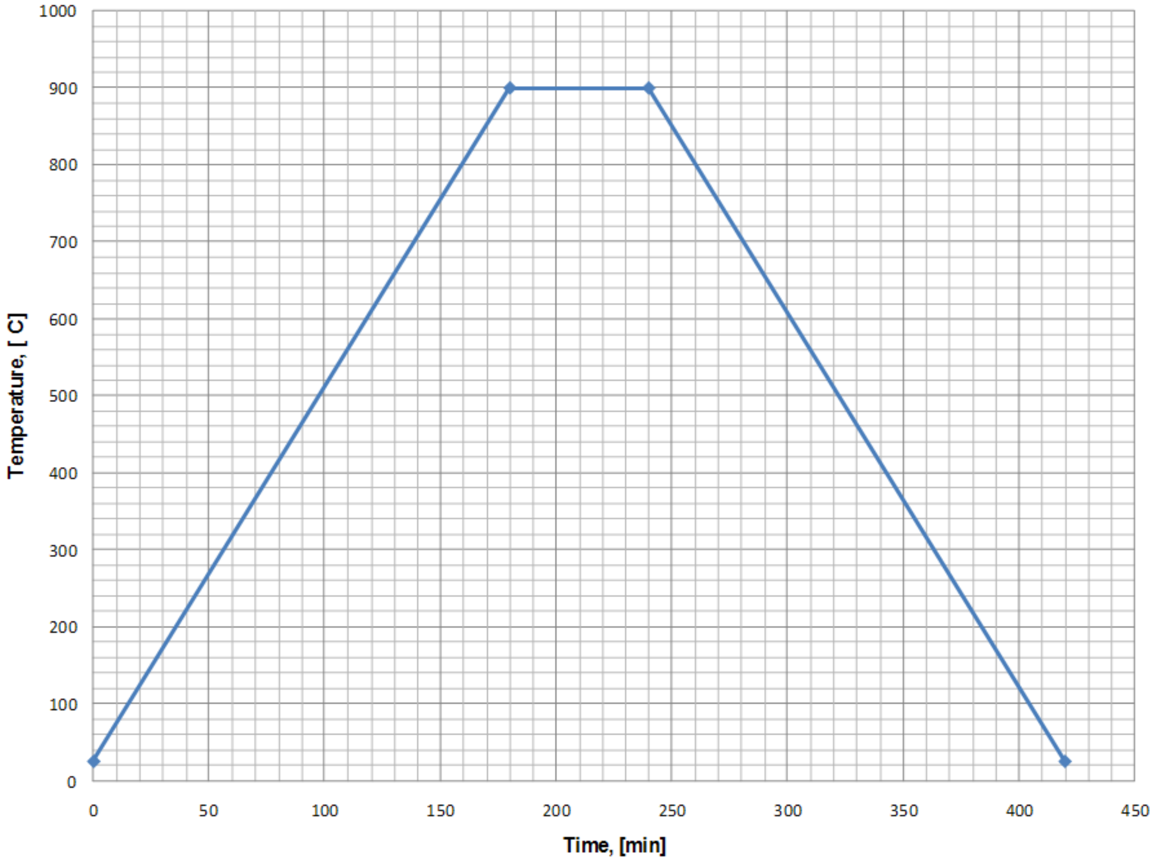

Figure 4.6: Typical temperature profile used for isothermal TGA of cBN-TiC cutting tools

After the TGA, each residual material was collected for examination and characterization. A SEM equipped with EDS was used to investigate the morphology and composition of the oxide scale.

4.2.5.2 Oxidation of cBN-TiC cutting tools

Oxidation experiments of cBN-TiC cutting tools were performed in a laboratory muffle furnace in still air. For each experiment, a Seco CBN100 PcBN cutting tool was put in an Al_2O_3 crucible. The crucible was respectively heated from room temperature up to temperatures of 900, 1000 and 1100°C at a rate of 5°C/min, maintained at this temperature for 60 min, and cooled to room temperature at the same rate. Typical temperature profile used for oxidation of cBN-TiC cutting tools is similar to that used for TGA of cBN-TiC cutting tools (Figure 4.6).

After the cycle of oxidation was completed, each sample was characterized with respect to its scale. XRD analysis was used to identify the phases in the oxide scale without metallographic preparation. Thereafter, the sample was cross-sectioned with an EDM saw across the scale. This cross-section was ground on a diamond coated wheel and polished with a diamond paste

(0.5 μm). After this step the polished sample was cleaned in acetone and ethanol and then dried. From then on, a SEM equipped with EDS was used to investigate the morphology, the composition and the thickness of the scale on the cross-section of the sample.

4.2.6 Static interaction experiments

4.2.6.1 Introduction

Very often, the processes by which cutting tool wear occurs are extremely complex. Generally, a single wear mechanism such as abrasion, plastic deformation, delamination, adhesion, chemical reaction or tribo-oxidation, cannot by itself explain the wear of cutting tool (169).

Therefore, in order to study the chemical interactions between cBN-TiC cutting tool material and ADI without the interference of mechanical wear mechanisms, mainly adhesion and abrasion wear mechanisms, static interaction experiments were performed. In these, polished slices of ASTM Grade 2 ADI and cBN-TiC cutting tool were held together under pressure of 200 MPa at 1100°C for 60 min.

Taking into account that C, Si and Mg are key elements in ADI on one hand and relatively reactive on the other hand, their interactions with the cBN-TiC cutting tool material need to be clearly established in conditions where their thermodynamic activities are particularly high, i.e. in their pure state.

The interaction of Si with cBN-TiC cutting tool material is particularly significant because of its relatively high concentration in the ADI matrix. Therefore, similar experiments were carried out using Si wafers and cBN-TiC cutting tool material in order to investigate interactions between them at pressure of 200 MPa and temperature of 1000 °C for 60°min.

4.2.6.2 Sample preparation

The static interaction couples were of sandwich-type as indicated in Figures 4.7 and 4.8. The ADI slices to be hot pressed together with a cBN-TiC cutting tool were of about 12x12x12 mm^3. They were polished on both parallel top and bottom surfaces down to 0.5 μm with alumina slurry. The cBN-TiC cutting tool was used in its as received condition. The Si wafers used in the hot pressing experiments were about 5x5x1 mm^3 in size and were in the as received condition as was the cBN-TiC cutting tools used with them. All materials were carefully cleaned and degreased in ethanol prior to assembling as shown in Figures 4.7 and 4.8.

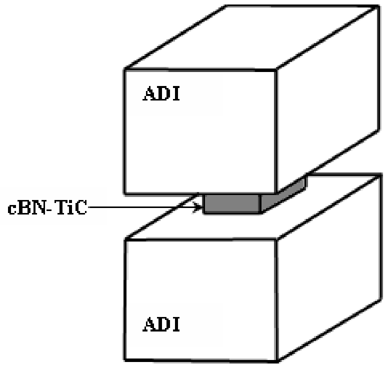

Figure 4.7: The ADI/cBN-TiC/ADI static interaction couple

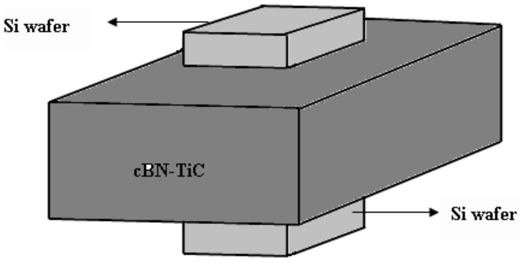

Figure 4.8: The Si/cBN-TiC/Si static interaction couple

4.2.6.3 Hot uniaxial pressing

A die assembly (Figure 4.9) containing the sandwich-type static interaction couple was the key-device for all these experiments. The lower and upper punches as well as the die (with its insert) were of graphite. Before hot pressing, the outer surfaces of the lower and upper punches as well as the inner surface of the die insert, i.e. the graphite surfaces designed to be in the hot-zone of the furnace, were coated with a hBN suspension (37 g of hBN powder in 100 ml of water) which had been stabilised with poly-vinyl pyrolidone (2 g). The suspension was stirred vigorously using a magnetic stirrer until the consistency of the entire suspension was uniform. The suspension was then used to coat the graphite surfaces.

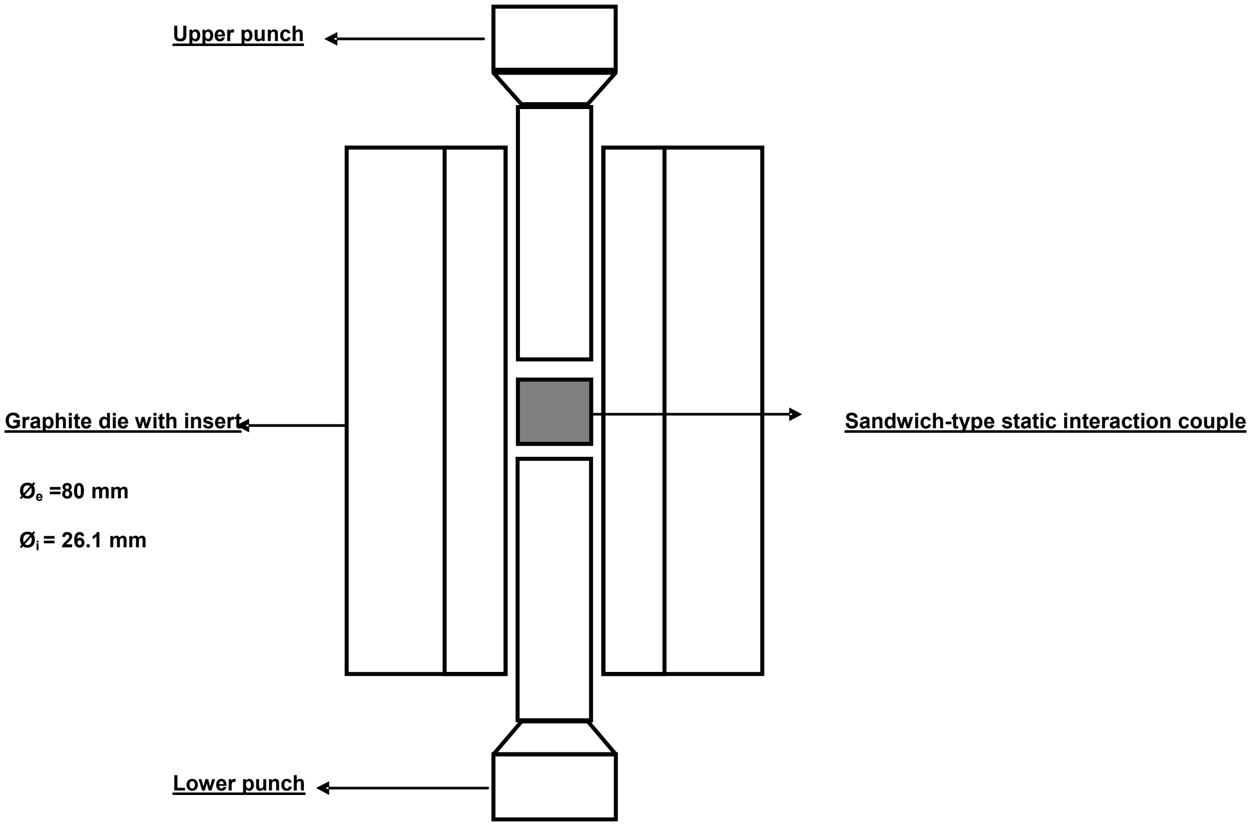

Figure 4.9: The schematic diagram of the uniaxial hot pressing die assembly

The die assembly was mounted inside a hot uniaxial press in several stages. The upper punch was fixed (threaded) to the top of the hot press furnace. The sandwich-type static interaction couple was assembled on top of the lower punch of the die assembly on a bench. The die (with insert) was then slid carefully around the lower punch and the whole was transported carefully from the bench to the bottom of the hot press furnace. The whole was then slowly raised until the static interaction couple was squeezed between the upper and lower punches. The hot press furnace was then closed.

For each hot uniaxial pressing experiment, the static interaction couple (Figures 4.7 and 4.8) was heated from room temperature to a temperature of 1000 °C or 1100 °C at a rate of 5 °C/min in an argon atmosphere. It was maintained at this temperature for 60 min, and cooled inside the furnace to room temperature at the same rate. The pressure was gradually applied to the sandwich from 700 °C until a pressure of 200 MPa was reached at which point the dwell time was measured. This pressure was regularly readjusted in order to keep it constant during the dwell time of 60 min. The magnitude of this pressure is very low compared to the normal pressure encountered at the flank and crater wear scars in machining experiments (order of GPa) (170). However such a pressure ensures good contact between the different elements of the interaction couple. During the cooling cycle, the pressure was no more readjusted. The pressure and the flow of argon were maintained during the cooling, down to room temperature. The temperature profile used for the hot uniaxial pressing experiments was similar to that used for isothermal TGA of cBN-TiC cutting tools (Figure 4.6).

The static interaction couples were sectioned with an EDM saw across the interaction interface. These sections were ground and polished with a diamond paste (0.5 µm). They were then cleaned in acetone and ethanol and dried. SEM equipped with EDS was used to characterize the interaction interface of the polished sections.

4.3 MAJOR EQUIPMENT

4.3.1 Hardness tester

A Leco V-100-A2 Vickers hardness testing machine was used to measure the hardness of ADI workpieces. Hardness tests were done using a load of 30 kgf and a dwell time of 15 s.

4.3.2 Optical microscope and image analysis software

An Olympus BX41M optical microscope coupled to an Olympus Camedia Camera and connected to a computer under the image analysis software AnalySIS® 5 was used to acquire optical micrographs, to measure the chip thickness as well as the width of the flank wear scar and to perform all image analysis tasks.

4.3.3 X-ray diffractometer

An X-ray Philips X'Pert MPD vertical diffractometer fitted with a copper anode was used for XRD analyses of ADI workpieces, cutting tools and oxidized cutting tools. The voltage used was 45 kV, the current 40 mA, the step size 0.05° 2θ, the scan step time 6.8 s and the scan type continuous.

Diffraction peak profile analysis and phase analysis of the X-ray diffractograms were done by means of the PANalytical X'Pert HighScore® version 1.0 d software with an in-built International Centre for Diffraction Data (ICSD) database. Collected XRD scans were background-corrected and $K_{\alpha2}$ stripped before determining peak position. Peaks were identified by comparing the acquired d-values to the values obtained from the database.

4.3.4 Scanning electron microscope (SEM)

A Philips XL 30 ESEM-FEG XL series field emission SEM equipped with an EDAX energy dispersive spectroscope (EDS) connected to a computer under the Genesis software was used to acquire SEM micrographs and chemical compositions in the course of the investigation of ADI workpieces, cutting tools, chips, worn cutting tools, oxidized cutting tools and static interaction couples. BSE imaging was used to enhance contrast between different phases, whereas SE imaging was used to show the topography of the surface.

4.3.5 Lathe

A rigid LA 200 L Liouy-Hsing CNC lathe (Figure 4.10) rated at 14.72 kW spindle power and a maximum spindle speed of 6000 rpm and using a Fanuc O*i*-TB CNC controller was used to perform dry finish turning experiments. This lathe has a 3-jaw hydraulic chuck, an 8-position hydraulic turret and a hydraulic tailstock.

Figure 4.10: The LA 200 L Liouy-Hsing CNC lathe used for the dry finish turning experiments

4.3.6 Triaxial dynamometer and multi-channel amplifier

A 3-component quartz piezoelectric dynamometer Kistler type 9257B (Figure 4.11) was used to measure the cutting forces during the dry finish turning experiments. This dynamometer has sensitivities of - 7.955 pC/N, - 7.95 pC/N and - 3.715 pC/N respectively for the x-axis, y-axis, and z-axis in the calibrated range 0-500 N. It has high rigidity and consequently a high natural frequency. Its high resolution enables the smallest dynamic changes in large forces to be measured.

Figure 4.11: The 3-component quartz piezoelectric dynamometer Kistler type 9257B

The dynamometer was mounted on the hydraulic turret of the lathe in such a way as to have the x-axis in the direction of the tangential cutting force, the y-axis in the direction of the thrust force, and the z-axis in the direction of the axial force.

A multi-channel charge amplifier Kistler type 5070A (Figure 4.12) was coupled to the dynamometer to amplify the dynamometer output signals into voltages appropriate for the data acquisition system. The output signals of this amplifier were fed into an A/D data acquisition card type 2855A4 mounted on a PCI port of a computer running the acquisition software for data logging. Dynoware data acquisition and evaluation software type 2825A-02 Version 2.4.1.3 was used for this purpose.

Figure 4.12: The Multi-channel amplifier Kistler type 5070A

4.3.7 Microhardness tester

A Leco M-400A microindentation hardness testing machine was used for chip hardness measurements. These measurements were made using a load of 50 gf and a dwell time of 10 s.

4.3.8 Transmission electron microscope (TEM)

A Philips 420 scanning transmission electron microscope (STEM) using a LaB_6 electron source at 120 kV and equipped with EDS was used for TEM investigations of chips and selected worn cutting tools. The thin samples were examined in the transmission and diffraction modes.

4.3.9 Muffle furnace

A muffle furnace Elite model No BRF16/5-2416 from Elite Thermal Systems Limited was used for the oxidation experiments of cBN-TiC cutting tools. This furnace could reach a maximum temperature of 1600°C.

4.3.10 TGA thermobalance

A Mettler-Toledo TGA/SDTA 851e thermobalance equipped with a Mettler STAR^{e} SW version 8.10 software was used for thermal analysis. The main features of this thermobalance were as follows:

- Measurement range: up to 5 g
- Temperature range: room temperature to 1600 °C

- Fast heating rate of 5 min from room temperature up to 1100 °C, cooling rate of 25 min from 1000 °C to 100 °C, temperature accuracy of 0.25%
- Automatic weight calibration

All experiments were performed in air. The heating rate was constant at 5 °C/min.

4.3.11 Hot uniaxial press

A hot uniaxial press Thermal Technology HP20-2560-FP20 (Figure 4.13) was used for the static interaction experiments carried out in this research. This facility consists of a hydraulic uniaxial press combined with a graphite resistance furnace. The graphite resistance furnace is heated under vacuum or inert atmosphere and is water-cooled. It has a maximum operating temperature of 2100°C and a programmable temperature profile. A rotary vacuum pump is attached to this press and is capable of vacuum levels of 10 mtorr. The hydraulic uniaxial press applies the load from the bottom to the die assembly mounted in the furnace through the upper and lower graphite punches. This press is capable of a maximum load of 100 000 N.

Figure 4.13: The hot uniaxial press Thermal Technology HP20-2560-FP20

For each static interaction experiment, the furnace was evacuated to a pressure below 300 mtorr (2×10^{-4} atm = 40 Pa), then flushed with high purity argon gas and evacuated again, and finally back filled with ultra high purity argon to pressures slightly above 1 atm (110-120 kPa). argon was allowed to flow through the furnace during the entire experiment.

5 RESULTS

5.1 WORK MATERIAL AND CUTTING TOOLS: CHARACTERIZATION

5.1.1 Hardness and microstructure of ASTM Grade 2 ADI

The hardness of the ASTM Grade 2 ADI workpieces was 312 HV_{30}. Image analysis of optical micrographs of unetched ASTM Grade 2 ADI samples (Figure 5.1) revealed a volume fraction of graphite of 15%, a distribution of graphite particles of 190 nodules/mm^2, an apparent mean graphite nodule size of 30 μm and a graphite nodule spacing of 72 μm.

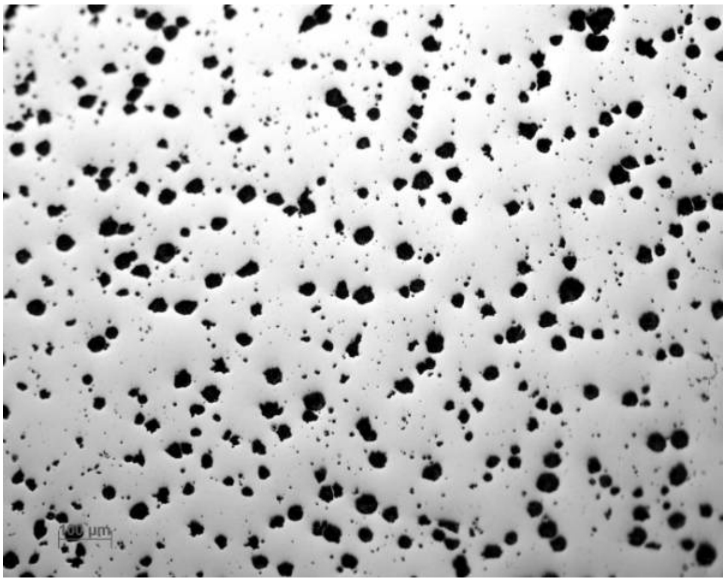

Figure 5. 1: Microstructure of the workpiece (ASTM Grade 2 ADI). Unetched, Optical microscope

The principal micro-constituents of ASTM Grade 2 ADI were graphite nodules embedded in a matrix of ausferrite (ferrite needles and stringer-like retained austenite) and island-like residual austenite (Figure 5.2).

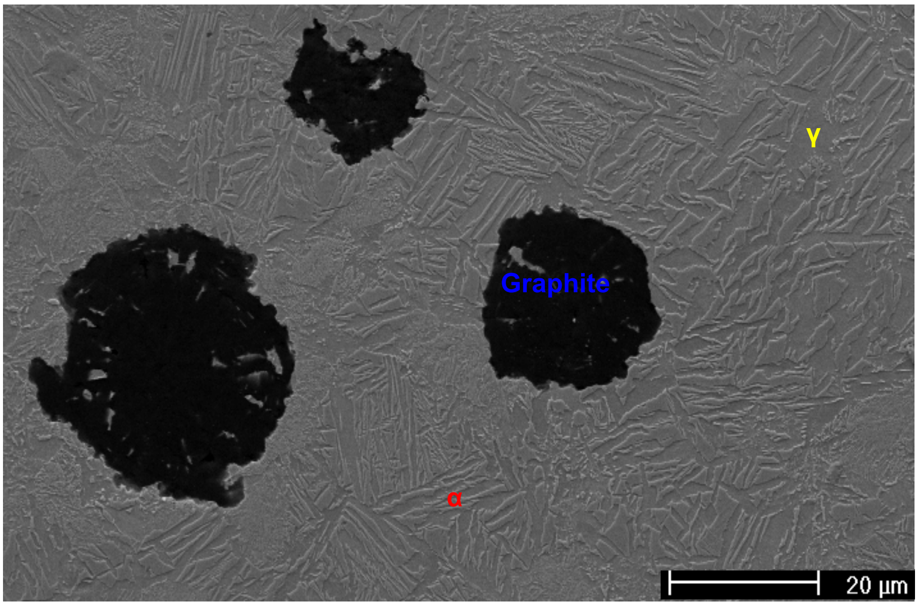

Figure 5.2: Microstructure of the workpiece (ASTM Grade 2 ADI). Etched, 4 % Picral, SEM, SE image

5.1.2 XRD of ASTM Grade 2 ADI

XRD analyses of the ASTM Grade 2 ADI confirmed the presence of ferrite and austenite as the major phases of the matrix (Figure 5.3).

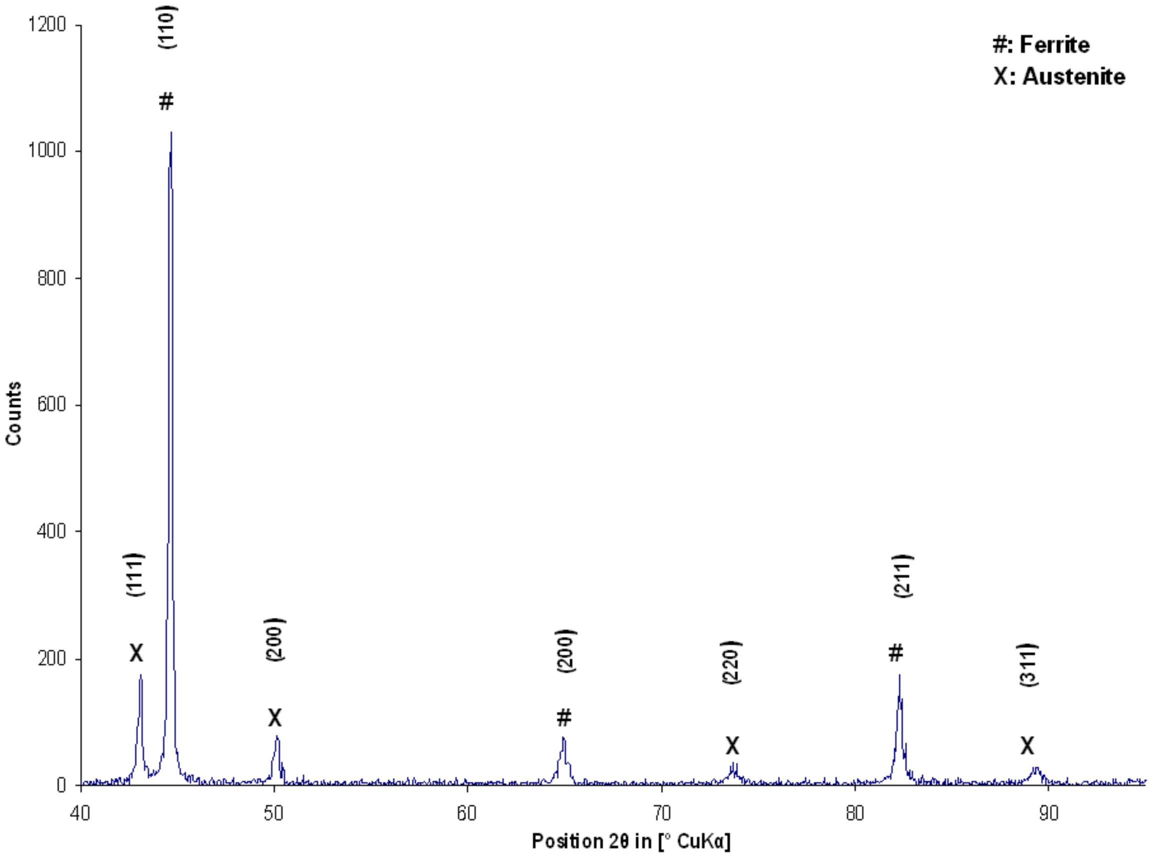

Figure 5.3: X-ray diffractogram of the ASTM Grade 2 ADI, using CuK$_α$ radiation

5.1.3 Microstructure of Seco CBN100 cutting tools

The microstructure of the Seco CBN100 cutting tools showed mainly two interpenetrating continuous phases of TiC and cBN (Figure 5.4). TiC appeared as a light grey phase and cBN appeared as a dark phase. The dark grey phase which appeared in some areas could be either TiB_2 or an Al-based phase. A white phase which appeared scarcely was WC. cBN-cBN contacts were not overwhelming in the microstructure. In SE imaging mode, the morphology of the surface gave the impression that cBN grains were protruding slightly in relation to the TiC binder (Figure 5.5).

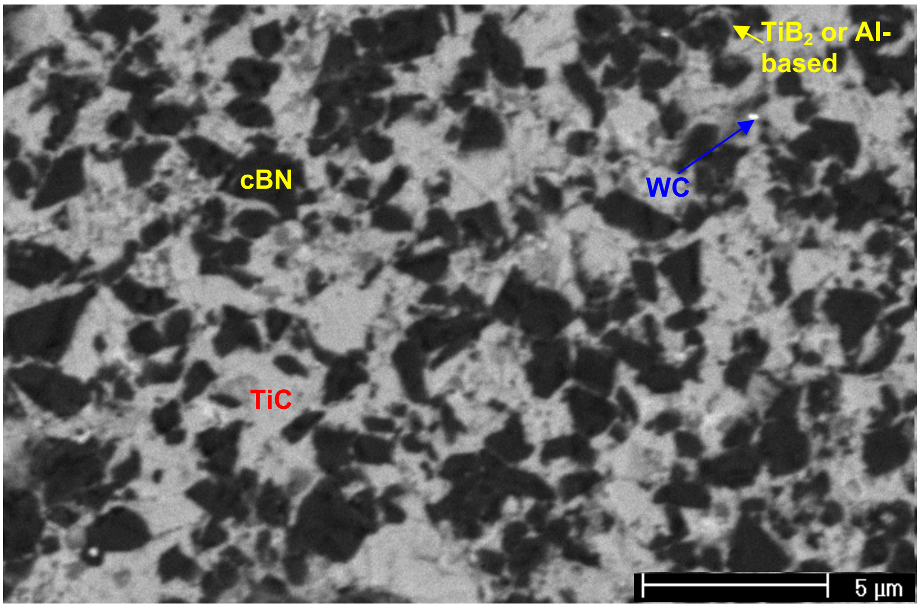

Figure 5.4: Microstructure of Seco CBN100 cutting tool, SEM, BSE image

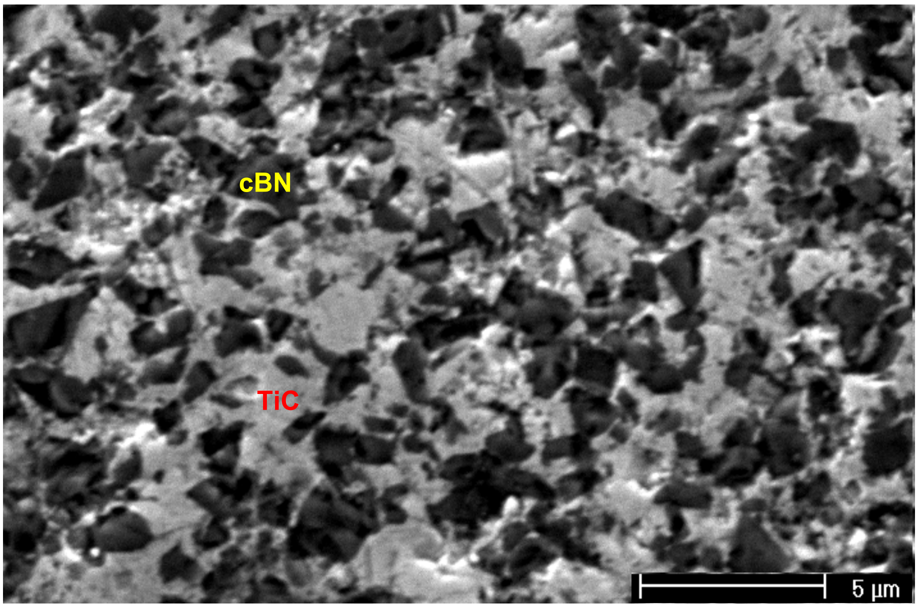

Figure 5.5: Microstructure of Seco CBN100 cutting tool, SEM, SE image

5.1.4 XRD of Seco CBN100 cutting tools

XRD analyses of Seco CBN100 cutting tools confirmed the presence of TiC and cBN as the major phases and indicated the presence of a minor phase, TiB_2 (Figure 5.6) that formed during sintering at the interface between cBN grains and TiC binder where it typically acted as a bonding agent.

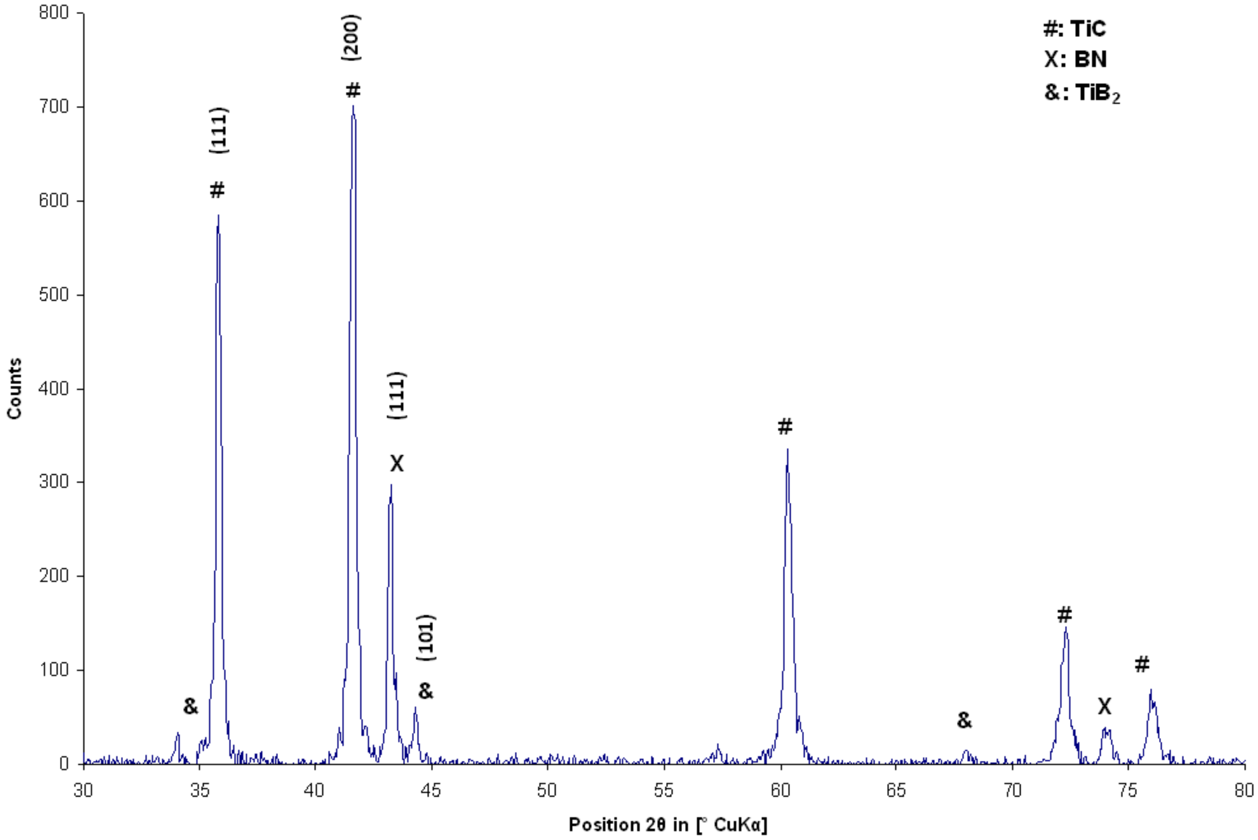

Figure 5.6: X-ray diffractogram of a Seco CBN 100 cutting tool, using CuK_α radiation

The ratio of the intensity of the XRD peak of TiB_2 from the (101) plane and that of cBN from the (111) plane, was 16.19%. This ratio which can be used as a measure of the concentration of TiB_2 in PcBN cutting tools, was higher than the highest critical ratio (12 %) suggested by Can et al. (53), indicating a relatively high amount of TiB_2.

The FWHM values of the XRD peaks of the (111) and (200) planes of TiC were 0.3000° 2θ using Cu K_α radiation. By reference to the values (> 0.2° 2θ, Cu K_α) suggested by Can et al. (53), these FWHM values reveal substantial peak broadening of the TiC binder indicative of either a finer grain size and or a substantial level of lattice defects or even a variation in the stoichiometry (53,56) of the TiC binder.

5.2 WEAR PERFORMANCE

5.2.1 Wear modes

Damage to the cutting tools over the entire range of cutting speeds was mainly in the form of flank and crater wear. In terms of wear initiation, early formation of a crater scar was noticeable at cutting speeds greater than 150 m/min (Figures 5.7 to 5.12). It is evident from these figures that the cutting speed has a major impact on deterioration process of cutting tools.

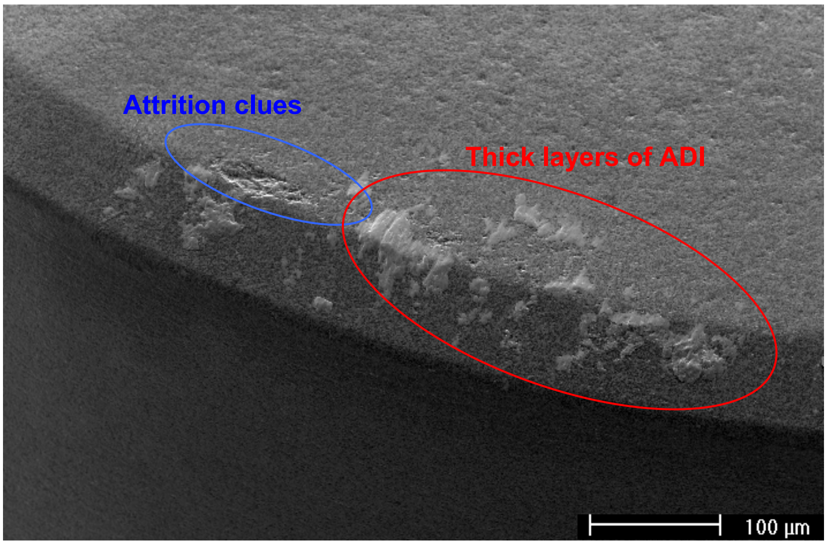

Figure 5.7: Wear scar of a cutting tool used at 50 m/min for 160.34 s (133.62 m). SEM, SE image

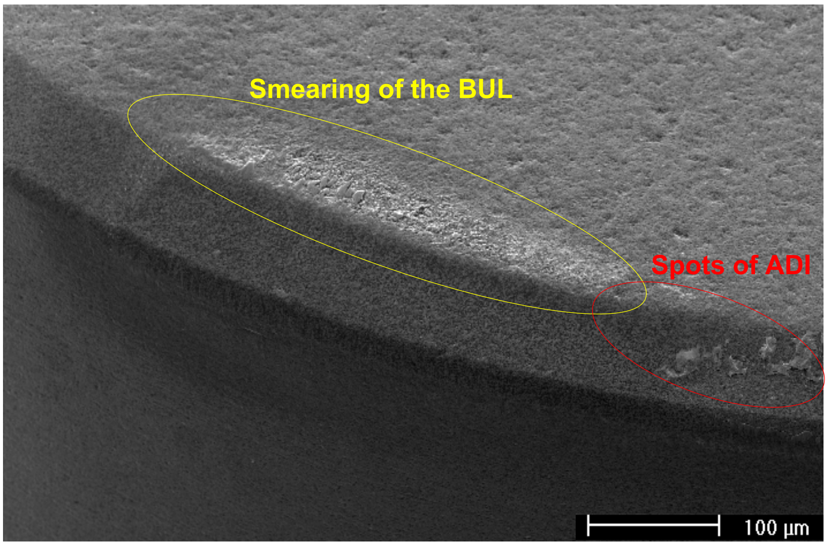

Figure 5.8: Wear scar of a cutting tool used at 100 m/min for 59.37 s (98.95 m). SEM, SE image

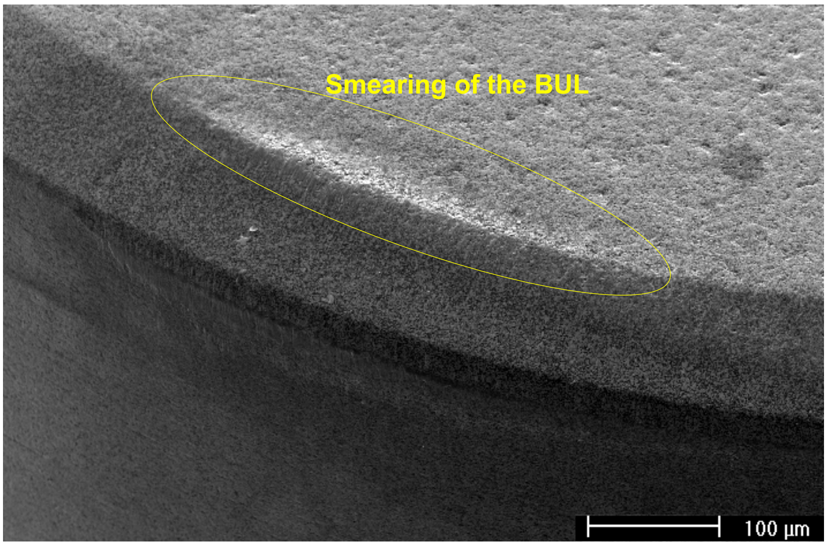

Figure 5.9: Wear scar of a cutting tool used at 150 m/min for 53.72 s (134.3 m). SEM, SE image

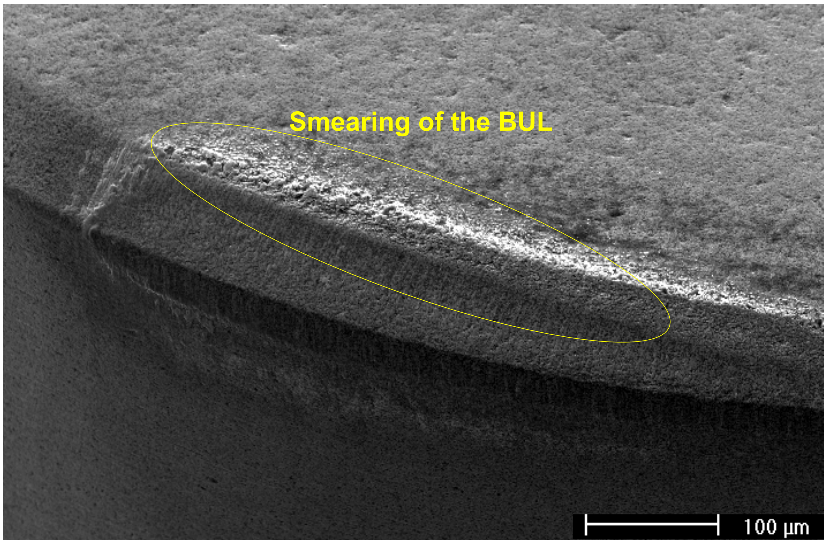

Figure 5.10: Wear scar of a cutting tool used at 300 m/min for 27.13 s (135.65 m). SEM, SE image

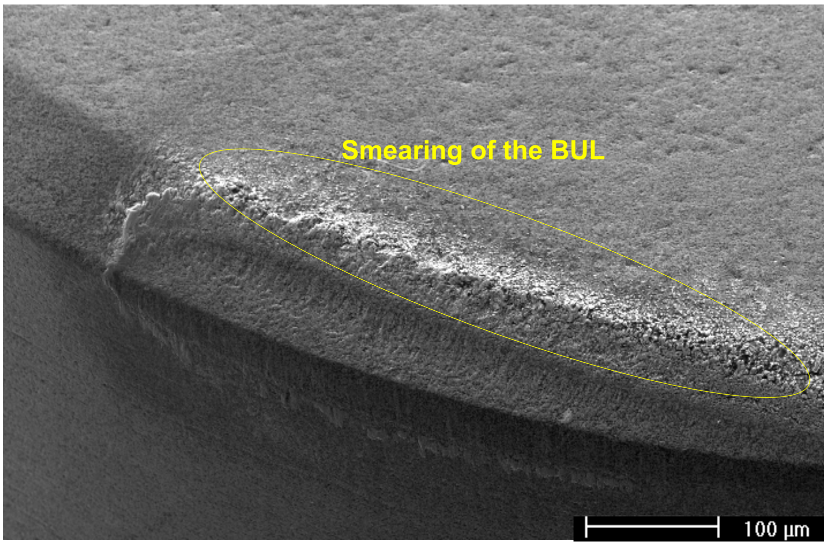

Figure 5.11: Wear scar of a cutting tool used at 500 m/min for 11.93 s (99.42 m). SEM, SE image

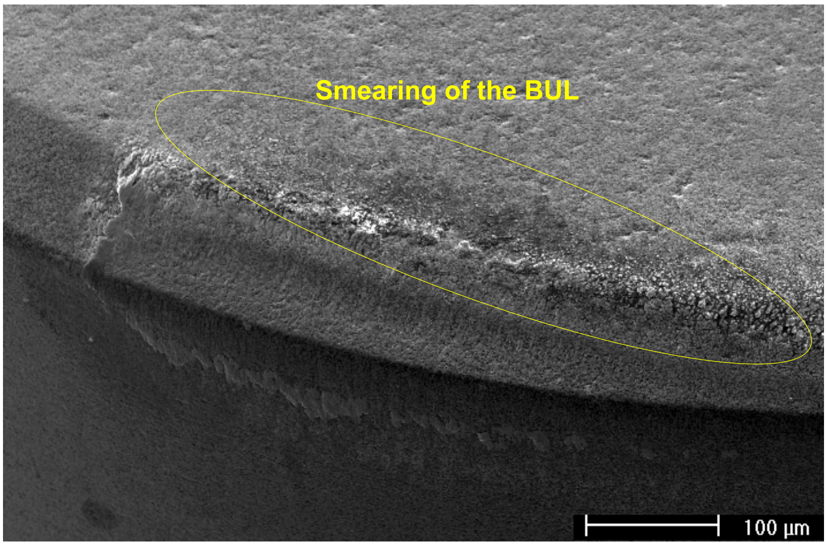

Figure 5.12: Wear scar of a cutting tool used at 600 m/min for 10.00 s (100 m). SEM, SE image

5.2.2 Maximum flank wear against cutting time and volume of flank wear per unit of engagement length against cutting length

Plots of maximum flank wear against cutting time are shown in Figure 5.13 for a number of cutting speeds. Plots of volume of flank wear per unit of engagement length against cutting length are shown in Figure 5.14 for a number of cutting speeds. These figures illustrate the dramatic effect of cutting speed on the cutting tool wear.

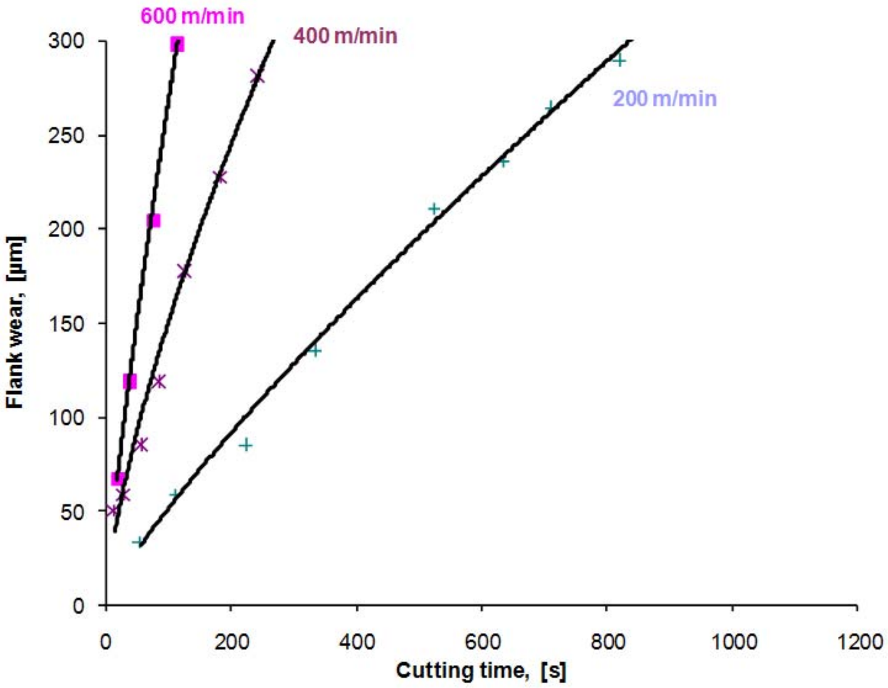

Figure 5.13: Flank wear V_{BC} versus cutting time

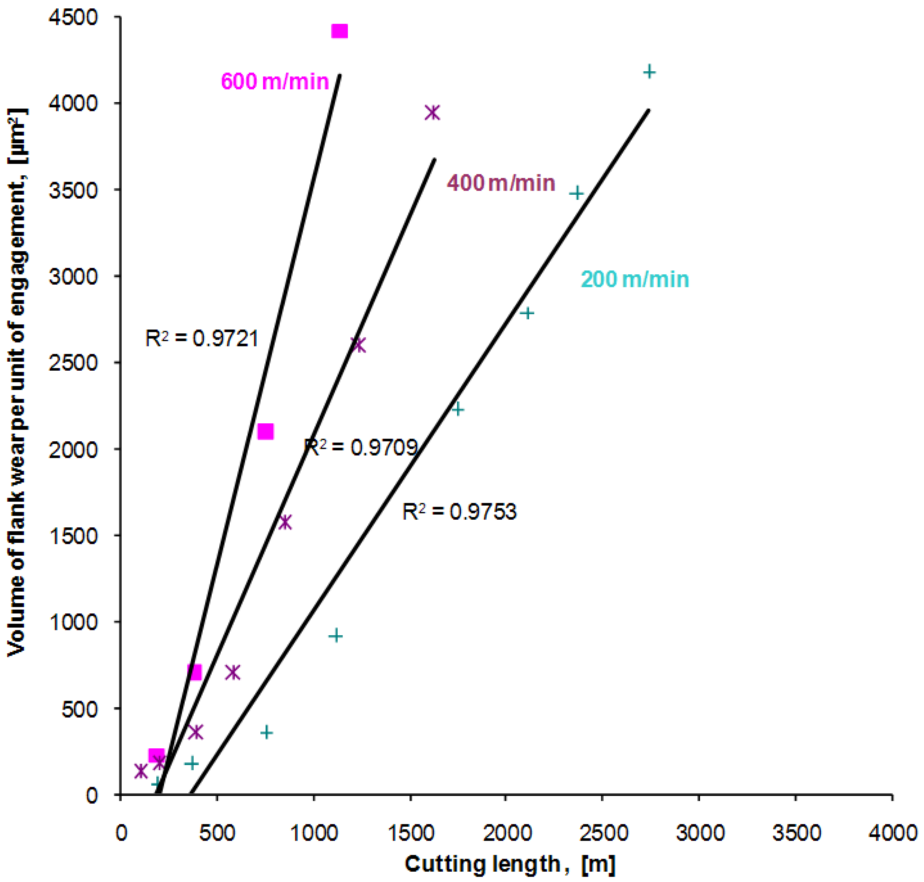

Figure 5.14: Volume of flank wear per unit of engagement length V_α against cutting length l_c

5.2.3 Effect of cutting speed on tool life and cutting length to end of tool life, Taylor cutting tool life equation

The effect of cutting speed on tool life and cutting length to end of tool life for Seco CBN100 cutting tools is summarized on Table 5.1 and Figure 5.15.

Table 5.1: Tool life and cutting length to end of tool life for Seco CBN100 cutting tools

Cutting speed, [m/min]	Tool life, [s]	Cutting length, [m]
50	17870.27	14891.89
100	3171.75	5286.24
150	1766.93	4417.32
200	832.98	2776.6
300	420.61	2103.05
400	266.12	1774.16
500	164.08	1367.33
600	115.29	1152.92
700	91.24	1064.44
800	56.14	748.57

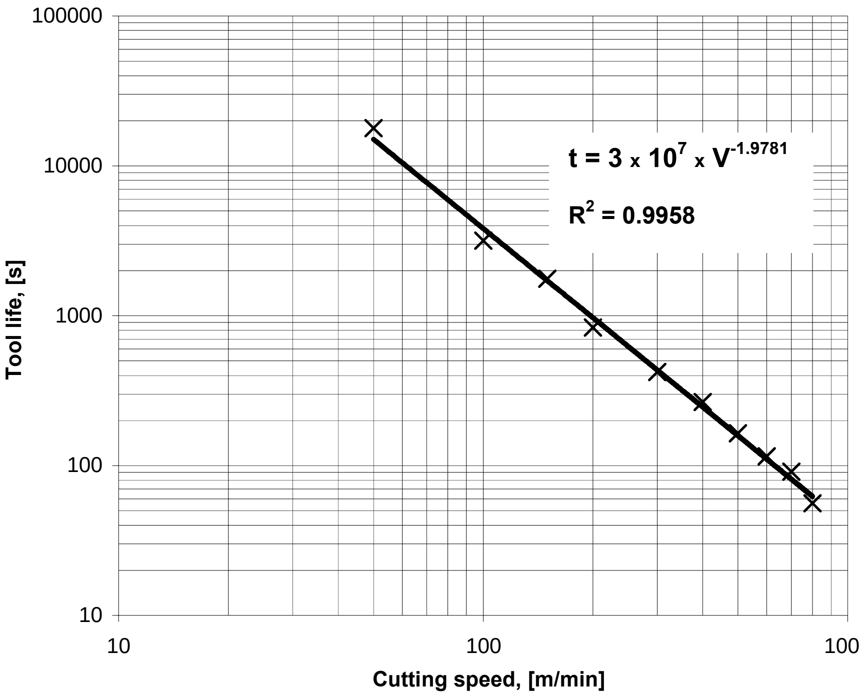

Figure 5.15: Effect of cutting speed on tool life for Seco CBN100 cutting tools

The Taylor cutting tool life equation was derived from the plot of tool life (s) vs cutting speed (m/min) in Figure 5.15 as:

$$t = 3 \times 10^7 \times V^{-1.9781}, \text{ with } R^2 = 0.9958 \qquad \textbf{(5.1)}$$

where *t* is the tool life (s), and V the cutting speed (m/min). R^2 is the regression coefficient.

The value of R^2 in Equation (5.1) indicates good agreement between the Taylor equation and the experimental tool life results over the range of cutting speeds used. The negative sign of the exponent in the Taylor cutting life equation indicates once again the dramatic effect of cutting speed on the cutting tool wear. The absolute value of the velocity exponent (1.9781) is much higher than 1 which is the absolute value of this exponent in cases where abrasive wear is the dominant wear mechanism (171). The higher value of this exponent indicates that abrasion was not the dominant wear mechanism throughout the range of cutting speeds used.

5.2.4 Flank wear rate and "ratio of volume of metal removed per unit of flank wear"

The flank wear rate and the "ratio of volume of metal removed per unit of flank wear" are shown in Figure 5.16. The "ratio of volume of metal removed per unit flank wear" decreased rapidly with increasing cutting speed up to a speed of about 300 m/min and more slowly with higher speeds. The flank wear rate showed a rapid increase with increasing cutting speed up to a speed of about 200 m/min. In the range 200–550 m/min the flank wear rate increased approximately linearly with cutting speed and more substantially for higher speeds.

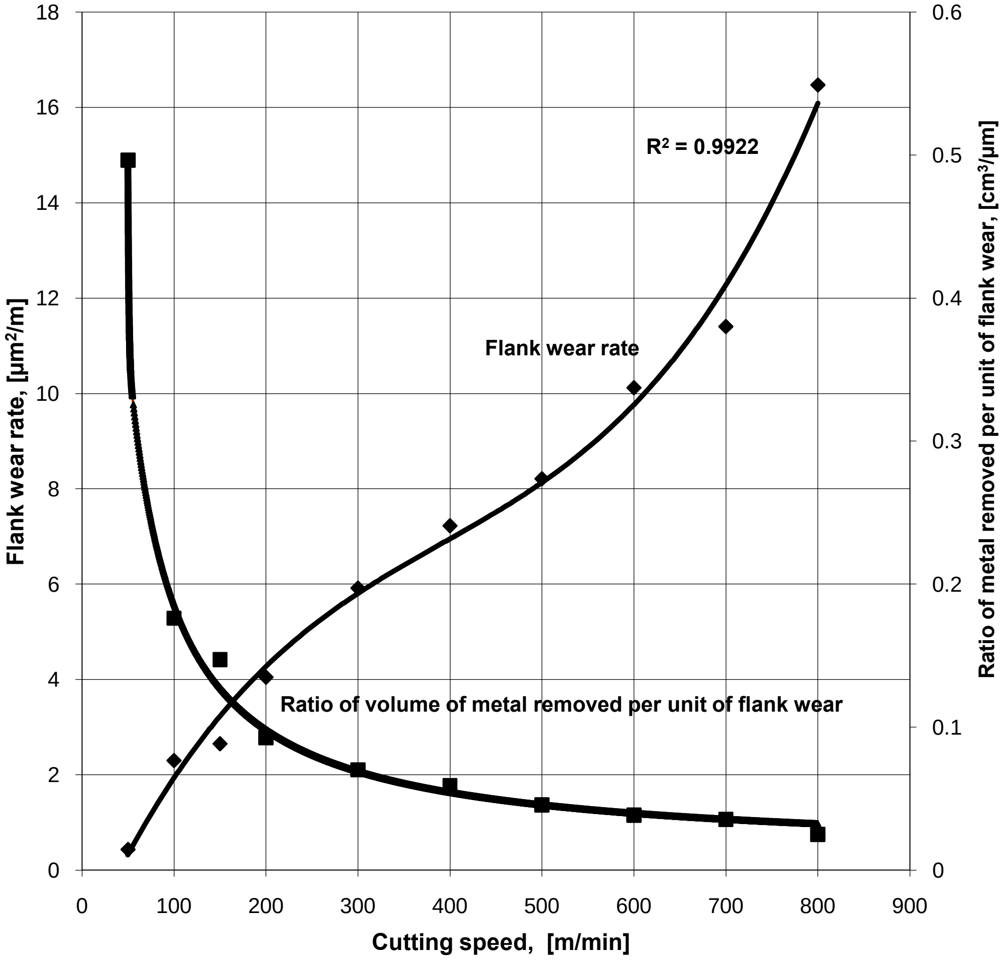

Figure 5.16: Effect of cutting speed on flank wear rate and the “ratio of volume of metal removed per unit of flank wear” of Seco CBN100 cutting tools

The significant changes in slope of the curve of flank wear rate for cutting speeds of 200 and 600 m/min are indicative of changes in the dominant tool wear mechanism. The high “ratio of metal removed per unit flank wear” obtained at cutting speeds below 150 m/min should recommend cutting speeds within this range. However, taking into account the relatively poor quality of surface finish obtained in this range of cutting speeds, cutting speeds in the range 150-550 m/min are recommended as compromise between “ratio of volume of metal removed per unit of flank wear”, flank wear rate and surface finish.

5.3 CUTTING FORCES

5.3.1 Static cutting forces

The static cutting forces corresponding to a cutting time of 1 s are shown in Figure 5.17. On the whole, they were relatively low. The static cutting forces increased rapidly with increasing cutting speed up to a speed of about 150 m/min. Between speeds of 150 and 200 m/min, they showed a dramatic decrease. At speeds over 200 m/min, they increased at a slow rate. For speeds of over 150 m/min, the static thrust force was higher than the static tangential force.

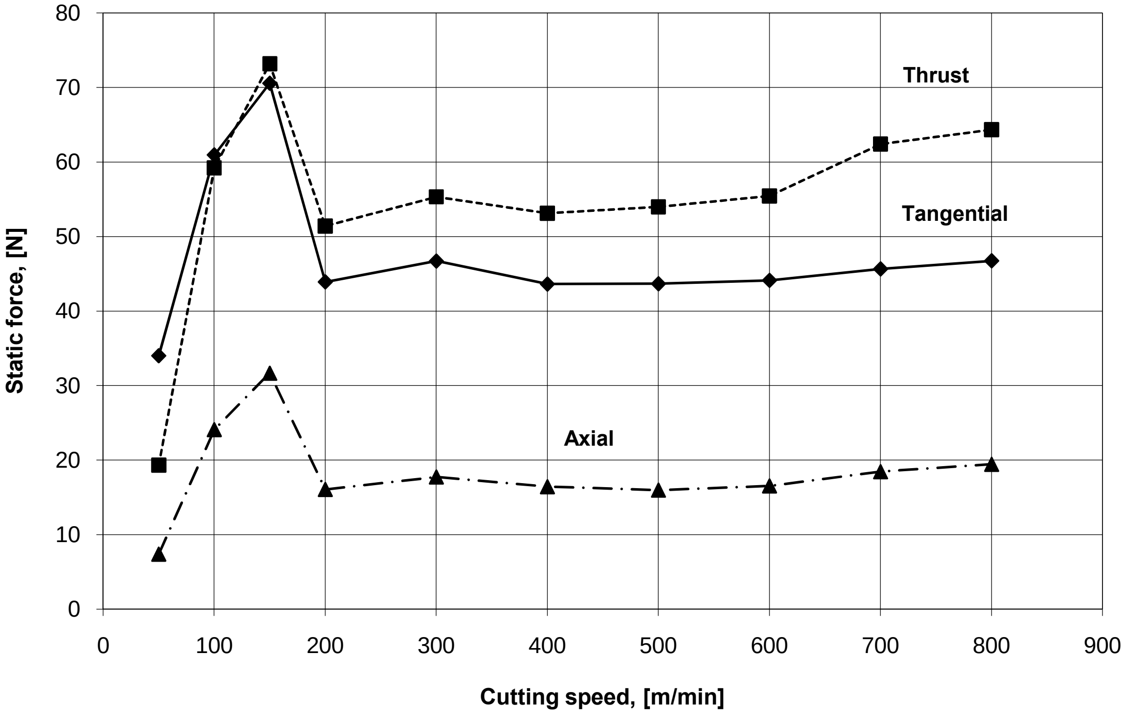

Figure 5.17: Effect of cutting speed on static cutting forces for Seco CBN100 cutting tools

The trend of cutting forces is indicative of the tribology at the tool-chip interface. The increase of cutting forces in the range 50-150 m/min indicated the formation of a BUE. As mentioned in Section 2.1.5, the largest fall in cutting forces occurs in the low-to-medium cutting speed range 150-200 m/min. The decrease in cutting forces between 150 and 800 m/min indicated the thermal softening in the flow zone as well as the formation of a lubricating film (superficial melting) at the tool-chip interface which assisted the decrease in the contact length. Beyond 200 m/min, the slight variation of cutting forces indicated that no sudden shift in the behaviour of ADI in the primary shear zone was significant.

The dynamic cutting forces corresponding to a cutting time of 1 s are shown in Figure 5.18. They decreased with increasing cutting speed up to a speed of about 200 m/min and increased at different rates at higher cutting speeds. The dynamic thrust force increased at the highest rate.

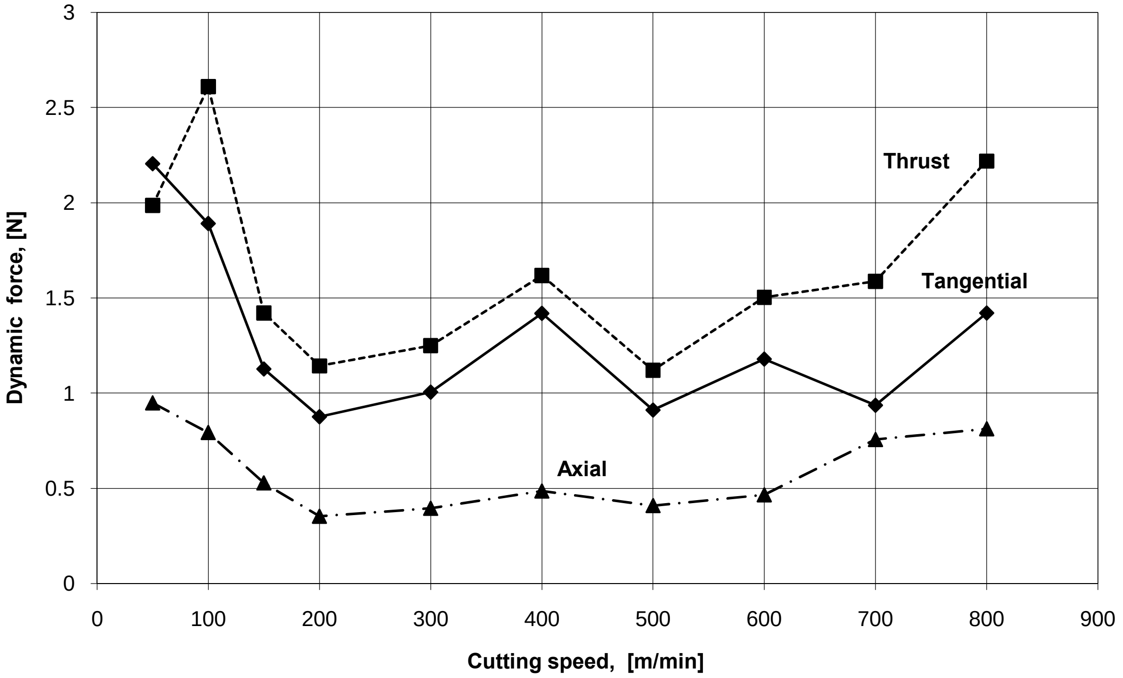

Figure 5.18: Effect of cutting speed on dynamic cutting forces for Seco CBN100 cutting tools

As mentioned in Section 2.1.7.1, the relatively high dynamic cutting forces in the range 50-150 m/min indicated an unsteady chip formation process. The negative rake angle used (-26°) also played a role in this regard. As mentioned in Section 2.1.5, the increase in dynamic cutting forces between 150 and 800 m/min indicated the formation of shear localized chips.

5.3.3 Effective friction coefficient

The effective friction coefficient (mean friction coefficient) on the cutting tool rake face was calculated from the static cutting forces corresponding to a cutting time of 1 s, based on the nominal rake angle and not the effective rake angle that takes into account the changes in rake angle brought about by the presence of the BUE or the crater wear scar. The plot of the effective friction coefficient at the cutting tool rake vs the cutting speed is shown in Figure 5.19.

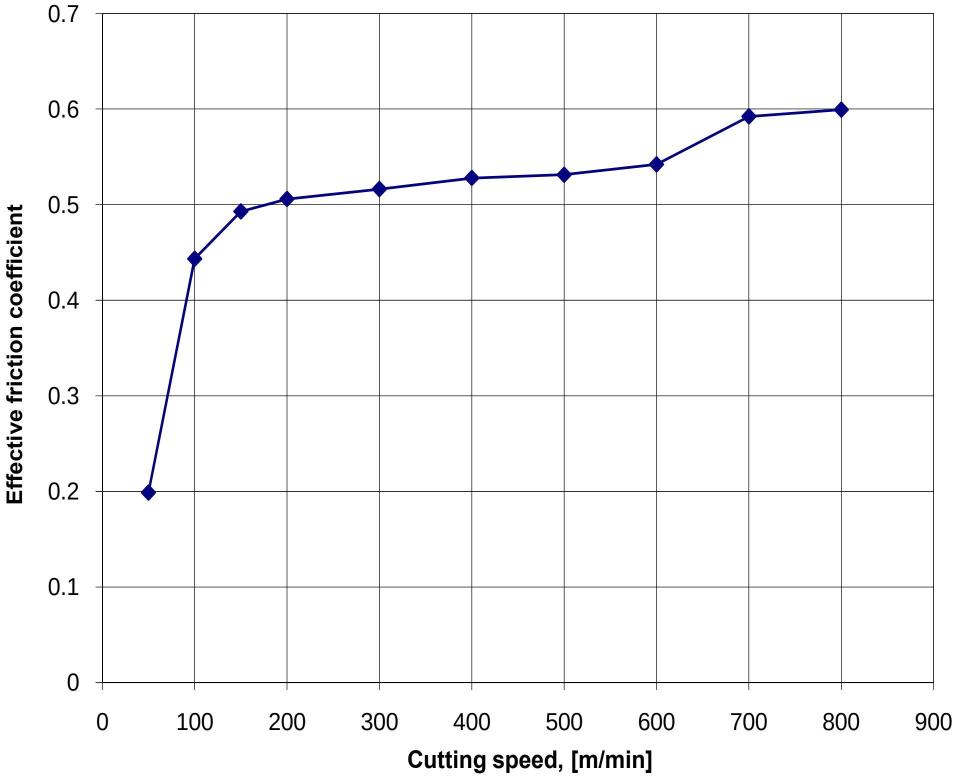

Figure 5.19: Effect of cutting speed on effective friction coefficient at the rake face of Seco CBN100 cutting tools

The effective friction coefficient at the cutting tool rake face increased rapidly as the cutting speed increased from 50 to 150 m/min and tended to increase only slightly beyond a cutting speed of 200 m/min.

These curve highlighted roughly 2 different ranges of cutting speeds, respectively 50-150 m/min and 150-800 m/min which, depicted different tribological conditions at the tool-chip interface. This should also shine a light on the variation of the contact length with the cutting speed.

5.4 CHIP CHARACTERISTICS

5.4.1 Chip temperature and chip colour

"Bluing" and chip oxidation started to be evident at cutting speeds greater than 200 m/min. In fact, from 200 m/min, chips started glowing in subdued light, indicating a temperature of 400 °C or higher (172).

For cutting speeds greater than 200 m/min, the colour of the chip underside turned light brown whereas the colour of the chip top side turned dark blue.

5.4.2 Chip underside morphology, surface finish and tool-chip interface tribology

At a speed of 50 m/min the surface finish of the workpiece was very poor and the chip underside was very rough (Figure 5.20). Some severely strained material was evident on the sliding surface of chips as was the case with the machined surface of the workpiece. The heavily deformed material indicated excessive or erratic BUE that periodically formed on the cutting edge resulting in poor surface finish of the workpiece. No slip areas were evident on the chip underside, probably indicating the predominance of seizure at the tool-chip interface.

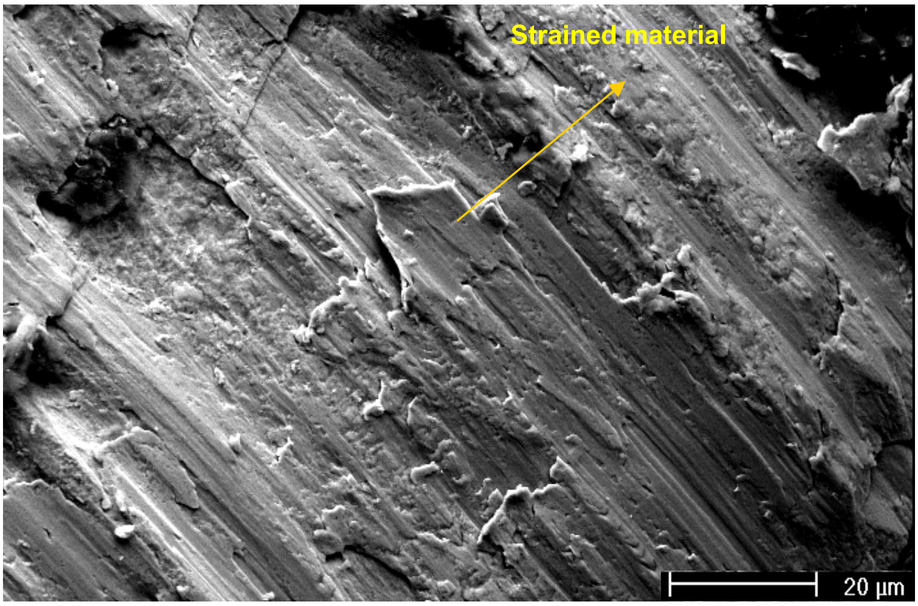

Figure 5.20: Underside of chip obtained at 50 m/min. SEM, SE image

At a cutting speed of 100 m/min the amount of strained material on the chip underside decreased (Figure 5.21). However there were always big discontinuities in the deformed material in areas occupied by graphite nodules.

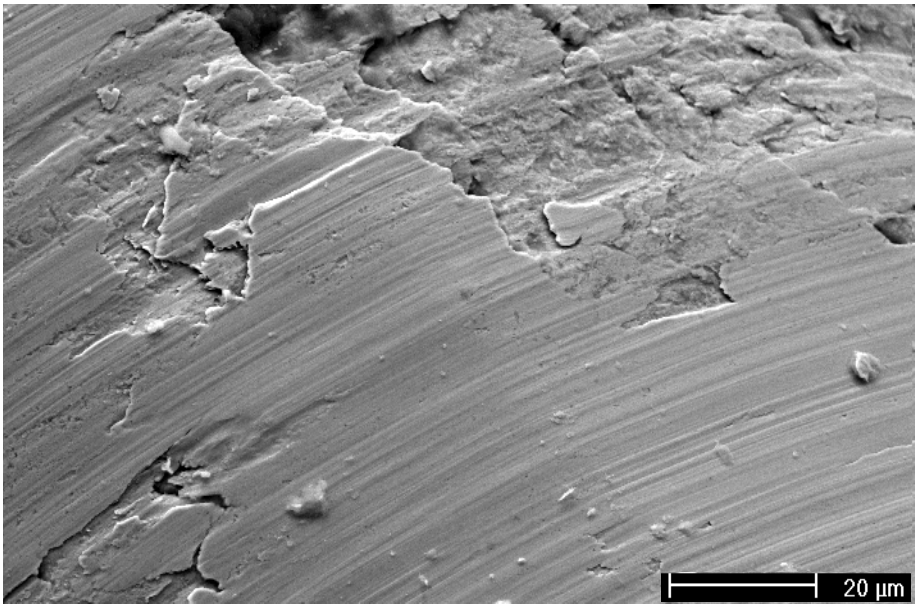

Figure 5.21: Underside of chip obtained at 100 m/min. SEM, SE image

At speeds of 150 m/min or more the streaks along the length of the chip underside were smooth (Figures 5.22 and 5.23). The extent of discontinuities on the chip underside decreased as the cutting speed increased. Streaks and micropores were more evident as the cutting speed increased as a result of softening and probably partial melting due to sliding of the chip against the rake face of the cutting tool (173). Apparently, no stick areas were evident on the chip underside, indicating probably the predominance of sliding at the tool-chip interface.

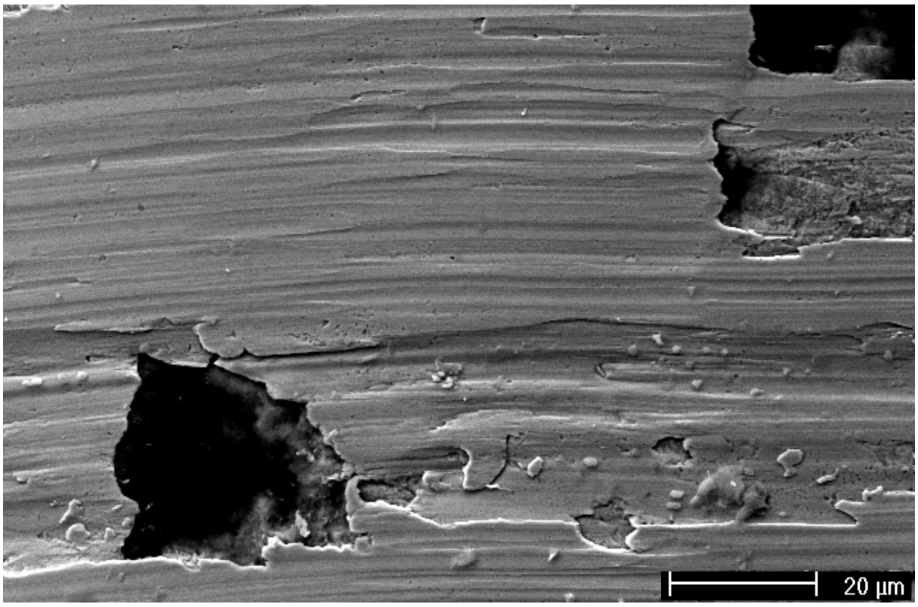

Figure 5.22: Underside of chip obtained at 150 m/min. SEM, SE image

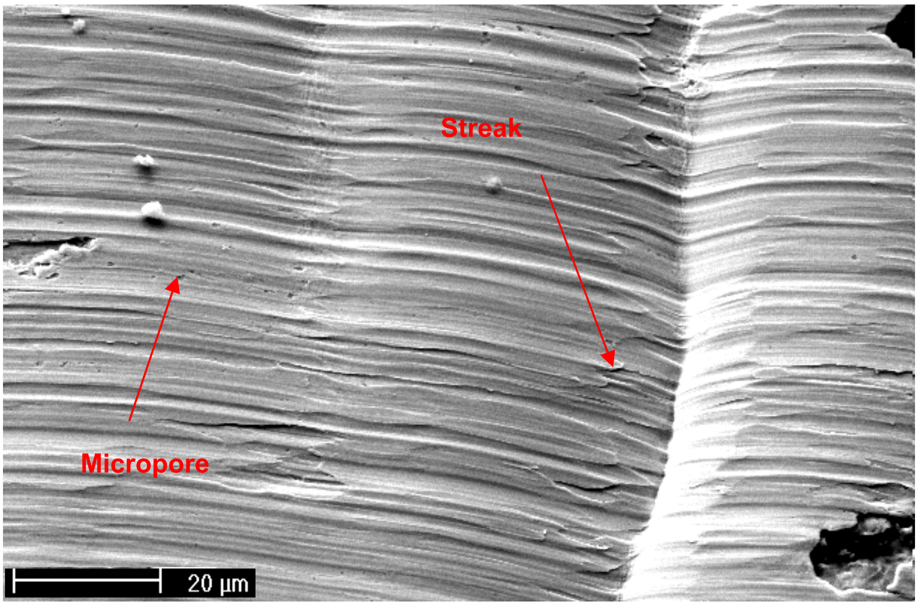

Figure 5.23: Underside of chip obtained at 700 m/min. SEM, SE image

5.4.3 Cross-section morphology of chips

The chips were continuous with occasional segmentation and highly coiled for cutting speeds of up to 150 m/min. The deformation pattern revealed that deformation occurred quite homogeneously in the entire chip. The flow-pattern in the secondary shear zone, which showed the level of shearing and frictional energy close to the tool–chip interface, was also visible (Figure 5.24). The formation of this secondary shear zone (stagnant zone) indicated the occurrence of seizure at the tool-chip or BUE-chip interface (27). Elongated graphite fragments, which accommodate large strains, significantly reducing the shear strain in the surrounding matrix (146), were found in some shear zones.

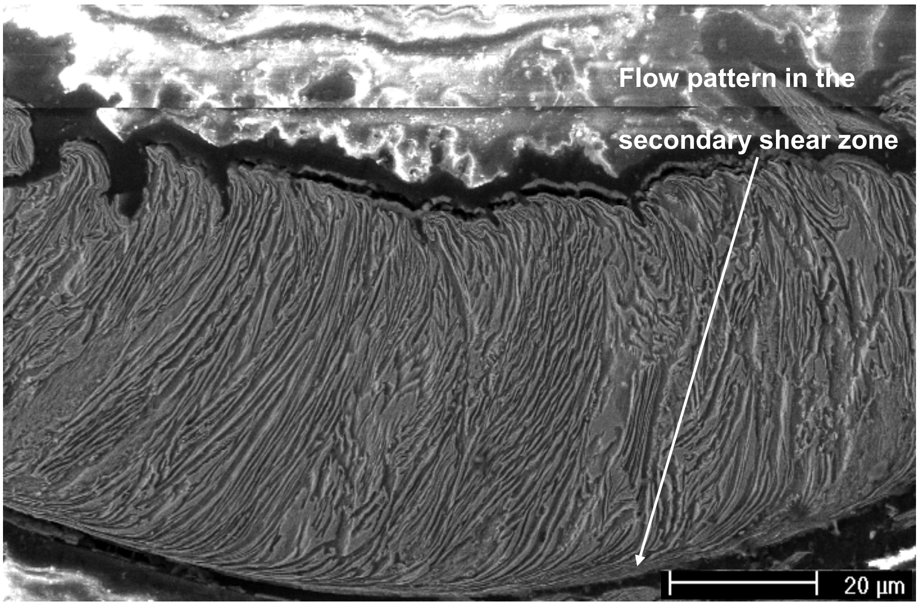

Figure 5.24: Microstructure of a chip obtained at 150 m/min. SEM, SE image

For cutting speeds between 150 and 200 m/min, the chip characteristics were intermediate between those of continuous and segmented chips. At cutting speeds above 200 m/min, the chips became more and more segmented and less coiled (Figure 5.25). The segmented chips consisted of individual segments that were slightly deformed and joined by narrow heavily strained bands.

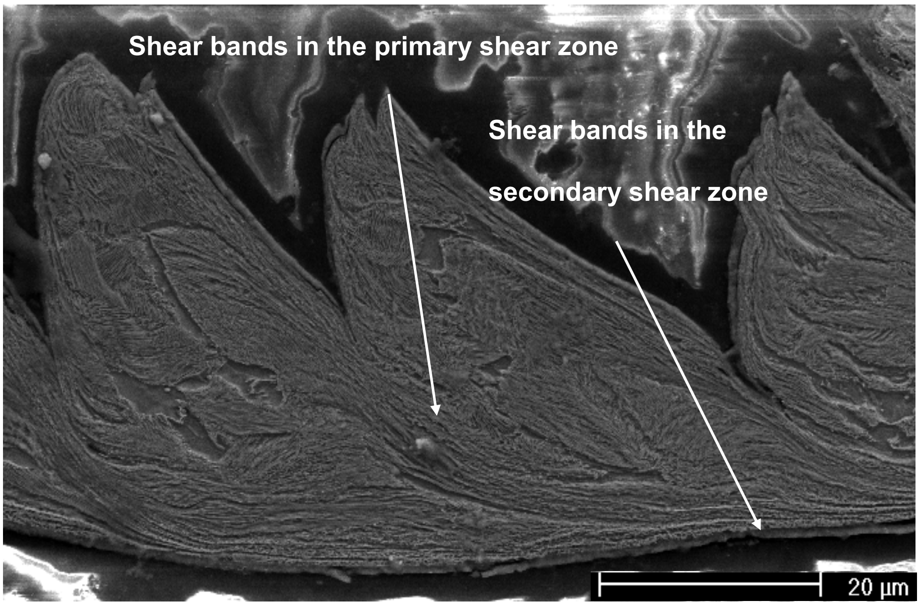

Figure 5.25: Microstructure of a chip obtained at 700 m/min. SEM, SE image

5.4.4 Average chip thickness and chip hardness

Plots of average chip thickness and chip hardness against cutting speed are shown in Figure 5.26. It can be seen that the average chip thickness decreased rapidly with increasing cutting speed up to about 200 m/min and very slowly for higher speeds.

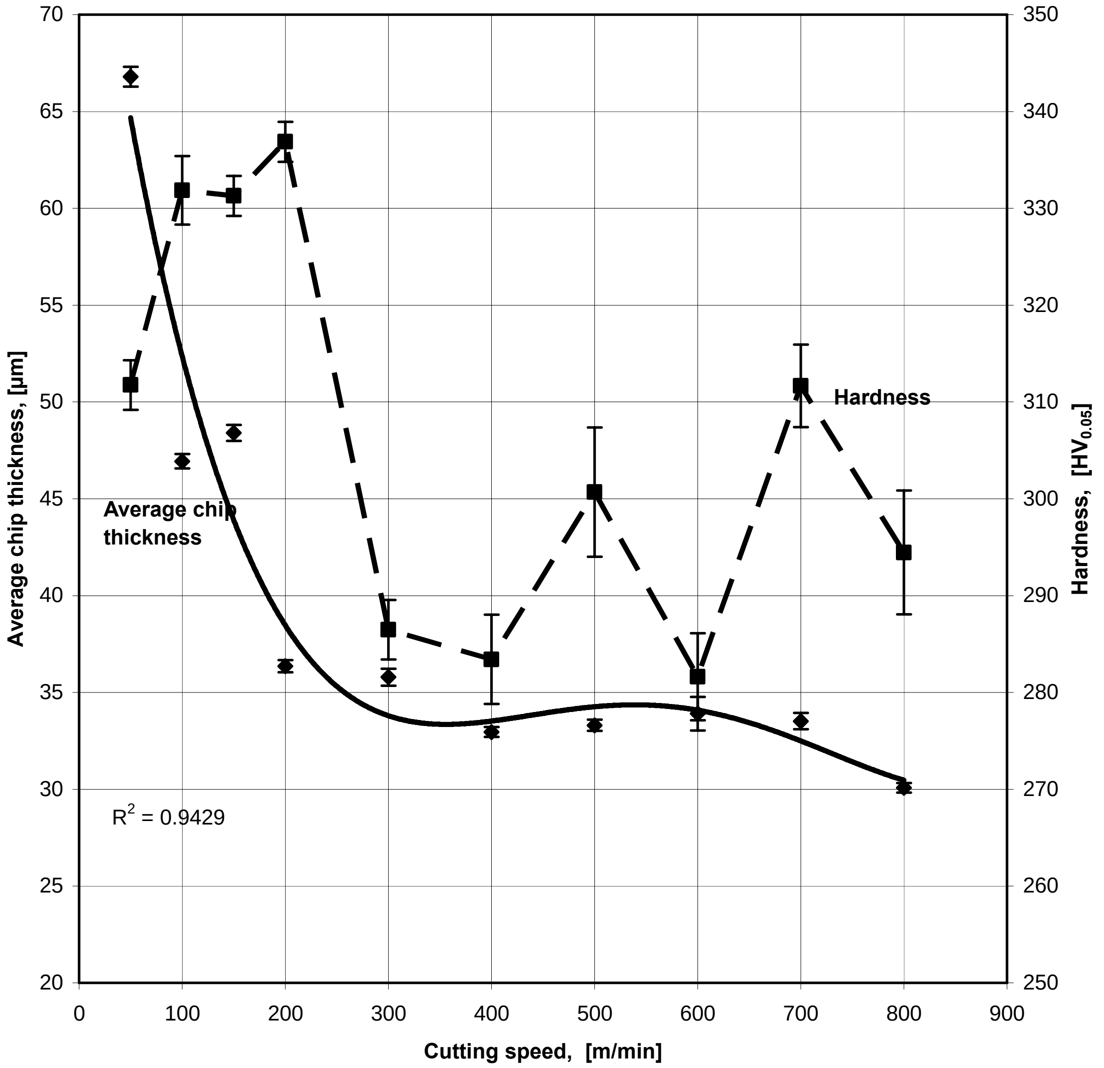

Figure 5.26: Effect of cutting speed on average chip thickness and hardness of ASTM Grade 2 ADI chips

Conversely chip hardness increased for speeds of up to 200 m/min and dropped precipitously between speeds of 200 and 300 m/min. At higher cutting speeds the chip hardness fluctuated significantly and did not show a clear trend. These fluctuations are probably the result of actual variations in hardness within chips, due to variations in the extent of strain hardening.

5.4.5 TEM investigation of chips

Examination in the STEM of the transitional region adjacent to the adiabatic shear lamella in the primary shear zone in chips produced at a cutting speed of 150 m/min revealed a texture of deformation that showed shear bands of about 80 nm wide separated by very thin laths (Figure 5.27).

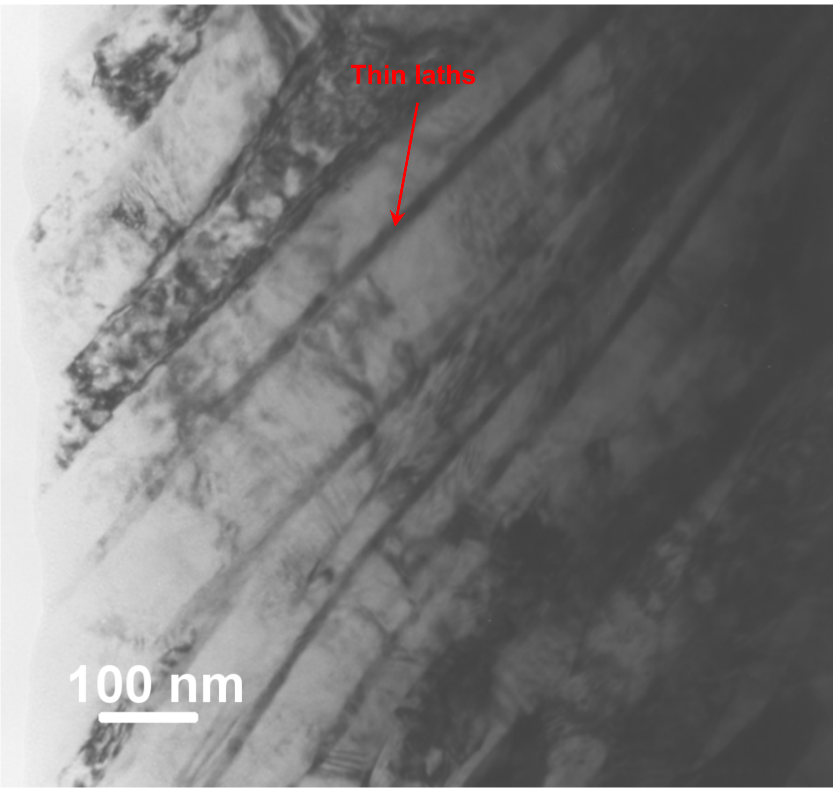

Figure 5.27: Transitional region adjacent to the adiabatic shear lamella in the primary shear zone close to the top of a chip obtained at 150 m/min. STEM, bright field image

A selected area diffraction pattern (SADP) from Figure 5.27 is presented in Figure 5.28. Its spotty pattern is indicative of relatively coarse (elongated) grains. Indexing of this SADP revealed the presence of (100) reflections corresponding to ferrite.

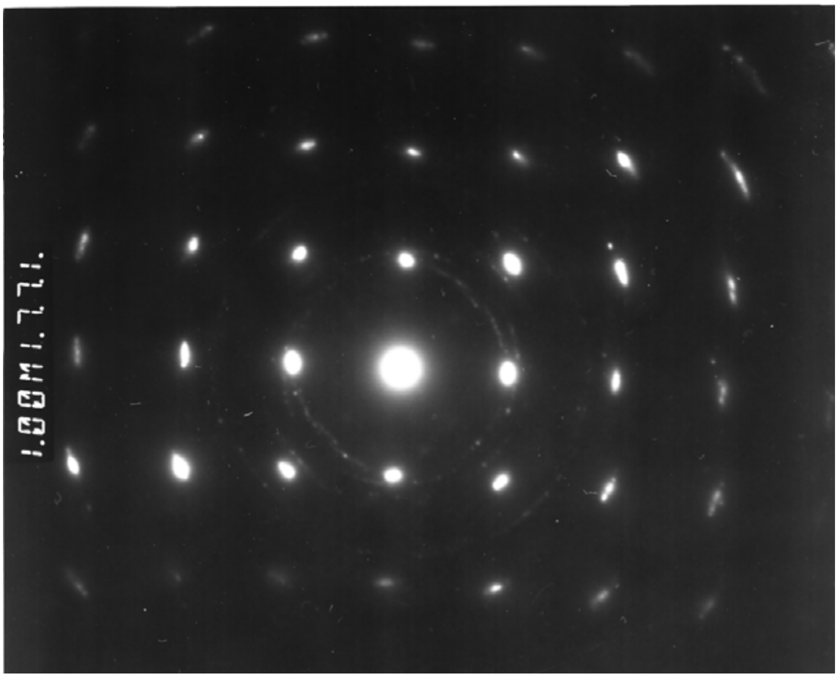

Figure 5.28: SADP from Figure 5.27

Examination in the STEM of the adiabatic shear lamella in the primary shear zone in chips produced at a cutting speed of 150 m/min did not reveal a deformation texture. On the contrary, this examination revealed the presence of randomly orientated grains with a grain size of about 100 to 200 nm (Figure 5.29). Going from the transitional region adjacent to the adiabatic shear lamella (Figure 5.27) inwards the adiabatic shear lamella itself, the ferrite shear bands as well as the very thin laths of residual or retained austenite underwent substantial refinement and blending to such an extent that residual or retained austenite could not be clearly distinguished from ferrite (Figure 5.29).

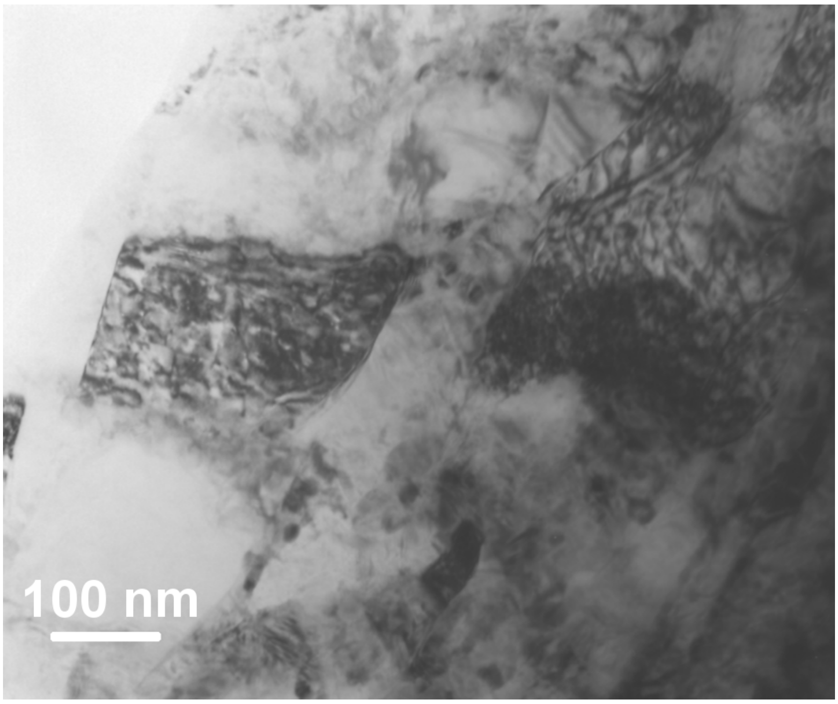

Figure 5.29: Adiabatic shear lamella in the primary shear zone close to the bottom of a chip obtained at 150 m/min. STEM, bright field image

In chips produced at a cutting speed of 150 m/min, the microstructure of the secondary shear zone (Figure 5.30) was similar to that of the of the primary shear zone (Figure 5.29). However, a SADP (Figure 5.31) from Figure 5.30 showed a greater continuity of diffraction rings indicative of relatively small randomly orientated grains. The intensity maxima on each ring correspond to the larger grains in the structure. The less intense, more continuous sections of each ring correspond to the more numerous smaller grains. Indexing from the central region of this SADP revealed the presence of (110), (200), (211) and (310) reflections for which the corresponding d-spacings show clearly that they relate to ferrite grains.

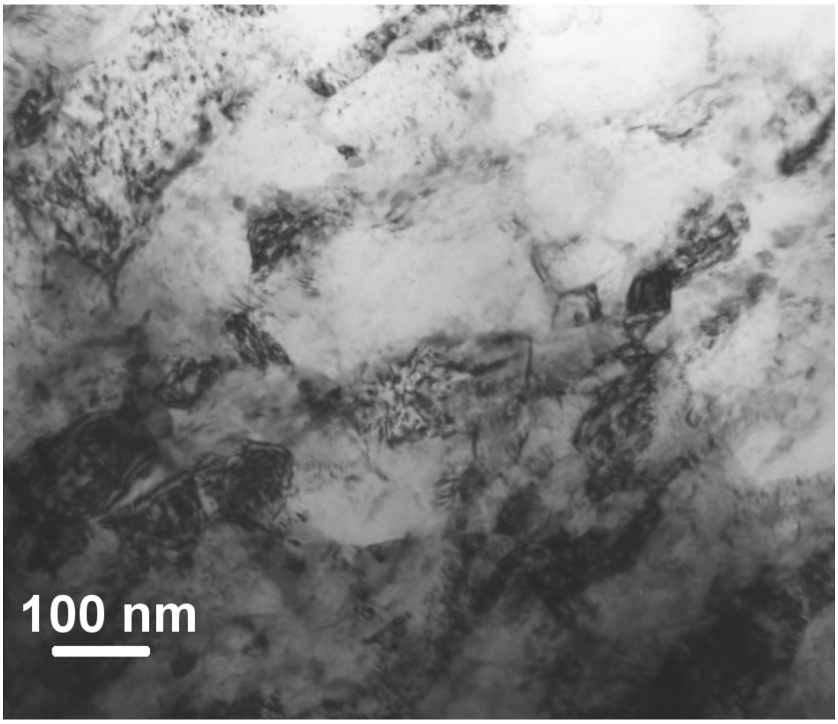

Figure 5.30: Secondary shear zone of a chip obtained at 150 m/min. STEM, bright field image

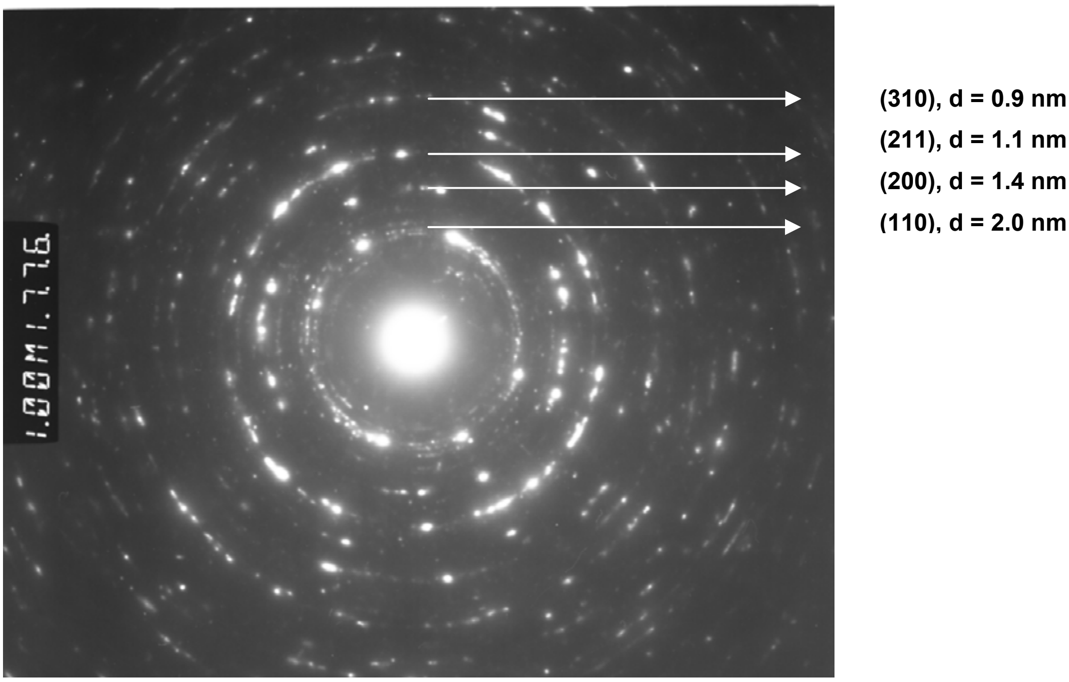

Figure 5.31: SADP from Figure 30

The microstructure of the transitional region adjacent to the adiabatic shear lamella in the primary shear zone in chips produced at a cutting speed of 200 m/min revealed a deformation texture that showed shear bands of about 80 nm wide separated by very thin laths (Figure 5.32).

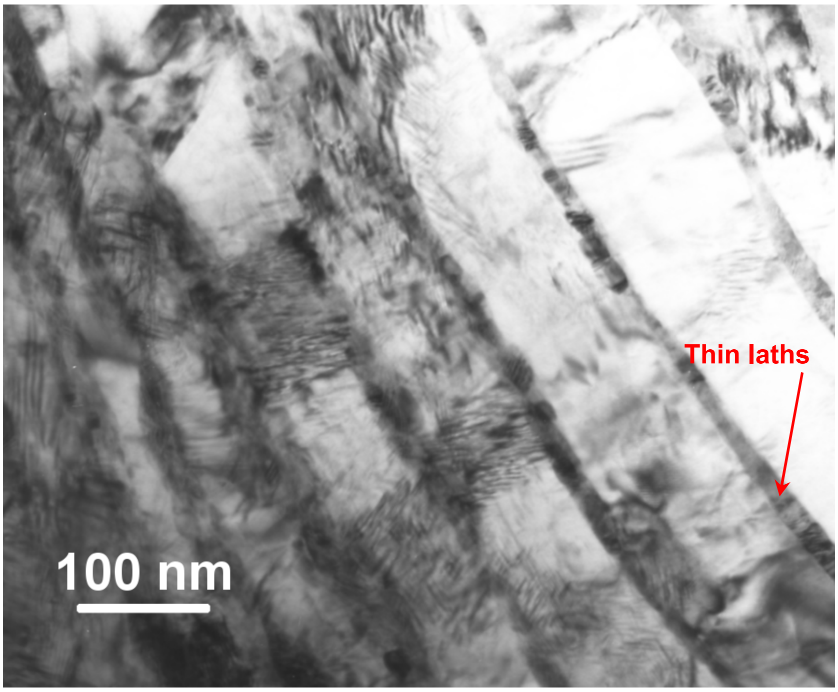

Figure 5.32: Transitional region adjacent to the adiabatic shear lamella in the primary shear zone close to the top of a chip obtained at 200 m/min. STEM, bright field image

The microstructure of the adiabatic shear lamella in the primary shear zone in chips produced at a cutting speed of 200 m/min did not reveal a deformation texture. On the contrary, this examination revealed the presence of randomly orientated grains with a grain size of about 100 nm (Figure 5.33). Going from the transitional region adjacent to the adiabatic shear lamella in the primary shear zone (Figure 5.32) inwards the adiabatic shear lamella itself, the ferrite shear bands as well as the very thin laths of residual or retained austenite underwent substantial refinement and blending to such an extent that residual or retained austenite could not be clearly distinguished from ferrite (Figure 5.33) even upon electron diffraction studies (Figure 5.34).

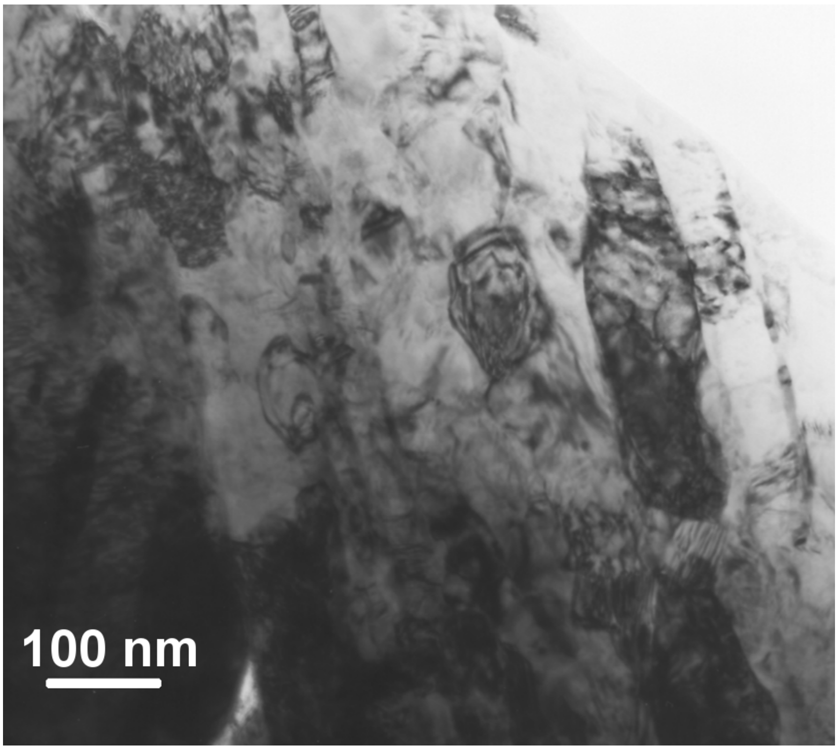

Figure 5.33: Adiabatic shear lamella in the primary shear zone of a chip obtained at 200 m/min. STEM, bright field image

Figure 5.34: SADP from Figure 33

Indeed, Figure 5.34 which represents a SADP from Figure 5.33 reveals a pattern of discontinuous rings that is indicative of relatively small grains. Indexing of this SADP revealed the presence of (100) reflections corresponding to ferrite.

Examination in the STEM of the adiabatic shear lamella in the secondary shear zone in chips produced at a cutting speed of 200 m/min did not reveal a deformation texture. This examination revealed the presence of randomly orientated grains with a grain size of about 100 nm (Figure 5.35). Within the adiabatic shear lamella itself, the ferrite shear bands as well as the very thin laths of residual or retained austenite underwent substantial refinement and blending to such an extent that residual or retained austenite could not be clearly distinguished from ferrite (Figure 5.35) even upon electron diffraction studies (Figure 5.36).

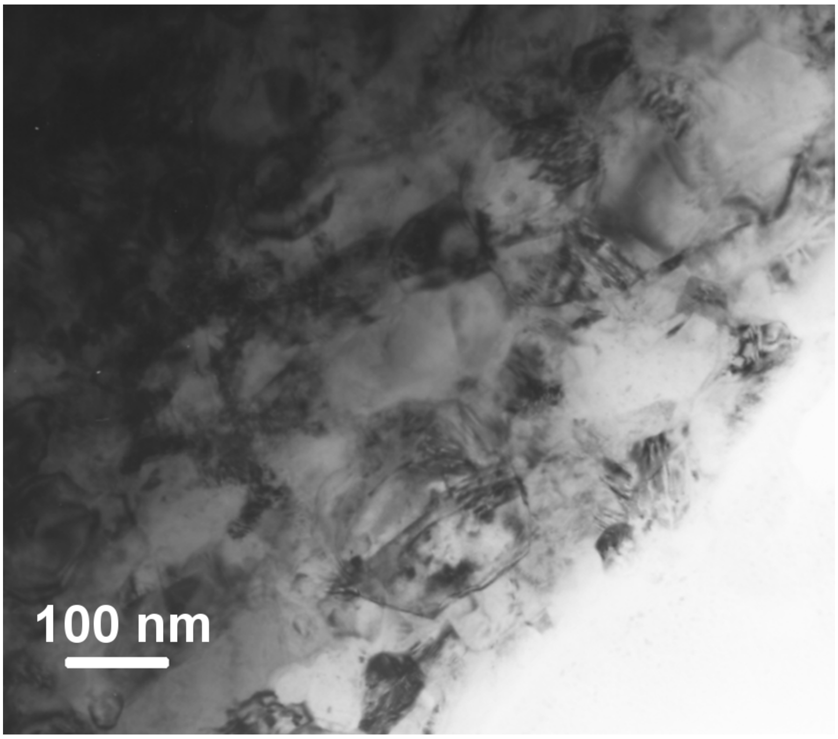

Figure 5.35: Secondary shear zone of a chip obtained at 200 m/min. STEM, bright field image

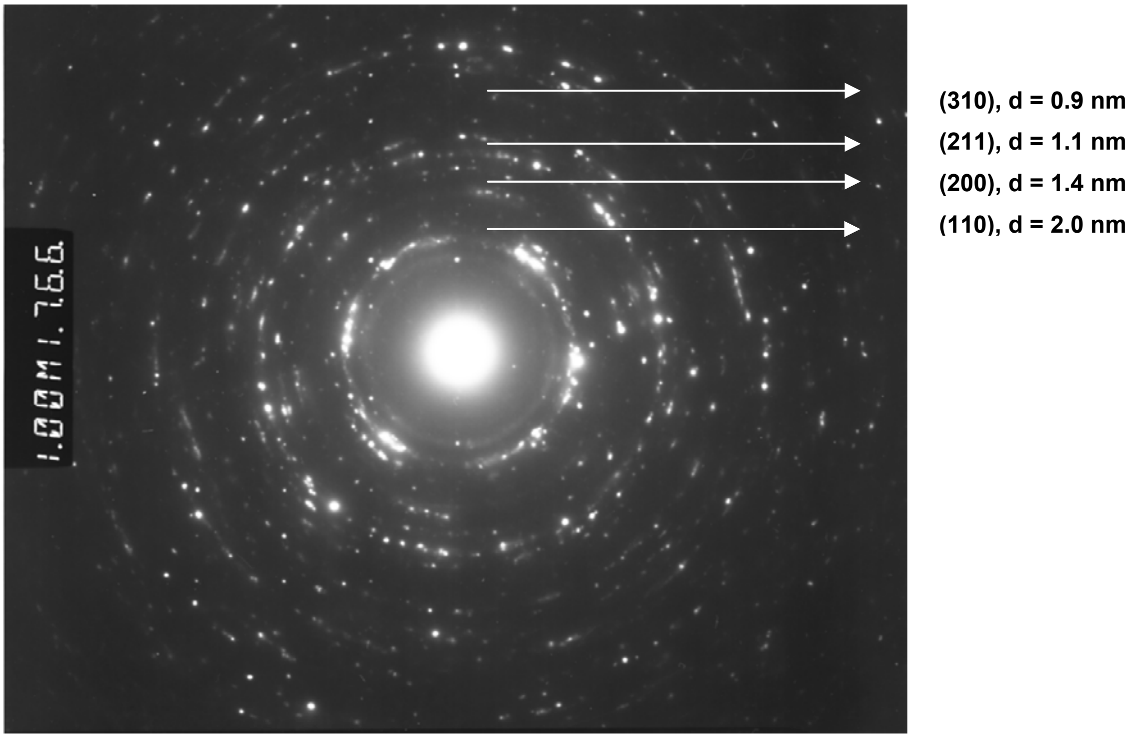

Figure 5. 36: SADP from Figure 5.35

Indeed, Figure 5.36 which represents a SADP from Figure 5.35 reveals semi-continuous rings corresponding to reflections from multiple randomly orientated small grains. The intensity maxima on each ring correspond to the larger grains in the structure. The less intense, more continuous sections of each ring correspond to the more numerous smaller grains. Indexing of this SADP from the central region revealed the presence of (110), (200), (211) and (310) reflections for which the corresponding d-spacings show clearly that they belong to ferrite.

Examination in the STEM of the adiabatic shear bands in the secondary shear zone in chips produced at a cutting speed of 800 m/min did not reveal a deformation texture but randomly orientated grains with a grain size of about 100 to 200 nm (Figure 5.37).

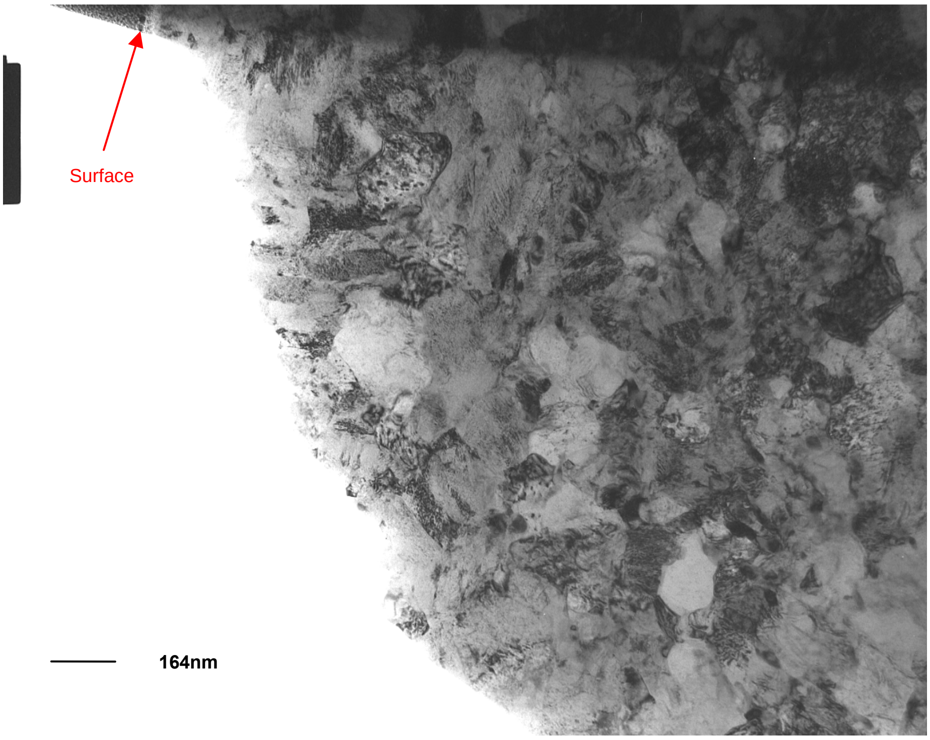

Figure 5.37: Secondary shear zone of a chip obtained at 800 m/min. STEM, bright field image

Discrete spots from cementite were not found in the SADPs of secondary shear zone of chips. Moreover, no diffuse continuous ring was found that could indicate the presence of (200) cementite reflections within the (110) ferrite ring (170). There was no evidence of FCC reflections that would indicate the presence of retained or residual austenite in any of the selected area diffraction patterns. Ferrite ring broadening or splitting, which may be expected from sufficiently tetragonal martensite (170) could also not be identified.

The refinement and random orientation of ferrite grains in the shear zones of chips indicated that recovery and recrystallization, or other phase transformations occurred within these zones during the cutting operation. Such refinement is expected to support the diffusion wear of the cBN-TiC cutting tools.

5.5 FAILURE OF CUTTING TOOLS, WEAR SCARS ON CUTING TOOLS, WEAR MECHANISMS

5.5.1 Wear modes

As already mentioned in Section 5.2.1, damage to the cutting tools over the entire range of cutting speeds was mainly in the form of flank and crater wear. In terms of wear initiation, early formation of a crater scar was noticeable at cutting speeds greater than 150 m/min (Figures 5.7 to 5.12).

For cutting speeds greater than 150 m/min, the crater wear scar showed three different areas (Figure 5.38): an entrance zone 1 close to the cutting edge partially covered with a relatively thick BUL, an area 2 in the valley of the crater wear slightly covered with a very thin BUL and an exit zone 3 almost completely covered with a smeared BUL.

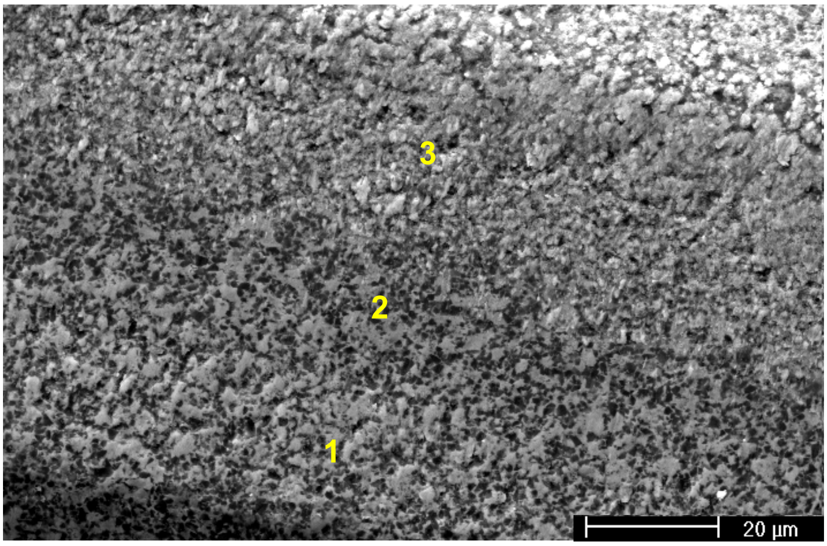

1: entrance zone **2:** valley **3:** exit zone

Figure 5. 38: Crater wear scar of a cutting tool used at 200 m/min for 40.49 s. SEM, SE image

Except for a BUE and a BUL, the wear scar of cutting tools did not show evidence of formation of deep grooves in the first 10 s or less of dry turning. The cutting edge remained intact for cutting times of less than 10 s (Figure 5.39).

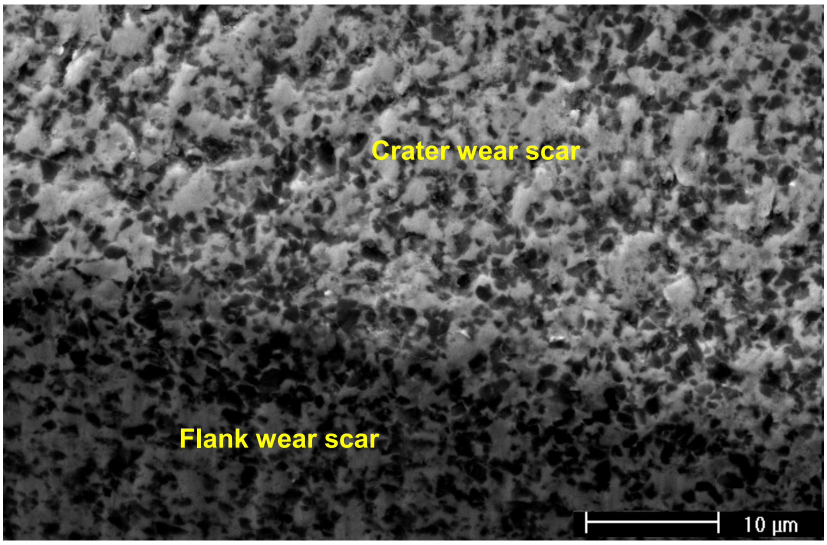

Figure 5.39: Edge of a cutting tool used at 200 m/min for 40.49 s. SEM, SE image

5.5.2 Contact lengths

From the wear scar images shown in Figures 5.7 to 5.12, it can be seen that the contact length of the chip on the rake face of the cutting tool decreases as the cutting speed increases.

The contact length corresponding to a cutting speed of 50 m/min appeared to be the highest, extending beyond the chamfer (Figure 5.7). At this cutting speed, and unlike at higher cutting speeds, thick layers of ADI were observed beyond the tool chamfer. Moreover, attrition wear clues appeared early at the leading edge of the cutting edge beyond the chamfer.

As cutting speed increased from 100 to 800 m/min, the contact length of the chip on the rake face of the cutting tool decreased slightly, locating itself exclusively on the chamfer of the cutting tool (Figures 5.8 to 5.12).

5.5.3 Adhering material on the wear scar: BUE and BUL

At cutting speeds lower than 150 m/min the adhering material on the crater scar occurred in spots or as a thick layers that appeared, in some areas, to be remnants of a BUE that broke off due to severe strain hardening (Figures 5.7, 5.8 and 5.40).

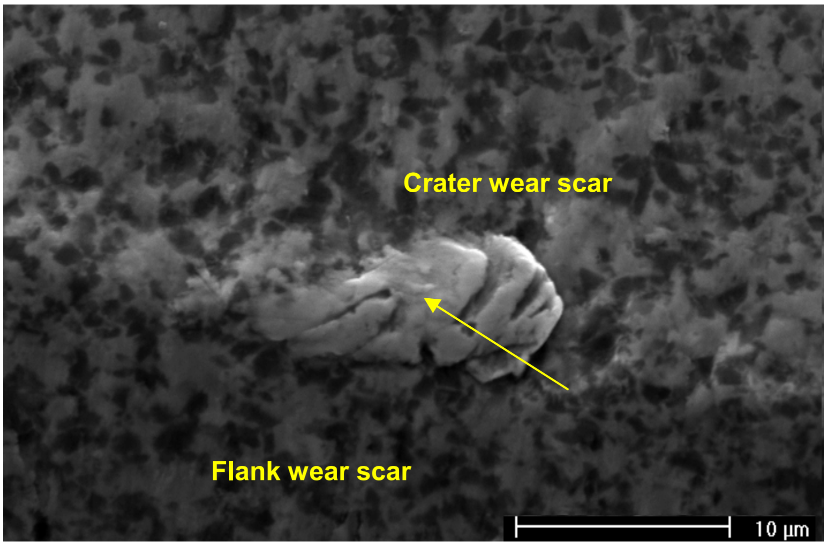

Figure 5.40: Cutting edge of a tool used at 150 m/min for 53.72 s showing a fragment of BUE at the cutting edge. SEM, SE image

At cutting speeds greater than 150 m/min, the material adhering to the rake face and the flank face was a BUL that smeared on the wear scars. Due to the higher cutting temperatures, this BUL did not undergo strain hardening. The underside of the chips showed much smoother surfaces with considerable ADI smearing (Figure 5.23). The surface coverage of the BUL appeared to increase with cutting speed.

In the entrance zone of the crater wear scar, the BUL appeared relatively thick and firmly attached to the TiC binder. The BUL on the cBN grains appeared relatively thin and loose. Fine grooves appeared on the BUL in the chip flow direction (Figure 5.41). In some areas of the entrance zone of the crater wear scar, the fine grooves on cBN grains gave the impression of cracking and delamination processes (Figure 5.42).

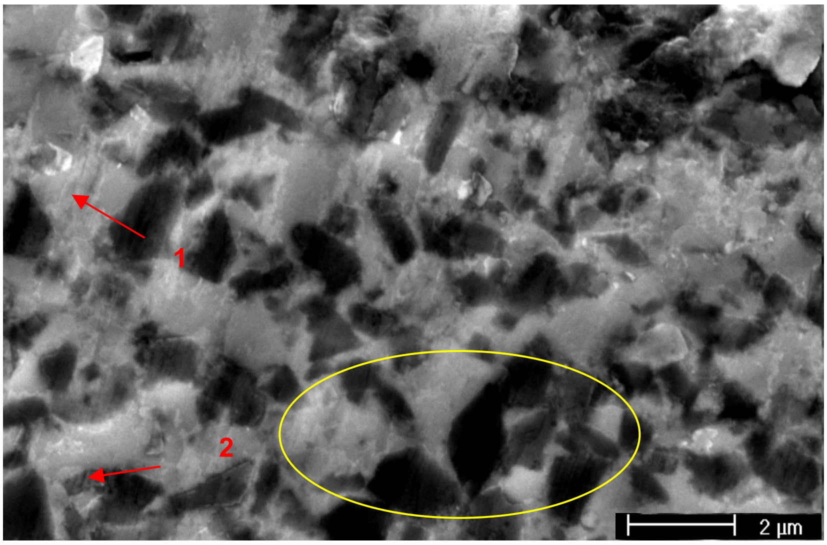

1: BUL on TiC binder **2:** BUL on cBN grain

Figure 5.41: Area in the crater wear scar of a cutting tool used at 100 m/min for 59.37 s. SEM, SE image

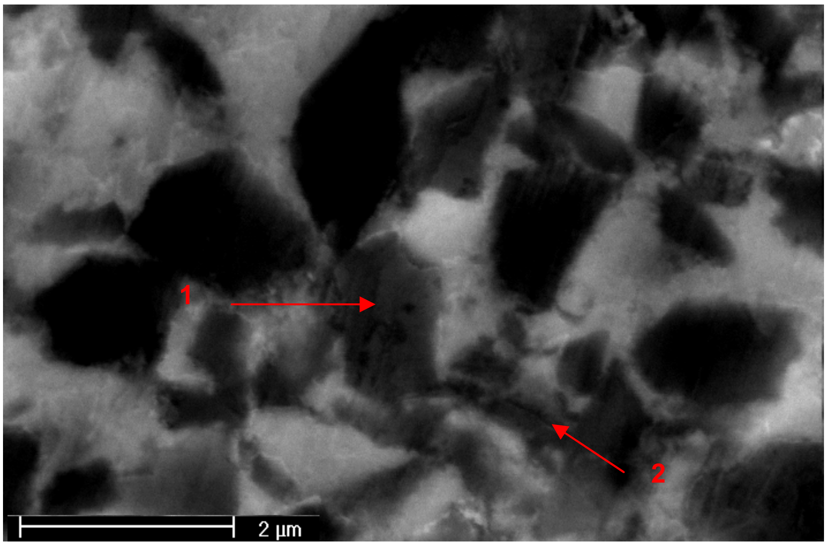

1: Delamination **2:** Cracking

Figure 5.42: Area in the crater wear scar of a cutting tool used at 100 m/min for 59.37 s. SEM, SE image

Attrition that originated from an adhesion process of ADI BUL on the cBN-TiC cutting tool resulted in plucking off of chunk of cutting tool or grain pull-out in some areas of the entrance zone of the crater wear scar (Figures 5.43 and 5.44).

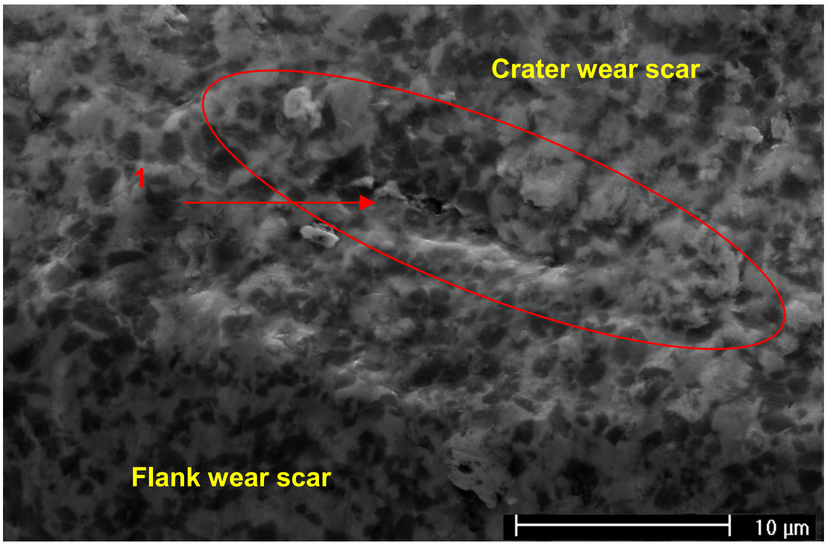

1: Plucking off of chunk of cutting tool

Figure 5.43: Cutting edge of a tool used at a cutting speed of 150 m/min for 53.72 s. SEM, SE image

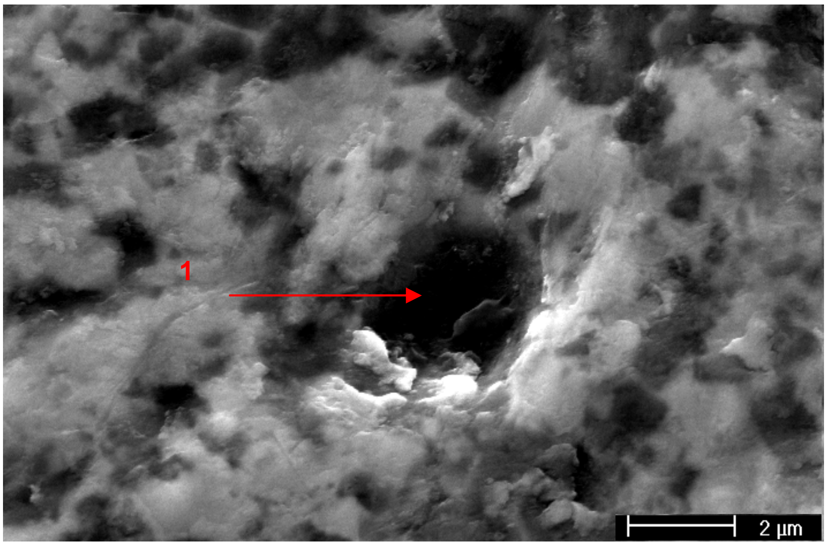

1: Grain pull-out

Figure 5.44: Entrance zone of the crater wear scar of a cutting tool used at 150 m/min for 53.72 s. SEM, SE image

Sticking of fragments of BUL on the cutting tool (Figure 5.45) and their subsequent removal by the rubbing chips or workpiece probably contributed to the formation of relatively deep grooves in the rake and flank faces of the tool as discussed at a later stage.

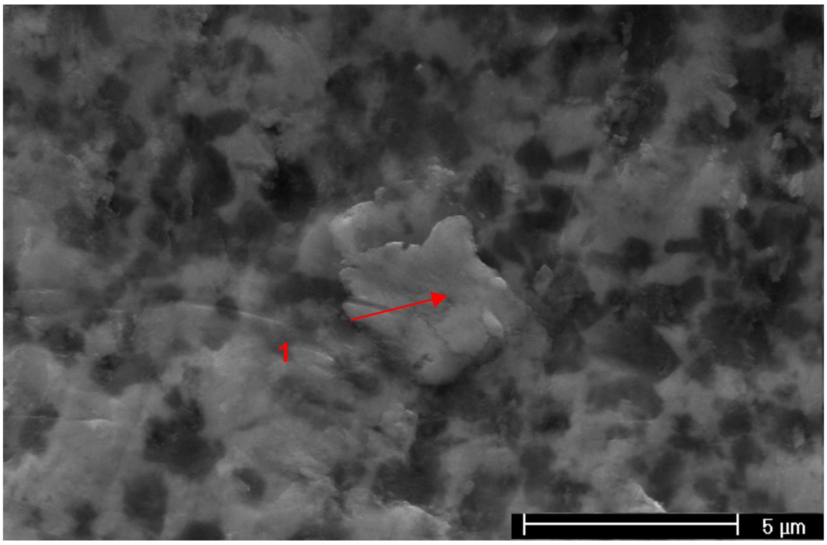

1: Fragment of BUL stuck in a groove aligned in the chip flow direction

Figure 5.45: Entrance zone of the crater wear scar of a cutting tool used at 150 m/min for 53.72 s. SEM, SE image

In the valley of the crater scar, the spongy structure of the BUL was more evident (Figures 5.46 and 5.47). The EDX analysis of the area in Figure 5.46 revealed substantial concentration of O, Al, Mg, Si and Fe on the wear scar.

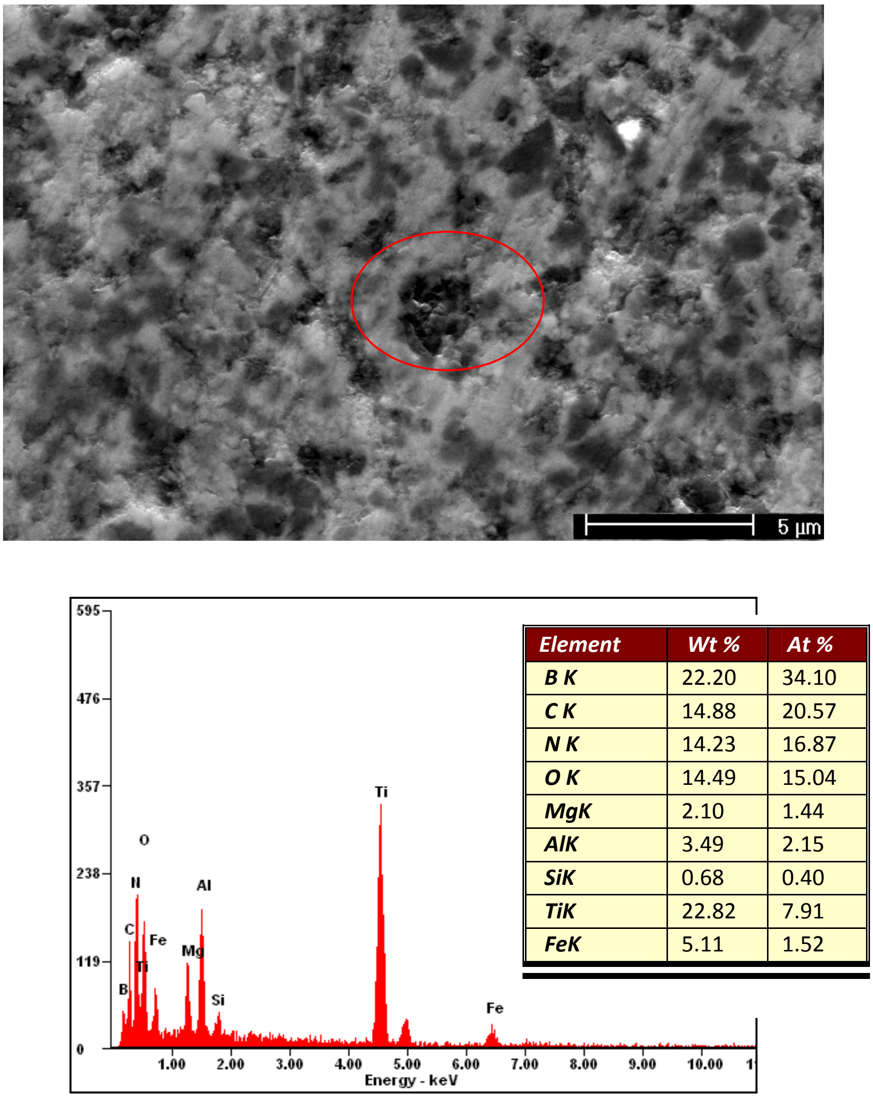

Element	*Wt %*	*At %*
B K	22.20	34.10
C K	14.88	20.57
N K	14.23	16.87
O K	14.49	15.04
MgK	2.10	1.44
AlK	3.49	2.15
SiK	0.68	0.40
TiK	22.82	7.91
FeK	5.11	1.52

Figure 5.46: Valley of the crater wear scar of a cutting tool used at 150 m/min for 53.72 s. EDX analysis of this entire area. SEM, SE image

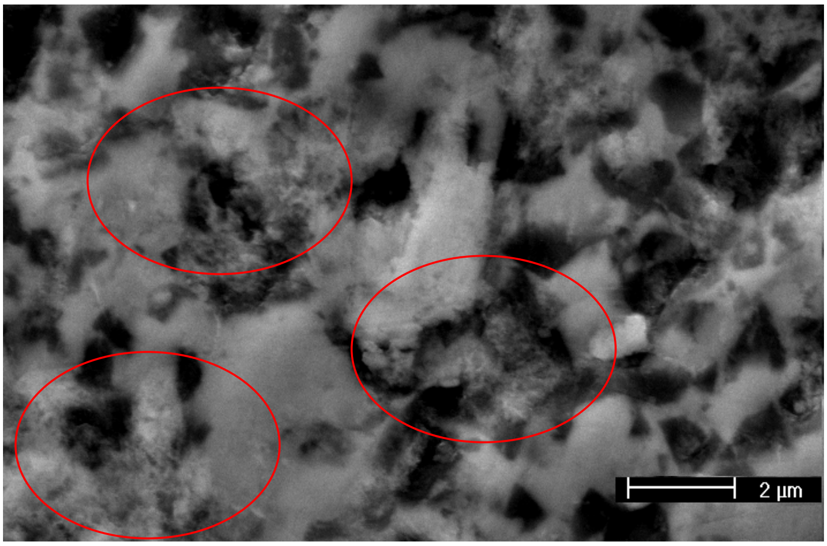

Figure 5.47: Valley of the crater wear scar of a cutting tool used at 200 m/min for 40.49 s showing spongy BUL particularly on cBN grains. SEM, SE image

A high magnification image of the area marked in Figure 5.46 showed a spongy, flaky BUL in combination with a cBN grain (Figure 5.48). It appears that the BUL did not adhere firmly to cBN grains as it did on the TiC binder. It was also evident that the cBN grains were recessed while the TiC binder was in relief and was covered by ADI BUL.

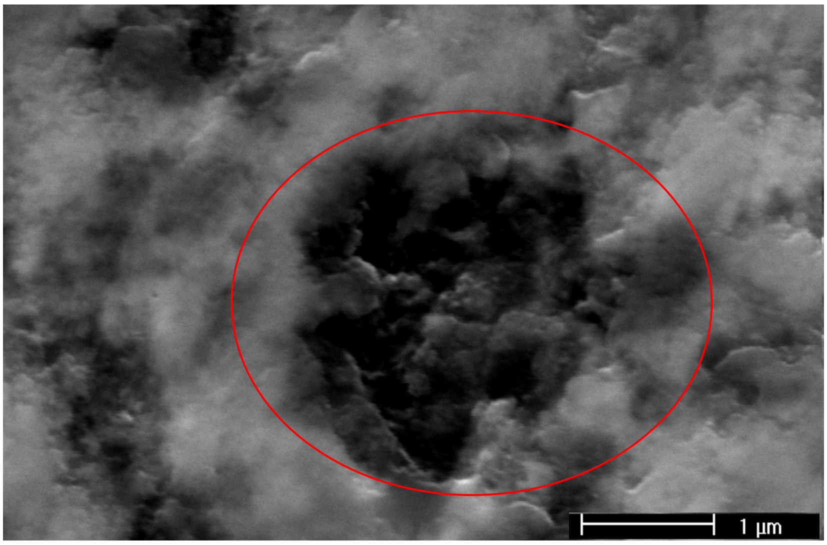

Figure 5.48: BUL in area marked in Figure 5.46. SEM, SE image

Figure 5.49 shows a cBN grain in the valley of a crater wear scar and a fragment of adhering BUL. EDX analysis of the fragment of the BUL revealed once again a substantial presence of Al, Mg, Si, Ti and Fe and a relatively low concentration of O.

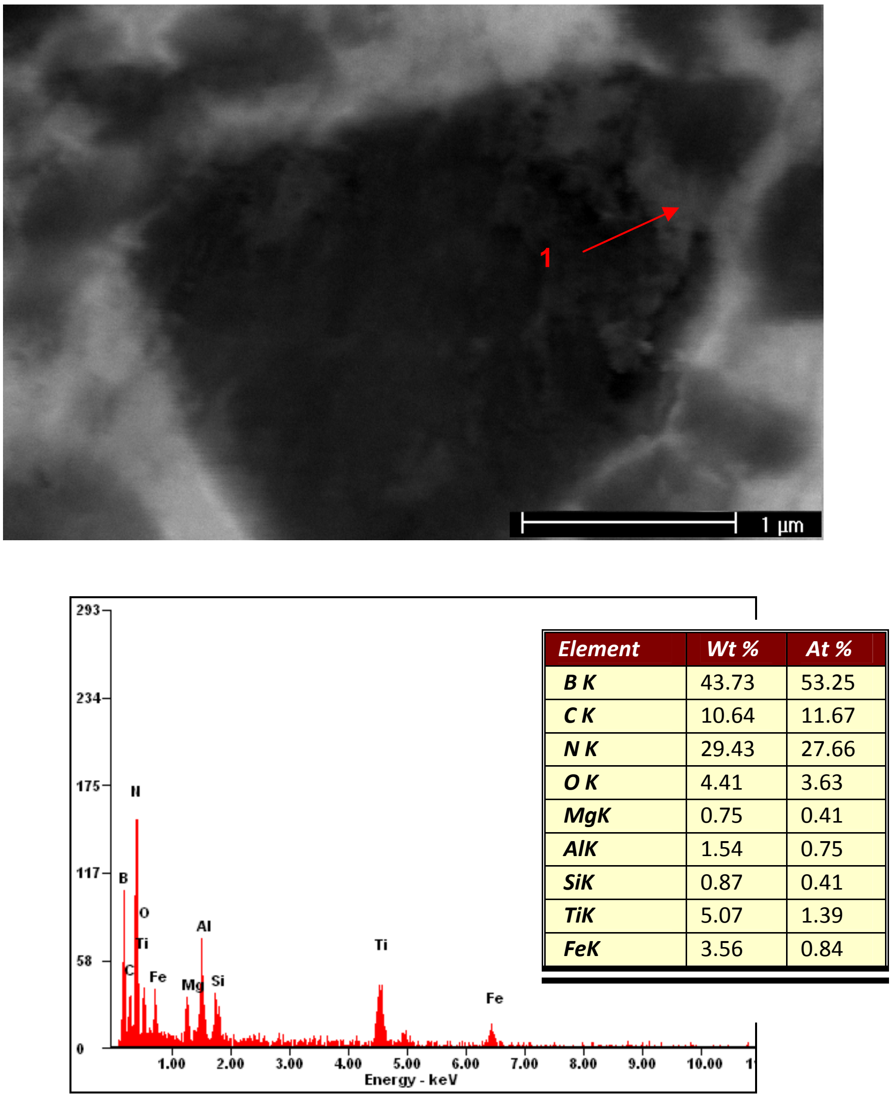

Element	Wt %	At %
B K	43.73	53.25
C K	10.64	11.67
N K	29.43	27.66
O K	4.41	3.63
MgK	0.75	0.41
AlK	1.54	0.75
SiK	0.87	0.41
TiK	5.07	1.39
FeK	3.56	0.84

Figure 5.49: Valley of the crater wear scar of a cutting tool used at 150 m/min for 53.72 s and EDX analysis of the fragment of BUL adhering to the cBN grain indicated in (1). SEM, SE image

Figure 5.50 shows an area at the exit of a crater wear scar that revealed a considerable smearing of the BUL with a morphology that indicated a relatively soft or viscous state that left a stringer-like BUL in the chip flow direction. EDX analysis of the TiC grain pointed out in Figure 5.50 revealed substantial concentrations of O, Mg, Al, Si and Fe. The presence of O is indicative of superficial oxidation of TiC in this specific zone.

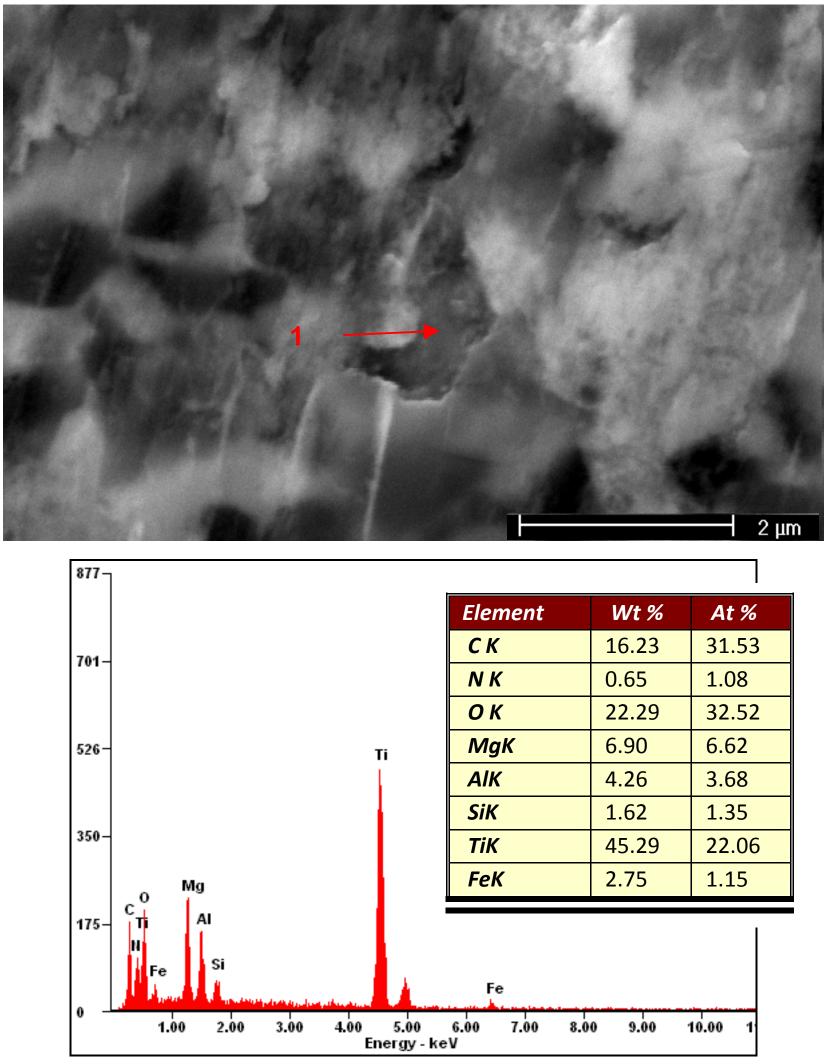

Element	*Wt %*	*At %*
C K	16.23	31.53
N K	0.65	1.08
O K	22.29	32.52
MgK	6.90	6.62
AlK	4.26	3.68
SiK	1.62	1.35
TiK	45.29	22.06
FeK	2.75	1.15

Figure 5.50: Area at the exit zone of the crater wear scar of a cutting tool used at 150 m/min for 53.72 s. EDX analysis of TiC binder indicated in 1. SEM, SE image

In some areas of the entrance zone of the crater scar, some cracking or fracture running in a direction that did not correspond to the chip flow direction appeared on cBN grains (Figure 5.51). In some areas of the valley of the crater scar, some cracking running parallel to the chip flow direction appeared on cBN grains (Figure 5.52).

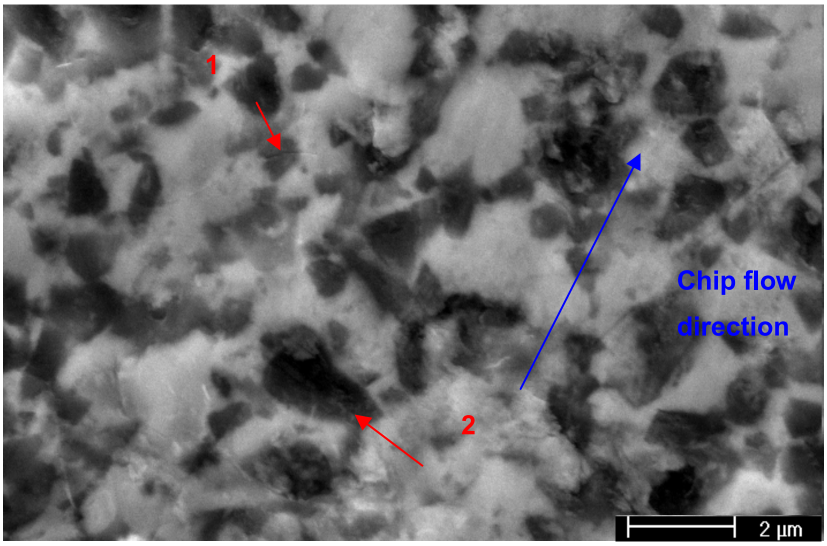

1: Crack in cBN grain **2:** Fractured cBN grain

Figure 5.51: Area in the entrance of a crater wear scar of a cutting tool used at 200 m/min for 40.49 s. SEM, SE image

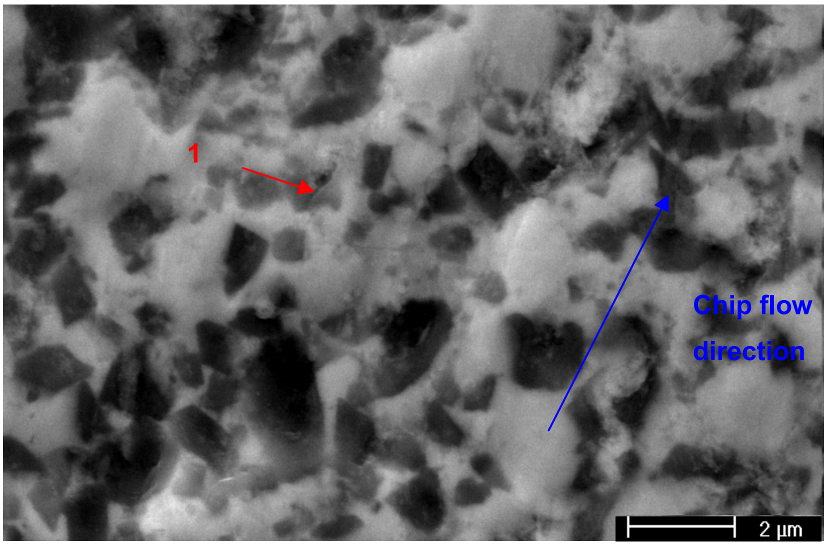

1: crack on cBN grain

Figure 5.52: Area in the valley of a crater wear scar of a cutting tool used at 200 m/min for 40.49 s. SEM, SE image

At the start of the cutting process, BUL interaction with cBN grains was not evident whereas BUL appeared on TiC binder (Figure 5.53). EDX analysis on the cBN grain marked in Figure 5.53 did not reveal clearly the presence of Fe from the ADI. However, it revealed substantial concentrations of Si, Mg, and O.

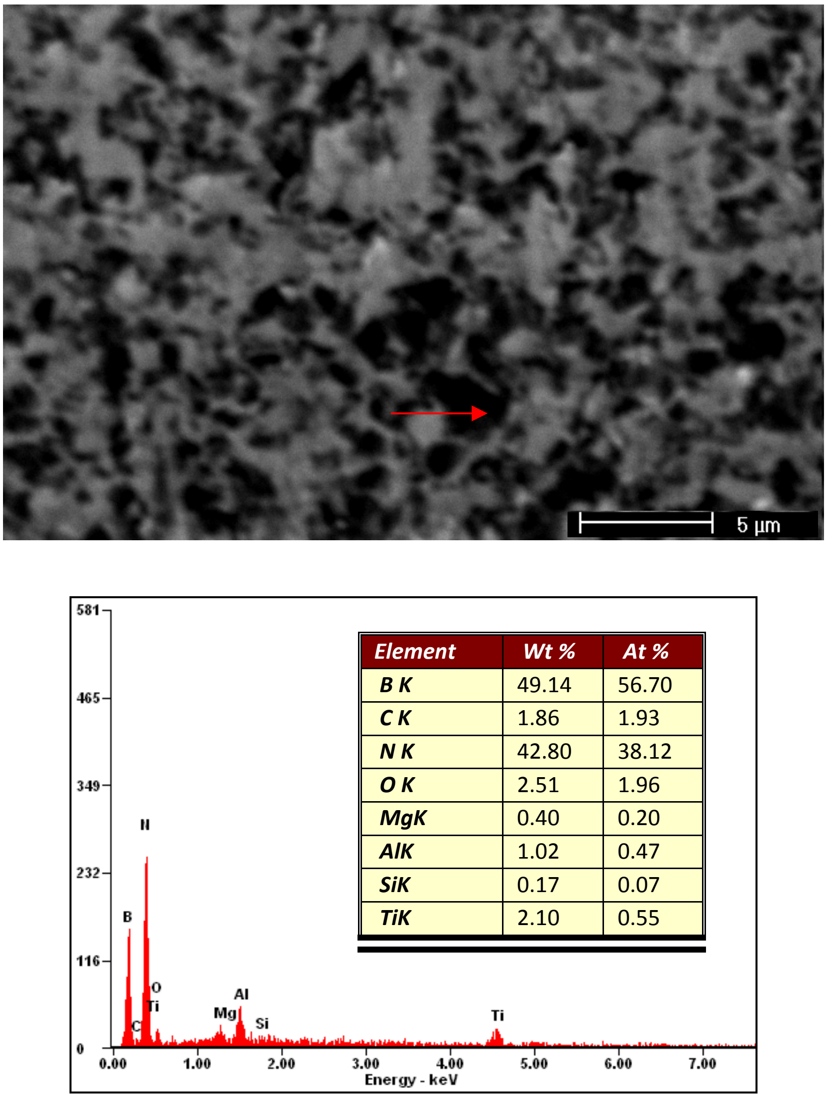

Element	Wt %	At %
B K	49.14	56.70
C K	1.86	1.93
N K	42.80	38.12
O K	2.51	1.96
MgK	0.40	0.20
AlK	1.02	0.47
SiK	0.17	0.07
TiK	2.10	0.55

Figure 5.53: Area in the flank wear scar of a cutting tool used at 600 m/min for 10.00 s. EDX analysis of a selected cBN grain. SEM, SE image

5.5.4 Surface layers built up on non-contact zones

Surface layers built up on non-contact zones of cutting tool appeared clearly for the entire range of cutting speeds used except for the cutting speed of 50 m/min (Figures 5.8 to 5.12). These surface layers appeared as a coating of spongy flaky structure of considerable thickness on the rake and flank faces of the cutting tools and could be considered to a certain extent as a heat affected zone around the wear scar.

The morphology of surface layers built up on non-contact zones on the rake and flank faces appeared to not be the same. It appeared spongier on the rake face and more compact on the flank face (Figures 5.8 to 5.12).

The morphology of the surface layers built up on the non-contact zone of the rake face appeared to change with cutting speed, i.e. with cutting tool wear rate. It also appeared to change from the trailing edge towards the leading edge of the cutting tool. As the cutting speed increased, the smearing of the BUL at the exit zone of the crater wear scar and the non-contact zone of the rake face towards the leading edge became more important (Figures 5.54 to 5.56).

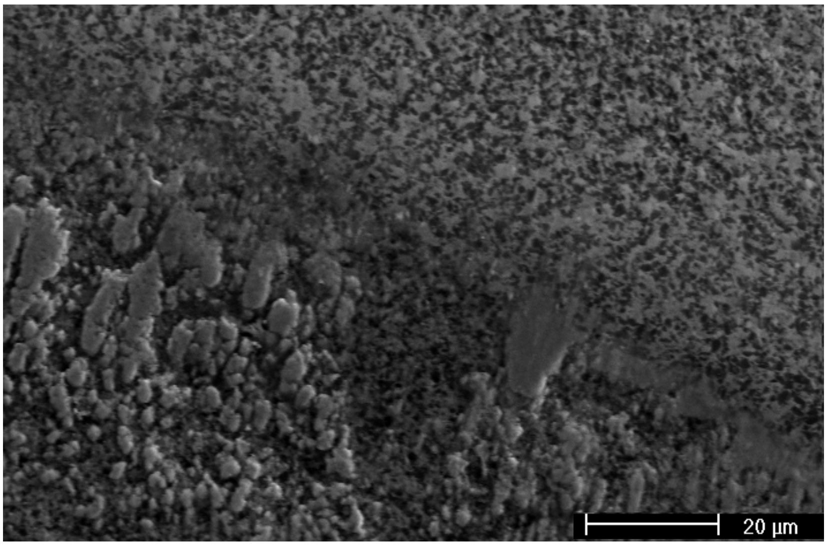

Figure 5. 54: Surface layer built up on the non-contact zone of the rake face towards the leading edge of a cutting tool used at 100 m/min for 59.37 s. SEM, SE image

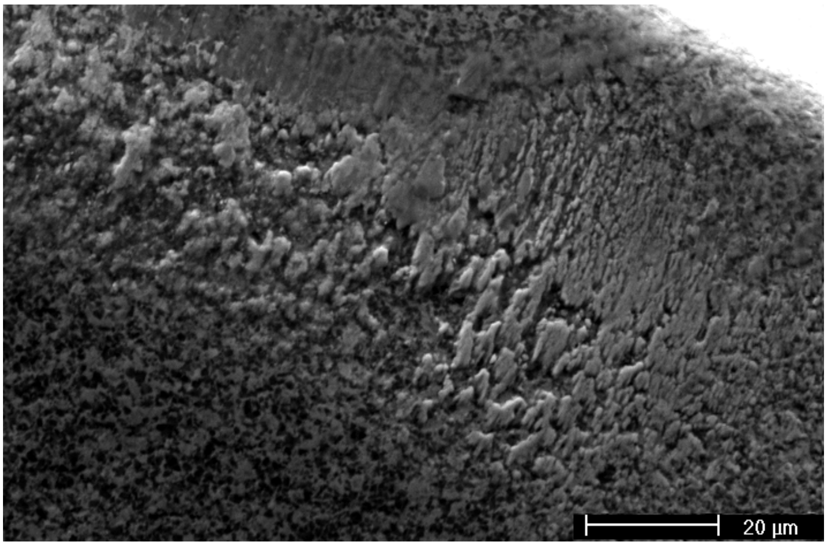

Figure 5.55: Surface layer built up on the non-contact zone of the rake face towards the leading edge of a cutting tool used at 200 m/min for 40.49 s. SEM, SE image

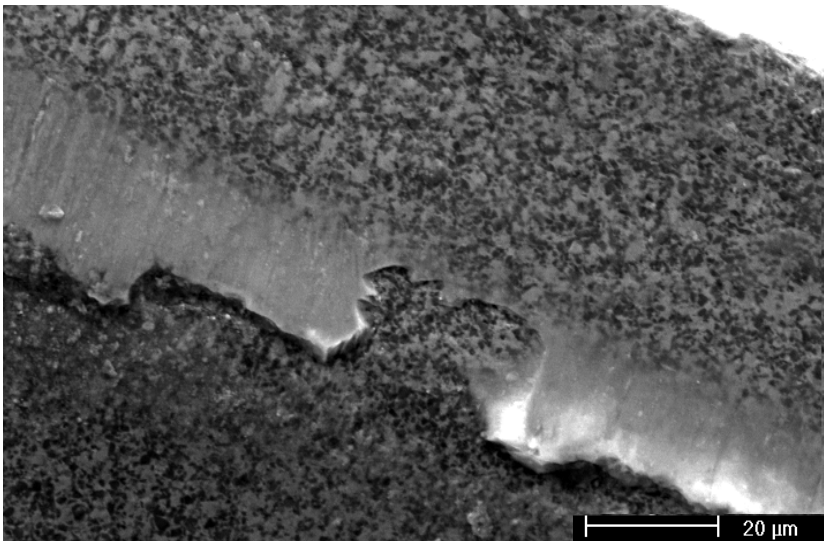

Figure 5.56: Surface layer built up on the non-contact zone of the rake face towards the leading edge of a cutting tool used at 800 m/min for 7.57 s. SEM, SE image

The exit of the crater wear scar towards the leading edge revealed considerable smearing of a thick BUL that was oxidized superficially (Figure 5.57). A high magnification image of the surface layer built up on the non-contact zone indicated by the rectangle in Figure 5.57 is shown in Figure 5.58, revealing its spongy flaky structure. Small rounded particles of less than 1 µm appeared mixed with relatively big particles of less than 3 µm. EDX analysis of this portion of surface layer revealed Mg, Si, Al, C, Fe and Ti. The presence of a substantial amount of O indicated that oxidation had taken place or that oxides had deposited in this area (Figure 5.58). It is likely that the C in the surface layer built up on the non-contact zone of the rake face would be in the form of graphite that was expelled from ADI chips at the tool-chip interface. A similar area is shown in Figure 5.59.

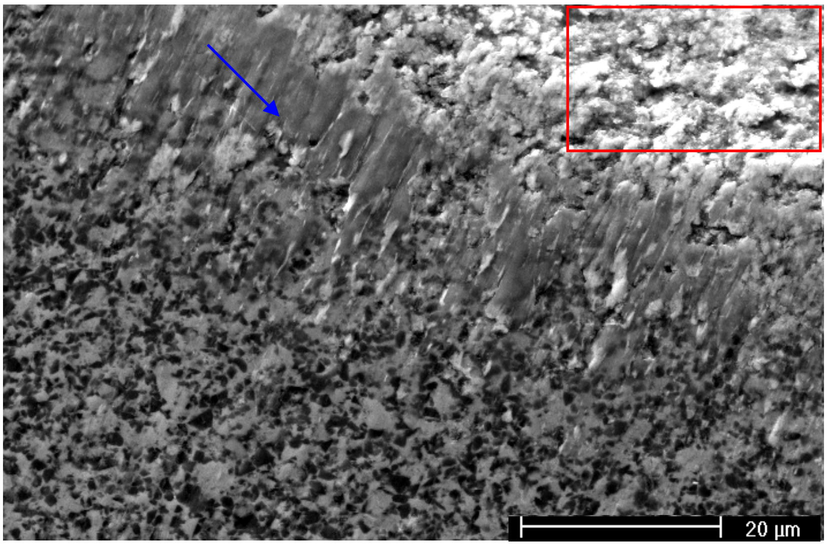

Figure 5.57: Exit zone of the crater wear scar towards the leading edge of a cutting tool used at 150 m/min for 53.72 s. SEM, SE image

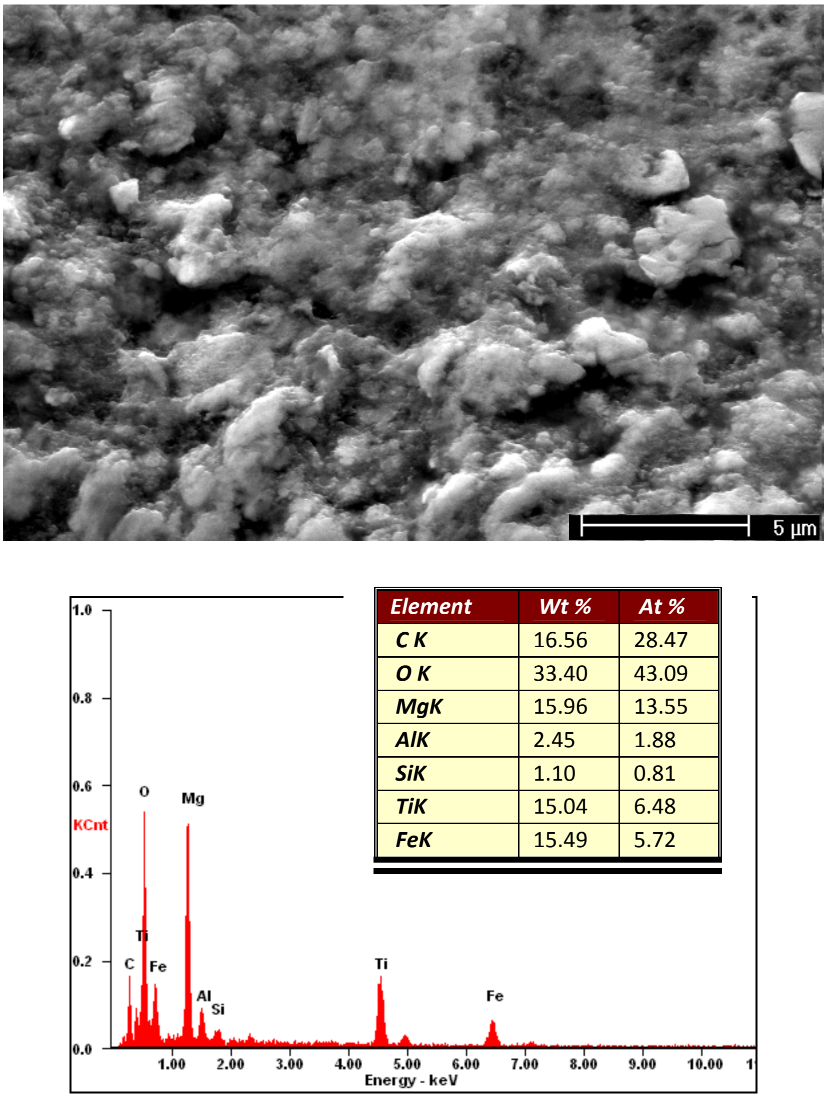

Element	*Wt %*	*At %*
C K	16.56	28.47
O K	33.40	43.09
MgK	15.96	13.55
AlK	2.45	1.88
SiK	1.10	0.81
TiK	15.04	6.48
FeK	15.49	5.72

Figure 5.58: Surface layer built up on the non-contact zone of the rake face towards the leading edge of a cutting tool used at 150 m/min for 53.72 s. EDX analysis of the area. SEM, SE image

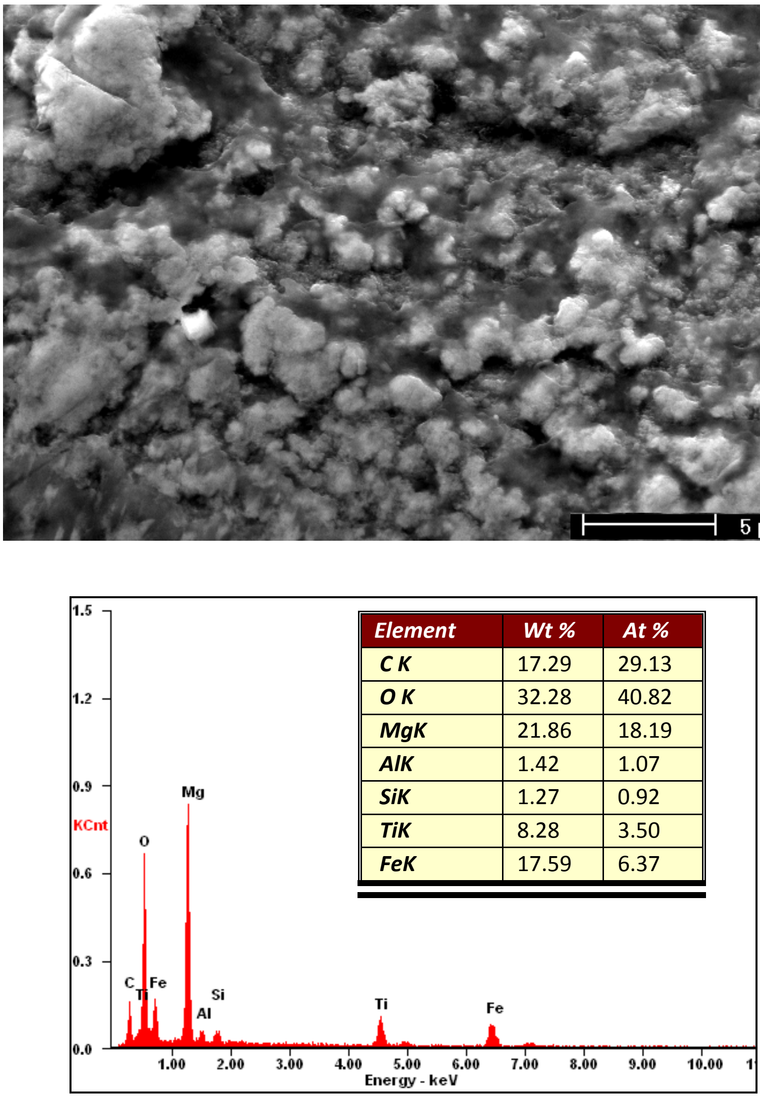

Element	Wt %	At %
C K	17.29	29.13
O K	32.28	40.82
MgK	21.86	18.19
AlK	1.42	1.07
SiK	1.27	0.92
TiK	8.28	3.50
FeK	17.59	6.37

Figure 5.59: Surface layer built up on the non-contact zone of the rake face towards the leading edge of a cutting tool used at 200 m/min for 40.49 s. EDX analysis of the area. SEM, SE image

In the late stages of dry turning, the morphology of surface layers built up on the non-contact zones of the rake face showed blisters and cracks on top of deposits of rounded particles. EDX analyses of the surface layers built up on the non-contact zones of the rake face revealed once again the intriguing presence of Mg, Si, and O, as well as Fe and Ti (Figure 5.60).

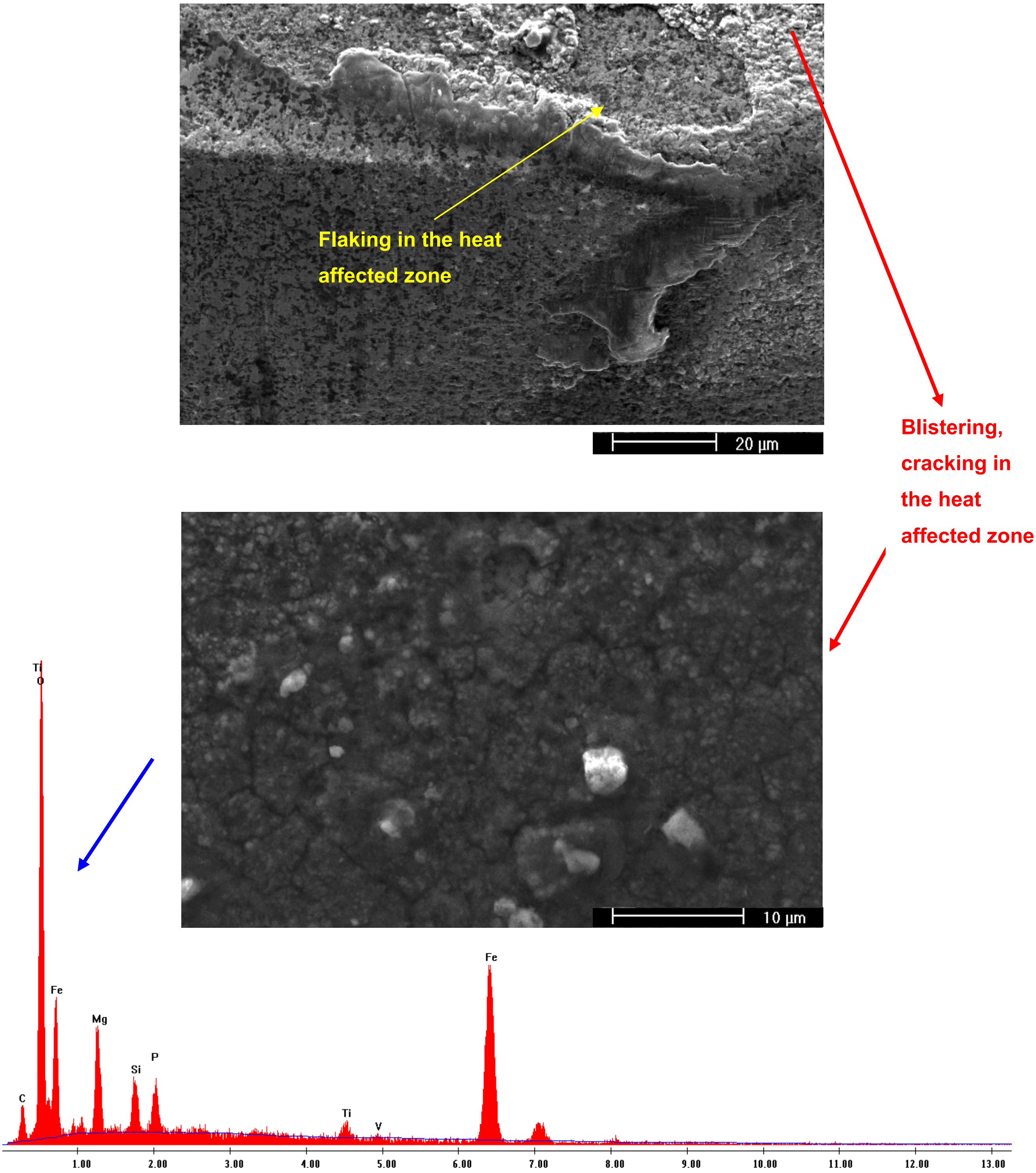

Figure 5.60: Surface layer built up on the non-contact zone of the rake face towards the leading edge of a cutting tool used at 600 m/min for 157.69 s. EDX analysis of the area. SEM, SE images

Adhesion between the surface layers built up on the non-contact zones and the tool substrate appeared to be rather weak. The surface layers built up on the non-contact zones partially peeled off when the thickness increased (Figure 5.60).

Surface layers built up on the non-contact zone of the flank face were made of thicker ADI BUL covered with a layer rich in Si and O with appreciable concentrations of Mg and Fe indicative of superficial oxidation, particularly towards the leading and trailing edges of the cutting edge (Figures 5.61 to 5.63).

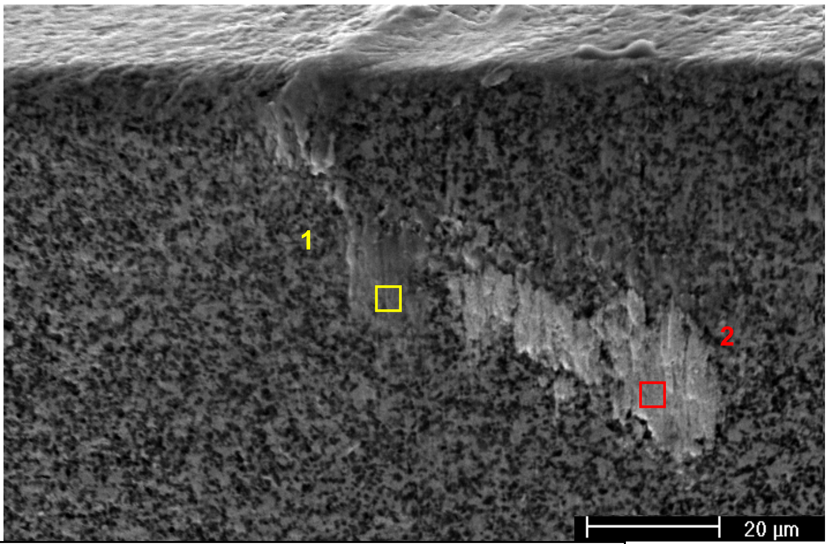

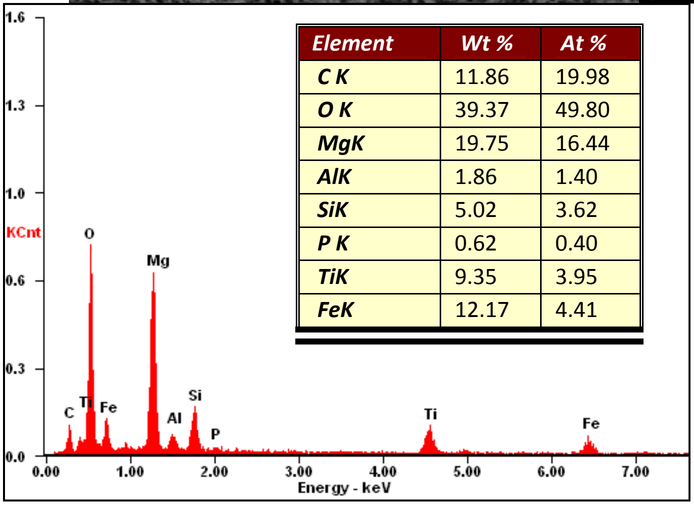

Element	Wt %	At %
C K	11.86	19.98
O K	39.37	49.80
MgK	19.75	16.44
AlK	1.86	1.40
SiK	5.02	3.62
P K	0.62	0.40
TiK	9.35	3.95
FeK	12.17	4.41

EDX on area 1

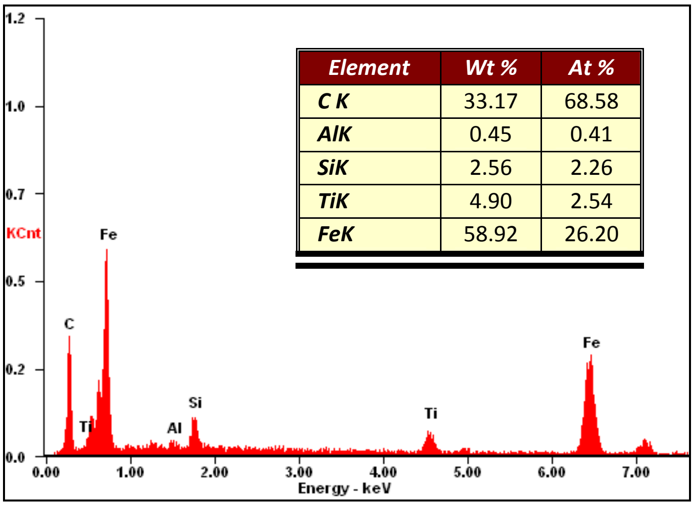

Element	Wt %	At %
C K	33.17	68.58
AlK	0.45	0.41
SiK	2.56	2.26
TiK	4.90	2.54
FeK	58.92	26.20

EDX on area 2

Figure 5. 61: Wear scar of a cutting tool used at 500 m/min for 11.93 s, showing the flank wear scar (towards the leading edge) and the surface layer built up. EDX on selected areas of the surface layer. SEM, SE image

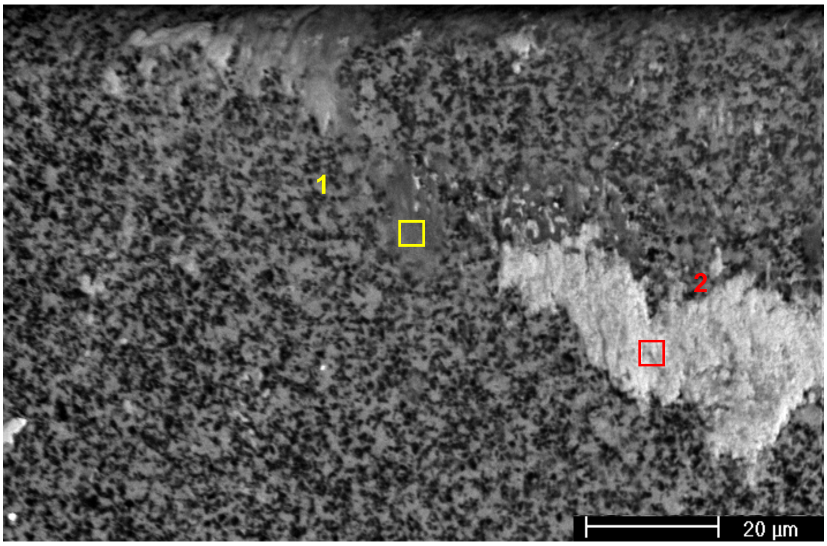

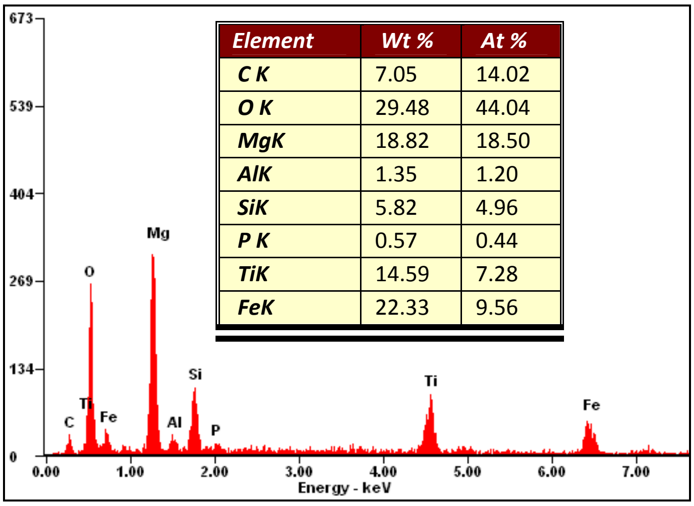

Element	Wt %	At %
C K	7.05	14.02
O K	29.48	44.04
MgK	18.82	18.50
AlK	1.35	1.20
SiK	5.82	4.96
P K	0.57	0.44
TiK	14.59	7.28
FeK	22.33	9.56

EDX on area 1

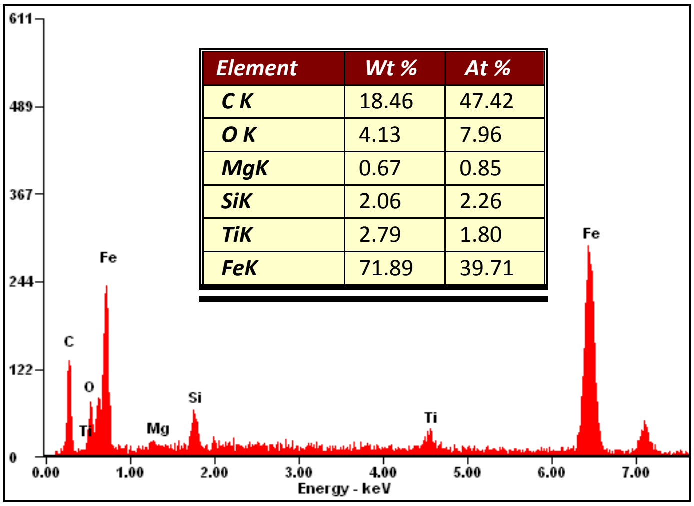

Element	Wt %	At %
C K	18.46	47.42
O K	4.13	7.96
MgK	0.67	0.85
SiK	2.06	2.26
TiK	2.79	1.80
FeK	71.89	39.71

EDX on area 2

Figure 5.62: Wear scar of a cutting tool used at 600 m/min for 10.00 s, showing the flank wear scar (towards the leading edge) and the surface layer built up. EDX on selected areas of the surface layer. SEM, BSE image

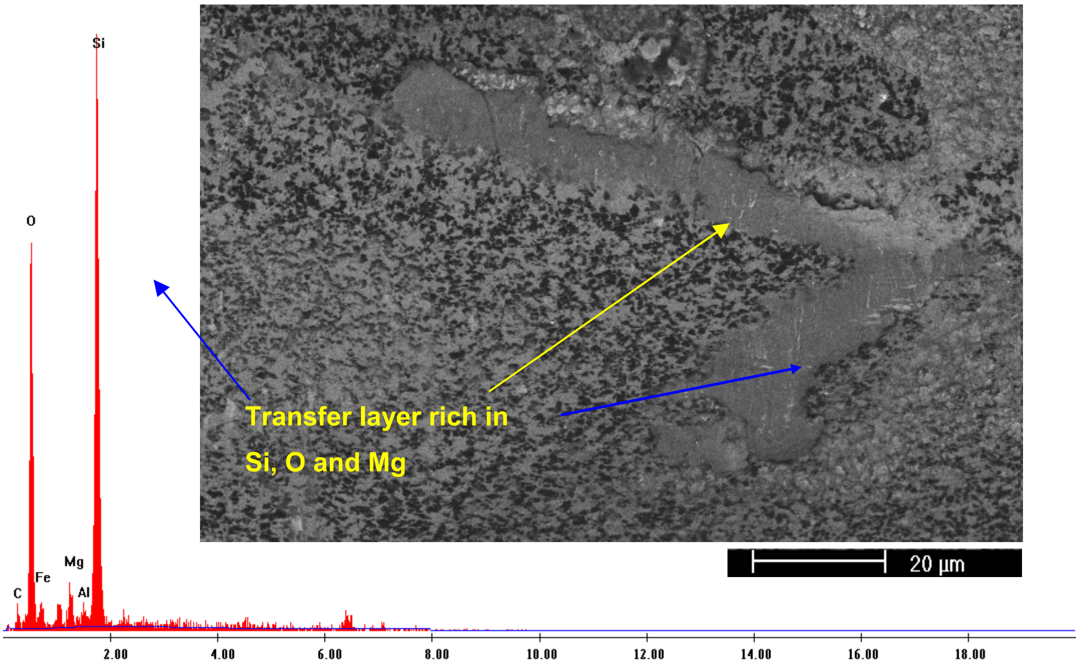

Figure 5.63: Wear scar of a cutting tool used at 600 m/min for 157.69 s showing the layer covering the BUL (towards the trailing edge). EDX analysis on a selected area of the latter layer. SEM, BSE image

5.5.4 Wear scar morphology at an advanced stage of dry turning

The morphology of the flank wear surface was similar to that of the crater wear surface showing grooves and adhering material (Figures 5.64 and 5.65). The grooves on the flank wear scar were vertical. Those on the crater scar were parallel to the chip flow direction.

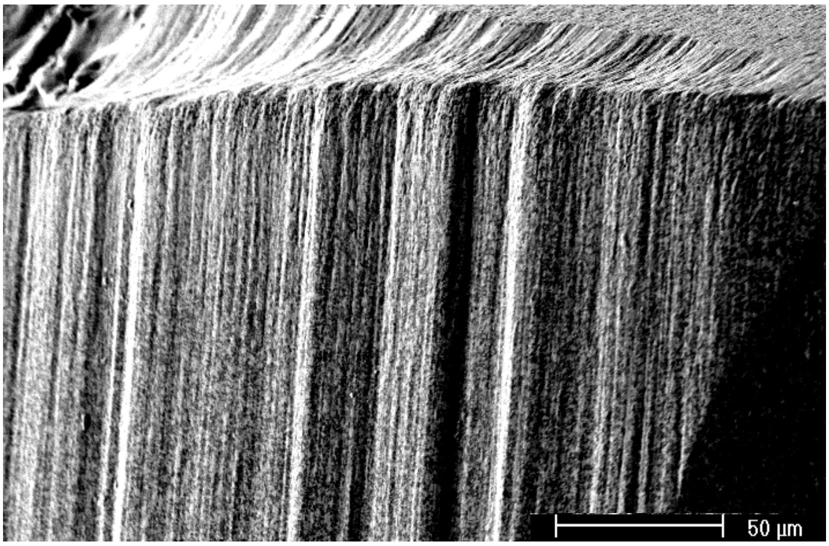

Figure 5.64: Wear scar morphology of a cutting tool used at 50 m/min for 12874.42 s, showing deep grooves on the flank and rake faces. SEM, SE image

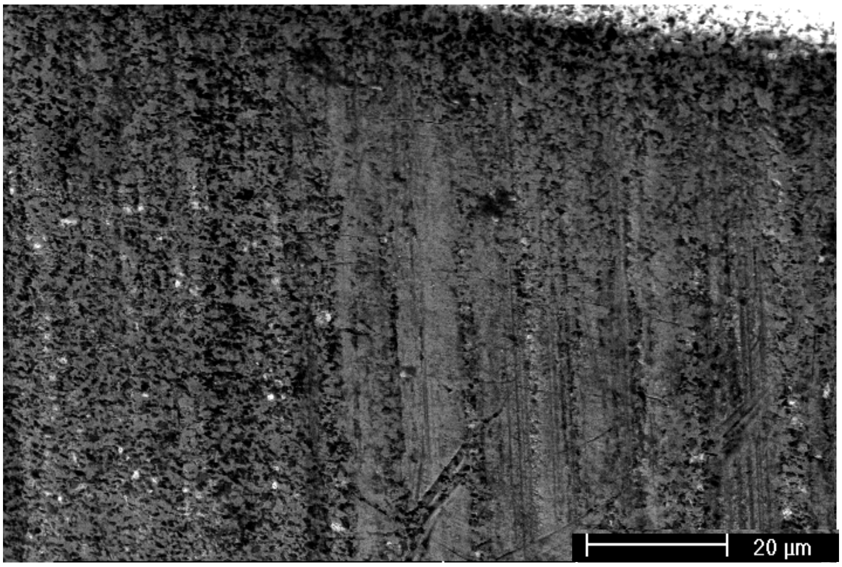

Figure 5.65: Flank scar morphology of a cutting tool used at 800 m/min for 42.73 s showing shallow grooves and adhering material. SEM, SE image

The grooves were deep for cutting speeds lower than 150 m/min (Figure 5.64). At cutting speeds greater than 150 m/min, the grooves were shallow and appeared to be filled with a BUL that was also grooved (Figure 5.65).

Within the broad grooves of the worn cutting tools, a detailed SEM investigation at high magnification revealed the presence of slight grooves on the cBN grains as well as the TiC binder (Figures 5.66 and 5.67).

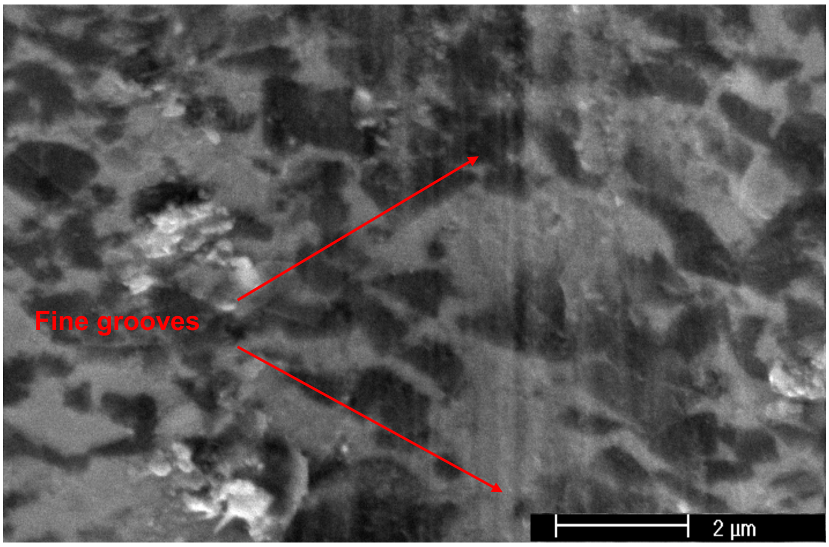

Figure 5.66: Flank wear scar morphology of a cutting tool used at 600 m/min for 157.69 s showing fine grooves and TiC binder slightly proud of cBN grains. SEM, SE image

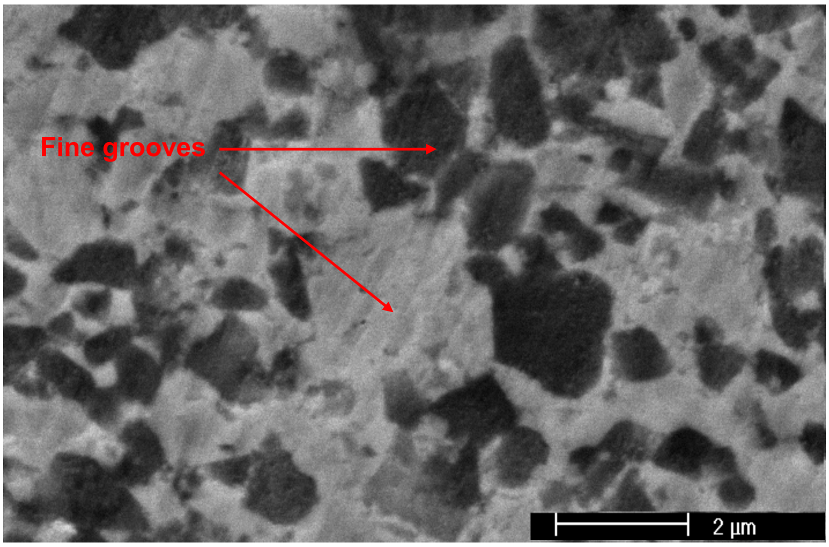

Figure 5.67: Crater wear scar morphology of a cutting tool used at 600 m/min for 157.69 s showing fine grooves and TiC binder slightly proud of cBN grains. SEM, SE image

5.5.6 TEM investigation of the cross sections of wear scars

STEM investigation at high magnification of the sections of the crater wear scar extracted with FIB technique (Figure 5.68) revealed the presence of a C-rich layer, a typical transfer layer containing Si, Mg and O and cracks through cBN grains and the TiC binder (Figure 5.69). The concentration of Mg typically rose at the transfer layer - tool interface. Fe was present in the form of a layer on the TiC binder and also in the form of small spots in the transfer layer. Al, Si and Fe were found relatively deep (about 0.5 µm) in the tool, at the boundary between cBN grains and TiC binder (Figure 5.70).

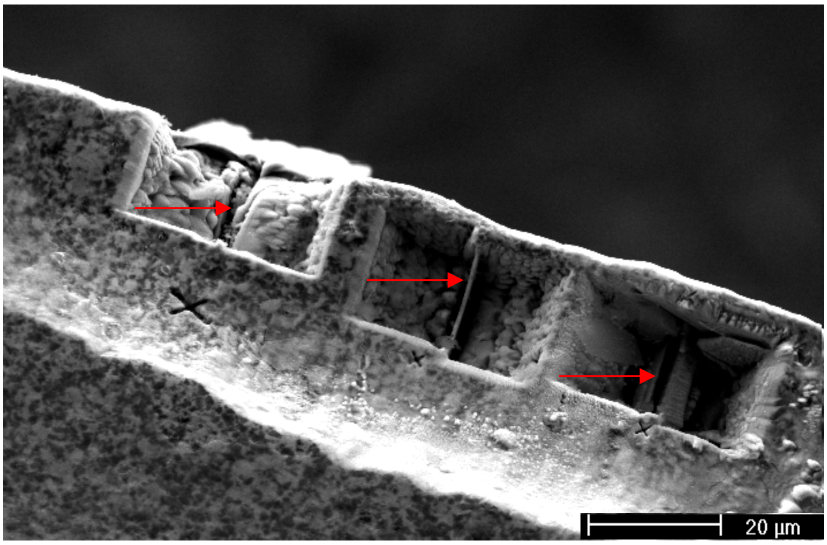

Figure 5.68: Crater wear scar of a cutting tool used at 800 m/min for 42.73 s showing areas where sections were extracted by FIB technique. SEM, SE image

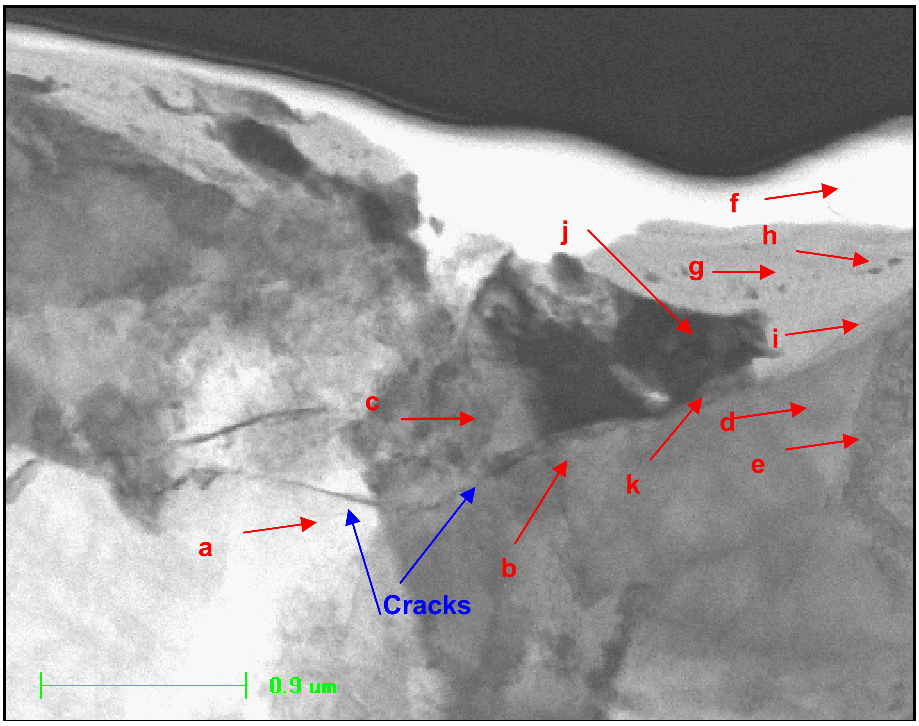

Spot	Area	Most abundant elements	Remarks
(a)	cBN grain		
(b,c,d,e)	TiC binder		
(f)	C-rich layer		
(g)	Transfer layer	Si, Mg, O, B, C	Traces of Al, Ti, Fe
(h)	Transfer layer	Si, Mg, O, N, B, C	Fe in small spots in the transfer layer. Traces of Al, Fe, Ti
(i)	Transfer layer-tool interface	Ti, Mg, Si, O, N, C, B	High Mg concentration. Traces of Fe
(j)	Fe layer		
(k)	Fe layer	Fe, Ti, Si, Mg, O	High Fe concentration at some distance below the crater scar. Traces of C, B,N

Figure 5.69: Section through a crater wear scar of a cutting tool used at 800 m/min for 42.73 s showing the transfer layer and cracks through cBN grains and TiC binder. EDX analyses on specific spots. STEM, bright field image

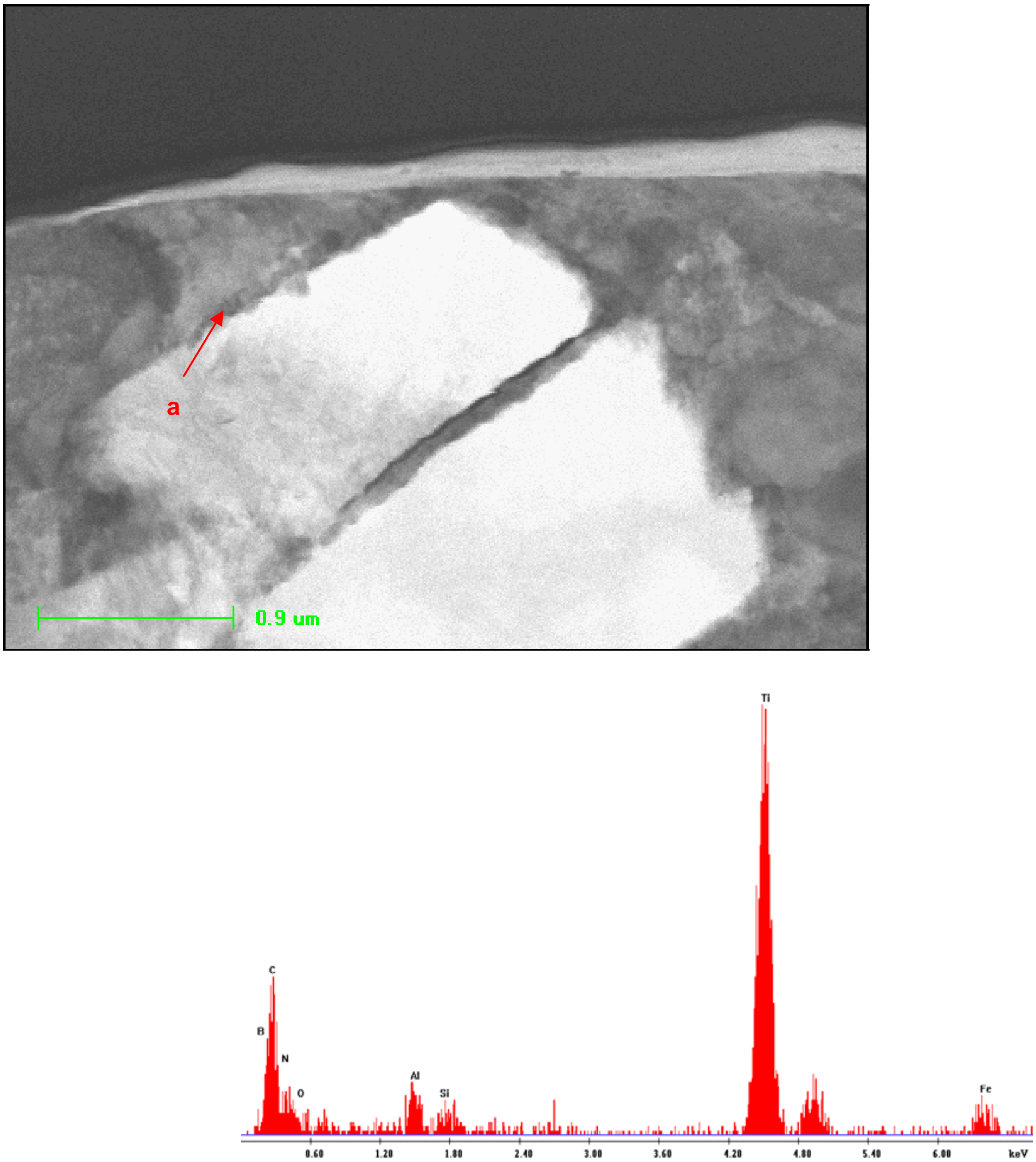

Figure 5.70: Section through a crater wear scar of a cutting tool used at 800 m/min for 42.73 s and EDX analysis of a grain boundary area "a" between a cBN grain and TiC binder below the surface. STEM, bright field image

5.6 TGA OF CBN-TIC CUTTING TOOLS

5.6.1 Anisothermal TGA of cBN-TiC cutting tools

The results of the anisothermal TGA of the cutting tool material in air (Figure 5.71) revealed that the onset of mass gain occurs at 550 °C. However, the mass gain became significant from

900 °C. From these preliminary results, isothermal TGA of cBN-TiC cutting tool material in air at 550, 900, 1000 and 1100 °C for 60 min were conducted. The results of these investigations are presented in Section 5.6.2.

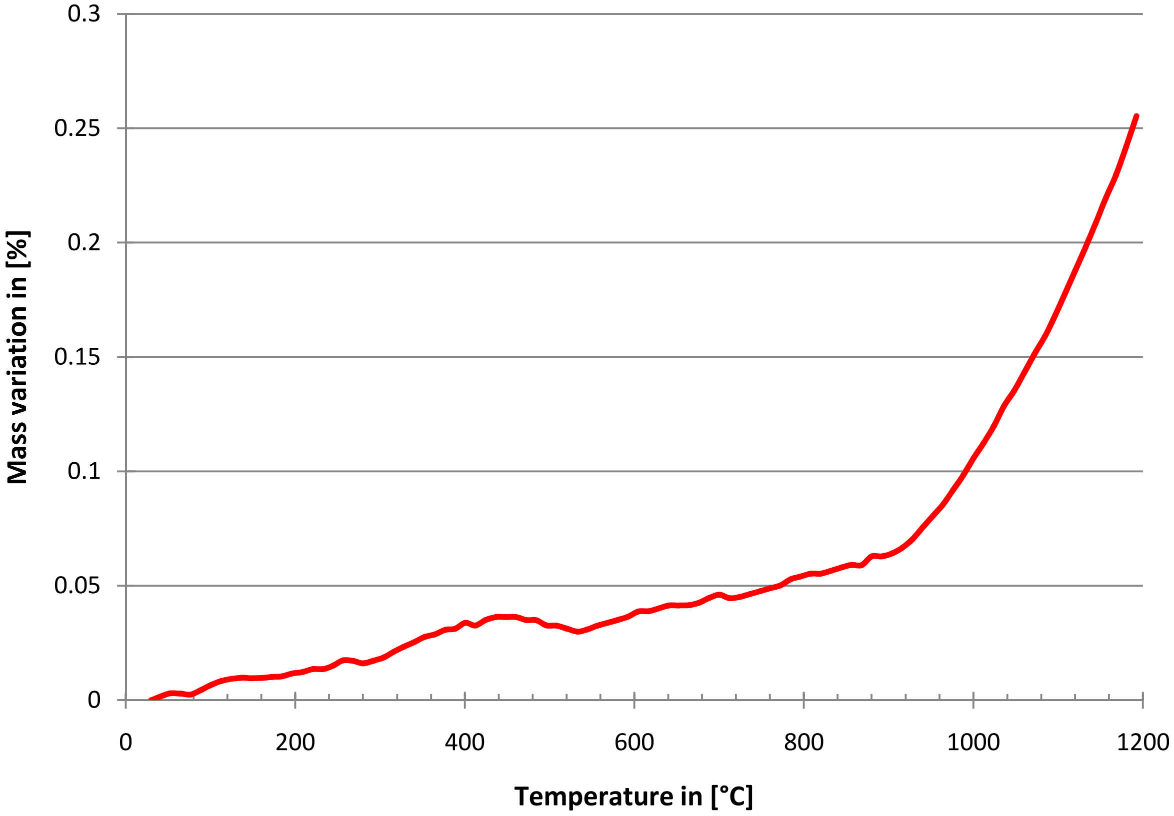

Figure 5.71: Anisothermal TGA of cBN-TiC cutting tool material

5.6.2 Isothermal TGA of cBN-TiC cutting tools

The results of the isothermal TGA of the cBN-TiC cutting tool material in air at 550, 900, 1000 and 1100 °C for 60 min are presented in Figure 5.72. These results showed that the isothermal oxidation of cBN-TiC cutting tool material obey a parabolic law within the temperature range 550-1100 °C and within 60 min. The mass gain at 550 °C was low, whereas it appeared to be much higher at 1100 °C. The overall mass gain of cBN-TiC cutting tool material during the oxidation experiments amounted 0.062, 0.156, 0.222 and 0.697 wt% respectively at 550, 900, 1000 and 1100 °C.

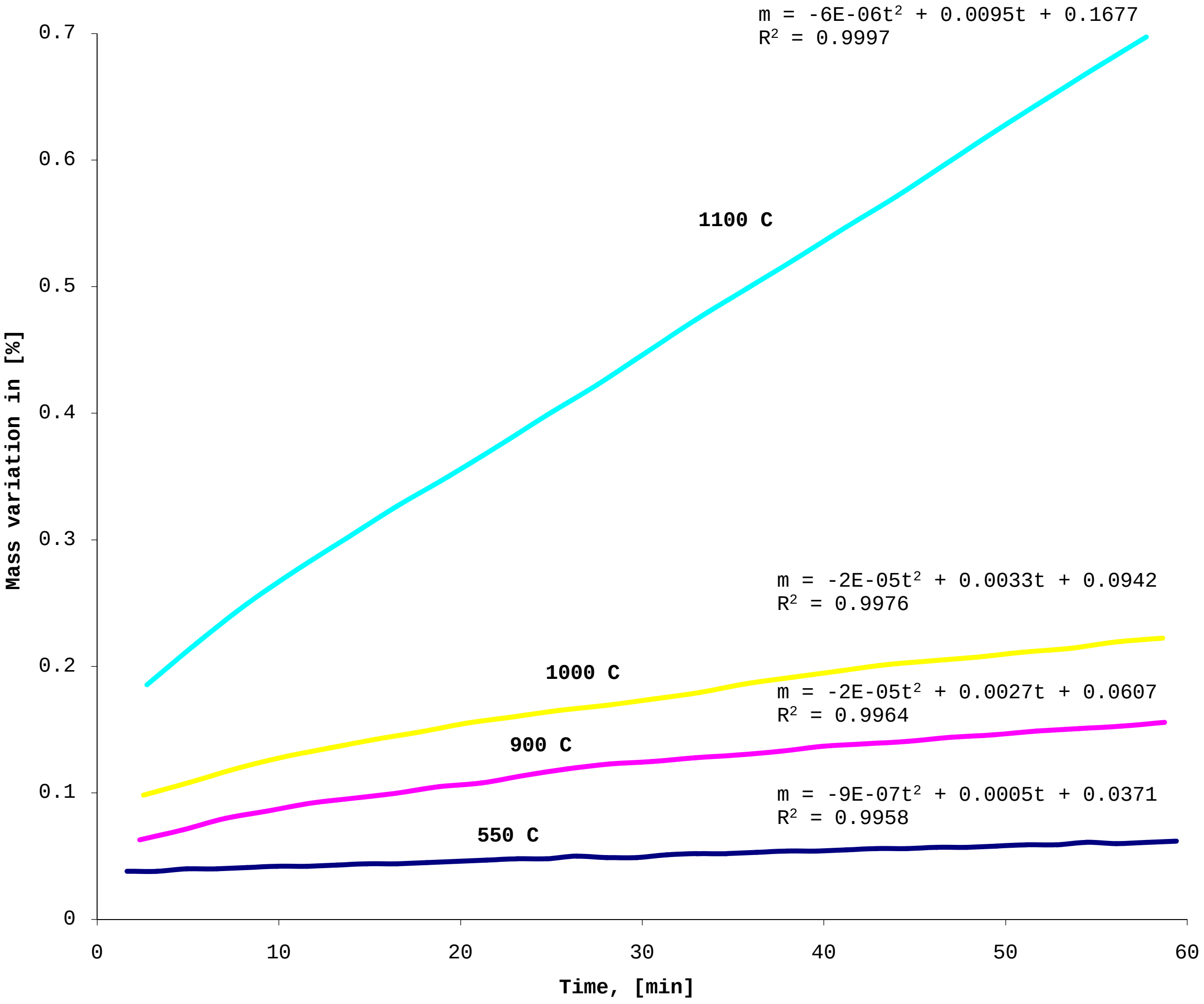

Figure 5.72: Isothermal TGA of cBN-TiC cutting tool material in air

All samples changed the colour after the isothermal TGA. However, no lustrous material appeared on the surface of samples that could suggest a significant presence of glassy B_2O_3. SEM investigation of the oxide scale of the samples ex-isothermal TGA gave some insight in the oxidation process of cBN-TiC cutting tool material.

5.6.2.1 Morphology of the oxide scale after isothermal TGA at 550 °C

Despite the slight change in the colour with regard to the original dark grey colour of cBN-TiC cutting tool material, results for the morphology investigation revealed that the oxidation at 550 °C did not produce a major oxide layer covering the entire surface of the sample (Figures 5.73 to 5.75). TiC grains showed particularly a significant amount of surface oxygen (Figures 5.73 and 5.74). cBN grains exhibited a slight amount of surface oxygen (Figure 5.75).

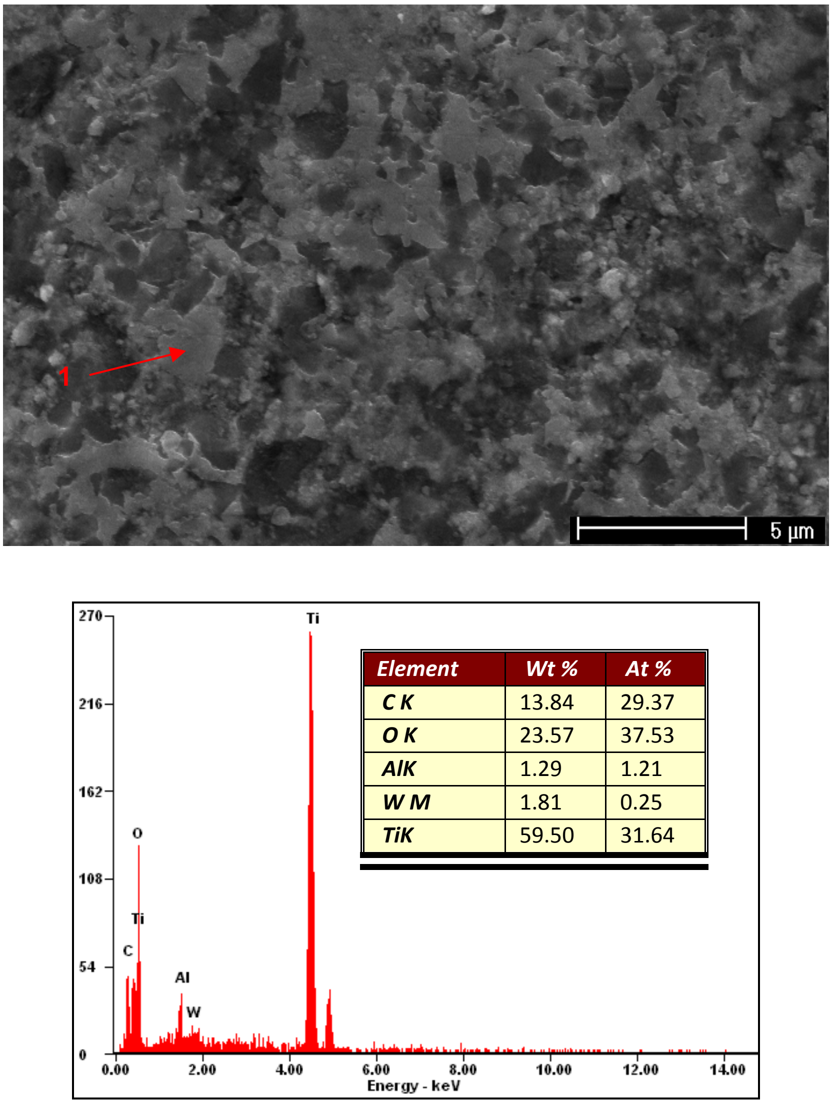

Element	Wt %	At %
C K	13.84	29.37
O K	23.57	37.53
AlK	1.29	1.21
W M	1.81	0.25
TiK	59.50	31.64

Figure 5.73: Morphology of the surface of cBN-TiC cutting tool material after isothermal TGA at 550 °C for 60 min. EDX analysis of TiC grain indicated (1). SEM, SE image

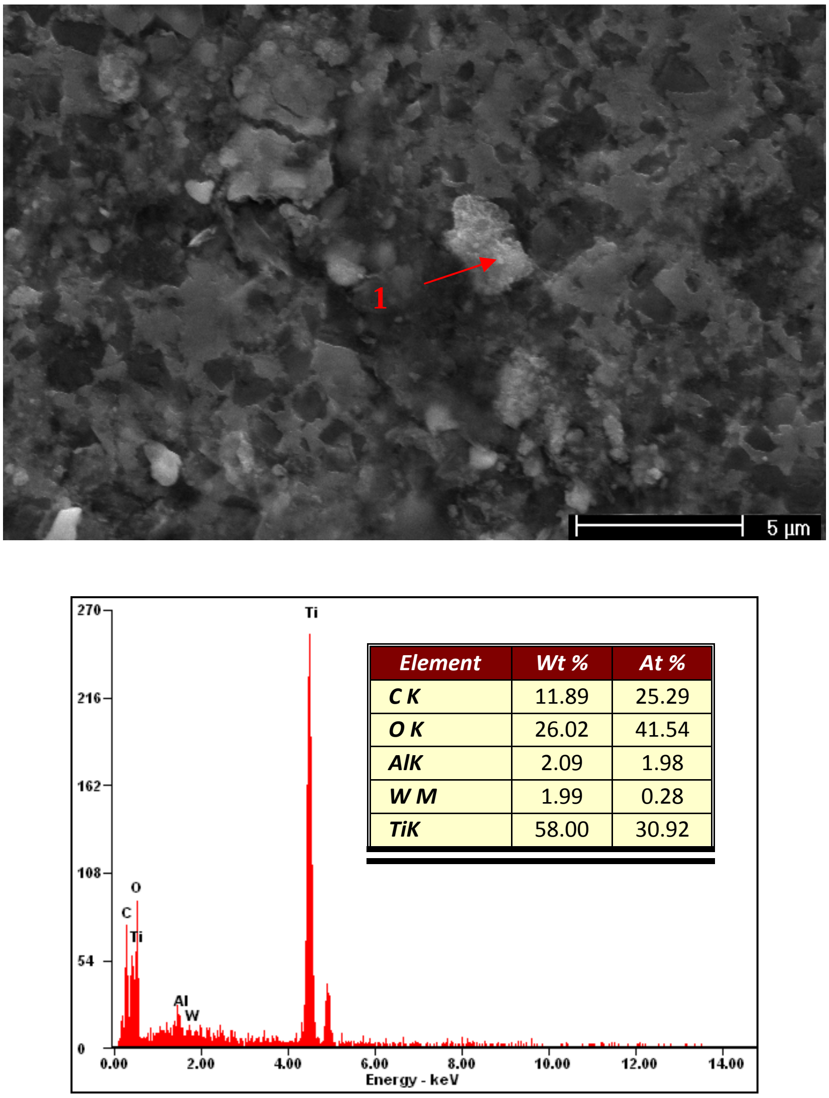

Element	Wt %	At %
C K	11.89	25.29
O K	26.02	41.54
AlK	2.09	1.98
W M	1.99	0.28
TiK	58.00	30.92

Figure 5.74: Morphology of the surface of cBN-TiC cutting tool material after isothermal TGA at 550 °C for 60 min. EDX analysis of the grain indicated (1). SEM, SE image

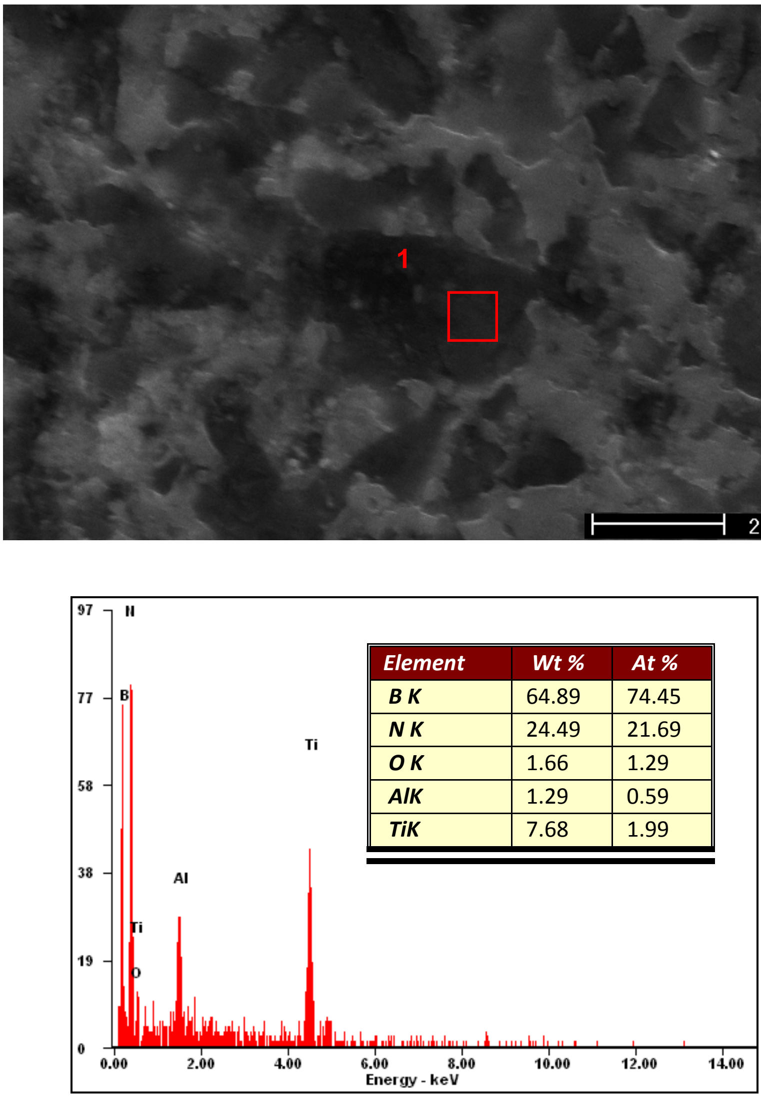

Element	Wt %	At %
B K	64.89	74.45
N K	24.49	21.69
O K	1.66	1.29
AlK	1.29	0.59
TiK	7.68	1.99

Figure 5.75: Morphology of the surface of cBN-TiC cutting tool material after isothermal TGA at 550 °C for 60 min. EDX analysis of cBN grain indicated (1). SEM, SE image

5.6.2.2 Morphology of the oxide scale after isothermal TGA at 900 °C

The sample showed a perceptible change in colour to light yellow with light green nuances compared with the original dark grey colour of the tool material. The results for the morphology investigation revealed that the oxidation at 900 °C produced a layer of oxide on the entire surface of the sample. This oxide layer was mainly of equiaxed grains of titanium oxide (Figures 5.76 and 5.77) with slight indications of aluminium oxide. A few cBN grains were evident on the surface. They disrupted the continuity of the oxide layer (Figure 5.77).

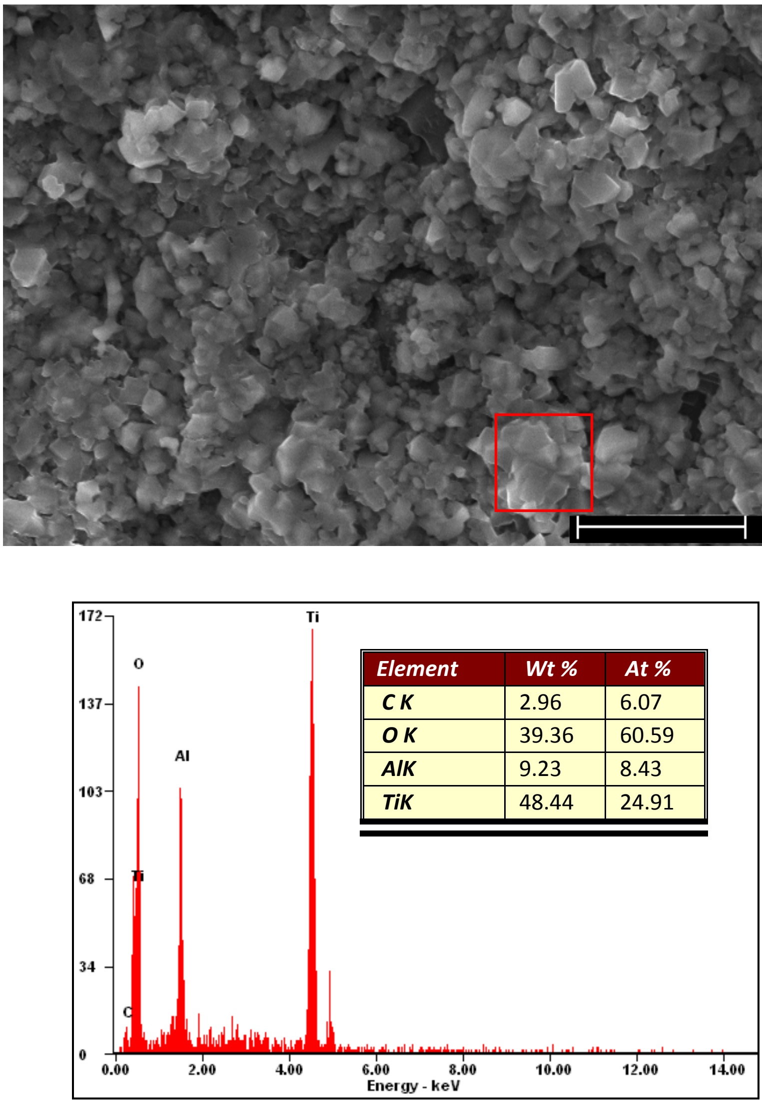

Element	Wt %	At %
C K	2.96	6.07
O K	39.36	60.59
AlK	9.23	8.43
TiK	48.44	24.91

Figure 5.76: Oxide layer on cBN-TiC cutting tool material after isothermal TGA at 900 °C for 60 min. EDX analysis of the selected area. SEM, SE image

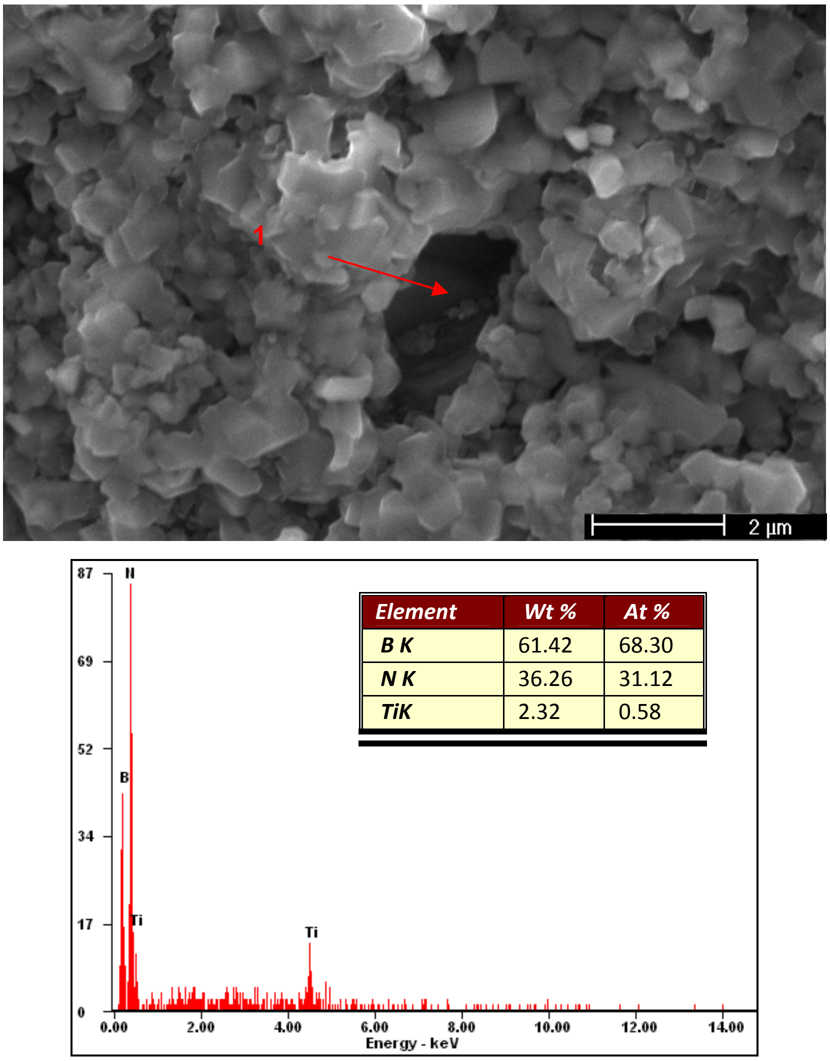

Element	Wt %	At %
B K	61.42	68.30
N K	36.26	31.12
TiK	2.32	0.58

Figure 5.77: Oxide layer on cBN-TiC cutting tool material after isothermal TGA at 900 °C for 60 min. EDX analysis of the cBN grain indicated (1). SEM, SE image

5.6.2.3 Morphology of the oxide scale after isothermal TGA at 1000 °C

The sample turned more yellow than that treated by isothermal TGA at 900 °C, losing more and more the green nuances. As for the isothermal TGA at 900 °C, the results for the morphology investigation revealed that the oxidation of cBN-TiC cutting tool material at 1000 °C produced a significant amount of an oxide constituted mostly of titanium oxide, covering the entire surface of the sample (Figure 5.78). The size of the grains of titanium oxide (Figure 5.78) clearly increased compared to the grain size obtained after isothermal TGA at 900 °C (Figure 5.76). The titanium oxide grains covered the cBN grains almost completely, no noticeable amount of oxygen being detected on the cBN grains that were not covered (Figure 5.79). The increased grain size indicated grain growth of titanium oxide, big grains growing at the expense of small grains (Figure 5.78). The concentration of aluminium oxide appeared quite high in some areas (Figure 5.80).

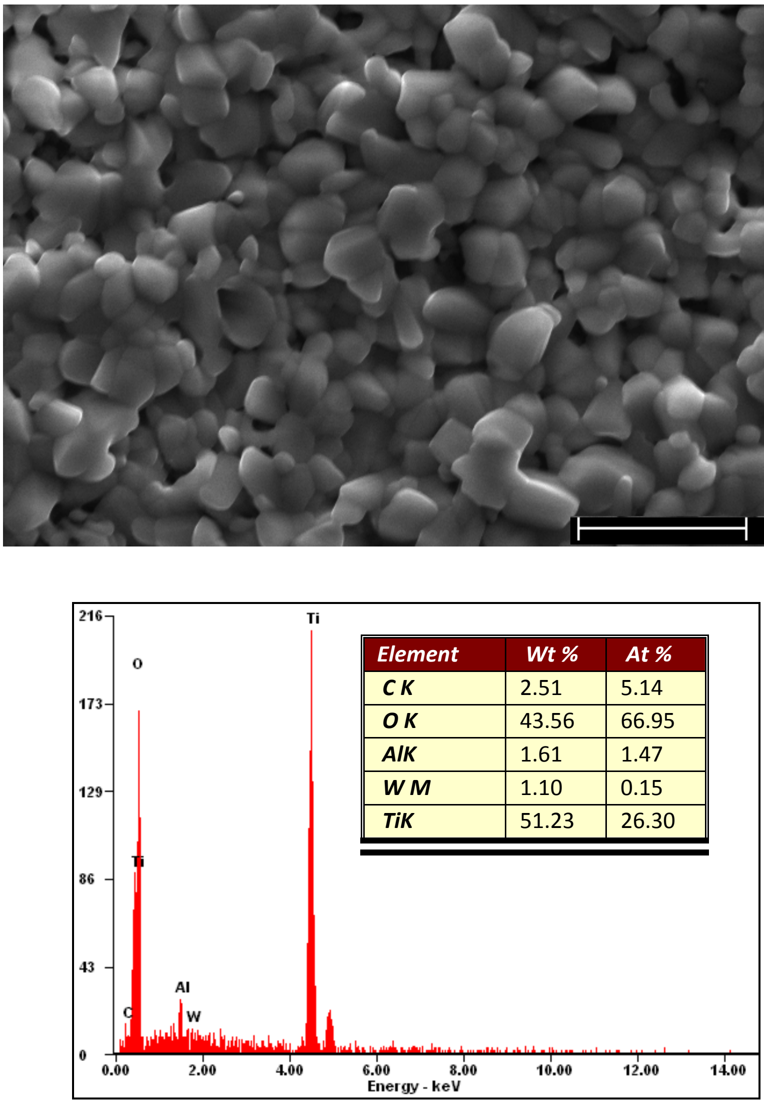

Element	Wt %	At %
C K	2.51	5.14
O K	43.56	66.95
AlK	1.61	1.47
W M	1.10	0.15
TiK	51.23	26.30

Figure 5.78: Oxide layer on cBN-TiC cutting tool material after isothermal TGA at 1000 °C for 60 min. EDX analysis of the image area. SEM, SE image

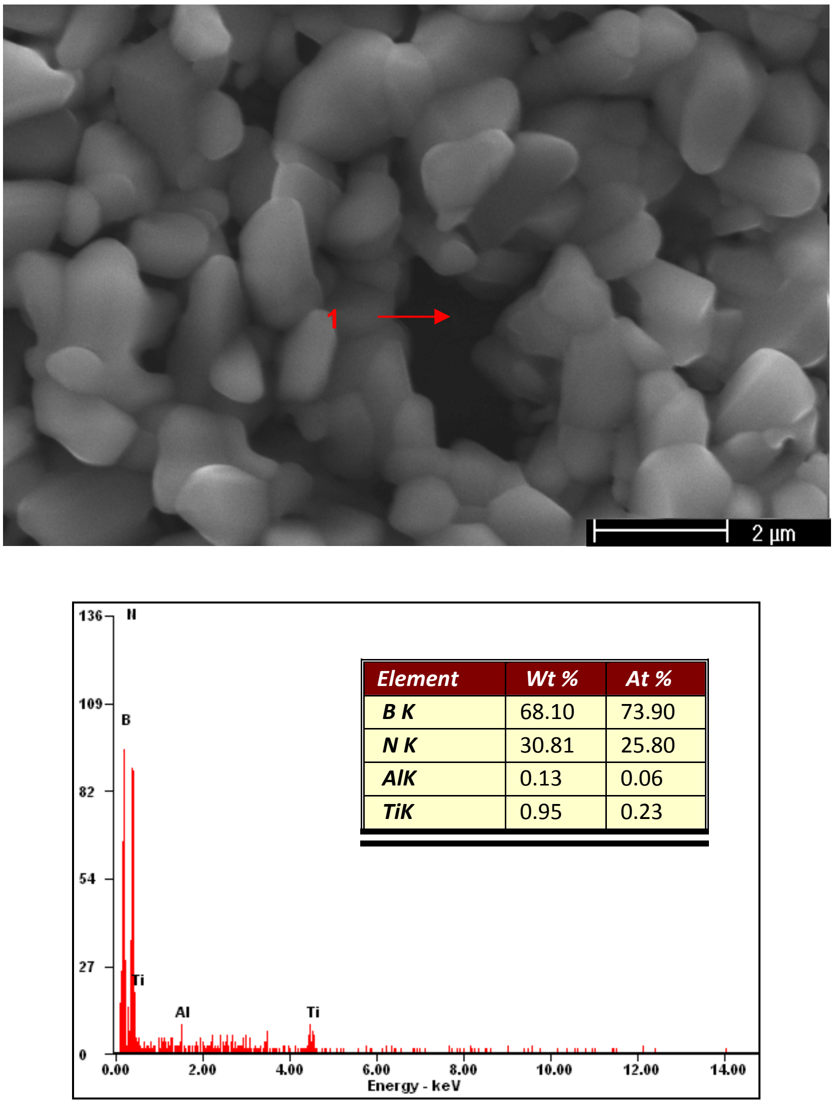

Element	***Wt %***	***At %***
B K	68.10	73.90
N K	30.81	25.80
AlK	0.13	0.06
TiK	0.95	0.23

Figure 5.79: Oxide layer on cBN-TiC cutting tool material after isothermal TGA at 1000 °C for 60 min. EDX analysis of the cBN grain indicated (1). SEM, SE image

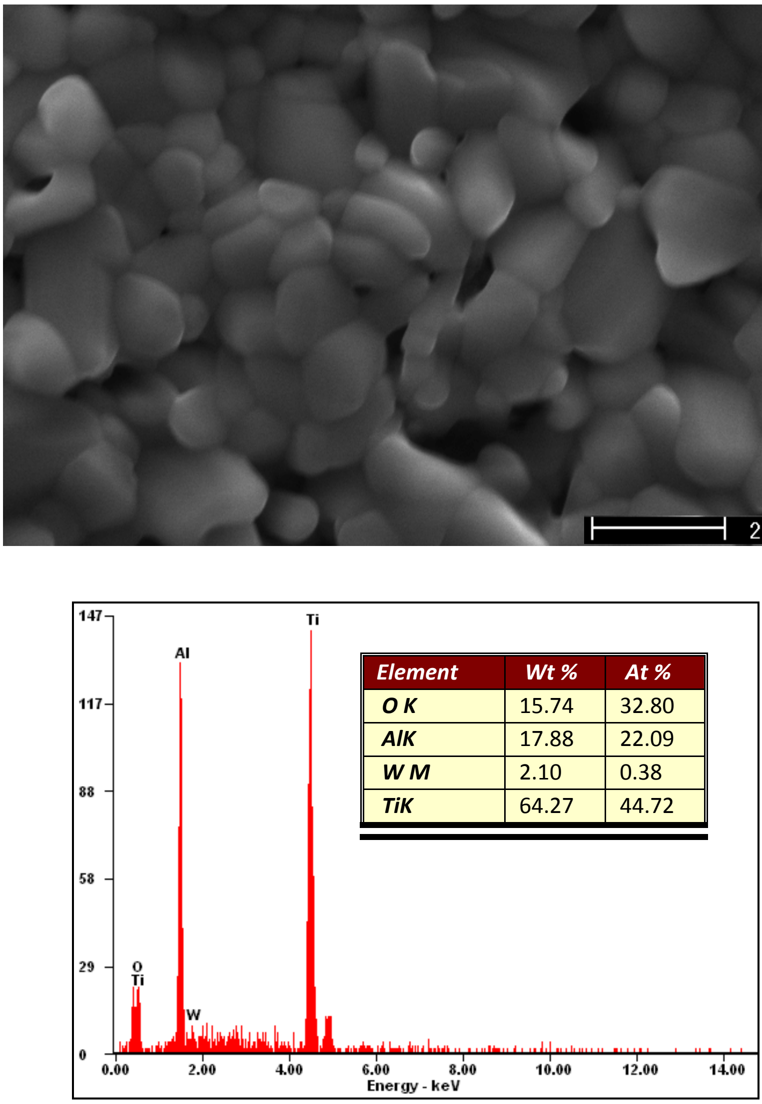

Element	Wt %	At %
O K	15.74	32.80
AlK	17.88	22.09
W M	2.10	0.38
TiK	64.27	44.72

Figure 5.80: Oxide layer on cBN-TiC cutting tool material after isothermal TGA at 1000 °C for 60 min. EDX analysis of the image area. SEM, SE image

5.6.2.4 Morphology of the oxide scale after isothermal TGA at 1100 °C

As far as the sample colour is concerned, it turned more yellow than it appeared after isothermal TGA at 1000 °C, without green nuances. As for the isothermal TGA at 1000 °C, the results of the morphology investigation revealed that the oxidation of cBN-TiC cutting tool material at 1100 °C produced a thicker oxide layer of titanium oxide close to TiO_2 in stoichiometry covering the entire surface of the sample (Figures 5.81 and 5.82).

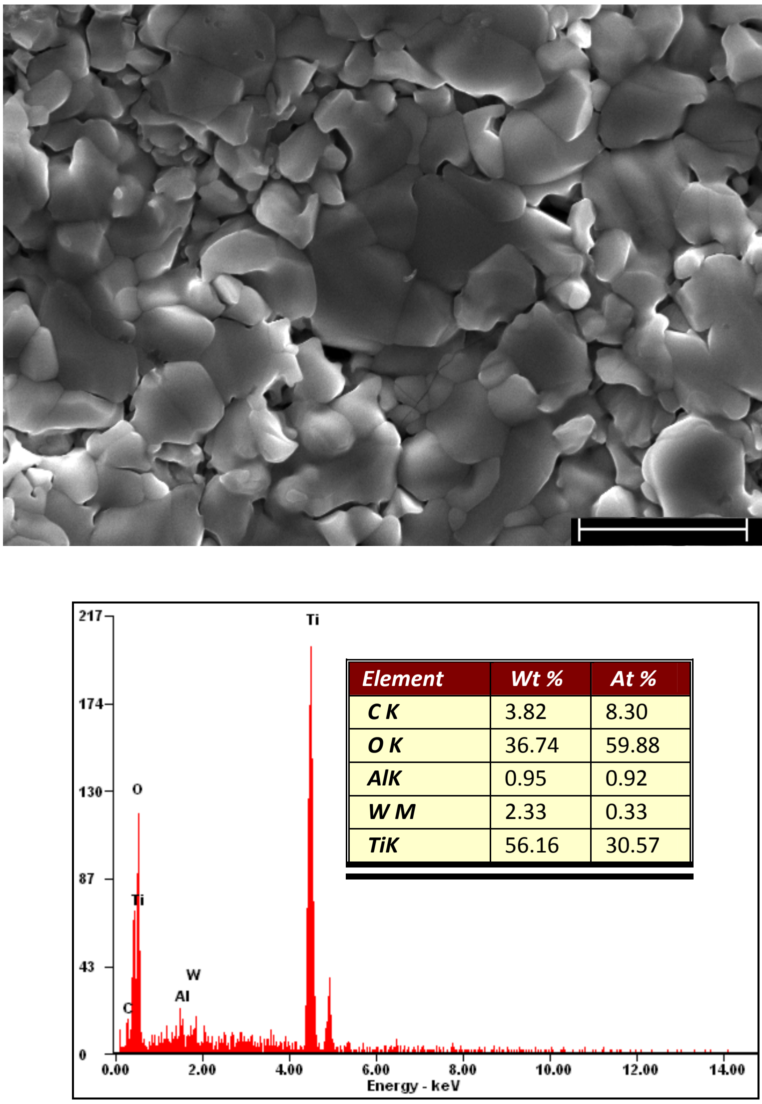

Element	*Wt %*	*At %*
C K	3.82	8.30
O K	36.74	59.88
AlK	0.95	0.92
W M	2.33	0.33
TiK	56.16	30.57

Figure 5.81: Oxide layer on cBN-TiC cutting tool material after isothermal TGA at 1100 °C for 60 min showing the coarsening of grains and grain cracking. EDX analysis of the image area. SEM, SE image

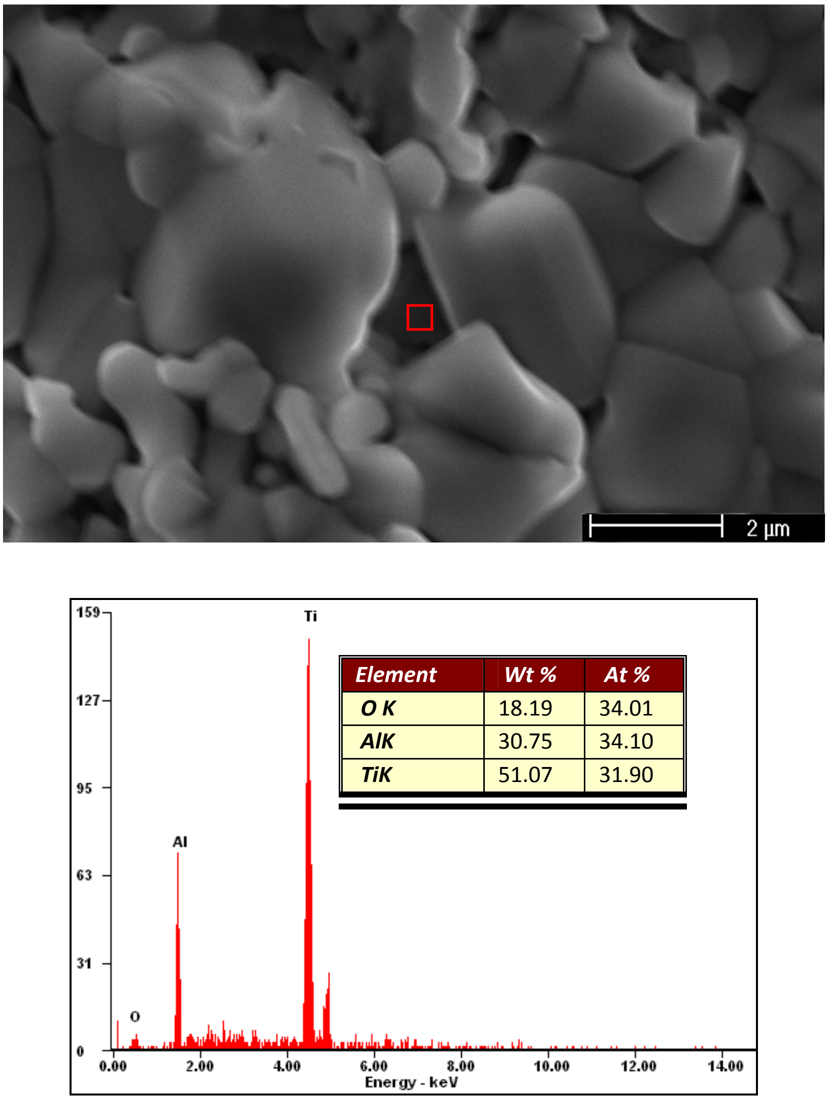

Element	Wt %	At %
O K	18.19	34.01
AlK	30.75	34.10
TiK	51.07	31.90

Figure 5.82: Oxide layer on cBN-TiC cutting tool material after isothermal TGA at 1100 °C for 60 min. EDX analysis of the selected area. SEM, SE image

The size of the grains of titanium oxide clearly increased compared to the grain size obtained after isothermal TGA at 1000 °C (Figures 5.78 and 5.81), covering the cBN grains almost completely. The growth process of the grains of titanium oxide was more evident than it was at 1000 °C (Figure 5.81).

Some cracking appeared in the oxide scale, probably due to either the volume expansion induced by the formation of titanium oxide or thermal stresses generated during cooling (Figure 5.81). Aluminium oxide islands appeared here and there in the titanium oxide scale (Figure 5.82).

5.7 OXIDATION OF CBN-TIC CUTTING TOOL MATERIAL

5.7.1 Microstructure and composition of the oxide scale

5.7.1.1 Isothermal oxidation at 550 °C

The microstructure of the cross-section of a cBN-TiC cutting tool that underwent isothermal oxidation at 550°C during 60 min is shown in Figure 5.83. It revealed neither perceptible outer oxide layer nor a perceptible inner oxygen-affected layer.

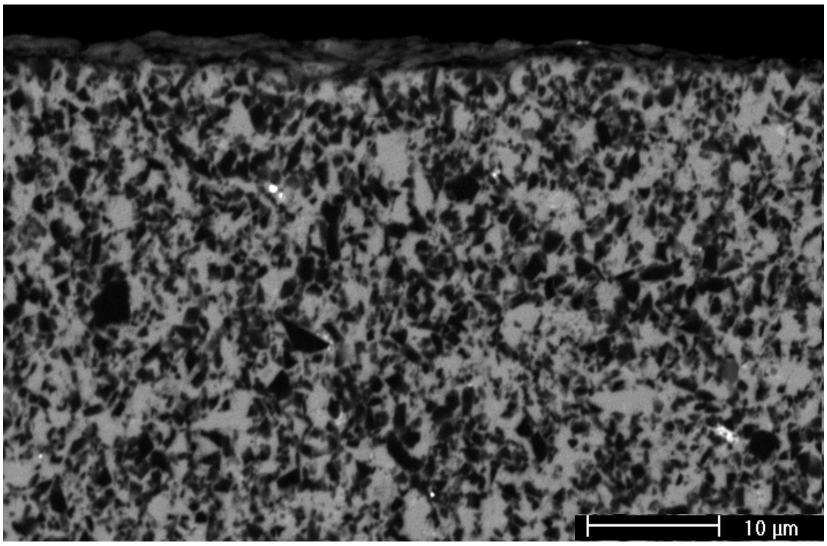

Figure 5.83: Section through a cBN-TiC cutting tool after isothermal oxidation at 550 °C for 60 min. SEM, BSE image

5.7.1.2 Isothermal oxidation at 900 °C

The microstructure of the cross-section of a cBN-TiC cutting tool that underwent isothermal oxidation at 900°C for 60 min is shown in Figure 5.84. It revealed a thin layer of surface scale and an oxygen-affected layer near the surface that contrasted clearly with the substrate. The inner oxygen-affected layer is a zone of internal oxidation. The EDX analyses of the oxygen-affected zone as well as the substrate are shown in Figure 5.84. In the oxygen-affected layer, it appeared that most of the Ti was in form of titanium oxide which contrasted clearly with TiC which appeared in the substrate as a light grey phase. However, the B in the oxygen-affected zone still appeared mainly as BN as was the case in the substrate. The outer scale layer consisted of 2 sub-layers, a white layer at the top corresponding to titanium oxide and a dark grey layer below it corresponding to aluminium oxide. The adherence of the oxygen-affected subscale layer to the substrate was quite good. The corresponding interface appeared quite regular.

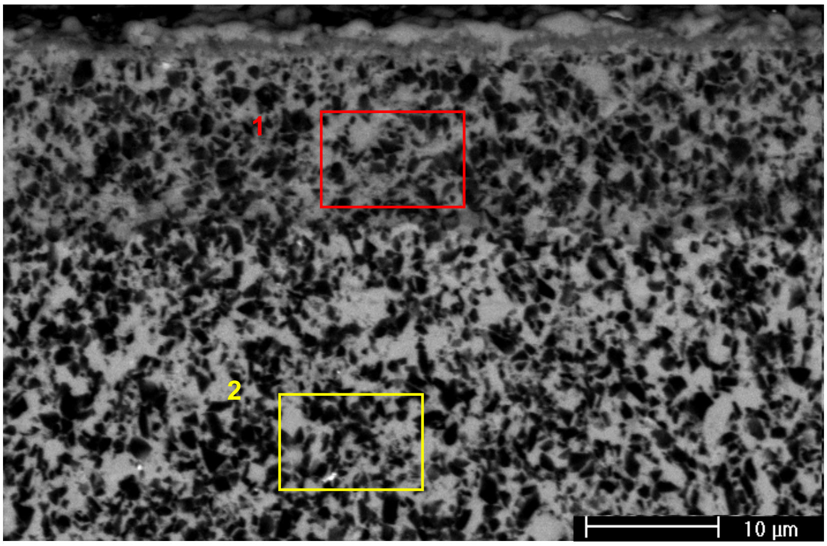

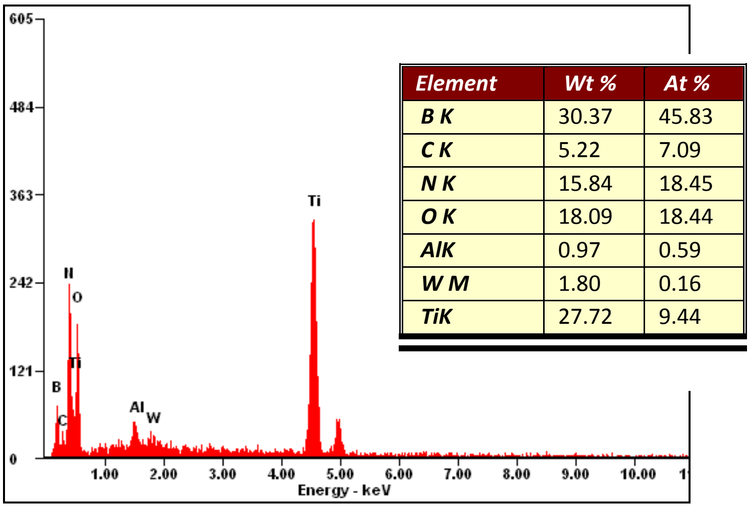

Element	Wt %	At %
B K	30.37	45.83
C K	5.22	7.09
N K	15.84	18.45
O K	18.09	18.44
AlK	0.97	0.59
W M	1.80	0.16
TiK	27.72	9.44

EDX in Area 1

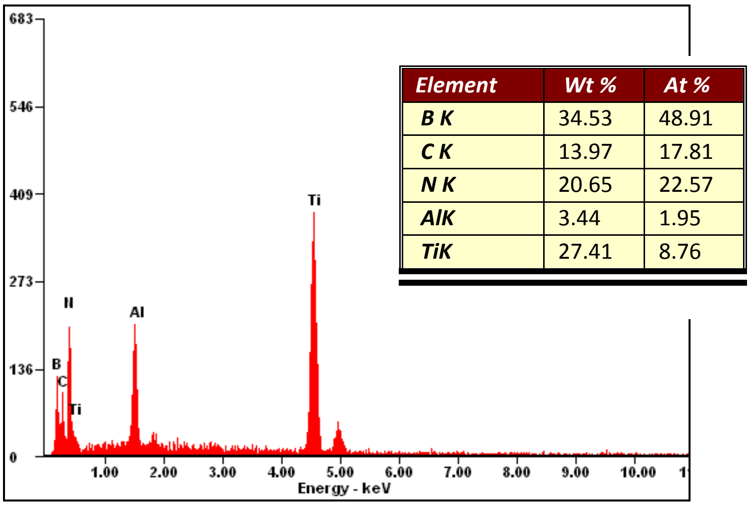

Element	Wt %	At %
B K	34.53	48.91
C K	13.97	17.81
N K	20.65	22.57
AlK	3.44	1.95
TiK	27.41	8.76

EDX in Area 2

Figure 5.84: Section through a cBN-TiC cutting tool after isothermal oxidation at 900 °C for 60 min. EDX analyses of selected areas. SEM, BSE image

5.7.1.3 Isothermal oxidation at 1000 °C

The microstructure of the cross-section of a cBN-TiC cutting tool after isothermal oxidation at 1000°C for 60 min is shown in Figure 5.85. It revealed a surface oxide and an inner oxygen-affected layer that contrasted clearly with the substrate. The inner oxygen-affected layer was due to internal oxidation. The EDX analyses of the oxygen-affected layer as well as the substrate are shown in Figure 5.85. In the inner oxygen-affected layer, it appeared once again that most of the Ti was in the form of titanium oxide which contrasted clearly with TiC which appeared in the substrate as light grey phase. The B in the oxygen-affected layer appeared mainly as boron oxide. The outer scale clearly consisted mainly of grains of titanium oxide (light grey) among which a dispersion of aluminium oxide grains (dark grey) could be easily recognized, particularly at the top of the scale. The substrate appeared to be slightly affected by oxygen (Figure 5.85). Thus, it appeared that when boron oxide formed, it was entrapped in the outer scale layer which consisted mainly of grains of titanium oxide. It can also easily be seen that, the volume fraction of the B-based phase in the substrate decreased in the oxygen-affected layer, indicating then the formation of boron oxide and its evaporation. The layer of titanium oxide grains appeared quite porous. The adherence of the oxygen-affected subscale layer to the substrate was still quite good. The corresponding interface appeared quite regular.

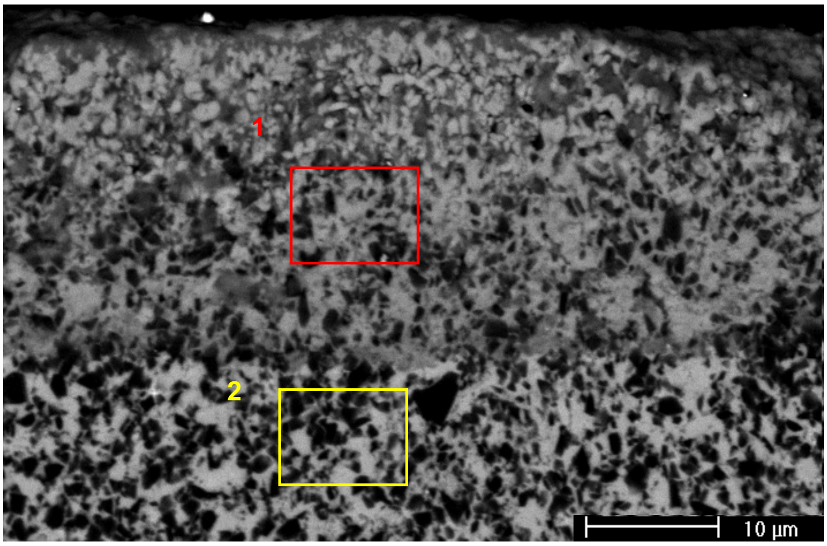

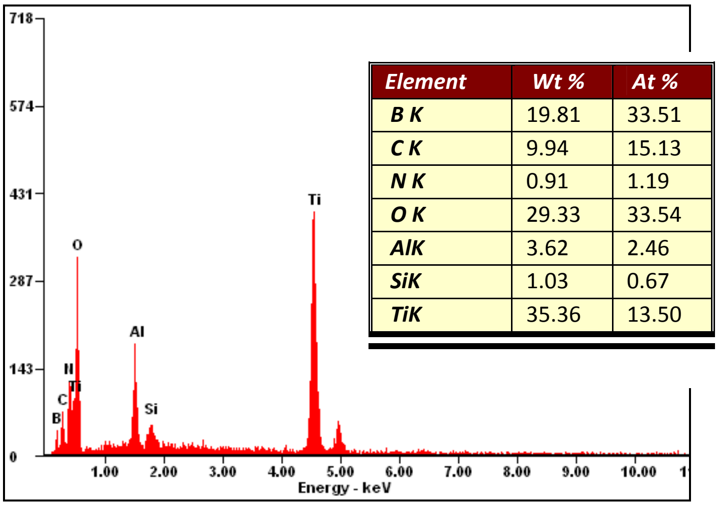

Element	Wt %	At %
B K	19.81	33.51
C K	9.94	15.13
N K	0.91	1.19
O K	29.33	33.54
AlK	3.62	2.46
SiK	1.03	0.67
TiK	35.36	13.50

EDX in Area 1

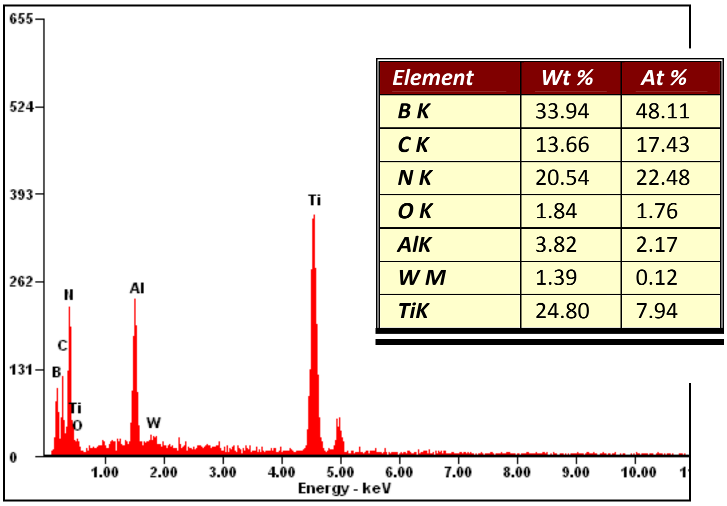

Element	Wt %	At %
B K	33.94	48.11
C K	13.66	17.43
N K	20.54	22.48
O K	1.84	1.76
AlK	3.82	2.17
W M	1.39	0.12
TiK	24.80	7.94

EDX in Area 2

Figure 5.85: Section through a cBN-TiC cutting tool after isothermal oxidation at 1000 °C for 60 min. EDX analyses of selected areas. SEM, BSE image

5.7.1.4 Isothermal oxidation at 1100 °C

The microstructure of the cross-section of a cBN-TiC cutting tool after isothermal oxidation at 1100°C for 60 min is shown in Figure 5.86. It revealed the formation of an oxidation scale composed of an outer scale layer and also an inner oxygen-affected layer that contrasted clearly with the substrate. The outer oxide layer is a zone of external oxidation whereas the inner oxygen-affected layer is a zone of internal oxidation. In the oxygen-affected layer, it appeared once again that most of the Ti is in the form of titanium oxide. The outer scale layer consisted mainly of grains of titanium oxide (light grey), columnar in some areas, below which a particular segregation of aluminium oxide grains (dark grey) became clearly perceptible (Figure 5.86). In some areas, the development of columnar grains of titanium oxide was not preponderant. Instead the outer scale layer showed a preponderant porosity coupled to a preponderant segregation of aluminium oxide (dark grey) (Figure 5.87). Conversely to the substrate, B in the oxygen-affected layer appeared mainly as boron oxide. Thus, it can be understood that when boron oxide formed, it was entrapped in the oxygen-affected layer which consisted mainly of grains of titanium oxide. It can also easily be seen that, with regard to the substrate, the volume fraction of the B-based phase decreased in the oxygen-affected layer, showing then the formation of boron oxide and its evaporation. Indeed, as already mentioned, it can be seen that the outer scale layer of titanium oxide grains appeared quite porous in some areas (Figure 5.87).

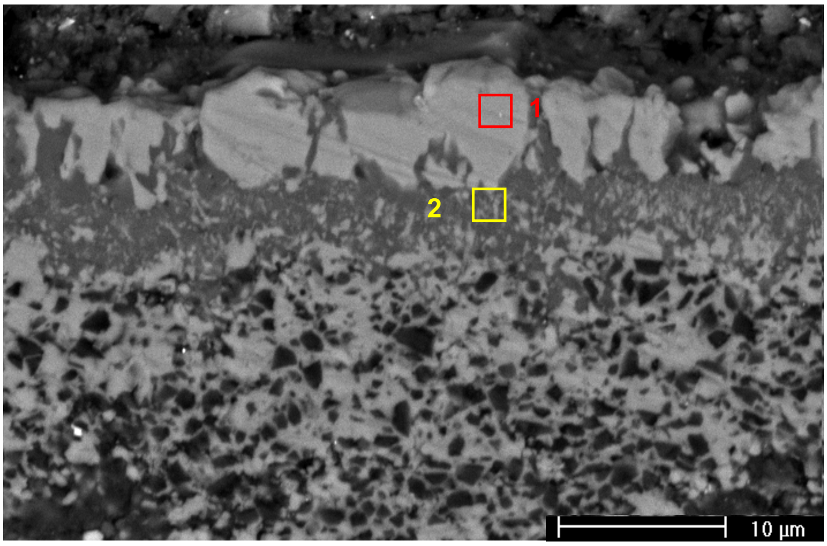

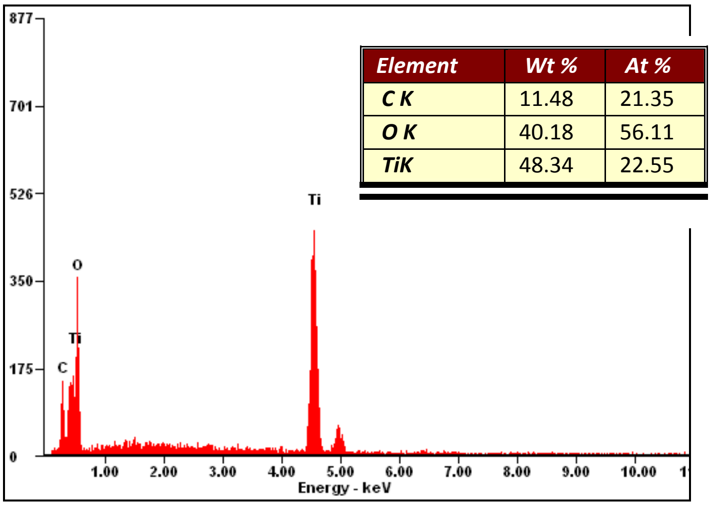

Element	*Wt %*	*At %*
C K	11.48	21.35
O K	40.18	56.11
TiK	48.34	22.55

EDX in Area 1

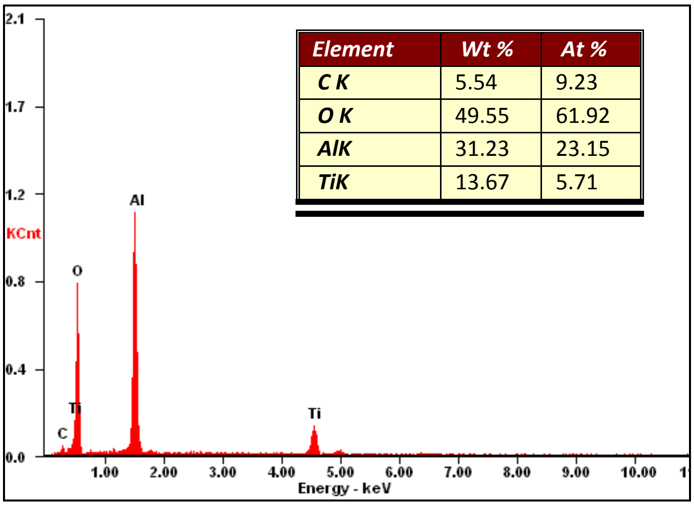

Element	*Wt %*	*At %*
C K	5.54	9.23
O K	49.55	61.92
AlK	31.23	23.15
TiK	13.67	5.71

EDX in Area 2

Figure 5.86: Section through a cBN-TiC cutting tool after isothermal oxidation at 1100 °C for 60 min. EDX of selected areas. SEM, BSE image

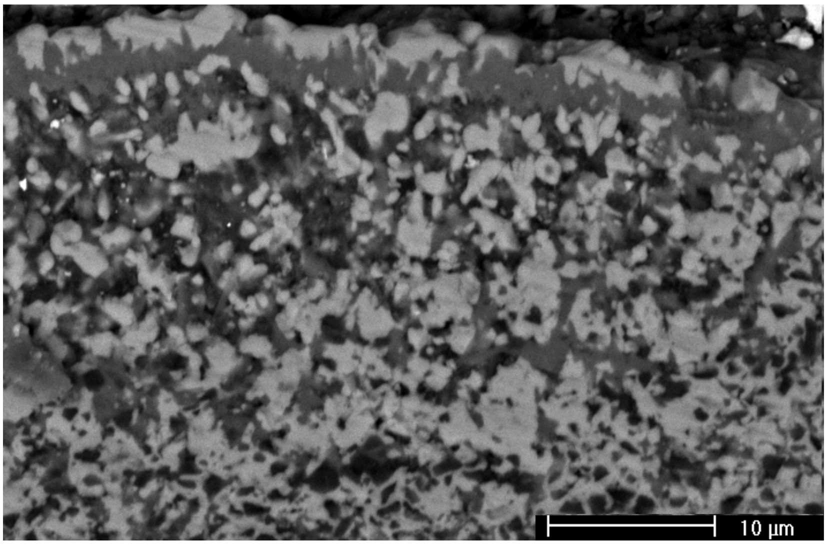

Figure 5.87: Section through a cBN-TiC cutting tool after isothermal oxidation at 1100 °C for 60 min. SEM, BSE image

The adherence of the oxygen-affected subscale layer to the substrate was poor. Indeed, in some areas, the flaking of the inner oxygen-affected layer off the substrate was evidenced by cracking at the interface

5.7.2 XRD of the oxide scale

XRD analyses of the oxide layer formed on cBN-TiC cutting tool after isothermal oxidation at 1000 °C for 60 min are shown in Figures 5.88 and 5.89. These analyses revealed the formation of TiO_2 and Al_2O_3 as major phases, as well as the formation of B_2O_3 that remained entrapped in the oxide scale in some areas but not in others. The absence of B_2O_3 in the X-ray diffractograms might indicate that either B_2O_3 formed in some areas and was amorphous or that it formed and evaporated. Whereas these XRD results still revealed the presence of cBN in the oxide scale, they did not reveal any TiC or TiB_2, thus indicating the preferential and complete oxidation of TiC and TiB_2. Finally, these XRD results also revealed that reaction between TiO_2 and B_2O_3 was not likely to take place below 1000 °C.

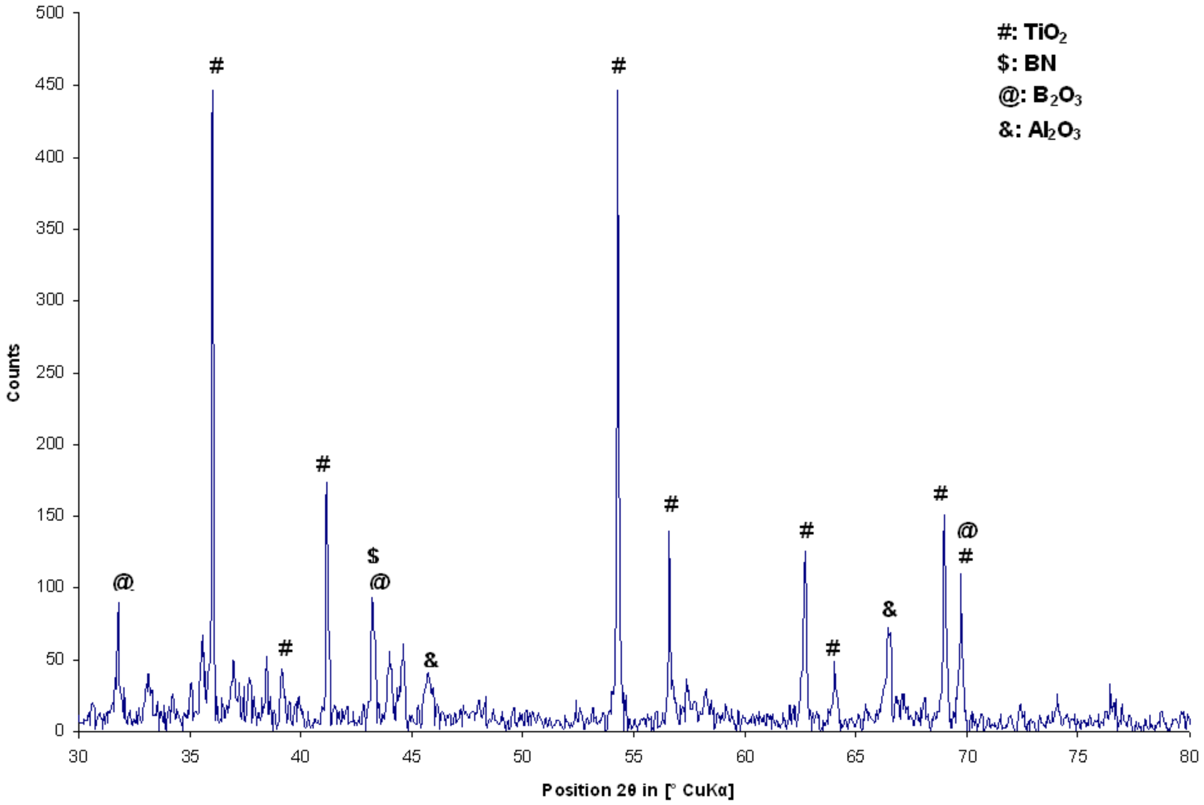

Figure 5.88: X-ray diffractogram of the oxide layer formed on cBN-TiC cutting tool material after isothermal oxidation at 1000 °C for 60 min, using CuK_{α} radiation. Analysis 1

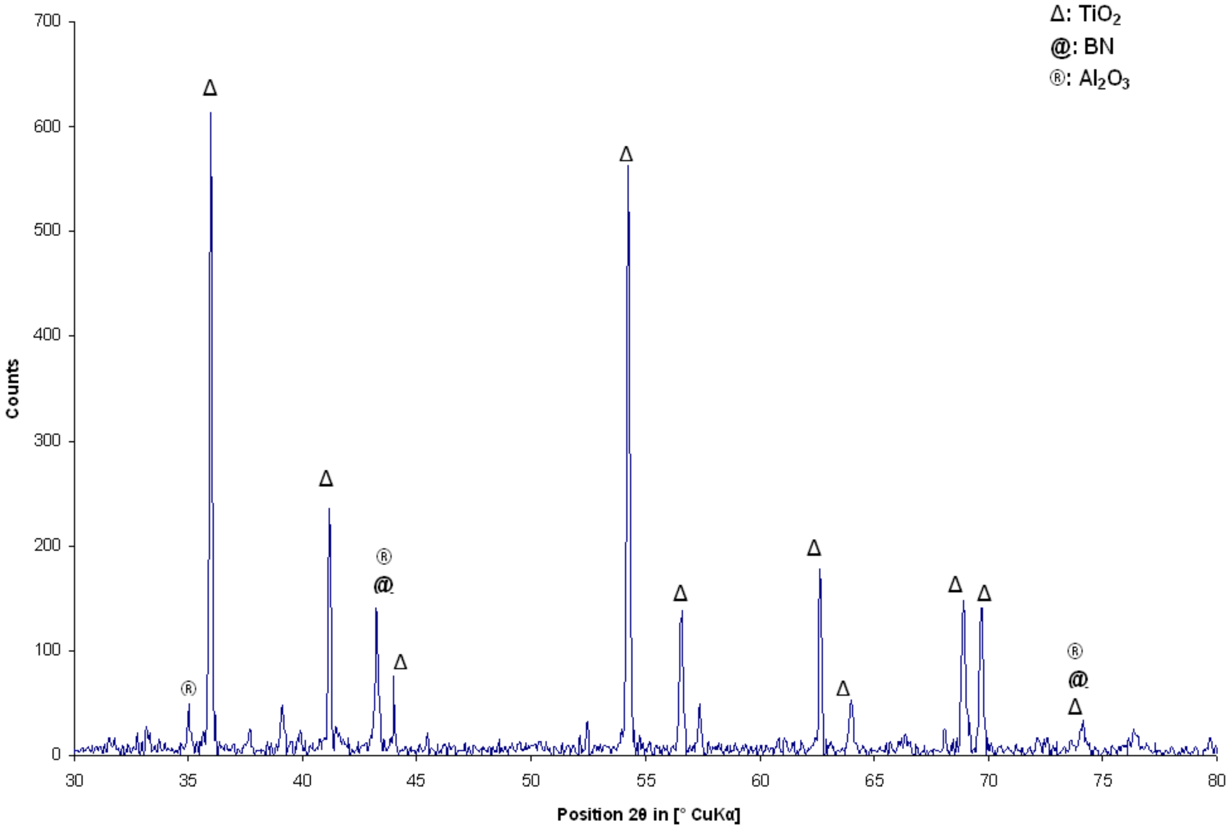

Figure 5.89: X-ray diffractogram of the oxide layer formed on cBN-TiC cutting tool material after isothermal oxidation at 1000 °C for 60 min, using CuK_{α} radiation. Analysis 2

5.7.3 Thickness of the scale layer

The thickness of the scale layer formed on cBN-TiC cutting tool after isothermal oxidation for 60 min, and corresponding to the thickness of the outer scale layer and the inner oxygen-affected layer put together, i.e. external oxidation and internal oxidation, is showed in Figure 5.90.

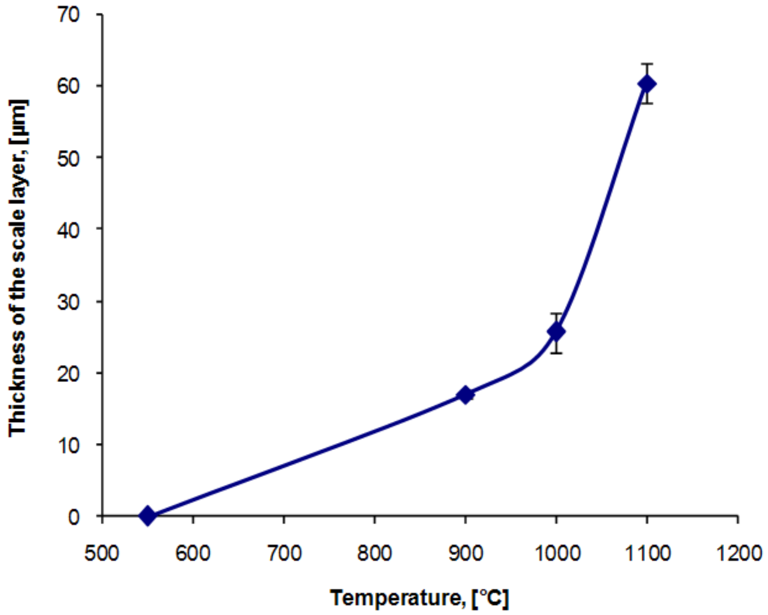

Figure 5.90: Thickness of the scale layer formed on cBN-TiC cutting tool after isothermal oxidation for 60 min at different temperatures

Such a variation of the thickness of the scale layer with regards to the temperature is indicative of the oxidation kinetics. Figure 5.90 shows that the oxidation of cBN-TiC cutting tools is thermally activated. It also shows that no state of passivation was reached. In other words, the oxidation scale formed on the surface of the cBN-TiC cutting tool was not compact, i.e. it was not impermeable to the inward diffusion of O_2.

5.8 STATIC INTERACTION COUPLES

5.8.1 ADI/cBN-TiC/ADI static interaction couples

Under the load applied, the cBN-TiC cutting tool insert receded into the relatively soft ASTM Grade 2 ADI samples, which made contact with the profiles of the cutting insert very efficient as required for diffusion tests.

The microstructure of the interface of the ADI/cBN-TiC/ADI static interaction couple after diffusion annealing at 1100 °C for 60 min appeared on the cross-section shown in Figure 5.91.

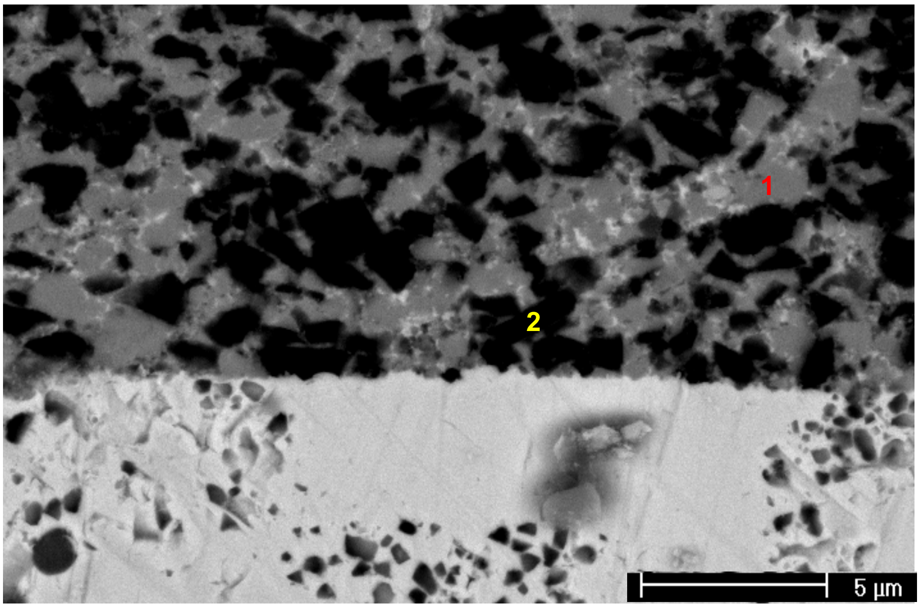

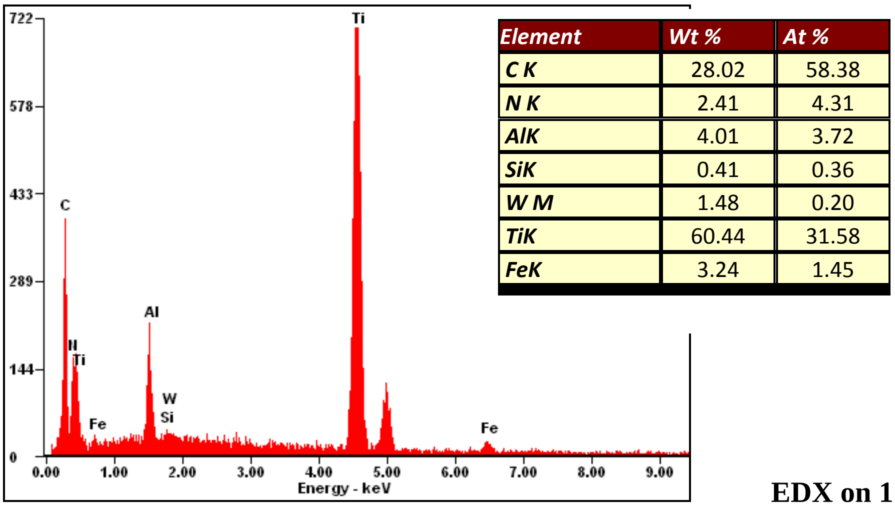

Element	Wt %	At %
C K	28.02	58.38
N K	2.41	4.31
AlK	4.01	3.72
SiK	0.41	0.36
W M	1.48	0.20
TiK	60.44	31.58
FeK	3.24	1.45

EDX on 1

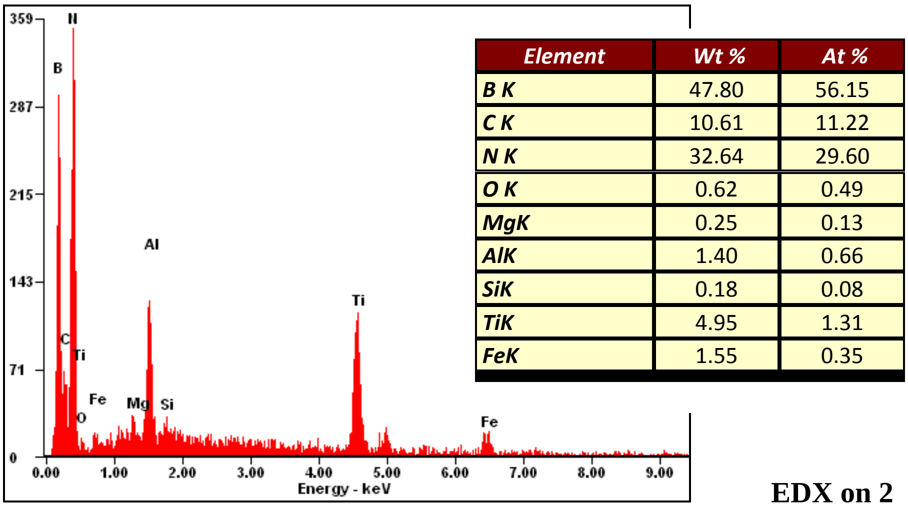

Element	Wt %	At %
B K	47.80	56.15
C K	10.61	11.22
N K	32.64	29.60
O K	0.62	0.49
MgK	0.25	0.13
AlK	1.40	0.66
SiK	0.18	0.08
TiK	4.95	1.31
FeK	1.55	0.35

EDX on 2

Figure 5.91: Cross-section of the ADI/cBN-TiC/ADI static interaction couple after isothermal annealing at 1100 °C for 60 min. EDX of the selected areas. SEM, BSE image

EDX analysis on a TiC grain close to the interface (Area 1) revealed the presence of Fe and Si, whereas EDX analysis in a cBN grain also close to the interface (Area 2) revealed the slight presence of Fe and Si (Figure 5.91). A high-magnification image of an area of the cBN-TiC cutting tool material close to the interface showed quite clearly the reprecipitation of Fe in the TiC phase (Figure 5.92).

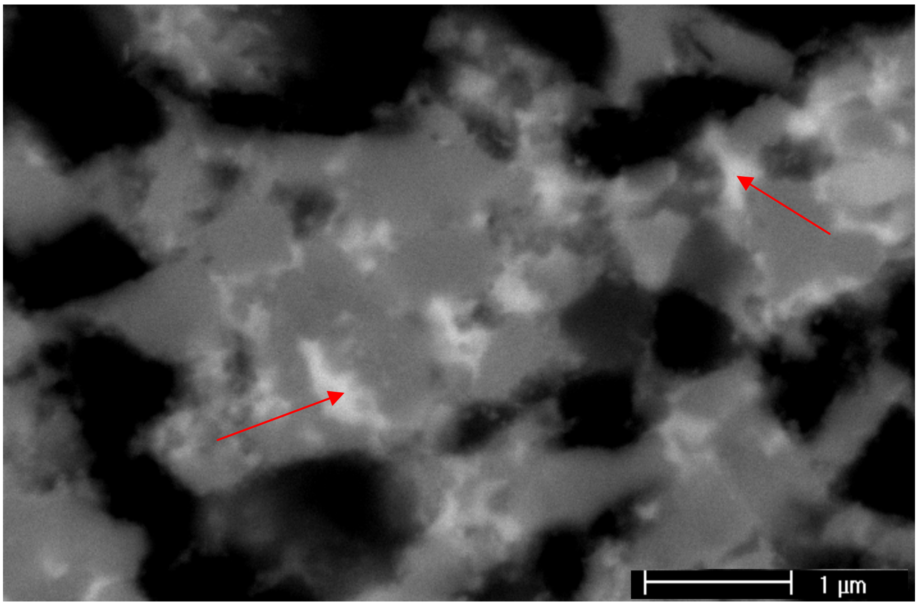

Figure 5.92: Cross-section of the ADI/cBN-TiC/ADI static interaction couple after isothermal annealing at 1100 °C for 60 min showing an area of the cBN-TiC cutting tool material close to the interface. SEM, BSE image

This reprecipitation of Fe in the TiC phase occurred because the solid solubility of Fe in TiC at equilibrium is very small at ambient temperature (< 1 at% Fe) whereas it is quite substantial at 1000 °C (23 at% Fe) (174). Fe atoms would diffuse in the TiC probably through the short-circuits of diffusion and also through the TiC lattice where they could substitute for Ti atoms (175,176). The nucleation and precipitation of Fe-grains in the TiC would occur probably at the same defects that function as short-circuits of diffusion.

Figure 5.93 shows another area of the interface of the ADI/cBN-TiC/ADI static interaction couple that reveals a preferential diffusion bonding of ADI to the TiC binder.

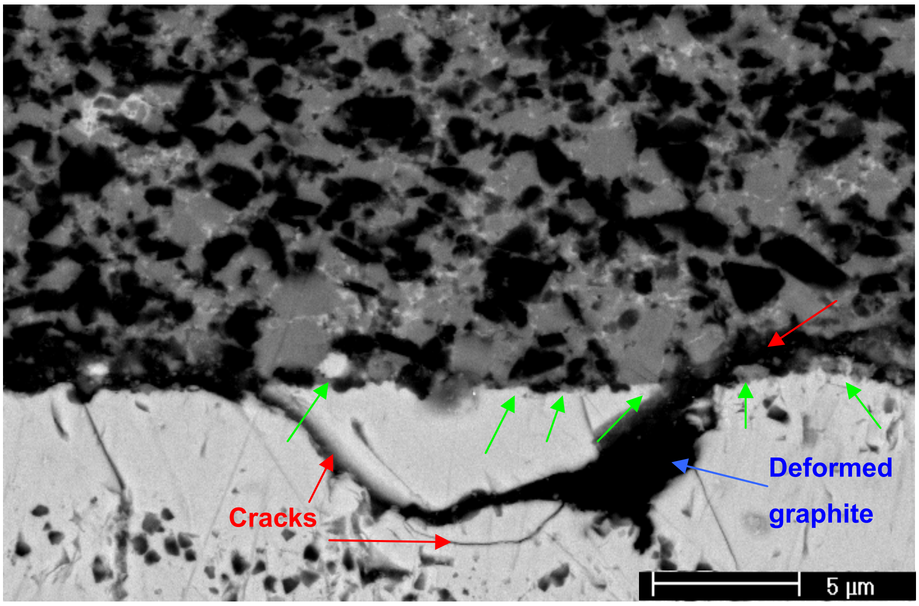

Figure 5.93: Cross-section of the ADI/cBN-TiC/ADI static interaction couple after isothermal annealing at 1100 °C for 60 min showing preferential bonding of ADI to TiC binder. SEM, BSE image

High magnification images of the interface are shown in Figures 5.94 to 5.96. EDX analyses on specific areas on the respective regions were indeed indicative of diffusion of Fe in TiC and Ti in ADI as well as an indication of interaction between cBN and Fe.

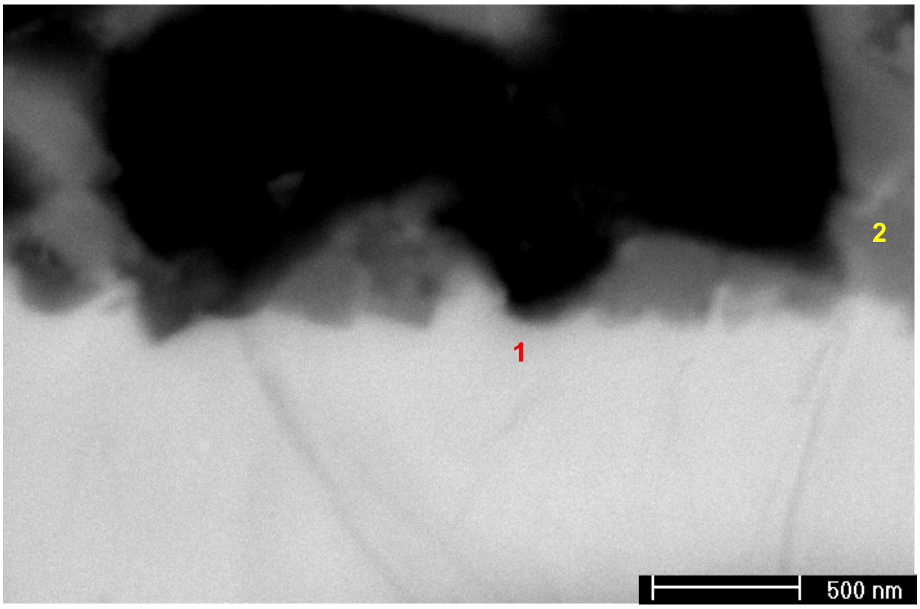

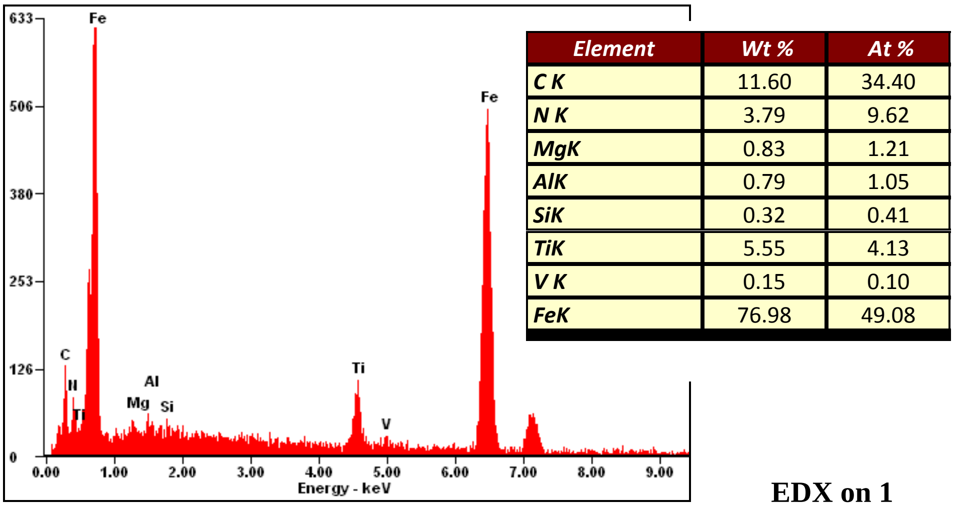

Element	Wt %	At %
C K	11.60	34.40
N K	3.79	9.62
MgK	0.83	1.21
AlK	0.79	1.05
SiK	0.32	0.41
TiK	5.55	4.13
V K	0.15	0.10
FeK	76.98	49.08

EDX on 1

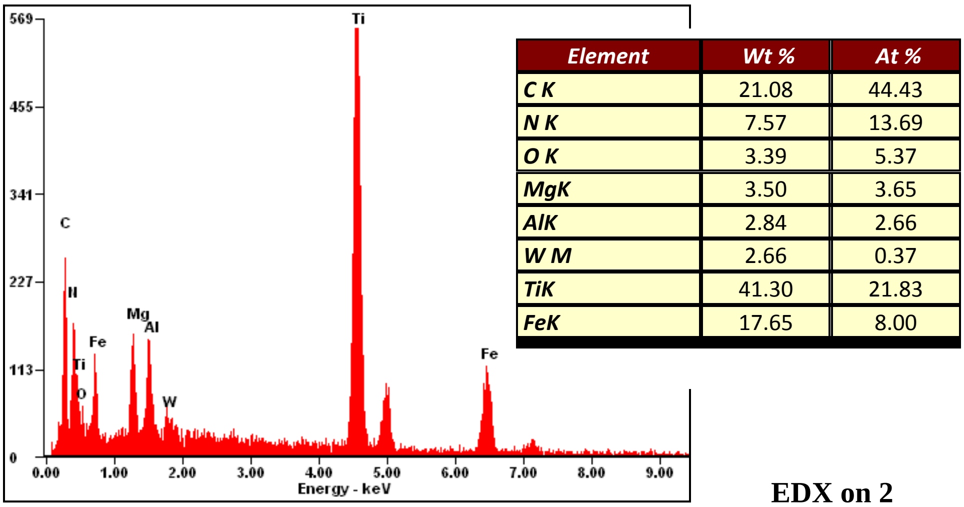

Element	Wt %	At %
C K	21.08	44.43
N K	7.57	13.69
O K	3.39	5.37
MgK	3.50	3.65
AlK	2.84	2.66
W M	2.66	0.37
TiK	41.30	21.83
FeK	17.65	8.00

EDX on 2

Figure 5.94: Cross-section of the ADI/cBN-TiC/ADI static interaction couple after isothermal annealing at 1100 °C for 60 min. EDX of the selected areas. SEM, BSE image

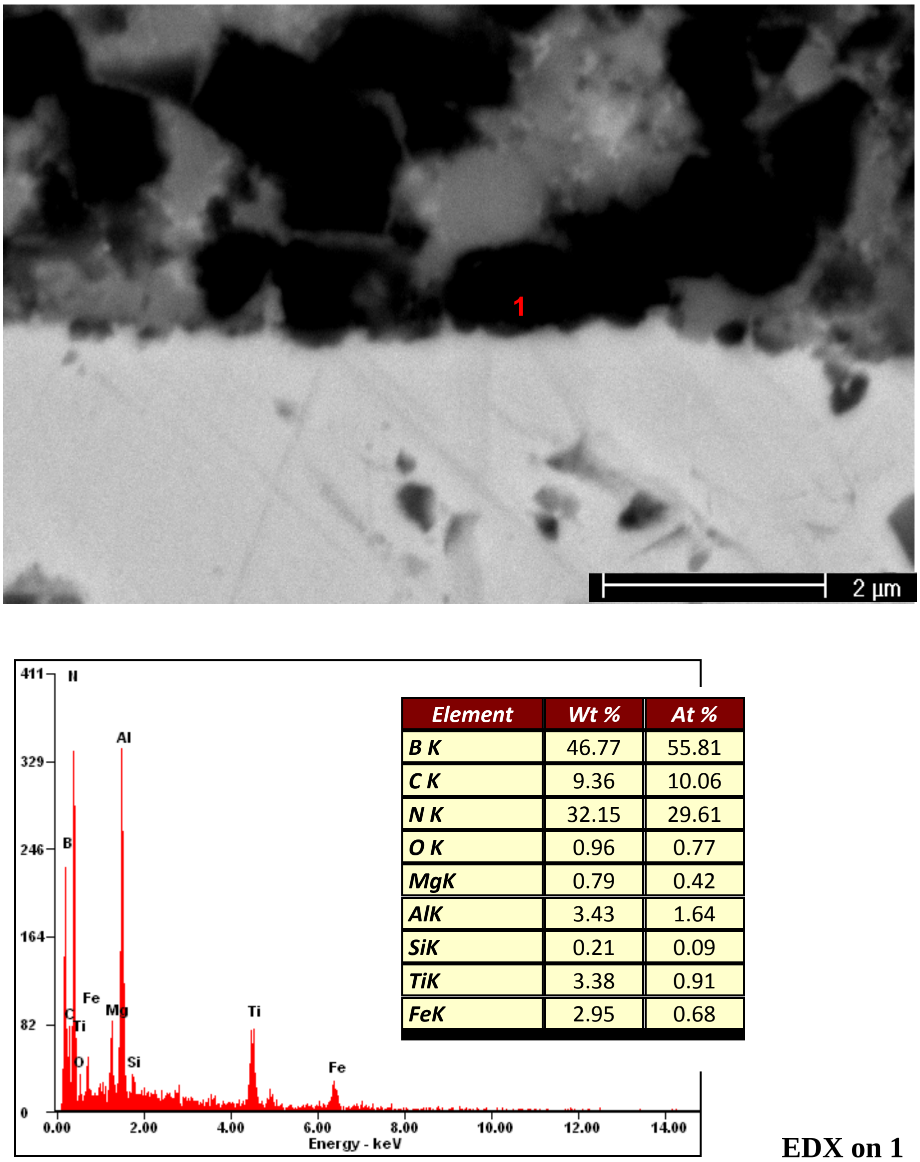

Element	Wt %	At %
B K	46.77	55.81
C K	9.36	10.06
N K	32.15	29.61
O K	0.96	0.77
MgK	0.79	0.42
AlK	3.43	1.64
SiK	0.21	0.09
TiK	3.38	0.91
FeK	2.95	0.68

EDX on 1

Figure 5.95: Cross-section of the ADI/cBN-TiC/ADI static interaction couple after isothermal annealing at 1100 °C for 60 min. EDX of the selected area. SEM, BSE image

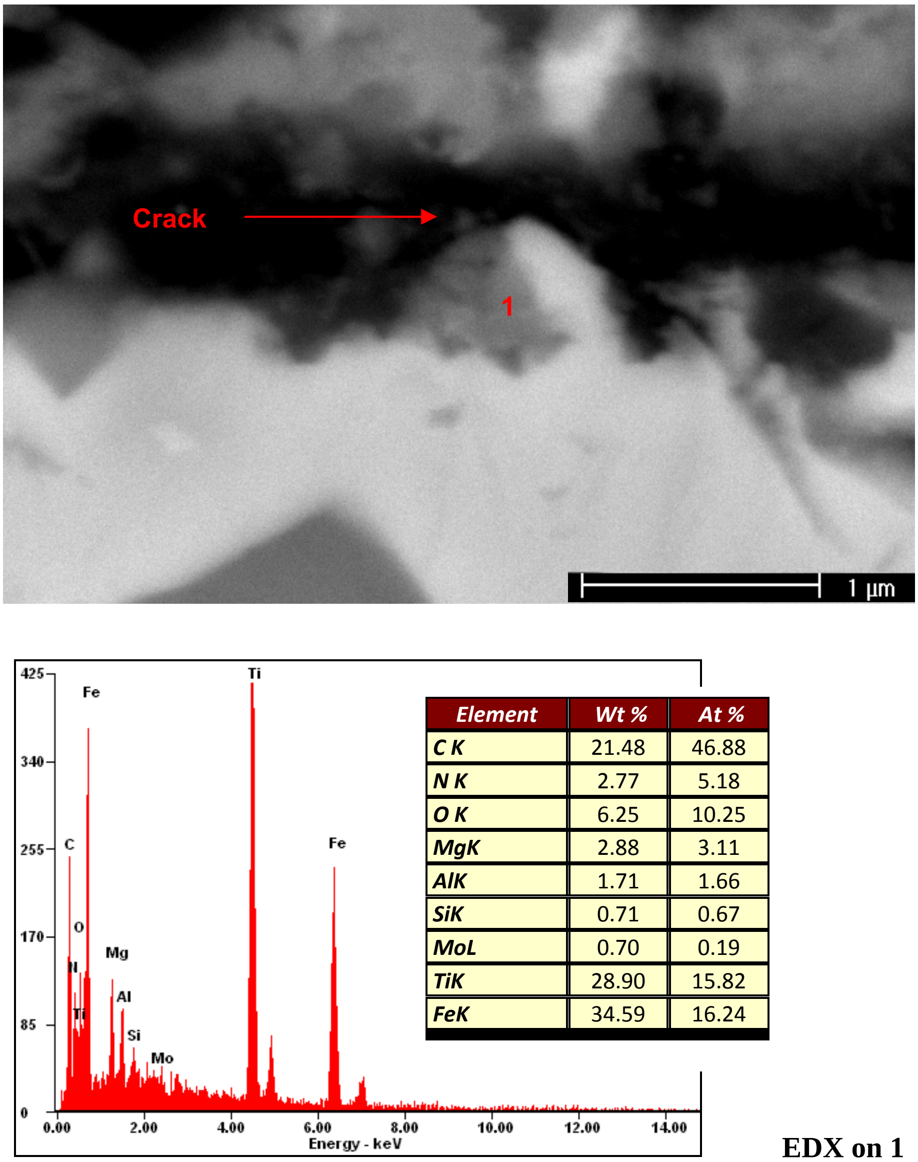

Element	Wt %	At %
C K	21.48	46.88
N K	2.77	5.18
O K	6.25	10.25
MgK	2.88	3.11
AlK	1.71	1.66
SiK	0.71	0.67
MoL	0.70	0.19
TiK	28.90	15.82
FeK	34.59	16.24

EDX on 1

Figure 5.96: Cross-section of the ADI/cBN-TiC/ADI static interaction couple after isothermal annealing at 1100 °C for 60 min. EDX of the selected area. SEM, BSE image

The evidence of the diffusion of Ti and N in ADI is also given in Figures 5.97 and 5.98 which represent other areas of the interface of the ADI/cBN-TiC/ADI static interaction couple. The ADI side of the interface appeared decorated with a Ti-C-N rich phase as well as a Fe-C rich phase. Indeed, EDX analyses in Figure 5.97 (Areas 2 and 3) as well as Figure 5.98 (Area 1) gave evidence of the reprecipitation of polyhedral compounds quite close to Ti(C,N) in stoichiometry. EDX analyses in Figure 5.97 (Area 1) showed evidence of the precipitation of iron carbide close to Fe_3C in stoichiometry in ADI near the interface.

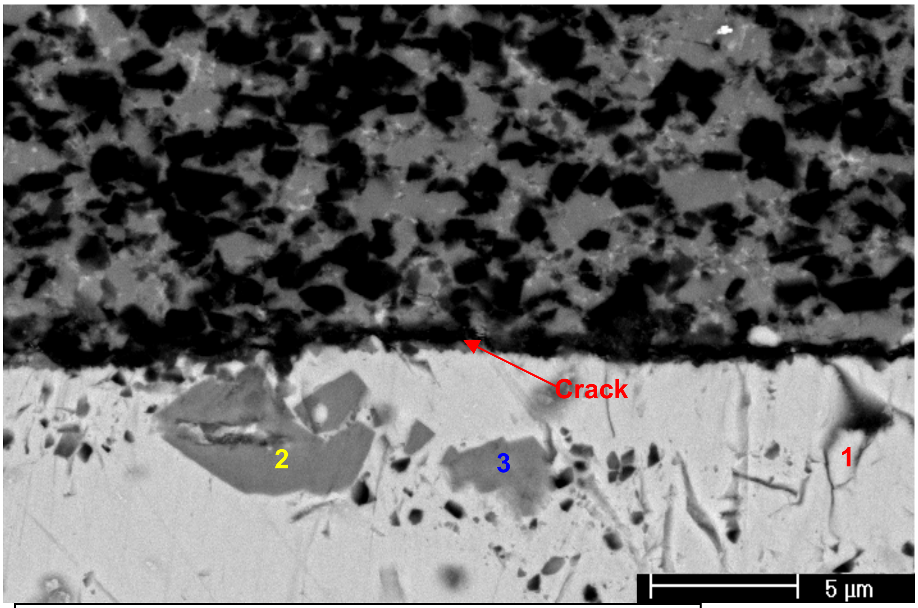

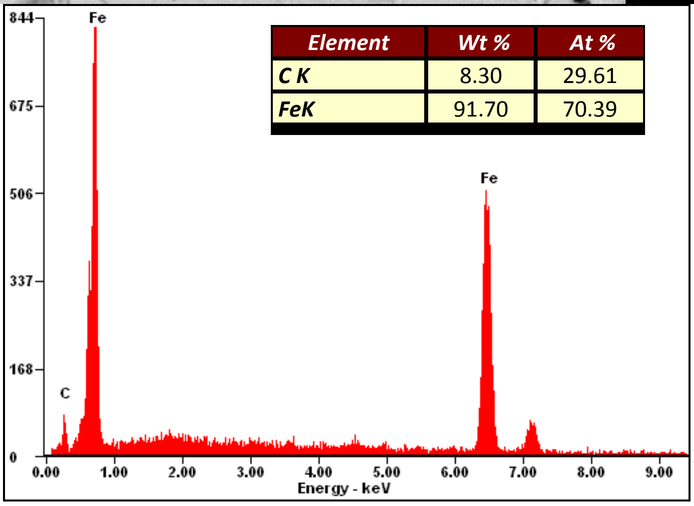

Element	Wt %	At %
C K	8.30	29.61
FeK	91.70	70.39

EDX on 1

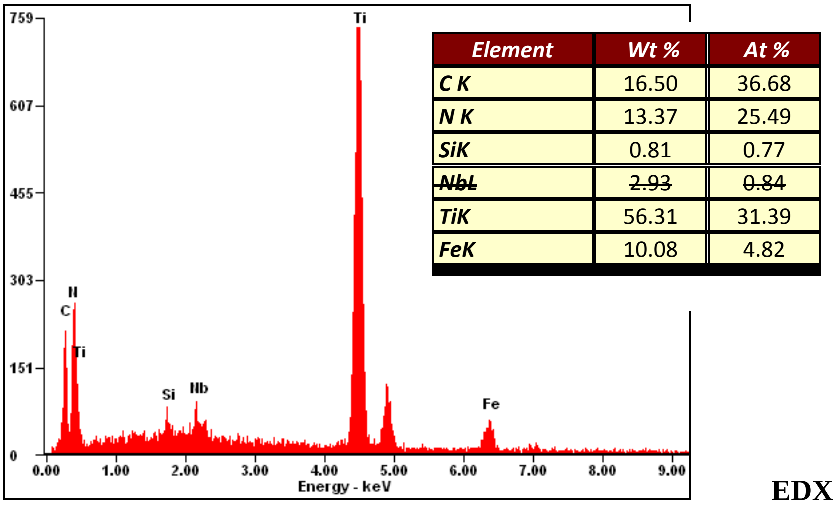

Element	Wt %	At %
C K	16.50	36.68
N K	13.37	25.49
SiK	0.81	0.77
~~NbL~~	~~2.93~~	~~0.84~~
TiK	56.31	31.39
FeK	10.08	4.82

EDX on 2

Figure 5.97: Cross-section of the ADI/cBN-TiC/ADI static interaction couples after isothermal annealing at 1100 °C for 60 min. EDX of the selected areas. SEM, BSE image

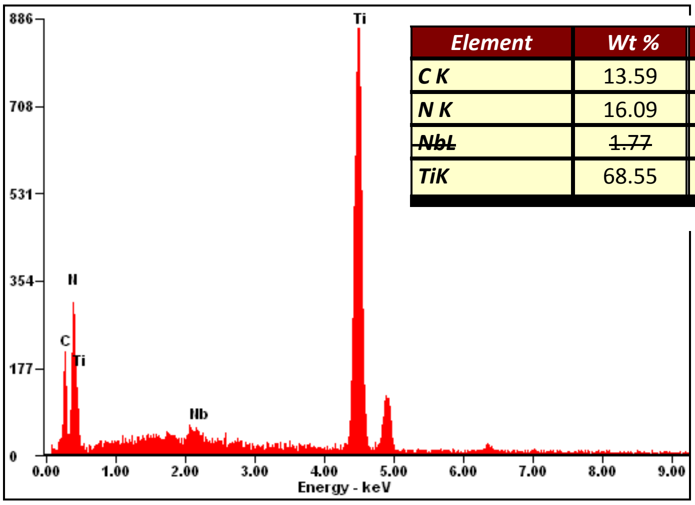

Element	Wt %	At %
C K	13.59	30.33
N K	16.09	30.80
~~NbL~~	~~1.77~~	~~0.51~~
TiK	68.55	38.36

EDX on 3

Figure 5.97 (Continued)

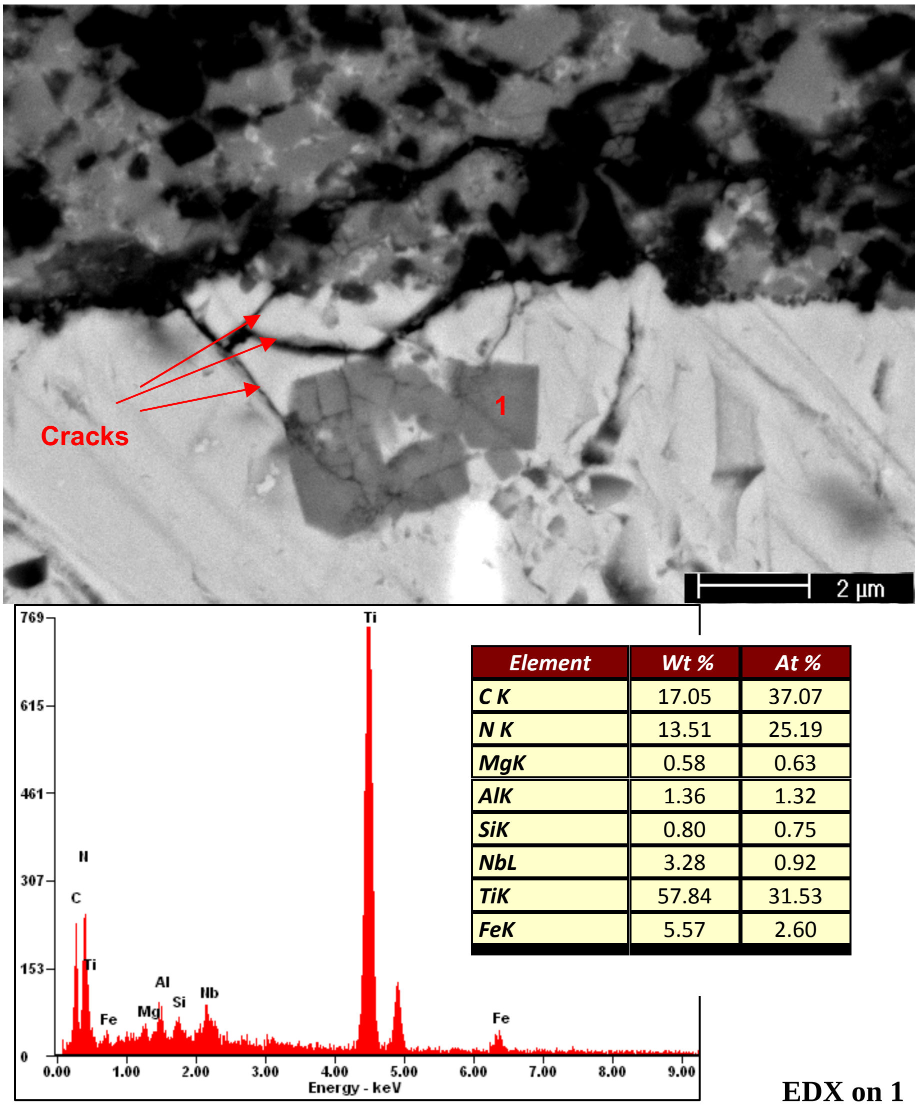

Element	Wt %	At %
C K	17.05	37.07
N K	13.51	25.19
MgK	0.58	0.63
AlK	1.36	1.32
SiK	0.80	0.75
NbL	3.28	0.92
TiK	57.84	31.53
FeK	5.57	2.60

EDX on 1

Figure 5.98: Cross-section of the ADI/cBN-TiC/ADI static interaction couples after isothermal annealing at 1100 °C for 60 min. EDX of the selected area. SEM, BSE image

In some areas cracking running close to the interface appeared, either on the cBN-TiC side (Figures 5.96 and 5.97) or the ADI side (Figures 5.93 and 5.98), probably due to the thermal expansion mismatch (thermal stresses). On the ADI side such cracking would be favoured by the presence close to the interface of deformed graphite which due to plastic deformation, become more or less lamellar (Figure 5.93).

5.8.2 Si/cBN-TiC/Si static interaction couples

The microstructure of the interface of the Si/cBN-TiC/Si static interaction diffusion couple after diffusion annealing at 1000 °C for 60 min is shown on the cross-section presented in Figure 5.99. Diffusion of cBN-TiC cutting tool material constituents in the silicon wafer was not evident in the single crystal silicon wafer. This allows understanding that at this temperature, diffusion of cBN-TiC cutting tool material elements in the lattice of Si should be very low, especially with regard to the diffusion along grain boundaries. However, the interaction between TiC and Si at the interface was quite evident. The silicon wafer side of the interface appeared decorated with a Ti–Si rich phase. Indeed, EDX analyses on Areas 3 and 1 at the interface revealed the formation of a titanium silicide compound. It appeared that the more the interaction product grew in size, the lower its C and Al contents.

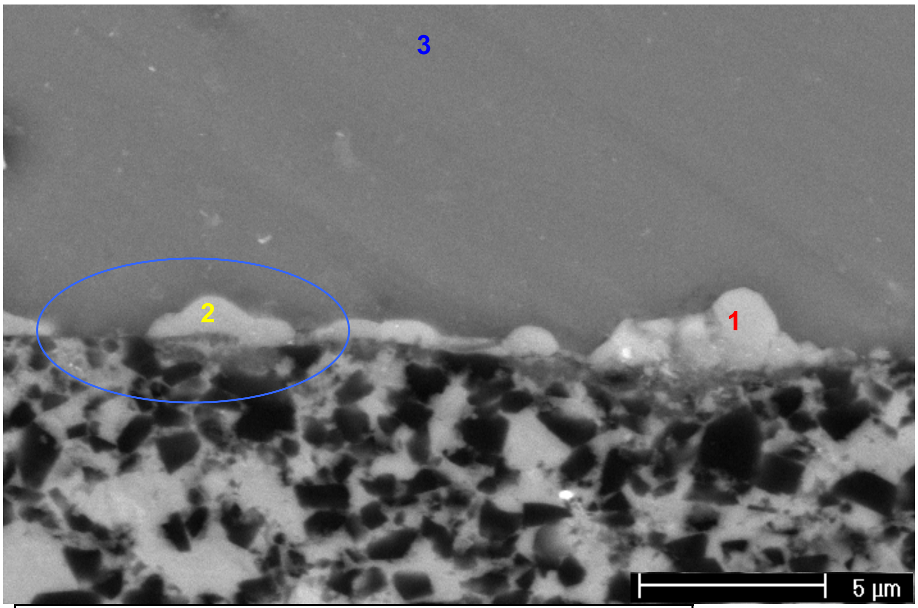

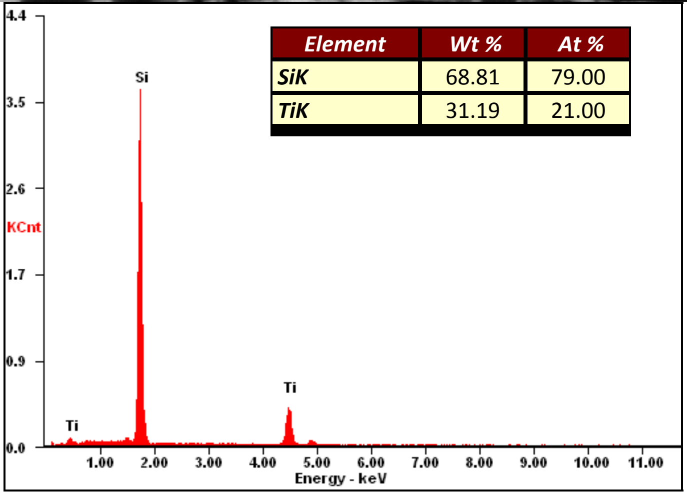

Element	Wt %	At %
SiK	68.81	79.00
TiK	31.19	21.00

EDX on 1

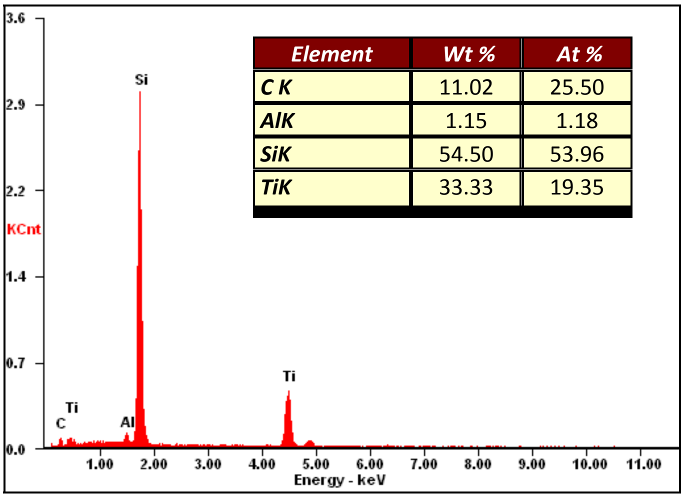

Element	Wt %	At %
C K	11.02	25.50
AlK	1.15	1.18
SiK	54.50	53.96
TiK	33.33	19.35

EDX on 2

Figure 5.99: Cross-section of the Si/cBN-TiC/Si static interaction couples after isothermal annealing at 1000 °C for 60 min. EDX of the selected areas. SEM, BSE image

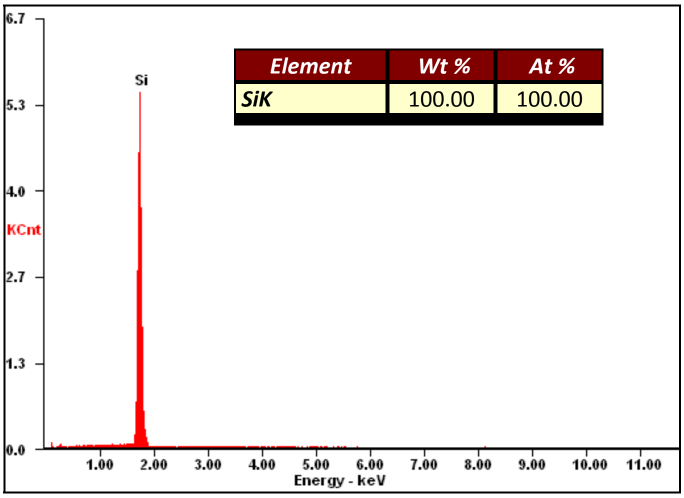

EDX on 3

Figure 5.99 (Continued)

High magnification images of the interface are shown in Figures 5.100 and 5.101. EDX analysis in Figure 5.100 – (Area 1) allowed detecting a slight interaction between cBN and Si. EDX analyses in Figure 5.100 – (Area 2) and Figure 5.101 – (Area 1) clearly showed diffusion of Si in the TiC phase and its subsequent reprecipitation due to its limited solubility in the TiC phase. Such diffusion would appear to be favoured by the presence of grain boundaries in the cBN-TiC cutting tool material. No cracking was evident at the interface.

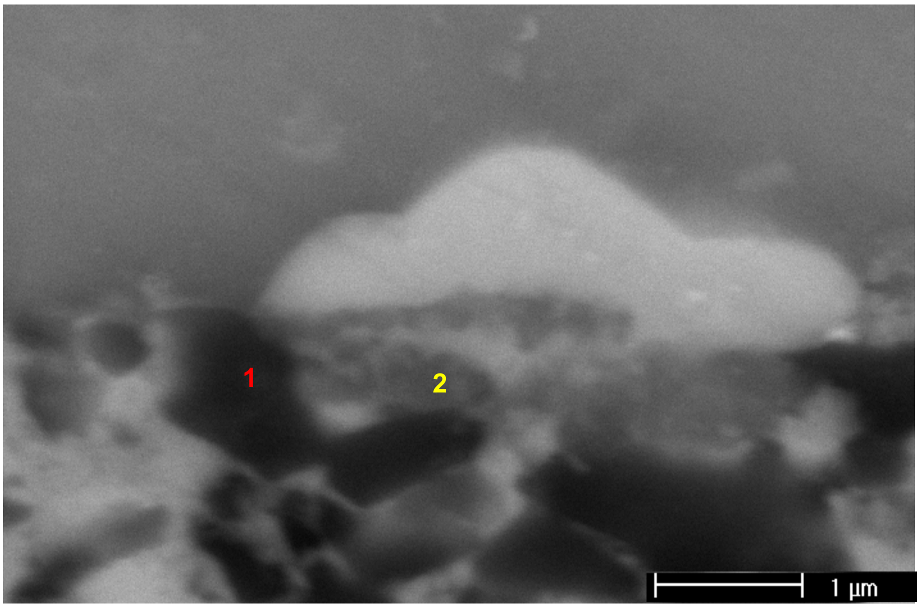

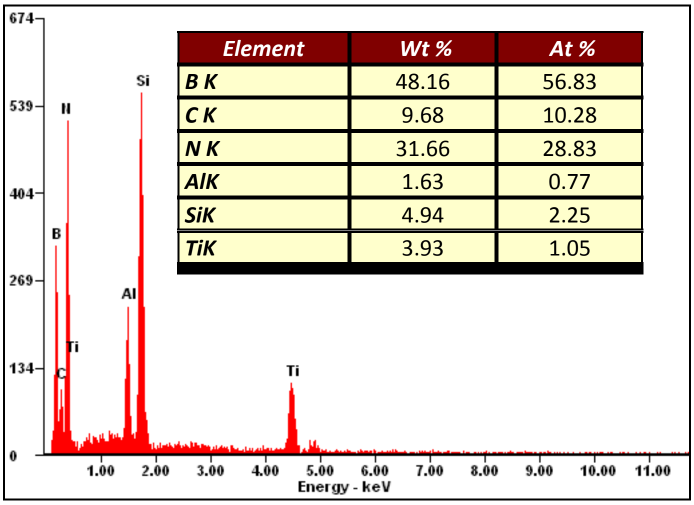

Element	Wt %	At %
B K	48.16	56.83
C K	9.68	10.28
N K	31.66	28.83
AlK	1.63	0.77
SiK	4.94	2.25
TiK	3.93	1.05

EDX on 1

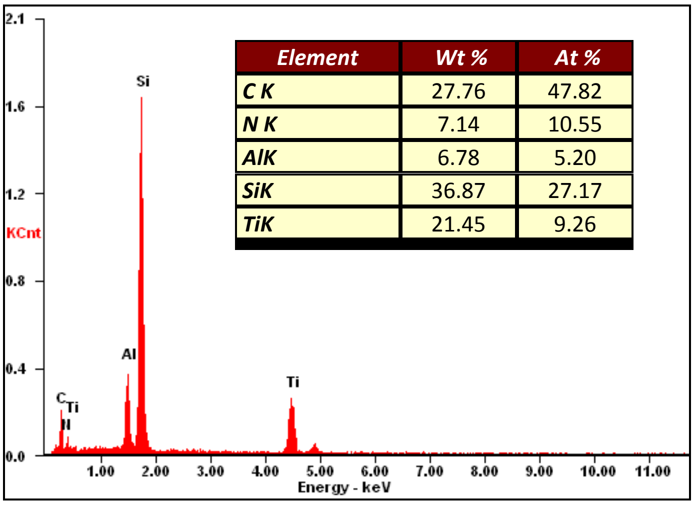

Element	Wt %	At %
C K	27.76	47.82
N K	7.14	10.55
AlK	6.78	5.20
SiK	36.87	27.17
TiK	21.45	9.26

EDX on 2

Figure 5.100: Cross-section of the Si/cBN-TiC/Si static interaction couple after isothermal annealing at 1000 °C for 60 min. EDX of the selected areas. SEM, BSE image

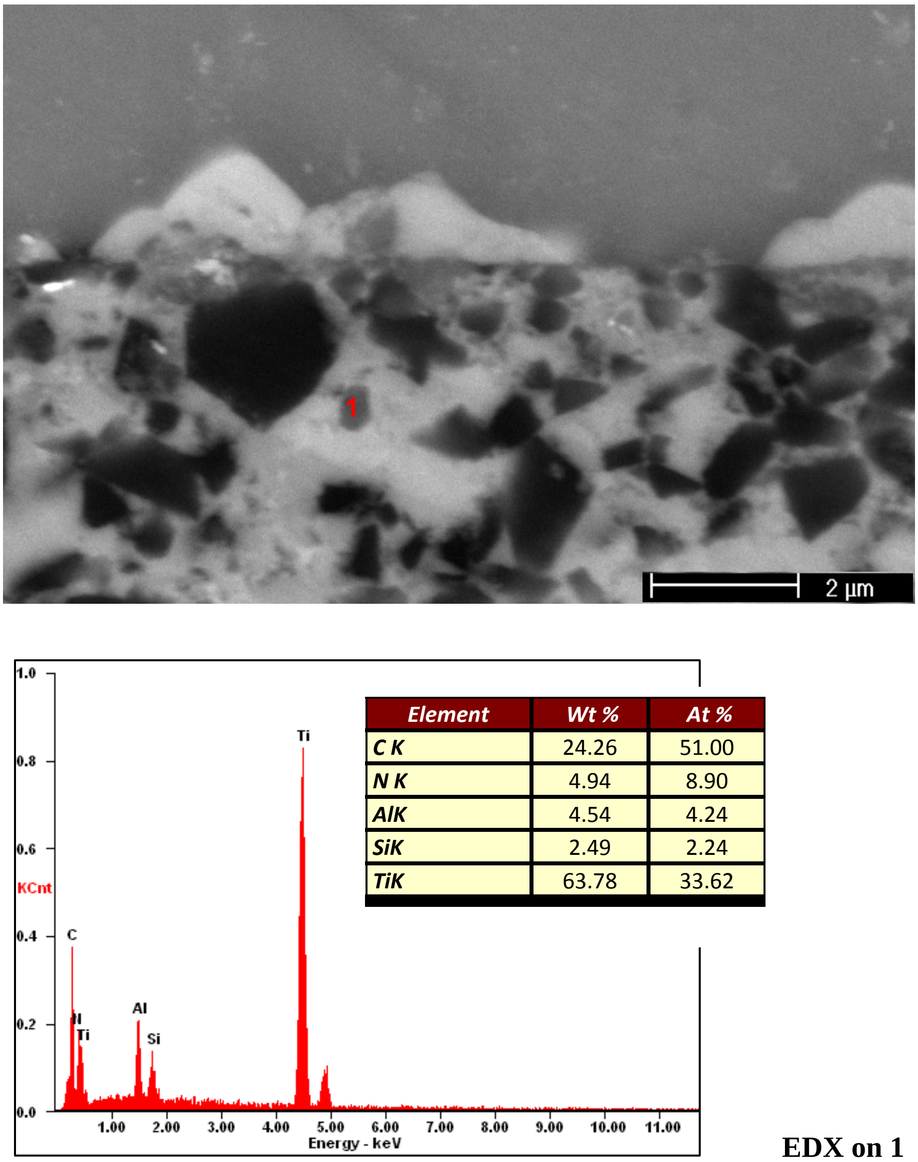

Element	Wt %	At %
C K	24.26	51.00
N K	4.94	8.90
AlK	4.54	4.24
SiK	2.49	2.24
TiK	63.78	33.62

EDX on 1

Figure 5.101: Cross-section of the Si/cBN-TiC/Si static interaction couple after isothermal annealing at 1000 °C for 60 min. EDX of the selected area. SEM, BSE image

6 DISCUSSION OF RESULTS

6.1 CUTTING TOOL CHARACTERIZATION

Taking into account that direct cBN-cBN contacts are not very frequent in the microstructure of Seco CBN100 cutting tools (Figures 5.4 and 5.5), the nature of phases at the grain boundaries, i.e. TiB_2, Al-based phases and even WC, should play a key-role in the wear behaviour of these cutting tools.

Because of the difference in thermal expansion of cBN grains, TiC binder and TiB_2 ($4.8 . 10^{-6}$, $7 . 10^{-6}$ and $8.1 . 10^{-6}$/° C respectively), the relatively high thermal expansion coefficient of TiB_2 could be a matter of concern as far as cracking and fracture of the cutting edge are concerned.

Under SE imaging, it was seen that cBN grains were in relief relative to the TiC binder (Figure 5.5). The protrusion of cBN grains relative to the TiC binder in the initial microstructure should play a key-role in the initiation of wear during the dry turning of ASTM Grade 2 ADI. Kato et al. (164) suggested that the cBN grains thus in relief might be exposed to cracking and plucking-off. Such plucking-off of cBN grains should then create holes or recesses in the tool surface, allowing the cycle of cracking and plucking-off to repeat continuously.

The considerable broadening of (111) and (200) XRD peaks of the TiC binder in the Seco CBN100 tool (Figure 5.6) indicated a very fine grain size and / or a substantial concentration of lattice defects or a variation in the stoichiometry (53,57) of the binder. Crack propagation in the TiC binder and / or plastic deformation of the binder during the machining process should therefore be delayed by the very fine grain size, provided that grain growth is inhibited by WC and Al_2O_3 grains which are found as contamination traces in the PcBN cutting tool material inherent to the processing (53).

6.2 MATERIAL ADHERING ON THE WEAR SCAR

Due to the high temperature and stress at the cutting edge for cutting speeds in the range 150-800 m/min, a BUL formed on the wear scar. The formation of this BUL on the wear scar was probably rendered possible by mutual solubility and chemical interactions (82) of ADI and cBN-TiC cutting tool constituents on one hand and the ductility and plastic flow of the ADI on the other, as discussed in Section 2.3.3.2. Because of thermal softening, the BUL probably formed with little multiplication of shear bands, i.e. under conditions similar to those prevailing during dynamic recovery and recrystallization.

Although fragmentary, the BUL smeared on the wear scar and appeared to be mechanically more stable on the wear scar than the BUE. The smearing of the BUL on the wear scar suggests that incipient melting probably occurred.

The thickness and area covered by the BUL changed with cutting speed (177). There was more smearing of the BUL on the exit zone towards the leading edge. Superficial oxidation of the BUL occurred particularly towards the leading edge on both crater and flank wear scars and also towards the trailing edge on the flank face.

It is evident that the BUL at the contact zones was the product of chemical interactions between ADI constituents, cBN-TiC cutting tool constituents and atmospheric O_2 (178).

6.3 SURFACE LAYERS BUILT UP ON NON-CONTACT ZONES

For cutting speeds in the range 150-800 m/min, the rounded particles (1-3 μm) that were found in the surface layers built up on non-contact zones (Figures 5.58 and 5.59) appear to have originated from the solidification of viscous or molten material which was squeezed out of the tool-chip and tool-workpiece interfaces (contact zones) and spread into the environment as a "cascade" of rounded particles under the action of normal and shear stresses (179). Deposition of these rounded particles on chips was not always perceptible. Thus, the presence of rounded particles in the surface layers built up on the non contact zones is evidence to suggest that superficial melting of the BUL probably occurred.

Graphite nodules at the contact zones underwent substantial comminution and their fragments were deposited on non-contact zones where at least some of them were seen to oxidize.

Inclusions liberated upon comminution of graphite nodules and ADI fragments detached from areas around the nodules also contributed to deposit formation in non contact zones.

Particles deposited on the non-contact zones could also be wear fragments that formed at the contact zones by attrition, delamination, abrasion, and similar processes.

6.4 CUTTING FORCES

The low feed (0.05 mm/rev), low depth of cut (0.2 mm) and low contact length (contact area) explain the low values of cutting force (180). Kinks on the curves of static cutting force at cutting speeds lower than 150 m/min (Figure 5.17) show the effect of the erratic or excessive BUE that probably occurred. In fact, during the cutting operation, the BUE acts as an extension of the cutting tool (180) and it usually reduces abnormally the static cutting force by restricting the contact of the chip with the cutting tool and increasing the effective rake angle.

The sudden drop in static cutting forces between 150 and 200 m/min as well as the drop in contact length could be the result of thermal softening in the secondary shear zone and particular distribution of shear stresses on the tool-chip interface that increased the shear angle (27). Because of the continuous increase in temperature along the tool-chip interface, the shear stress probably decreases from the tool cutting edge to the point at which the sticking region terminates. Above 200 m/min the balance between the effects of strain hardening and thermal softening resulted in a very slight increase in static cutting forces.

For speeds of 150 m/min or more, the static thrust force was bigger than the static tangential force because of the large negative rake angle (27,181) (−26°) and probably due to a higher crater wear rate. The decline of the BUE returned the effective rake angle to the nominal rake angle, thus increasing the static thrust force above the static tangential force which was also further reduced by the reduction of the shear strain in the primary shear zone.

At cutting speeds lower than 150 m/min, the fragmentation of chips and the instability of the BUE (formation and fracture) induced additional dynamic cutting forces. The decrease in dynamic cutting force in the range of cutting speeds 50-200 m/min could be attributed to the decrease in breaking frequency of chips (Figure 5.18).

Beyond 150 m/min chips were longer but started to become segmented and the wear rate increased significantly. The segmentation of chips, the flank wear, as well as the crater wear imply an increase in dynamic cutting force. Thus, in order to produce workpieces at lower dynamic cutting forces cutting speeds in the range 150-500 m/min are indicated.

6.5 EFFECTIVE FRICTION COEFFICIENT, TOOL-CHIP INTERFACE TRIBOLOGY

The large negative rake angle of the cBN-TiC cutting tools used in the present research resulted in relatively high thrust forces and consequently relatively high mean normal stresses on the rake face and relatively low effective friction coefficient and low tool-chip contact length (27).

The morphologies of the crater wear scar, the chip underside, the chip and surface layers on the non-contact zones of the rake face and the effect of cutting speed on the effective friction coefficient at the rake face allow at least partial insight into the tool-chip interface tribology during the dry finish turning of ADI with cBN-TiC cutting tools.

Under seizure conditions without temperature gradient, shear stresses are constant whatever the normal stresses, whereas under sliding conditions, the friction coefficient is constant whatever the shear stresses. Thus, once seizure conditions exist at the tool-chip interface, the variation of the effective friction coefficient at the rake face with the cutting speed should be related to the variation of either mean normal stresses or mean shear stresses or both (27).

The large negative rake angle of the cutting tools used in the present research also resulted in the formation of BUE at low cutting speeds. The occurrence of a BUE is evidence of seizure, particularly close to the cutting edge. Although cracking and shearing in the secondary shear zone of chips as well as the relatively low depth of cut (0.2 mm) used in the present research also played a role in BUE formation (27), the latter indicates adhesion or strain hardening.

Taking into account the effects of seizure at the tool-chip interface, the increase in effective friction coefficient at cutting speeds of 50-150 m/min (Figure 5.19) should be related to an increase in flow stress of the ADI chips. Changes in strain, strain rate and temperature within this range of cutting speeds were such that the reduction of flow stress of the ADI chips at the tool-chip interface was minor.

However, the BUE increased the effective rake resulting in relatively high values of effective friction coefficient at the tool-chip interface at low cutting speeds.

The slight increase in effective friction coefficient at the tool-chip interface at cutting speeds of 150-800 m/min was due to variations in the mean normal and shear stresses at the tool-chip interface. Indeed, changes in strain, strain rate and temperature in this range of cutting speeds resulted in a significant decrease in chip flow stress. A gradient of shear stresses within the sticky (seizure) zone at the tool-chip interface would be expected due to the corresponding gradient of temperature (27).

For cutting speeds in the range 150-800 m/min, the considerable smearing of the BUL in the exit zone of the crater wear scar and the non-contact zone of the rake face (Figures 5.9 to 5.12) probably reduced the effective friction coefficient due to liquid formation and lubrication.

Farhat (173,182) suggested that a liquid lubricating film could increase the effective friction coefficient in some cases or produce the contrary effect in some other cases, depending on cutting speed. It is generally observed that for lubricated cutting an increase in cutting speed leads to an increase in the mean coefficient of friction at the tool rake face (27).

6.6 CHIP LENGTH AND CURVATURE

At a feed of 50 µm/rev and with a mean graphite nodule size of 30 µm and a graphite spacing of 72 µm, the probability of cutting the matrix itself in the primary shear zone would be limited. Furthermore, the incompatibility of plastic deformation between the graphite nodules and the ausferrite matrix induced from time to time, micro-voids, micro-cracks and ductile fracture in the primary shear zone and sometimes in the secondary shear zone, particularly at lower cutting speeds.

Under these conditions segmentation of the chip in the primary shear zone even at very low cutting speed appears to be likely. This could explain the variety of chip morphologies observed at lower cutting speeds (Figure 5.24). However, the low feed (0.05 mm/rev) increased the compressive stress in the primary shear zone (183) which probably suppressed the geometrical softening effect by crack closure.

Shorter chips produced at cutting speeds of 50 and 100 m/min under conditions of relatively homogeneous high strain (low shear angle) and low strain rate indicated clearly cutting conditions whereby lower cutting temperatures occurred. Indeed, their colour remained more or less the same as that the colour of the ADI workpiece.

On the contrary, relatively long chips produced at cutting speeds greater than 150 m/min under conditions of relatively localized low strain (high shear angle) and high strain rate indicated cutting conditions whereby higher cutting temperatures were generated (184). Indeed, their colour turned dark blue on the upperside or light brown on the underside.

The curling of chips was more pronounced at cutting speeds lower than 150 m/min. This could be indicative of considerable homogeneous plastic deformation and strain hardening of the chips. It could also point to a difference in the distribution of stresses in the primary and secondary shear zones between the two ranges of cutting speeds.

6.7 AVERAGE CHIP THICKNESS AND CHIP HARDNESS

The large negative rake angle of the cBN-TiC cutting tools used in the present research resulted in a relatively low shear angle (27), and a substantial amount of plastic deformation in the primary shear zone of chips and as well as a large average chip thickness. Indeed, at a cutting speed of 50 m/min, long contact length, high average chip thickness (high deformation) and high hardness were recorded (Figure 5.26).

The gradual, continuous and asymptotic decrease in the average chip thickness (Figure 5.26) was due to the gradual, continuous and asymptotic increase of the shear angle that occurs when the cutting speed increases. The increase in shear angle with increased cutting speed is linked to strain hardening in the primary shear zone or according to Oxley's model, to a decrease of flow stress (thermal softening) in the secondary shear zone (22).

When considering chip hardness and average chip thickness (Figure 5.26) interesting trends emerge with regard to the interplay between strain hardening and thermal softening. At speeds of up to 100 m/min chip hardness increased due to strain hardening. The practically constant hardness of chips produced at 100-200 m/min was probably due to increased chip temperature resulting in a balance between strain hardening and recovery processes. At speeds between 200 and 300 m/min, the hardness dropped substantially probably due to recrystallization in deformed chips. At speeds in excess of 300 m/min the hardness appeared to be constant indicating recrystallization in the chips. This appears to be consistent with the nearly constant chip thickness obtained at speeds of between 300 and 800 m/min (Figure 5.26).

For cutting speeds in the range 150-800 m/min, the considerable smearing of BUL in the exit zone of the crater wear scar and the non-contact zone of the rake face (Figures 5.9 to 5.12) suggests that it could play a role in the generation of a steep shear stress gradient at the rake face (27). This will lead to a reduction of the tool-chip contact length as well as an increase in the shear angle and, consequently, in a reduction in average chip thickness. Definitely the decrease of the average chip thickness is to put among others on the account of the formation of a lubricating film at the tool-chip interface.

6.8 SHEAR LOCALIZATION IN THE PRIMARY AND SECONDARY SHEAR ZONE

At cutting speeds below 150 m/min the formation of BUE and continuous chips should be related to the relatively small depth of cut (200 µm). Indeed, the formation of BUE and continuous chips indicated that in the primary shear zone, the material fracture strain was higher than the equilibrium strain and that the equilibrium strain was lower than the critical strain for a microsoftening event (22,180). The relatively long contact length associated with the formation of these chips would explain the intense plastic deformation in the corresponding secondary shear zones.

The asymptotic decrease in average chip thickness (Figure 5.26) agrees with the formation of segmented chips (185). Since ADI is a relatively ductile material, the formation of segmented chips (Figure 5.25) is related to shear localization in the primary or/and secondary shear zones. Shear localization was revealed metallographically in the primary and secondary shear zones by the presence of shear bands whose microstructure contrasted clearly with that of the chip segments (Figure 5.25).

At cutting speeds greater than 150 m/min, the formation of shear-localized chips indicated that the thermal softening allowed the chips to continue deforming in the primary shear zone rather than fracture. Indeed, the material fracture strain remained higher than the equilibrium strain which exceeded that required for microsoftening (22,180).

At cutting speeds greater than 150 m/min, strain rate hardening due to dislocation damping at the tool–chip interface gave rise to high temperatures that activated the onset of shear localization in the secondary shear zone. The temperature in this zone increased even further with the onset of shear localization. Clearly, a cyclic stick-slip mechanism was established at the rake face whereby seizure and sliding alternated. Strain hardening caused seizure on the rake face which impeded chip flow and lowered the shear angle. An instant later, the secondary shear zone weakened due to thermal softening and a lower strain rate. The shear angle then increased and the chip flowed on the rake face (180).

However, shear localization in the secondary shear zone was reduced by the superficial melting on the chip underside, through its lubrication effect. In fact, the increase in average chip thickness that should be favoured by the onset of shear localization in the secondary shear zone (183) was negligible above a cutting speed of 200 m/min (Figure 5.26). This confirms the formation of a lubricating transfer layer that maintains the tribological conditions at the tool–

chip interface more or less constant (Figure 5.19). The consequence of this is a nearly constant average chip thickness ([186]).

6.9 MICROSTRUCTURE OF PRIMARY AND SECONDARY SHEAR ZONES OF CHIPS

Adiabatic shear band microstructures such as those that formed in the primary and secondary shear zones of ADI chips at cutting speeds equal to or greater than 150 m/min can range from highly elongated grains, to equiaxed grains possessing a high degree of misorientation and finally, to small recrystallized grains (187).

The transition from spot patterns to semi-continuous ring patterns (Figures 5.28 and 5.31, 5.34 and 5.36) observed in the SADPs of shear zones of ADI chips produced at cutting speed equal to or greater than 150 m/min indicates a substantial refinement in the size of the reflecting phases and their random orientation with regard to the surrounding lattice. Only ferrite was clearly identified. Thus, such refinement in the size of ferrite grains should be the result of particular processes, probably recovery and recrystallization or recovery and recrystallization combined with others processes as described further.

However, it has to be pointed out that the thermo-mechanical history of the primary and secondary shear zones is complex as temperature gradients exist in the primary and secondary shear zones.

Because the driving force for recovery and recrystallization comes from plastic deformation, it might be expected that plastic deformation in the shear zones would occur in advance of static recovery and recrystallization.

In this view, it can be understood that plastic deformation in the secondary shear zone takes place particularly in the sticky (seizure) zone located in the entrance zone of the crater scar whereas static recovery and recrystallization occur thereafter (once shear deformation ceases) probably in the sliding zone at the exit zone of the crater scar and perhaps beyond when the chip leaves the contact with the rake face if cooling is relatively slow.

The recrystallization process depends on initial grain size, strain, strain rate, temperature and time. At low strain rate, when the recrystallization temperature is exceeded, strain and time are very important. However, at high strain rate, the effect of strain rate on recrystallization is essential. Recovery kinetics is generally very fast compared to recrystallization kinetics in the sense that recovery does not involve a process of nucleation which, generally requires an incubation time.

The lifetime of adiabatic shear bands is very short because the rapid strain in the shear band relieves the local stress which inhibits further strain. Thus, the duration of the temperature rise of adiabatic shear bands is of the order of ms (15).

In terms of static recovery and recrystallization, the fast rate of change in the primary and secondary shear zones during this very short time period could only be explained by the substantial amount of plastic deformation and the high temperature involved. On this subject, it is also appropriate to point out that the substantial amount of plastic deformation in the shear zones lowers the recrystallization temperature estimated to be in the range 600-675 °C (180).

The refinement of ferrite grains in the primary and secondary shear zones of ADI chips appeared to be indicative of the amount of plastic deformation as might have been expected. The increase in cutting speed did not result in a substantial decrease of the size of ferrite grains in the primary and secondary shear zones (Figures 5.29, 5.30, 5.33, 5.35, and 5.37).

The refinement of ferrite grains in the shear zones of ADI chips could also be considered as a consequence of the combination of the substantial amount of plastic deformation and the occurrence of the transformations ferrite-austenite and austenite-ferrite. The occurrence of the ferrite-to-austenite transformation would be the consequence of having the temperature within the shear zones beyond the critical eutectoid temperature Ac_1 (± 730 °C + undercooling ΔT). The substantial amount of plastic deformation should speed up the ferrite-to-austenite transformation. Such a transformation should refine the size of austenite grains produced. The reverse austenite-to-ferrite transformation upon cooling should further refine the ferrite grains.

While the chip slides on the crater wear scar, the shear zones are heated progressively up to a maximum temperature and then cooled. The cooling of these shear zones continues further in the presence of air after the chip leaves the crater wear scar. However, as mentioned in Section 2.1.6.3, when the chip leaves the crater wear scar that part of the secondary shear zone which passes off on the underside of the chip cools very fast to the temperature of the chip body which acts as a relatively lukewarm “chill” since, cooling by metallic conduction is very efficient compared to cooling in air. The increase in temperature of the bulk of the chip due to heat from the secondary shear zone is slight because of the relatively large volume of the bulk of the chip.

In such conditions, a very rapid cooling of the austenite grains in air is unlikely to occur and one should not expect transformation of austenite to martensite.

This would also mean that an austenite-to-ferrite+graphite transformation occurred preferentially during a portion of the travel of the chip on the crater wear scar and possibly beyond, when the chip breaks contact with the wear scar.

In the case of strain induced transformation of retained austenite to martensite in the shear zones, such martensite might be expected to undergo some tempering. However, the TEM investigation of the primary and secondary shear zones of ADI chips did not reveal any martensite or austenite or metastable carbide (Figures 5.31 and 5.36). Of course, in the SADPs, martensite reflections might be obscured by ferrite reflections, both having similar crystal structures.

It has to be mentioned however that it has been recently shown that existing kinetic models for static recrystallization cannot account for the formation of recrystallized grains within the shear bands in the time scale and temperature history corresponding to adiabatic shear band formation and subsequent cooling (187).

The duration of the temperature rise in shear bands is significantly lower than normally associated with static recrystallization (188). As such, static recrystallization mechanisms relying on diffusion processes might lack time to account for the recrystallized microstructures observed in the primary and secondary shear zones of chips. It was reported that migrational recrystallization does not even occur in shear bands during cooling, after plastic deformation. The fast deformation and short cooling times of adiabatic shear bands inhibit grain-boundary migration (189).

It was suggested that the formation of recrystallized grains in adiabatic shear bands occurs simultaneously with the formation of the shear bands. Such a formation would involve mechanical means, i.e. rotational recrystallization, which needs concurrent plastic deformation (189).

It was proposed, particularly for metals, that recrystallization under the rapid deformation and cooling conditions in adiabatic shear bands involves three steps: subgrain formation, subgrain mechanical rotation, and subgrain boundary refinement (reorientation/accommodation) during cooling (187,189).

The nano-sized equiaxed grains that appeared in the secondary shear zone of chips at cutting speeds greater than 150m/min were the result of dynamic recovery and recrystallization in this zone. At cutting speeds greater than 150 m/min, shear bands in the secondary shear zone probably transformed partially.

6.10 WEAR BEHAVIOUR

It is well known that in the Taylor equation, the cutting speed influences tool life through its effect on temperature (171). It is then likely that thermally activated wear mechanisms were active over a wide interval of the range of cutting speeds used.

When considering flank wear rate (Figure 5.16), chip hardness and average chip thickness (Figure 5.26) as well as effective friction coefficient at the rake face (Figure 5.19), strong indications emerge with regard to tool wear mechanisms. At speeds of up to 200 m/min, temperatures are relatively low, the chip strain-hardens and abrasion (a mechanical effect) would be expected to be the dominant wear mechanism. This is in line with the earlier occurrence of attrition wear clues on the rake face at 50 and 100 m/min (Figures 5.7 and 5.8).

At speeds between 200 and 300 m/min temperatures are high and clear evidence recrystallization of in shear zones of chips emerges. Under these conditions diffusion wear is expected to dominate. This would be in line with the earlier development of crater wear scars (Figures 5.9 to 5.12). This mechanism appears to remain dominant at speeds of up to about 600 m/min. The increased flank wear rate at speeds in excess of 600 m/min can probably be attributed to further temperature increases which facilitate diffusion but also accelerate oxidation which becomes a significant contributor to tool wear. Liquation at these high cutting speeds can also be expected to enhance wear of the tool. Clearly there are synergistic effects between the four phenomena.

6.11 WEAR MECHANISMS

6.11.1 Adhesion wear

At cutting speeds less than 150 m/min, rough torn surfaces obtained on the underside of chips as well as rough surfaces obtained on the cutting tool wear scars (Figures 5.20 and 5.64) are typical of preponderant adhesion wear which occurred through the formation of adhering material (BUE or BUL) on the cutting tool under particular conditions of seizure as discussed earlier in Section 2.3.3.

In order to accommodate the relative movements of the workpiece and chips with regard to the cutting tool during adhesive contact, the asperities in the workpiece and the chips deformed into a series of shear bands (74) because of their low flow stress compared to that of the cutting tool.

Upon shearing, strain hardening and cracking in this series of shear bands, fragments of ADI were ultimately left on the cutting tool forming patches of BUE. Upon successive adhesions, successive layers built up on these initial patches of BUE. The BUE strain hardened and thickened progressively before becoming unstable and being plucked off the cutting tool.

Despite the relatively low temperature at cutting speeds lower than 150 m/min and the restriction of atmospheric O_2 at the tool-chip and tool-workpiece interfaces, oxide films on all nascent ADI surfaces (82,190), although thin, should effectively suppress or reduce successive adhesions. However, the sliding of chips and workpiece on the cutting tool is expected to remove these thin oxide films resulting in successive adhesions that lead at the final stage to severe adhesion wear of the cutting tool.

Commonly, the highly strain-hardened patches of BUE are removed through the cutting tool (Figures 5.43 to 5.45) resulting in tool attrition (191). The cutting tool surface becomes grooved and exposes the tool to a new cycle of adhesion and abrasion wear. Attrition wear could also mask other wear mechanisms such as delamination.

At cutting speeds greater than 150 m/min, the occurrence of BUL on the wear scar surfaces and surface layers built up on non contact zones is important evidence of adhesion wear (177). In addition to the discussion on BUL formation in Section 6.6.2, it should be mentioned that diffusion of elements like C, Si and Mg in the BUL (Figure 5.69) towards the interface probably contributed in reducing the extent of successive adhesion events for cutting speeds greater than 150 m/min. The superficial oxidation of nascent ADI surfaces as well as of the ADI BUL transferred to the cutting tool, became so rapid that a relatively thick and stable oxide film in the form of a “glaze” spread over the worn surface and effectively reduced adhesion wear. The much smoother surfaces with considerable ADI smearing obtained on the tool scars as well as the underside of chips (Figure 5.23) are indeed characteristic of mild adhesion wear (71).

Based on the structure and composition of the BUL, it emerged that the adhesion of ADI on TiC grains was more intense (Figure 5.41) than on cBN grains where a BUL with a loose spongy morphology was evident (Figures 5.46 to 5.49).

It appeared from the results obtained that adhesion wear occurs first followed by diffusion wear and abrasion wear. If the BUL offered some protection to the cutting tool against abrasion and adhesion wear as suggested by the scratched pattern in Figure 5.65, it should be pointed out that the adhesion of the BUL strengthened its chemical interaction (diffusion wear) with the cutting tool material (192).

6.11.2 Abrasion wear

The presence of regular shaped wear patterns of deep grooves as well as fine grooves on the wear scars (Figures 5.64 and 5.65) is evidence that an abrasion wear mechanism operated. However, it is important to point out that, except for clues of earlier cracking due to stress concentration and delamination on cBN grains (Figures 5.41 and 5.42, 5.51 and 5.52), the abrasion mechanism was not the trigger wear mechanism. The evidence shows that abrasion was triggered by adhesion and diffusion wear mechanisms.

It is suggested here that abrasion wear started with the cBN grains that lost support from the cutting tool (193) because of microfracture at boundaries with the TiC binder or due to cracking induced by imperfections and irregularities on the surface (164), particularly close to the cutting edge. The fragments of cBN grains liberated in this way act as abrasive particles and perpetuate the abrasion process by acting, among others, as micro-indenters on the cutting tool.

No perceptible elongation of wear grooves in the flow direction was evident (Figure 5.64) indicating that superficial plastic deformation was negligible**.**

At cutting speeds greater than 150 m/min, abrasion wear was attenuated due to the BUL that appeared to adhere on the wear tracks (Figure 5.65). The low flank wear rate at cutting speeds less than 150 m/min (Figure 5.16) where abrasion wear appear to be preponderant, shows that cBN-TiC cutting tools have appreciable resistance to abrasion wear at relatively low cutting speeds.

6.11.3 Diffusion wear, dissolution wear

At cutting speeds greater than 150 m/min, the resultant high temperature which favoured dynamic recrystallization and phase transformations in the shear zones, also favoured thermally activated wear on the cBN-TiC cutting tools. This was evidenced by the early appearance of the crater wear scar at cutting speeds greater than 150 m/min.

Contrary to the rough morphology of wear surfaces produced by adhesion and abrasion wear, the morphology of wear surfaces produced by chemical wear are generally smooth and show some minute irregularities at relatively high magnification.

The composition of the BUL on cBN grains for cutting speeds greater than 150 m/min (Figure 5.49) is a good indication of chemical reactions between cBN grains and the environment including the stock.

The grooves on wear surfaces of tools used at cutting speeds greater than 150 m/min were not solely due to abrasion wear. The wear pattern which consisted of shallow ridges and valleys (Figures 5.65 to 5.67) is indicative of diffusion wear (173). However, these shallow ridges and valleys probably arise from a combination of mechanical abrasion, diffusion, and oxidation effects. In fact, at cutting speeds greater than 150 m/min, where contact stresses and temperatures are high, diffusion of elements from the cutting tool into the chips and workpiece and / or diffusion of elements from the ADI into the cutting tool as well as oxidation processes set in to produce species that are softer and less resistant to abrasion.

The presence of Si and Fe approximately 0.5 μm below the crater scar of the cutting tool (Figure 5.70), at the boundaries between cBN grains and the TiC binder strongly indicates diffusion of elements from the ADI into the cutting tool.

Diffusion of ADI constituents into the cutting tool material (particularly diffusion of Fe and Si into the TiC binder through the grain boundaries or eventually cracks) should have induced structural changes which are seen as potential sources of the degradation of the cutting tool and its wear resistance.

The susceptibility of PcBN cutting tools to diffusion wear was also reported by other authors. Zimmermann et al. (194) reported on the depletion of B on the crater wear scar of cBN-TiC cutting tools used in the machining of a case-hardened steel at a cutting speed of 240 m/min. They suggested that the mechanism behind such depletion was a tribochemical reaction in which BN dissolves or diffuses into the flowing chip due to extremely high stresses and temperatures. While investigating the chemical interactions between PcBN cutting tools with ceramic binder and carbon steel, Narutaki and Yamane (195) suggested that, the grain boundaries and not the cBN grains are the source of B that diffuses towards the Fe side.

Concerning the mechanism of the potential diffusion or dissolution of TiC in Fe, the following finding of Shimada et al. (196,197,198) and Zhang and Koka (199) can be helpful. The latter reported that thermo-migration of C atoms in TiC towards the surface starts at 350-400°C. Upon heating of TiC, C atoms short-range diffuse towards the surface where they segregate as an amorphous or crystalline graphite layer, leaving behind some free Ti atoms. Indeed, TiC is conventionally considered as an interstitial solid solution wherein C atoms occupy interstices of the Ti lattice. TiC is often substoichiometric with respect to C (200). Thus, because of the relatively low activity of C in ferrite or austenite in ADI, the TiC binder can effectively dissolve in ADI according to Equation (6.1) and reprecipitate as TiC or Fe_3C (174) since the solubility of C in Fe is limited.

$$TiC_{(S)} = \underline{Ti} + \underline{C} \qquad \textbf{(6.1)}$$

Concerning the mechanism of the potential diffusion or dissolution of B in Fe, it has to be mentioned that the thermal decomposition of cBN (Equation 6.2) starts at 2490 °C at atmospheric pressure. Thus, it is improbable that dissolution of B in ADI (Equation 6.3) at the tool-chip and tool-workpiece interfaces takes place due to such decomposition.

$$BN_{(S)} = B_{(S)} + \tfrac{1}{2}\{N_2\} \qquad \textbf{(6.2)}$$

$$B_{(S)} = \underline{B} \qquad \textbf{(6.3)}$$

However, B may enter the ADI through the oxidation of cBN (Equation 6.4). However, since the solubility of B_2O_3 in Fe is very low (201), the dissolution of B in Fe could only take place via a mechanism able to reduce B_2O_3 to elemental B. Another possibility is the dissolution of TiB_2, located at the grain boundaries of cBN-TiC, in Fe. Indeed the solubility of TiB_2 in Fe at relatively high temperature is appreciable (201).

$$BN_{(S)} + \tfrac{3}{4}\{O_2\} = \tfrac{1}{2} B_2O_{3\,(S)} + \tfrac{1}{2}\{N_2\} \qquad \textbf{(6.4)}$$

The reduction of B_2O_3 to elemental B might involve Mg from the ADI (Equation 6.5).

$$B_2O_3\ _{(S)} + 3\ \underline{Mg} = 2\ B\ _{(S)} + 3\ MgO\ _{(S)} \qquad \textbf{(6.5)}$$

Taking into account the limited solubility of B in Fe (202), the dissolution of B in ADI (Equation 6.3) could be expected to be followed by its reprecipitation in the form of Fe_2B. The corresponding global chemical reaction could then be written as (Equation 6.6):

$$B_2O_3\ _{(S)} + 3\ \underline{Mg} + 4\ Fe\ _{(S)} = 3\ MgO\ _{(S)} + 2\ Fe_2B\ _{(S)} \qquad \textbf{(6.6)}$$

This would be in line with the opinion of Klimenko et al. (179) who suggested that during the machining of bearing steel with PcBN cutting tools, B_2O_3 forms at the contact zones, softens and melts before being squeezed out on non-contact zones where it evaporizes. They suggested that the chemical interaction of BN and Fe ended up with the formation of Fe-Fe_2B eutectics which self-lubricate the tool-chip interface.

This is also in line with the opinion of Farhat (173) who reported the formation of Fe–Fe_2B type eutectics on the tool-chip and tool-workpiece interfaces during the machining of mould steel with PcBN cutting tools.

On this specific matter, the Fe-corner on the Fe-B-C phase diagram presented in Figure 6.1 gives an insight on the influence of C on the eutectic Fe-Fe_2B and the influence of B on the eutectic Fe-Fe_3C. It emerges from this phase diagram that the presence of C is likely to decrease the melting temperature of the Fe-Fe_2B eutectic, whereas the presence of B is likely to decrease the melting temperature of the eutectic Fe-Fe_3C. It appears that B can dissolve in Fe_3C forming $Fe_3(C,B)$. Up to 18 at% B is soluble in Fe_3C. C can also dissolve in Fe_2B up to a certain extent where $Fe_{23}(C,B)_6$ or $Fe_3(C,B)$ can start forming.

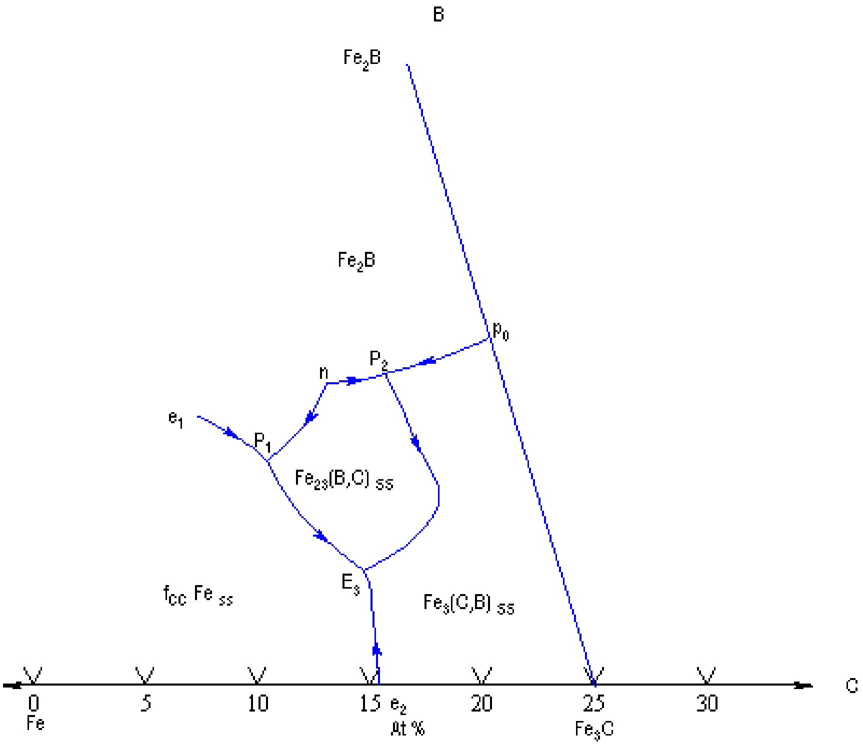

Ternary invariant points:

P_1 = $Fe_2B + Fe + Fe_{23}(C,B)_6$

P_2 = $Fe_2B + Fe_{23}(C,B)_6 + Fe_3(C,B)$

E = $Fe + Fe_{23}(C,B)_6 + Fe_3(C,B)$

Figure 6. 1: Fe-corner of the Fe-B-C phase diagram (203)

6.11.4 Influence of microstructure refinement in the shear zones on diffusion wear

It may be expected that the microstructure refinement in the primary and secondary shear zones of chips obtained at cutting speeds greater than 150 m/min could increase the diffusion rate in the chips and enhance the diffusion of cutting tool constituents into the chips.

The temperature up to which grain boundary diffusion is faster than lattice diffusion increases with decreasing grain size (204). It may thus be expected that the formation of nano-sized grains in the primary and secondary shear zones increases sensibly such a temperature and favours grain boundary diffusion of cutting tool material constituents into ADI chips.

Diffusion wear may be expected to be important in the seizure zone, particularly in the presence of a stagnant layer or BUL. It is suggested that the stagnant layer or BUL in the seizure zone, can undergo dynamic recrystallization. Small grains produced in this particular situation can have a strong interaction with the cutting tool material in terms of diffusion.

However, it is probable that diffusion processes slow down as concentration gradients decline with time.

From this analysis, it appears that clues of diffusion wear should be sought in the BUL on the wear scar rather than in the secondary shear zone of chips. The TEM investigation of chips did not reveal clearly any clues of diffusion wear as did the TEM investigation of the BUL in sections of cutting tools (Figures 5.69 and 5.70).

However, if the microstructure refinement occurred after the chip broke contact with the crater wear scar, the interaction of nano-sized grains produced in the secondary shear zone of the chips with the cutting tool constituents should be very limited or could not occur at all. In fact, in such a situation the dislocation pipes produced due to huge amounts of shear strain in the primary and secondary shear zones of the chips could act as diffusion paths. The interaction of dislocation pipes with the cBN-TiC cutting tool constituents should then play a role in the interaction between the ADI chips and the cutting tool material. Small atoms like C, B and N from the cutting tool could be expected to be involved in such wear mechanism. Still, it should be mentioned that such diffusion of cBN-TiC cutting tool material constituents in the dislocation pipes produced in the chip shear zones should delay the process of dynamic recovery or recrystallization.

6.11.5 Chemical reaction wear

At cutting speeds greater than 150 m/min, the chemical composition of the BUL on contact zones as well as surface layers built up on the non-contact zones revealed substantial amounts of Fe, C, Si, Mg, O and Ti (Figures 5.46, 5.58 to 5.63 and 5.69). Si, Mg, O and Ti were detected on cBN grains (Figures 5.49 and 5.53) while Fe, Si, Mg and O were detected on TiC grains (Figure 5.50). It thus appears that constituents in the BUL on contact zones and non-contact zones of the tools are the products of thermally activated chemical reactions between constituents of the cutting tool, constituents of ADI and atmospheric O_2. This indicates clearly that these thermally activated tribochemical reactions play a key-role in tool wear.

The affinity of Mg and Si for O can also explain the presence of Si and Mg in the surface layers built up on non-contact zones.

A thermodynamic analysis of the following reactions (Equations 6.7 to 6.15) was carried out with the aid of the software package FactSage 5.4.1 in order to evaluate their possibilities of occurrence. FactSage 5.4.1 is a fully integrated thermo-chemical database program capable of among others, performing thermodynamic calculations as well as supplying data and properties of various stoichiometric compounds. It was found that all the reactions are exothermic in the temperature range 500-1200 °C. Based on the negative values of free energies in the temperature range 500-1200 °C, it is concluded that they are likely to take place, at temperatures over 500 °C, under standard conditions (Figure 6.2, Equations 6.7 to 6.15).

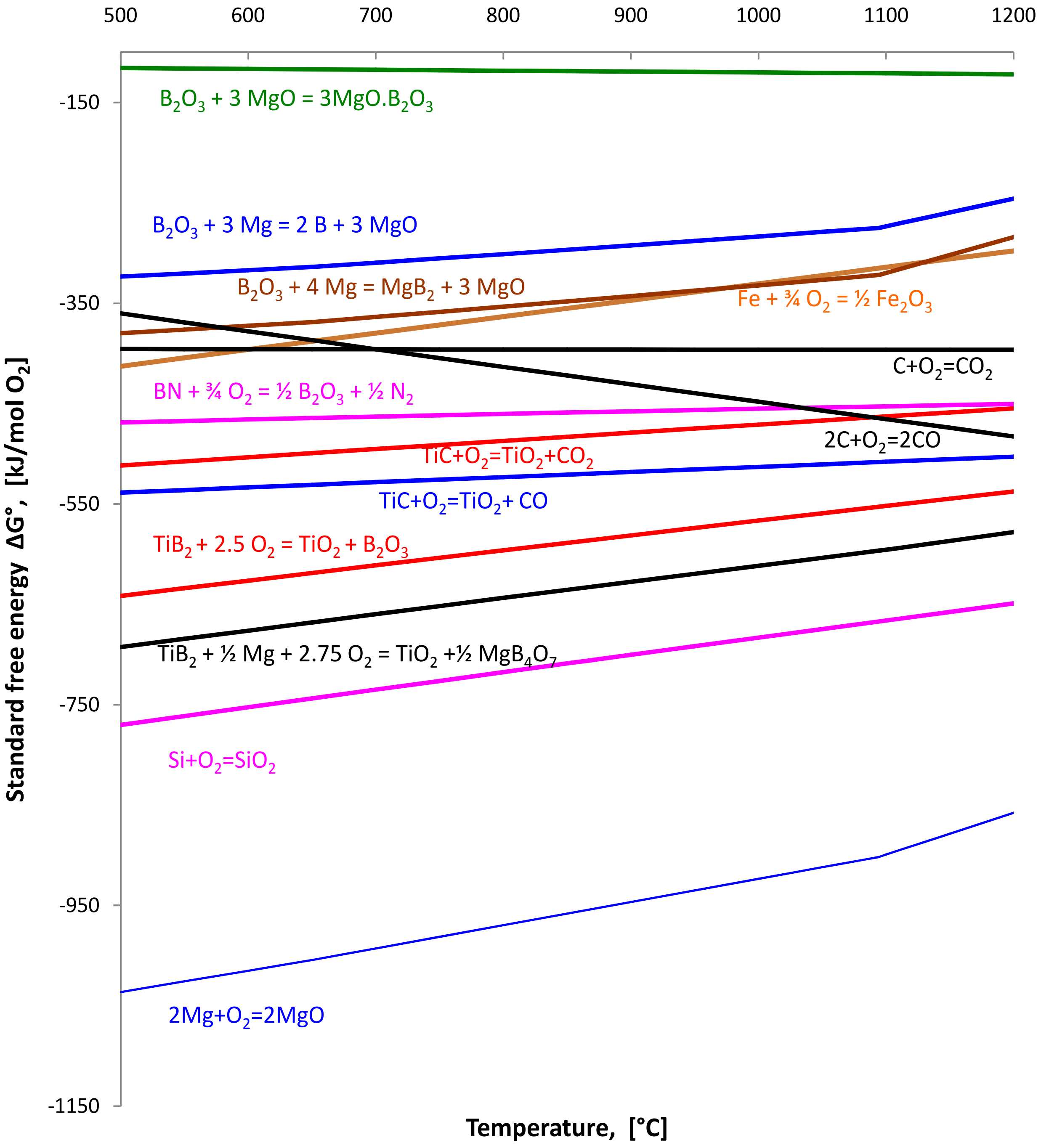

Figure 6. 2: Standard free energy of some potential chemical reactions in the system “Seco CBN 100-ADI- air” (Calculated with FactSage 5.4.1.)

Seco CBN100

$TiB_2 + 2.5\ O_2 = TiO_2 + B_2O_3$ $\Delta G^\circ_{773} = -641.724$ kJ/mol O_2 **(6.7)**

$TiC + 2\ O_2 = TiO_2 + CO_2$ $\Delta G^\circ_{773} = -\ 511.801$ kJ/mol O_2 **(6.8)**

$BN + \frac{3}{4}\ O_2 = \frac{1}{2}\ B_2O_3 + \frac{1}{2}\ N_2$ $\Delta G^\circ_{773} = -\ 468.875$ kJ/mol O_2 **(6.9)**

ADI BUL

$2\ Mg + O_2 = 2\ MgO$ $\Delta G^\circ_{773} = -\ 1036.208$ kJ/mol O_2 **(6.10)**

$Si + O_2 = SiO_2$ $\Delta G^\circ_{773} = -\ 770.190$ kJ/mol O_2 **(6.11)**

$Fe + \frac{3}{4}\ O_2 = \frac{1}{2}\ Fe_2O_3$ $\Delta G^\circ_{773} = -\ 412.859$ kJ/mol O_2 **(6.12)**

$C + O_2 = CO_2$ $\Delta G^\circ_{773} = -\ 395.625$ kJ/mol O_2 **(6.13)**

ADI BUL-Seco CBN100 interactions

$TiB_2 + \frac{1}{2}\ Mg + 2.75\ O_2 = TiO_2 + \frac{1}{2}\ MgB_4O_7$ $\Delta G^\circ_{773} = -\ 692.542$ kJ/mol O_2 **(6.14)**

$B_2O_3 + 3\ Mg + 4\ Fe = 3\ MgO + 2\ Fe_2B$ $\Delta G^\circ_{773} = -\ 416.280$ kJ/mol O_2 **(6.15)**

During machining, shearing of the ADI matrix and graphite nodules appears to bring about an accumulation of Mg on the wear scar surfaces and the non-contact zones, probably in the form of microscopic oxide particles. The presence of a BUL containing Mg (Figure 5.69) indicates that this Mg accumulation might also take place by chemical reaction (Equations 6.10 and 6.14).

The reaction between Si from the BUL and atmospheric O_2 to form SiO_2 (Equation 6.11) is, thermodynamically, the most likely to occur. Thus, the oxidation of the ADI BUL might be expected to form an oxide rich in SiO_2.

The presence of Si on the BUL, especially at the leading and trailing edges, as well as at the non-contact zones (Figures 5.60 to 5.63 and 5.69) could be better understood by reference to the behaviour of Si during the high temperature oxidation of ferrous alloys. Many studies (205-208) reported that upon oxidation of ferrous alloys, Si is found in the form of a continuous and amorphous Si layer in the scale or as SiO_2 networks at the grain boundaries of the substrate.

Although TiB_2 is a minor phase, reactions between it and O_2, and between O_2 and Mg (Equations 6.7 and 6.14) are very detrimental to the overall behaviour of the cutting tool. Reactions involving TiB_2 and thermally induced cracks through this constituent can be expected to have synergistic effects on cBN grain pull-out.

The TiC binder might be expected to react with atmospheric O_2 (Equation 6.8) to a lesser extent because the BUL on it protects it against oxidation.

BN reacted with atmospheric O_2 (Equation 6.9) forming B_2O_3 which, is commonly in a glassy or vitreous state and melts at 450 to 475 °C under 1 atm. (202). However, because of its evaporation, the B_2O_3 that formed was not likely to be found on the wear scar surfaces or the surface layers built up on non-contact zones.

At cutting speeds greater than 150 m/min, the smearing of material on the sliding side of the chips (Figure 5.23) indicated partial melting of compounds formed by reaction between the workpiece, the tool and atmospheric O_2 (173).

These low melting compounds were squeezed out of the tool-chip and tool-workpiece interfaces (contact zones) and spread to the adjacent non-contact zones, giving it a rough and cracked appearance under the action of normal and shear stresses (Figure 5.56, 5.58 to 5.60). The presence of Si, Mg and O in the BUL (Figure 5.69) in large concentrations is clear evidence of chemical reactions.

Blistering and cracking of the non-contact zones of the tools appear to be due to a combination of thermal stresses and oxidation and diffusion reactions (209). This cracking might be evidence of chemical reactions between TiB_2 at the grain boundaries of the cutting tool material and atmospheric O_2, producing B_2O_3 which evaporates. Indeed, no clear evidence of the presence of B_2O_3 in the surface layers built up on the non-contact zones was found (Figures 5.58 and 5.59)

6.11.6 TEM investigation of sections through wear scars

The TEM investigation of sections of wear scars produced at cutting speeds greater than 150 m/min revealed indications of interactions between ADI constituents, cutting tool material constituents and atmospheric O_2 at the BUL (Figures 5.69 and 5.70). The BUL on the crater wear scar was a sandwich of 3 layers: a very thin C rich layer, an intermediate layer and a Fe layer in preferential contact with the TiC binder.

The C rich layer probably originated from thermo-migration of C from the TiC binder towards the surface as mentioned in Section 6.6.3. It could also originate from the comminution of graphite nodules and the subsequent accretion of the fragments of such nodules into a "glaze". The C rich layer contained slight amounts of B, N, O, Mg, Al and Si.

The intermediate layer contained mainly Si, O, Mg and slight amounts of B, C and N. It also contained very low amounts of Al and Ti. The amount of Fe in the intermediate layer appeared to decrease from the entrance zone towards the valley of the crater wear scar.

The Fe layer in preferential contact with the TiC binder contained small amounts of B, C, N and O and slight amounts of Mg, Al, Si and Ti. This would mean that diffusion of Mg, Al, Si and Ti towards the intermediate layer was active depleting the Fe layer in these elements towards the intermediate layer side.

Close to the TiC binder side, the Fe layer in preferential contact with the TiC binder contained small amounts of Ti, Si, Mg and O and very slight amounts of B and N. The TiC binder close to the crater wear scar contained slight amounts of B, N, O and Fe. In some areas, the amounts of Fe in the TiC binder increased significantly.

The Fe layer in preferential contact with the TiC binder appeared to strangely settle in areas where cracks connected. This finding is in line with what Subramanian et al. (210) reported in their investigation on the characterization of the interfacial layer at the tool-chip interface in the context of machining of steel and CGI with cBN-TiC cutting tools. They reported the penetration of Fe in the cBN-TiC cutting tool along grain boundaries to a distance of up to 15 μm. They suggested a chemical penetration of Fe and other solutes from the workpiece into the cBN-TiC cutting tool that is assumed to drive a chemical degradation of the overall wear resistance of the cutting tool material by the formation of brittle structures at grain boundaries.

It is also well known that for ceramic materials, frictional forces can induce subsurface planar cracks that can lead to delamination wear (98). The TEM investigation of the crater wear scar obtained at 800 m/min revealed the presence of intragranular cracking in a cBN grain as well as the surrounding TiC binder (Figure 5.69). These cracks appeared to be one crack that underwent deflection as it exited the cBN grain and entered the TiC grain. They were underneath the crater surface, although the crack in the TiC emerged at one end in a region where a Fe layer was found.

6.12 OXIDATION OF CBN-TIC CUTTING TOOL MATERIAL

It emerged from the curve in Figure 5.90 that the scale layer that formed on cBN-TiC cutting tools upon oxidation was not able to provide an effective protection against oxidation. This should be linked to its morphology that appeared to be highly porous (Figures 5.85 and 5.87). This is also supported by the fact that during the isothermal TGA, the main mass gains occurred during the dwell period of the heating profile (Figure 5.72).

Wherever islands of cBN grain appeared in the oxide scale, no noticeable surface oxygen was detected on them (Figures 5.75, 5.77 and 5.79), indicating the evaporation of B_2O_3 which formed on them. Indeed, B_2O_3 which melts at 450 to 475 °C under 1 atm (202) should naturally be in the liquid state during oxidation above 500°C. It should then be mentioned that the mass gains in Figure 5.72 were in fact lowered by the evaporation of B_2O_3 that formed in line with Equation 6.9 as well as the desorption of gas products like CO_2 and N_2 (Equations 6.8 and 6.9).

The presence of the inner oxygen-affected layer underneath the relatively dense outer scale layer shows that the latter was not completely resistant to oxygen penetration (Figures 5.84 and 5.85). The inward diffusion of O_2 through the semi-protective outer scale layer should have occurred via easy oxygen diffusion paths, such as grain boundaries or microscopic channels between grains (Figures 5.77, 5.79 and 5.81).

The morphology of the outer scale layer and inner oxygen-affected layer changed significantly as the oxidation temperature increased (Figures 5.84 to 5.86). In addition to the grain coarsening (Figures 5.76, 5.78 and 5.81) and increased segregation of Al_2O_3 in the outer scale layer (Figures 5.76, 5.80, 5.82, and 5.86), it was clear that the formation and evaporation of B_2O_3 at each temperature affected the morphology of the inner oxygen-affected zone significantly. Thus, the porosity of the oxide scale would come to a certain extent from the formation and evaporation of B_2O_3. Naturally, this porosity also comes from the desorption of gas products like CO_2 and N_2 that formed from oxidation reactions (Equations 6.8 and 6.9), and the specific volume misfits of the different phases involved. It thus appears that the oxidation of cBN-TiC cutting tool material is governed by the inward diffusion of O_2 through the highly porous oxide scale.

The oxidation experiment demonstrated that under the selected conditions, the TiC binder of the cutting tool material was not inert but showed extensive oxidation, producing brittle TiO_2 crystallites (Figure 5.86) which, can be easily removed by abrasion wear. The salient occurrence of TiO_2 peaks on X-ray diffractograms (Figures 5.88 and 5.89) clearly supports this view. This result supports the assertion that during machining of ADI, an oxidation wear mechanism participates in the degradation of the overall wear resistance of cBN-TiC cutting tools beyond a threshold cutting speed, particularly through the preferential oxidation of the TiC binder.

Oxidation of TiC has been described by some researchers as a gradual, exothermic and one dimensional diffusion process consisting of 4 consecutive steps: TiC → oxycarbide (TiC_xO_{1-x}) → suboxides such as TiO, Ti_3O_5 or Ti_4O_9 → anatase → rutile (TiO_2). Intermediate oxides are seen at temperatures below 700 °C. Above that, all the intermediate oxides are converted to TiO_2 (211). It is then likely that during the isothermal TGA and the oxidation experiments at 550 °C, this whole chain of reactions did not go to completion. Concerning the growth of TiO_2, it was reported that, depending on defect concentration, this growth is governed by either outward diffusion of interstitial Ti ions or inward diffusion of O ions via vacancies (212). The fact that the size of the TiO_2 grains in the outer scale layer increased with increased temperature (Figures 5.76, 5.78 and 5.81) indicated that there was outward diffusion of Ti atoms during the process of oxidation.

The evidence of segregation of Al oxide in the outer scale layer (Figures 5.77, 5.82 and 5.86) suggests that Al in the cBN-TiC cutting tool material would also exist in the form of Al or bonded forms of Al, such as AlN, AlB_2, Ti aluminide and / or combinations thereof. This evidence also shows clearly that no reaction between TiO_2 and Al_2O_3 took place. Indeed, no possibilities of reaction between TiO_2 and Al_2O_3 exist below 1200°C (213).

As far as the presence of B_2O_3 in the oxide layer is concerned, it should be mentioned that no possibilities of its mutual dissolution with Al_2O_3 that also formed in the oxide layer exist. Possibilities of reaction between Al_2O_3 and B_2O_3 to form $Al_4B_2O_9$ or $Al_{18}B_4O_{33}$ still exist (213). Taking into account the volume fractions of Al-based phases and cBN in the cBN-TiC cutting tool material, it is quite clear that the Al_2O_3 that formed might only react with a slight amount of B_2O_3.

In the same way, it should be mentioned that the solubility of TiO_2 in B_2O_3 is very small (4.25 mol % at 1000 °C) and that no possibility of dissolution of B_2O_3 in TiO_2 exists (213). Moreover, no possibilities of reaction between TiO_2 and B_2O_3 exist (213), particularly below 1000 °C. Taking all this into account, it is quite clear that the TiO_2 and B_2O_3 that formed during the TGA or the oxidation experiments remained quite separate and divorced completely upon cooling to ambient temperature. This is in line with the XRD results (Figures 5.88 and 5.89) which do not show any reaction product from B_2O_3 and TiO_2.

The oxidation of TiB_2 into B_2O_3 and TiO_2 was reported in many investigations. It has been reported that the oxidation of TiB_2 in air begins at a temperature of 480 °C (214). With reference to Equations 6.7 and 6.14, it is then possible that the TiB_2 that formed as sintering product at the grain boundaries in the cBN-TiC cutting tool material oxidized preferentially during the TGA and oxidation experiments. The absence of TiB_2 XRD peaks in Figures 5.88 and 5.89 supports this view.

It should then be mentioned once again that such oxidation should be very harmful to the overall wear resistance of cBN-TiC cutting tools. Indeed, in the same way that TiB_2 plays a role in the densification and toughening of cBN-TiC cutting tools, in the same way the oxidation of TiB_2 should play a critical role in the degradation of the wear properties of these cutting tools. Thus, the high hardness of TiB_2 cannot be used in full measure because of its insufficient resistance to oxidation.

In summary, it emerged that, particularly in the context of machining where abrasion wear intervenes to eliminate any form of passivation, the cBN-TiC cutting tool material is not oxidation-resistant in air above 550 °C (Figures 5.73 and 5.74).

6.13 STATIC INTERACTION COUPLES

6.13.1 ADI/cBN-TiC/ADI static interaction couples

Taking into account the indication of superficial melting that occurred at the tool-chip interface for cutting speeds greater than 150 m/min, the temperature of 1100°C at which the annealing diffusion of the ADI/cBN-TiC/ADI static interaction couple was done allowed simulating conditions close to the melting temperature of ADI which is about 1150°C.

Strong indications of diffusion of Fe in the TiC binder (Figures 5.91, 5.94 and 5.96) as well as the reprecipitation of Fe in TiC (Figure 5.92) were evident. Such diffusion of Fe can only be understood in the context of diffusion along grain boundaries.

Strong indications of dissolution of TiC and diffusion of Ti and C (Figures 5.91, 5.94 and 5.96) as well as reprecipitation of TiC in Fe (Figures 5.97 and 5.98) were evident. Such a process could involve, in the first instance, the dissolution of C in Fe and in the second instance, the diffusion in Fe of Ti left behind.

The reprecipitation in Fe of this C in the form of Fe_3C or Ti(C,N) (Figures 5.97 and 5.98) is evidence of depletion in Si of the ADI close to the interface and thus evidence of diffusion of Si towards the cBN-TiC side. The Si atom is relatively small and its diffusion in the TiC binder might take place by lattice as well as grain boundary diffusion.

The evidence of diffusion of N in Fe and its reprecipitation in the form of Ti(C,N) (Figures 5.97 and 5.98) is a strong indication of the dissolution of N-bearing phases such as Ti(C,N) and BN in Fe. However, strong indications of diffusion of Fe and Si in cBN grains were not really evident (Figures 5.91 and 5.95).

Upon their investigation on cBN-TiC/Fe static interaction couples at 1300 °C, Giménez et al. (203) came to the conclusion that Fe diffused in the cBN-TiC cutting tool up to a depth of about 150 µm. They also found that C diffused into the Fe and that segregation of Ti occurred towards the interface. The latter finding would be in line with the thermo-migration of C atoms in TiC discussed in Section 6.6.3.

Accordingly, the intrinsic substoichiometry of TiC could also play a role in the interaction of TiC with ADI. In his investigation of the interaction between non-stoichiometric TiC and molten Fe-C alloys, Frage (215) came to the conclusion that non-stoichiometric TiC tended towards its stoichiometric composition by absorbing C dissolved in the metallic binder or by releasing Ti to the melt.

It could also be imagined that the influence of Si as well as other elements in ADI on the henrian activities of B, N, Ti and C in austenite and ferrite might also play a role in the interaction between cBN-TiC cutting tool material and ADI.

Giménez et al. (203) used computational thermodynamics to assess the solubilities of TiB_2, TiC and cBN in Fe and ended with results that are summarized in Figure 6.3. At 1200°C, for example, the calculated solubility of TiB_2 in Fe is 0.012×10^{-6} m^3/mol (184).

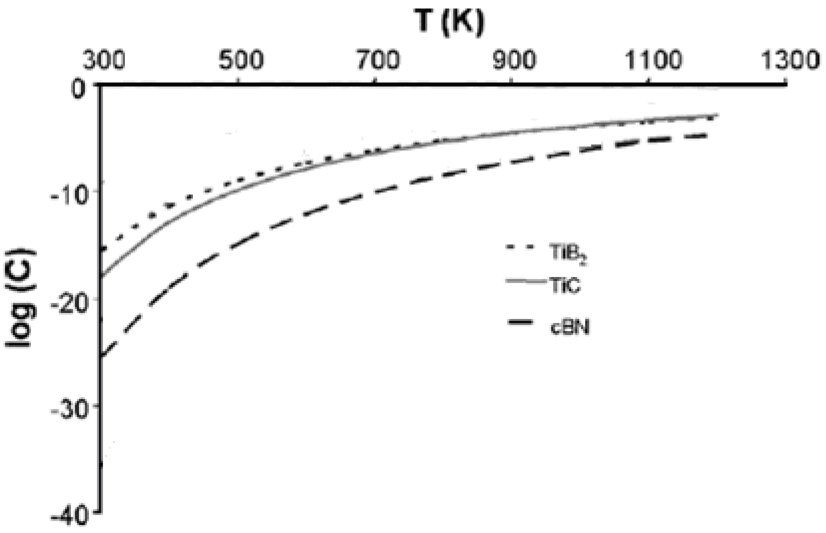

Figure 6.3: Solubilities C (m^3/mol) of TiB_2, TiC and cBN in Fe in the temperature range 300-1300 °K (203)

These results show that although the solubilities of TiB_2, TiC and cBN are very low at relatively low temperatures, they increased significantly at high temperatures to the extent that they should not be neglected.

Taking into account the increase in solubility due to the Gibbs-Thomson effect or capillarity effect (216), especially for nano-sized particles and relatively high pressures, it should be mentioned, particularly for TiB_2 particles which are very small in the cBN-TiC cutting material, that an even greater solubility should be expected.

It is proposed here that at high temperatures, TiB_2 particles dissociate in contact with the chips and the workpiece according to Equation 6.16.

$$TiB_2 + \underline{C} = 2\,\underline{B} + TiC \qquad \textbf{(6.16)}$$

The formation of TiB_2 at the grain boundaries of cBN-TiC cutting tools has a negative effect on the wear rate of the tools in the dry high speed machining of ASTM Grade 2 ADI because of its relative solubility in Fe and its predilection to oxidation.

The interaction between Fe and TiC in the cutting tool in the static interaction experiments (Figures 5.94 to 5.96) indicates that the adhesion of the ADI BUL on the cutting tool is stronger on the TiC binder than on the cBN grains (Figure 5.93). This, together with the cracking occurring close to the interface (Figures 5.93, 5.96 to 5.98), give insights into the mechanisms of BUL formation and adhesion wear.

6.13.2 Si/cBN-TiC/Si static interaction couples

The morphology of the Ti-rich phase approximating $TiSi_{4-x}$ that formed at the interface towards the side of the Si wafer (Figures 5.99 to 5.101) indicates that there is a mobile reaction front where Ti atoms that diffuse from the TiC binder through the Ti-Si rich phase meet and react with Si atoms. This should continue up to the stage where the TiC grains in the cutting tool material are exhausted.

It is suggested that Si atoms diffuse in the TiC binder through the grain boundaries and reprecipitate there probably as Si_xC. The non-stoichiometry of TiC would once again play a role in this process by providing C atoms for reaction.

The diffusion of Si in the TiC binder and its eventual reprecipitation as Si_xC give an indication of how the degradation of the wear resistance of cBN-TiC cutting tool can occur during the machining of ASTM Grade 2 ADI.

The strong evidence of interaction of Si and TiC in the cBN-TiC cutting tools obtained from the static interaction couples (Figures 5.99 to 5.101) clearly indicates that during the machining of ADI with cBN-TiC cutting tools, bonding of ADI to the tools occurs preferentially through the TiC binder. This evidence also shows that adhesion wear plays a key-role in the crater and flank wear rates, particularly in the wear initiation stage. Indication is also given on how the depletion in Si of the ADI can occur at the tool-chip and tool-workpiece interfaces.

7 CONCLUSIONS AND RECOMMENDATIONS FOR FUTURE WORK

7.1 CONCLUSIONS

PcBN cutting tools present the possibility of dry machining ADI components with a good surface finish. The problem, however, is that in this particular context, not much is understood about the relationship between the wear mechanisms involved and the wear performance of PcBN cutting tools. Both ADI and PcBN are relatively new materials, which are not very well understood. This lack of understanding could cost a lot if the application of PcBN cutting tools is extended to the machining of ADI without appropriate prior investigations.

Little research has been performed to explain the wear mechanisms of PcBN cutting tools when machining ADI. The task of integrating, in a broad picture, the effect of cutting speed on wear performance, static and dynamic cutting forces, effective friction coefficient, chip characteristics, and wear mechanisms on the one hand, and the role played by the BUL in the wear process, oxidation behaviour, and chemical interactions on the other does not appear to have been undertaken thus far. This work outlines such an undertaking, utilizing a series of experiments and analyses to elucidate the interplay between important machining factors.

When dry turning ASTM Grade 2 ADI with cBN-TiC cutting tools using a depth of cut of 0.2 mm and a feed of 0.05 mm/rev with a relatively large negative rake angle (- 26 °), flank wear and crater wear were the main wear modes for cutting speeds in the range 50-800 m/min.

Cutting speeds in the range 150-500 m/min were found to be optimum under the finish machining conditions used. Within this range, better surface finish, lower dynamic cutting forces, acceptable cutting tool life, lower flank wear rate and a lower "ratio of volume of metal removed per unit of flank wear" were achieved.

At cutting speeds lower than 150 m/min, the fragmentation of chips and the instability of the BUE controlled the dynamic cutting forces. At speeds greater than 150 m/min, shear localization within the primary and secondary shear zones of chips was the key-process controlling the static and dynamic cutting forces.

At cutting speeds lower than 150 m/min, long contact length, high average chip thickness, high chip hardness and curling of chips were recorded.

A substantial refinement of ferrite in the primary and secondary shear zones of the chips was obtained at cutting speeds greater than 150 m/min due to shear localization and dynamic recovery and recrystallization.

At cutting speeds greater than 150 m/min, the superficial melting of the BUL reduced shear localization in the secondary shear zone of chips and aided the reduction of the tool-chip contact length, the increase of shear angle and, consequently the reduction in average chip thickness.

The absolute value of the velocity exponent of the Taylor cutting tool life equation indicated that abrasion wear and thermally activated wear were the main wear mechanisms within the range of cutting speeds used. The same indications on tool wear mechanisms emerged when considering flank wear rate, chip hardness, average chip thickness and effective friction coefficient.

Excessive BUE as well as adherent layer that formed at cutting speeds less than 150 m/min were removed through the cutting tool resulting in tool attrition that activated abrasion wear. The low flank wear rate at these cutting speeds showed that cBN-TiC cutting tools have appreciable resistance to abrasion wear at relatively low cutting speeds.

At cutting speeds greater than 150 m/min, the BUL reduced the extent of adhesion and abrasion wear and increased the extent of diffusion wear. The BUL on the crater wear scar was a sandwich of approximately 3 layers: a very thin C rich layer, an intermediate layer containing mainly Si, Mg, and O, slight amounts of B, C and N and very low amounts of Al and Ti as well as a Fe layer in preferential contact with the TiC binder. Surface micro-cracks assisted the anchorage of the BUL on the wear scars and probably the diffusion of Fe and Si in the cBN-TiC cutting tools. The BUL on the non-contact zones contained substantial amounts of C, Si, Mg, O and Ti. The superficial melting of the BUL also increased to some extent the wear rate of cBN-TiC cutting tools.

The cBN-TiC cutting tool material is not oxidation-resistant in air above 550 °C and the scale that formed on cutting tools is not able to provide effective protection against oxidation. The formation and evaporation of B_2O_3 affected the morphology of the scale in terms of porosity. No mutual dissolution or reaction between B_2O_3 and TiO_2 that formed in the scale, which could be expected to reduce such porosity, was evident. The thermally activated oxidation of cBN-TiC cutting tools involves intense outward diffusion of Ti and Al.

Synergistic action of chemical reactions of TiB_2 with O_2 and Mg, dissolution of TiB_2 in Fe, dissolution of TiC and cBN in the BUL, as well as thermally induced cracking supported cBN grain pull-out, a significant component of the wear rate.

Diffusion of Fe and Si in the cBN-TiC cutting tools occurred through the grain boundaries of TiC. Their reprecipitation in the TiC as Fe, Si_xC or $TiSi_{4-x}$ degrades the wear resistance of cBN cutting tools.

The thermally activated interactions of Fe and TiC and, Si and TiC clearly indicate that during the machining of ADI with cBN-TiC cutting tools, bonding of BUL to the tool occurs preferentially through the TiC binder. These interactions also indicate that adhesion plays a key-role in flank and crater wear.

The knowledge generated in this work should contribute towards improved design and processing of PcBN cutting tools for use in the machining of ADI.

7.2 RECOMMENDATIONS FOR FUTURE WORK

In order to secure a broad database, dry finish turning experiments need to be carried out over a range of depths of cut and feeds.

Dry finish turning experiments need to be extended to less ductile ADI grades such as ASTM Grade 3 or ASTM Grade 4 in order to obtain an in-depth insight of the influence of the ductility of ADI on the wear behaviour of the cBN-TiC cutting tools.

In order to clearly highlight the impact of TiB_2 on the behaviour of cBN-TiC cutting tools, it is suggested that cBN-TiC cutting tools with and without TiB_2 be tested.

The anchorage of BUL on surface micro-cracks and the diffusion of Fe and Si along subsurface micro-cracks highlight the need to investigate further the source of such micro-cracks in the cBN-TiC cutting tools.

Dry finish turning experiments in inert atmosphere should be carried out in order to bring out more clearly the contribution of the oxidation processes to the wear of cBN-TiC cutting tools.

The particular influence of the binder on wear rate should be investigated further by testing PcBN cutting tools containing different binders such as TiC_{1-x}, TiN_{1-x} and $Ti(C_x,N_{1-x})$.

REFERENCES

---

1. Gekonde, H.O., Subramanian, S.V., High speed machining of ductile iron, *AFS Transactions* 120 (1995) 309-317
2. Matsumoto, M., Barash, M.M., Review of Cutting Technology of Hard Materials, *Proceedings of the Sixth International Conference on Production Engineering*, Osaka, Japan, 1987, pp. 116-122
3. Chou, Y.K., Evans, C., Barash, M.M., Experimental investigation on cubic boron nitride turning of hardened AISI 52100 steel, *Journal of Materials Processing Technology* 134 (2003) 1-9
4. Heath, P.J., Ultrahard Tool Materials, in ASM International Handbook Committee, *Metals Handbook 9th Edition Volume 16-Machining*, 1989, ASM International, USA, pp. 105-117
5. Standardised guidelines for machining cast iron, Technology Offer, TO_IWT_GA, Germany, Fri, http://www.ircnet.lu, October 24, 2003
6. Yescas-Gonzalez, M.A., *Modeling the Microstructure and Mechanical Properties of Austempered Ductile Irons*, Ph.D. thesis, University of Cambridge, Department of Materials Science and Metallurgy, November 2001, pp. 1-14
7. Cakir, M.C., Bayram, A., Isik ,Y., Salar, B., The effects of austempering temperature and time onto the machinability of austempered ductile iron, *Materials Science and Engineering A* 407 (2005) 147-153
8. Klocke, F., Klopper, C., Lang, D., Essig, C., Fundamental wear mechanisms when machining austempered ductile iron (ADI), *Annals of the CIRP* 56 (1) (2007) 73-76
9. Klocke, F., Klöpper, C., Machinability Characteristics of Austempered Ductile Iron (ADI), *2002 World Conference on ADI, Conference on Austempered Ductile Iron (ADI) for Casting Producers, Suppliers and Design Engineers*, Galt House Hotel, Louisville, Kentucky USA, September 26-27, 2002, Cosponsored by the Ductile Iron Society/American Foundry Society
10. Brandenberg K., Machining austempered ductile iron, *Manufacturing Engineering* 128 (5) (2002) 125-130
11. Vleugels, J., Fabrication, wear and performance of ceramic cutting tools, *Advances in Science and Technology* 45 (2006) 1776-1785
12. DeGarmo, E.P., Black, J.T, and Kohser, R.A. *Materials and Processes in Manufacturing 9th Edition*, John Wiley & Sons, Inc, USA, 2003, pp. 480-512, 515-547, 548-582, 777-807
13. Trent, E.M, Wright ,P.K., *Metal Cutting 4th Edition*, Butterworth Heinemann, Woburn, USA, 2000, pp. 9-20, 21-55, 57-96, 97-131, 339-369
14. Groover, M.P., *Fundamentals of Modern Manufacturing, Materials, Processes, and Systems 2nd Edition*, John Wiley & Sons, Inc, pp. 475-498, 534-564, 565-584
15. Black, J.T., Mechanics of Chip Formation, in ASM International Handbook Committee, *Metals Handbook 9th Edition Volume 16-Machining*, 1989, ASM International, USA, pp 7-12

16. Komanduri, R., Schroeder, T.A., On shear instability in machining a Nickel-Iron base superalloy, *Transactions of the ASME, Journal of Engineering for Industry* 108 (1986) 93-100
17. Stephenson, D.A., Agapiou, J.S., *Metal Cutting Theory and Practice 2nd Edition*, Taylor & Francis Group, 2006, pp. 371-424, 425-457
18. Black, J.T., Flow stress model in metal cutting, *Transactions of the ASME, Journal of Engineering for Industry* 101 (1979) 403-415
19. von Turkovich, B.F., Dislocation Theory of Shear Stress and Strain Rate in Metal Cutting, in *Advances in Machine Tool Design and Research*, Pergamon Press, 1967, pp. 531
20. Kececioglu, D., Shear strain rate in metal cutting and its effects on shear flow stress, *Transactions of ASME* 80 (1958) 158-168
21. Kalpakjian, S., Schmid, S., *Manufacturing Engineering and Technology 5th Edition*, Upper Saddle River, Prentice-Hall, Inc, New Jersey, 2006, pp. 534-568
22. Subramanian, S.V., Gekonde, H.O., Zhu, G., Zhang, X., Role of microstructural softening events in metal cutting, *Machining Science and Technology* 6 (3) (2002) 353-364
23. Zener, C., Hollomon, J.H., Effects of strain rate upon plastic flow of steel, *Journal of Applied Physics* 15 (1944) 22-32
24. Holzer, A.J., Wright, P.K., Dynamic plasticity: a comparison between results from mechanical testing and machining, *Journal of Materials Science and Engineering* 51 (1981) 81-92
25. Cohen, P.H., Forces, Power, and Stresses in Machining, in ASM International Handbook Committee, *Metals Handbook 9th Edition Volume 16-Machining*, 1989, ASM International, USA, pp. 13-18
26. Zhu, G., Subramanian, S.V., Modeling the Effect of Dynamic Softening of Material on Mechanics of Metal Cutting, *6th CIRP International Workshop Modeling of Machining Operations*, Hamilton, Canada, 2003, pp. 81-93
27. Bailey, J.A., Friction in metal machining: mechanical aspects, *Wear* 31 (1975) 243-275
28. Williams, J.E., Rollason, E.C., Metallurgical and practical machining parameters affecting built-up-edge formation in metal cutting, *Journal of the Institute of Metals* 98 (1970) 144-153
29. Stephenson, D.A., Agapiou, J.S., op. cit., pp. 503-549
30. Merchant, M.E., Basic mechanics of the metal-cutting process, *Transactions of the ASME, Journal of Applied Mechanics* 11 (1944) A168-A175
31. Kendall, L.A., Tool Wear and Tool life, in ASM International Handbook Committee, *Metals Handbook 9th Edition Volume 16-Machining*, 1989, ASM International, USA, pp. 37-48
32. Rowe, G.W., Smart, E.F., Experiments on Lubrication Breakdown in Friction Tests and in Cutting of Metal on a Lathe, *Proceedings of the Institution of Mechanical Engineers, 3rd Lubrication and Wear Convention*, London, 1965
33. Shaw, M.C., *Metal Cutting Principles*, Oxford University Press, Oxford, 1984, pp. 206-264

34. Anagonye, A., Stephenson, D.A., Modeling cutting temperatures for turning inserts with various tool geometries and materials, *Transactions of the ASME, Journal of Manufacturing Science and Engineering* 124 (3) (2002) 544-552

35. da Silva, M.B., Wallbank, J, Cutting temperature: prediction and measurements methods – a review, *Journal of Materials Processing Technology* 88 (1999) 195-202

36. Cook, F.H., Finnie, I., Shaw, M.C., Discontinuous chip formation, *Transactions of the ASME* 76 (2) (1954) 153-162

37 Gekonde, H.O., Subramanian, S.V., Influence of Phase Transformation on Tool Crater Wear, *1st French and German Conference on High Speed Machining*, 1997, pp. 49-62

38. Komanduri, R., Hou, Z.-B., On thermoplastic shear instability in the machining of a titanium alloy (Ti-6Al-4V), *Metallurgical and materials Transactions A* 33 9 (2002) 2995-3010

39. Sullivan, K.F., Wright, P.K., Smith, P.D., Metallurgical appraisal of instabilities arising in machining, *Journal of Metals Technology* 5 (6) (1978)181-189

40. Bayer, A.M., Becherer, B.A., High-Speed Tool Steels, in ASM International Handbook Committee, *Metals Handbook 9th Edition Volume 16-Machining*, 1989, ASM International, USA, pp 51-59

41. Pinnow, K.E., Stasko, W., P/M High-Speed Tool Steels, in ASM International Handbook Committee, *Handbook 9th Edition Volume 16-Machining*, 1989, ASM International, USA, pp 60-68

42. Stephenson, D.A., Agapiou, J.S., op.cit., pp. 141-167

43. Trent, E.M, Wright, P.K., op. cit., pp. 132-174, 227-249

44. Komanduri, R., Samanta, S.K., Ceramics, in ASM International Handbook Committee, *Metals Handbook 9th Edition Volume 16-Machining*, 1989, ASM International, USA, pp. 98-104

45. Knotek, O., Loffler, F., Kramer, G., Applications to Cutting Tools, in Bunshah, R.F., *Handbook of Hard Coatings, Deposition Technologies, Properties and Applications*, Noyes Publications, Park Ridge, New Jersey, USA, William Andrew Publishing, LLC, Norwich, New York, USA, 2001, pp. 370-410

46. Buljan, S.T., Wayne, S.F., Wear and design of ceramic cutting tool materials, *Wear* 133 (1989) 309-321

47. Heath, P.J., Ultrahard Tool Materials, in ASM International Handbook Committee, *Metals Handbook 9th Edition Volume 16-Machining*, 1989, ASM International, USA, pp. 105-117

48. Liu, J., Vohra Y.K., Tarvin J.T., Vagarali, S.S., Cubic-to-rhombohedral transformation in boron nitride induced by laser heating: In situ Raman-spectroscopy studies, *Physical Review B Condensed matter and materials physics* 51 (13) (1995) 8591-8594

49. Yu, W.J., Lau, W.M., Chan, S.P., Liu, Z.F., Zheng, Q.Q., Ab initio study of phase transformations in boron nitride, *Physical review B. Condensed matter and materials physics* 67 (1) (2003) 014108.1-014108.9

50. Solozhenko, V., in Edgar, J., editor, *Properties of Group III Nitrides*, Kansas State University, INSPEC USA, 1994, pp. 43-70

51. Brookes, C.A., The Mechanical Properties of Cubic Boron Nitride-a Perspective Review, in Almond A.E., Brookes, C.A., Warren, R., (editors), *Science of Hard Materials Institute of Physics Conference Series* N° 75 Bristol: Adam Hilger; 1986, pp. 207–220
52. Seco, *Secomax PcBN Technical Guide 2006*, Seco Tools AB, SE-737 82 Fagersta, Sweden, 2006, pp. 5, 8, 68-192
53. Can, N., Andersin, S.A., Cubic Boron Nitride Compact*, Patent, World Intellectual Property Organization*, International Bureau, WO 2006/046125 A1, PCT/IB2005/003221, 4 May 2006
54. Rong, X.Z., Tsurumi, T., Fukunaga, O., Yano, T., High-pressure sintering of cBN-TiN-Al composite for cutting tool application, *Diamond and Related Materials* 11 (2002) 280-286
55. Element Six, Raw materials, Cutting Tools Blanks, PCBN, http://www.e6.com, 2001-2004
56. Benko, E., Barr, T.L., Hardcastle, S., Hoppe, E., Bernasik, A., Morgiel, J., XPS study of the cBN–TiC system, *Ceramics International* 27 (6) (2001) 637–643
57. Benko, E., Stanislaw, J.S., Królicka, B., Wyczesany, A., Barr, T.L., cBN-TiN, cBN-TiC composites: chemical equilibria, microstructure and hardness mechanical investigations, *Diamond and Related Materials* 8 (1999) 1838-1846
58. Harris, T.K., Brookes, E.J., Taylor, C.J., The effect of temperature on the hardness of polycrystalline cubic boron nitride cutting tool materials, *International Journal of Refractory Metals & Hard materials* 22 (2004) 105–110
59. Chou, Y.K., Evans ,C.J., Barash, M.M., Experimental investigation on CBN turning of hardened AISI 52100 steel, *Journal of Materials Processing Technology* 134 (2003) 1-9
60. Poulachon, G., Moisan, A., Jawahir, I.S., Tool-wear mechanisms in hard turning with polycrystalline cubic boron nitride tools, *Wear* 250 (2001) 576-586
61. Hooper, R.M., Brookes, C.A., Microstructure and Wear of Cubic Boron Nitride Aggregate Tools, in Almond, A.E., Brookes, C.A., Warren, R., (editors), *Science of Hard Materials Institute of Physics Conference Series* No 75 Bristol: Adam Hilger; 1986. pp. 907–917
62. Walmsley, J.C., Lang, A.R., TEM studies of Syndax-3, compared with Syndite and Amborite, *Ultrahard Mater Appl Tech* 4 (1988) 61–75
63. Santhanam, A.T., Tierney, P., Cemented Carbides, in ASM International Handbook Committee , *Metals Handbook 9th Edition Volume 16-Machining*, 1989, ASM International, USA, pp. 71-89
64. Brookes, C.A., Lambert, W.A., *Ultrahard Materials Application Technology (De Beers)*, Hornbeam Press Ltd (1982), pp.128
65. Harris, T.K., Brookes, E.J., Taylor, C.J., The flow stress of PCBN cutting tool materials at high temperatures, *International Journal of Refractory Metals & Hard materials* 19 (2001) 267-273
66. Sachdev, H., Haubner, R., Nöth, H., Lux, B., Investigation of the c-BN/h-BN phase transformation at normal temperature, *Diamond and related Materials* 6 (1997) 286-292
67. Stachowiak, G.W., Stachowiak, G.B., Wear behaviour of ceramic cutting-tools, *Key Engineering Materials* 96 (1994) 137-164

---

68. Dawson, T.G., *Machining Hardened Steel with Polycrystalline Cubic Boron Nitride Cutting Tools*, Ph.D. Thesis, Georgia Institute of Technology, June 2002, pp. 11-41
69. Kerridge, M., Lancaster, J.K., The stages in a process of severe metallic wear, *Proceedings of the Royal Society London Series A* 236 (1956) 250-264
70. Vingsbo, O., Wear and Wear Mechanisms, *Proceedings of the International Conference on Wear of Materials*, Dearborn, Michigan, 16-18 April 1979, Ludema, K.C., Glaeser, W.A., Rhee, S.K., (editors), Publications American Society of Mechanical Engineers, New York, 1979, pp. 620-635
71. Stachowiak, G.W., Batchelor, A.W., *Engineering Tribology*, Butterworth Heinemann, 2005, pp. 533-552
72. Sasada, T., Norose, S., Mishina, H., The Behaviour of Adhered Fragments Interposed between Sliding Surfaces and the Formation Process of Wear Particles, *Proceedings of the International Conference on Wear of Materials*, Dearborn, Michigan, 16-18 April 1979, Ludema, K.C., Glaeser, W.A., Rhee, S.K., (editors) Publications American Society of Mechanical Engineers, New York, 1979, pp. 72-80
73. Stachowiak, G.W, Batchelor, A.W., op. cit., pp. 619-667
74. Kayaba, T., Kato, K., The Analysis of Adhesive Wear Mechanism by Successive Observations of the Wear Process in SEM, *Proceedings of the International Conference on Wear of Materials*, Dearborn, Michigan, 16-18 April 1979, Ludema, K.C., Glaeser, W.A., Rhee, S.K., (editors), Publications American Society of Mechanical Engineers, New York, 1979, pp. 45-56
75. Dearnley, P.A., Grearson, A.N., Evaluation of principal wear mechanisms of cemented carbides and ceramics used for machining titanium alloy IMI 318, *Material Science Technology* 2 (1986) 47-58
76. Trent, E.M, Wright, P.K., op. cit., pp. 157-159
77. Xiao, H., Wear behaviour and wear mechanism of ceramic tools in machining hardened alloy steel, *Wear* 139 (1990) 439-451
78. Buckley, D.H., Miyoshi, K., Friction and wear of ceramics, *Wear* 100 (1984) 333-353
79. Zum Ghar, K.H., Sliding wear of ceramic-ceramic, ceramic steel and steel-steel pairs in lubricated and unlubricated contact, *Wear* 133 (1989) 1-22
80. Stachowiak, G.W., Stachowiak, G.B., Batchelor, A.W., Metallic film transfer during metal-ceramic unlubricated sliding, *Wear* 132 (2) (1989) 361-381
81. Carter, G.M., Hooper, R.M., Henshall, J.L., Guillou, M.O., Friction of metal sliders on toughened zirconia ceramic between 298 and 973 °K, *Wear* 148 (1991) 147-160
82. Bowden, F.P., Tabor, D., *The Friction and Lubrication of Solids*, Oxford University Press, 2001, pp. 299-312
83. Gane, N., Breadsley, R., Measurement of the Friction and Wear of PSZ and other Hard Materials Using a Pin on Disc Machine, *Proceeding of the International Tribology Conference* , Melbourne, The Institution of Engineers, Australia, National Conference Publication No 87/18, December, 1987, pp. 187-192

84. Braghini, A.J., Coelho, R.T., An investigation of the wear mechanisms of polycrystalline cubic boron nitride (PcBN) tools when end milling hardened steels at low/medium cutting speeds, *International Journal Advanced Manufacturing Technology* 17 (4) (2001) 244-257
85. Cooper, C.V., Rollend, C.L., Krouse, D.H., The unlubricated sliding wear behavior of a wrought cobalt-chromium alloy against monolithic ceramic counterfaces, *Transactions of the ASME, Journal of Tribology* 111 (1989) 668-674
86. Fehlner, F.P., Mott, N.F., Low temperature oxidation, *Oxidation of Metals* 2 (1970) 59-99
87. Archard, J.F., Single contacts and multiple encounters, *Journal of Applied Physics* 32 (1961) 1420-1425
88. Rabinowicz, E., *Friction and Wear of Materials*, Wiley, New York, 1965
89. Tonshoff, H.K., Wobker, H.G., Influence of surface integrity on the wear of ceramic cutting tools, *Lubrication Engineering* July (1991) 579-583
90. Kim, W., Kwon, P., Understanding the mechanisms of crater wear, *Trans. NAMRI/SME* 29 (2001) 383-390
91. Swain, M.V., Microscopic observations of abrasive wear of polycrystalline alumina, *Wear* 35 (1975) 185-189
92. Stachowiak, G.W., Batchelor, A.W., op. cit., 2005, pp. 483-532
93. Moore, M.A., Douthwaite, R.M., Plastic deformation below worn surfaces, *Metallurgical Transactions* 7A (1978) 1833-1839
94. Challen, J.M., Oxley, P.L.B., An explanation of the different regimes of friction and wear using asperity deformation models, *Wear* 53 (1979) 229-243
95. Brandt, G., Flank and crater wear mechanisms of alumina-based cutting tools when machining steel, *Wear* (112) 1986 39-56
96. Moore, M.A., King, F.S., Abrasive wear of brittle solids, *Wear* 60 (1980) 123-140
97. Braza, J.F., Cheng, H.S., Fine, M.E., Silicon nitride wear mechanisms: rolling and sliding contact, *Tribology Transactions* 32 (1989) 439-446
98. Stachowiak, G.W, Batchelor, A.W., op. cit., pp. 571-592
99. Rigney, D.A., Glaeser, W.A., The significance of the near surface microstructure in the wear process, *Wear* 46 (1978) 241-250
100. Buckley, D.H., *Surface Effects in Adhesion, Friction, Wear and Lubrication*, Elsevier, Amsterdam, 1981
101. Suh, N.P., The delamination theory of wear, *Wear* 25 (1973) 111-124
102. Jahanmir, S., The relationship of tangential stress to wear particle formation mechanisms, *Wear* 103 (1985) 233-252
103. Stachowiak, G.W., Batchelor, A.W., op. cit., 2005, pp. 554-570
104. Batchelor, A.W., Stachowiak, G.W., Predicting synergism between corrosion and abrasive wear, *Wear* 123 (1988) 281-291

105. Stachowiak, G.W., Batchelor, A.W., op. cit., 2005, pp. 593-618

106 Gruss, W.W., Cermets, in ASM International Handbook Committee, *Metals Handbook 9th Edition Volume 16-Machining*, 1989, ASM International, USA, pp. 90-97

107. Silva, R.F., Gomes, J.M., Miranda, A.S., Vieira, J.M., Resistance of Si_3N_4 ceramic tools to thermal and mechanical loading in cutting of iron alloys, *Wear* 148 (1991) 69-89

108. Casto, S.L., Valvo, E.L., Ruisi, V.F., Lucchini, E., Maschio, S., Wear mechanism of ceramic tools, *Wear* 160 (1993) 227-235

109. Broskea, T.J., PcBN Tool Failure Mechanism Analysis, GE Superabrasives, Worthington, Ohio, Industrial Diamond Association, Intertech 2000, Vancouver, British Columbia, Canada, July 17-21, 2000

110. Stachowiak, G.W., Stachowiak, G.B., Unlubricated wear and friction of toughned zirconia ceramics at elevated temperatures, *Wear* 143 (1991) 277-295

111. Libsch, T.A., Becker, P.C., Rhee, S.K., Friction and Wear of Toughened Ceramics against Steel, *Proceeding JSLE International Tribology Conference*, 8-10 July 1985, Tokyo, Japan, Elsevier, pp. 185-190

112. Brandt, G., Mikus, M., An electron microprobe and cathodoluminescence study of chemical reactions between tool and workpiece when turning steel with alumina-based ceramics, *Wear* 115 (1987) 243-263

113. Zoya Z.A., Krishnamurthy R., The performance of CBN tools in the machining of titanium alloys, *Journal of Materials and Processing Technology* 100 (2000) 80-86

114. Sorelmetal, *Ductile Iron Data for Design Engineers*, Rio Tinto Iron & Titanium Inc, 770 Sherbrooke Street West, Suite 1800 Montreal, Quebec, Canada, H3A 1G, 1990

115. ADI, www.aditreatments.com/what.htm

116. Gundlach, R.B., Janowak, J., Austempered ductile iron combines strength with toughness and ductility, *Metal Progress* 128 (2) (1985) 19-26

117. Wm Lee Castings Specialists, Austempered Ductile Iron, www.wmlee.co.uk

118. Chang L.C., Carbon content of austenite in austempered ductile iiron, *Scripta Materialia* 39 (1) 35-38

119. Garin, L., Mannheim, R.L., Strain-induced martensite in austempered ductile iron (ADI), *Journal of Materials Processing Technology* 142-144 (2003) 347-351

120. Janowak, J.F., Gundlach, R.B., Development of a ductile iron for commercial austempering, *AFS Transactions* 91 (1983) 377– 388

121. Wu, Z.U., Chen, Y.J., Shih, T.S., Phase transformation in austempered ductile iron by microjet impact, *Materials Characterization* 48 (2002) 43-54

122. Yescas, M.A., Bhadeshia, H.K.D.H., MacKay, D.J., Estimation of the amount of retained austenite in austempered ductile irons using neural networks, *Materials and Science Engineering A* 311 (2001) 162-173

123. Chen, C., Johansson, M., Vuorinen, J., The Stability of Austenite in ADI, *International ADI and Simulation Conference*, May 28-30, 1997
124. Gregorutti, R.W., Sarutti, J.L., Sikora, J., Microstructural stability of austempered ductile iron after sub-zero cooling, *Materials Science and Technology* 19 (2003) 831-835
125. Putatunda, S.K., Development of austempered ductile cast iron (ADI) with simultaneous high yield strength and fracture toughness by a novel Two-step austempering process, *Materials Science and Engineering A* 315 (2001) 70–80
126. Hayrynen, K.L., Brandenberg, K.R., Keough, J.R., Applications for austempered cast iron, *AFS Transactions* 02-084 (2002) 1-10
127. Yang, J., Putatunda, S.K., Improvement in strength and toughness of austempered ductile cast iron by a novel Two-step austempering process, *Materials & Design* 25 (2004) 219–230
128. Yescas, M.A., Bhadeshia, H.K.D.H., Model for the maximum fraction of retained austenite in austempered ductile cast iron, *Materials Science and Engineering A* 333 (2002) 60-66
129. Chang, L.C., An analysis of retained austenite in austempered ductile iron, *Metallurgical and Materials transactions* 34 (2) (2003) 211-217
130. Warrick, R.J., Althoff, P., Druschitz, A.P., Lemke, J.P., Zimmerman, K., Mani, P.H., Rackers, M.L., Austempered ductile iron castings for chassis applications, *SAE Technical, Paper Series SAE 2000 World Congress,* Detroit, Michigan March 6–9, 2000
131. Harris, D. A., Tech, B., Maitland, R.J., The products of the isothermal decomposition of austenite in a spheroidal graphite cast iron, *Iron and Steel* (1970) 53-60
132. Kim, Y.J, Shin, H., Park, H., Dae Lim, J., Investigation into mechanical properties of austempered ductile cast iron (ADI) in accordance with austempering temperature, *Materials Letters* 62 (2008) 357-360
133. Advanced Cast Products, ADI, www.advancedcast.com, April 2004
134. *Typical Properties of ADI*, www.appliedprocess.com/html/Typical_Properties_of_ADI.pdf., February 2002
135. Druschitz, A. P., Fitzgerald, D. C, MADI introducing a New, Machinable, Austempered Ductile Iron, SAE Technical paper series, *2003 SAE World Congress*, Detroit, Michigan March 3-6, 2003
136. Stephenson, D.A., Agapiou, J.S., op. cit., pp. 598-601
137. ASM International Handbook Committee, Machinability of cast irons, in *Metals Handbook 9th Edition Volume 16-Machining*, 1989, USA, pp. 645-665
138. Trent, E.M, Wright, P.K., op. cit., pp. 293-296
139. Trigger, K.J., Zylstra, L.B., Chao, B.T., Tool forces and tool-chip adhesion in the machining of nodular cast iron, *Transactions of the ASME* 74 (1952) 1017-1027
140. Ham, I., Hitomi, K., Thuering, G.L., Machinability of nodular cast irons Part I Tool forces and flank adhesion, *Transactions of the ASME, Journal of Engineering for Industry* 83 (1961) 142-154

141. Hitomi, K., Thuering, G.L., Machinability of nodular cast irons Part II Effect of cutting conditions on flank adhesion, *Transactions of the ASME, Journal of Engineering for Industry* 84 (1962) 142-154
142. Putatunda, S.K., Kesani, S., Tackett, R., Lawes, G., Development of austenite free ADI (Austempered Ductile Cast Iron), *Materials Science and Engineering A* 435-436 (2006) 112–122
143. Putatunda, S.K., Ambooken, M.T., Pullum, B.J., Thermo-magnetic processing of ductile cast iron, *Materials Science and Engineering A* 460-461 (2007) 31–38
144. Moncada, O.J., Spicacci, R.H., Sikora, J.A., Machinability of austempered ductile iron, *AFS Transactions* 10-98 (1998) 39-45
145. Yamamoto, S., Nakajima, H., Miyaji, H., Mechanisms of poor machinability of austempered ductile iron, *The iron and Steel Institute of Japan* 81 (7) (1995) 721-726 (in Japanese)
146. Dearnley, P.A., A metallurgical evaluation of tool wear and chip formation when machining pearlitic grey cast irons with dissimilar graphite morphologies, *Wear* 101 (1985) 33-68
147. Gekonde, H.O., Subramanian, S.V., High speed machining of ductile iron, *AFS Transactions* 120 (1995) 309-317
148. Klocke, F., Klöpper, C., Machinability Characteristics of Austempered Ductile Iron (ADI), *2002 World Conference on ADI, Conference on Austempered Ductile Iron (ADI) for Casting Producers, Suppliers and Design Engineers*, Galt House Hotel, Louisville, Kentucky USA, September 26-27, 2002, Cosponsored by the Ductile Iron Society/American Foundry Society
149. Srivastava, A.K., Finn, M.E., Machinability of cast iron, TechSolve–The Manufacturing Solutions Center, Cincinnati, Ohio, www.techsolve.org/pdf/
150. Pashby, I.R., Wallbank, J., Boud, F., Ceramic tool wear when machining austempered ductile iron, *Wear* 162-164 (1993) 22-33
151. Klocke, F., Klopper, C., Lang, D., Essig, C., Fundamental wear mechanisms when machining austempered ductile iron (ADI), *Annals of the CIRP* 56 (1) (2007) 73-76
152. Brandenberg K., Machining austempered ductile iron, *Manufacturing Engineering* 128 (5) (2002) 125-130

153 Chou, Y. K., Liu, J., Ion implantation of superhard ceramic cutting tools, *Journal of Materials Engineering and Performance* 13 (2004) 398-405

154 Subramanian, S.V., Cast iron for use in high speed machining with cubic boron nitride, *Patent*, *United State Patent* US 6,395,107 B1, 28 May 2002

155 Subramanian, S.V., Gekonde, H.O.; Zhang, X., Gao, J., Inclusion engineering of steels for high speed machining, *CIM Bulletin* 91 (1998) 107-115

156 Ramanujachara, K., Subramanian, S.V., Micromechanisms of tool wear in machining free cutting steels, *Wear* 197 (1996) 45-55

157. Seker, U., Hasirci H., Evaluation of machinability of austempered ductile irons in terms of cutting forces and surface quality, *Journal of Materials Processing Technology* 173 (2006) 260–268

158. Masuda, M., Sato, T., Kori, T., Chujo, Y., Cutting performance and wear mechanism of alumina-based tools when machining austempered ductile iron, *Wear* 174 (1994) 147-153
159. Seah, K.H.W., Sharma, S.C., Machinability of alloyed austempered ductile iron, *International Journal of Machine Tools and Manufacture* 35 (10) (1995) 1475–1479
160. Wada, T., Fujiwara, J., Hanasaki, S., Yasutomi, M., Tool wear in cutting of ADI, *Transactions of the Japan Society of Mechanical Engineers C* 64 (626) (19981025) 4065-4071 (in Japanese)
161. Goldberg, M., Berry, J.T., Littlefair, G., Smith, G., A Study of the Machinability of an ASTM Grade 3 Austempered Ductile Iron, *2002 World Conference on ADI, Conference on Austempered Ductile Iron (ADI) for Casting Producers, Suppliers and Design Engineers*, Galt House Hotel, Louisville, Kentucky USA, September 26-27, 2002, Cosponsored by the Ductile Iron Society/American Foundry Society
162. Guo, X.H., Rui, Y.N., Zhu, S.L., Dong, G.Y., Study on ceramic cutter's wear mechanism when dry cutting austempered ductile iron (ADI), *Mocaxue Xuebao Tribology* 26 (1) (2006) 73-78 (in Chinese)
163. Shintani, K., Kato, H., Fujimura, Y., Yamamoto, A., Cutting performance of cBN tools in machining of austempered bainitic spheroidal graphite cast iron, *Journal of the Japan Society of Precision Engineering* 56 (12) (19901205) 2261-2266 (in Japanese)
164. Kato, H., Shintani, K., Fujimura, Y., Wear performance of cBN tool in machining of ADI (Effect of tool life on sintered elements), *Transactions of the Japan Society of Mechanical Engineers C* 57 (541) (19910925) 3027-3031 (in Japanese)
165. Taylor, A., *X-Ray Metallography*, John Wiley and Sons, Inc., New-York, London, 1961
166. International Standard, ISO 3685-1977(E)-Tool life testing with single point turning tools, Switzerland, 1977
167. Barry, J., Byrne, G., Cutting tool wear in the machining of hardened steels Part I: alumina/TiC cutting tool, *Wear* 247 (2001) 139-151
168. Li, X.S., Low, I.M., Cutting forces of ceramic cutting tools, *Key Engineering Materials* 96 (1994) 81-136
169. Kalin, M., Vižintin, J., Vleugels, J., Van Der Biest, O., Chemical reactivity of silicon nitride with steel and oxidised steel between 500 and 1200°C, *Materials Science and Engineering A* 281 (2000) 28-36
170. Barry, J., Byrne, G., TEM study on the surface white layer in two turned hardened steels, *Materials Science and Engineering A* 325 (2002) 356–364
171. Arsecularatne, J.A., Zhang, L.C., Montross, C., Wear and tool life of tungsten carbide, PcBN and PCD cutting tools, *International Journal of Machine Tools & Manufacture* 46 (2006) 482-491
172. Colours of heated metals, www.sizes.com/materls/colors_of_heated_metals.htm, 2007
173. Farhat, Z.N., Wear mechanism of CBN cutting tool during high-speed machining of mold steel, *Materials Science and Engineering A* 361 (1-2) (2003) 100–110

174. Villars, P., Prince, A., Okamoto, H., (editors), *Handbook of Ternary Alloy Phase Diagrams*, Volume 5, ASM International, Materials Park, Ohio, 1997, pp. 6838-6851

175. Wilhelmsson, O., Bijelovic, S., Lindquist, M., André, B., Wiklund, U., Svedlindh, P., Jansson U., Deposition and characterization of magnetic Ti–Fe–C nanocomposite thin films, *Thin Solid Films* 518 (2010) 2607–2616

176. Bijelovic, S., Råsander, M., Wilhelmsson, O., Lewin, E., Sanyal, B., Jansson, U., Eriksson, O., Svedlindh, P., Wear-resistant magnetic thin film material based on a $Ti_{1-x}Fe_xC_{1-y}$ nanocomposite alloy, *Physical review B* 81 (2010) 014405-1 014405 -9

177. Lahiff, C., Gordon, S., Phelan, P., PCBN tool wear modes and mechanisms in finish hard turning, *Robotics and Computer-Integrated Manufacturing* 23 (2007) 638–644

178. Qi, H.S., Mills, B., Formation of a transfer layer at the tool-chip interface during machining, *Wear* 245 (2000) 136–147

179. Klimenko, S.A., Mukovoz, Y.A., Lyashko, V.A., Vashchenko, A.N., On the wear mechanism of cubic boron nitride base cutting tools, *Wear* 157 (1992) 1-7

180. Trent, E.M., Wright, P.K., op. cit., pp. 42-79

181. Poulachon, G., Moisan, A.L., Hard turning: chip formation mechanisms and metallurgical aspects, *Transactions of the ASME* 122 (2000) 406-412

182. Farhat, Z.N., Microstructural characterization of WC-TiC-Co cutting tools during high-speed machining of P20 mold steel, *Materials Characterization* 51 (2003) 117–130

183. Subramanian, S.V, Gekonde, H.O., Zhang, X., Gao, J., Design of steels for high speed machining, *Ironmaking and steelmaking* 26 (5) (1999) 333-338

184. Vleugels, J., Van Der Biest., O., Chemical wear mechanisms of innovative ceramic cutting tools in the machining of steel, *Wear* 225–229 (1999) 285–294

185 Barry, J., Byrne, G., The mechanism of chip formation in machining hardened steels, *Transactions of the ASME* 124 (2002) 528-535

186. Rech, J., Influence of cutting tool coatings on the tribological phenomena at the tool-chip interface in orthogonal dry turning, *Surface & Coatings Technology* 200 (2006) 5132-5139

187. Hines, J.A., Vecchio, K.S., Ahzi, S., A model for microstructure evolution in adiabatic shear bands, *Metallurgical and Materials Transactions A* 29 (1) (1998) 191-203

188. Meyers, M.A., *Dynamic Behaviour of Materials*, John Wiley & Sons, Inc., New York, NY, 1994

189. Meyers, M.A., Nesterenko, V.F., LaSalvia, J.C., Xue Q., Shear localization in dynamic deformation of materials: microstructural evolution and self-organization, *Materials Science and Engineering A* 317 (1-2) (2001) 204–225

190. Tomashov, N.D., *Theory of Corrosion and Protection of Metals*, Macmillan, New York, 1966

191. Nabhani, F., Wear mechanisms of ultra-hard cutting tools materials, *Journal of Materials Processing Technology* 115 (2001) 402-112

192. Pavel, R., Marinescu, I., Deis, M., Pillar, J., Effect of tool wear on surface finish for a case of continuous and interrupted hard turning, *Journal of Materials Processing Technology* 170 (2005) 341–349

193. Luo, S.Y., Liao, Y.S., Tsai, Y.Y., Wear characteristics in turning high hardness alloy steel by ceramic and CBN tools, *Journal of Material Processing Technology* 88 (1999) 114–21

194. Zimmermann, M., Lahres, M., Viens, D.V., Laube, B.L., Investigations of the wear of cubic boron nitride cutting tools using Auger electron spectroscopy and X-ray analysis by EPMA, *Wear* 209 (1997) 241–246

195. Narutaki, N., Yamane, Y., Tool wear and cutting temperature of CBN tools in machining of hardened steels, *Annals of the CIRP* 28 (1979) 23–28

196. Shimada, S., Nishisako, M., Inagaki, M., Yamamoto, K., Formation and microstructure of carbon-containing oxide scales by oxidation of single crystals of zirconium carbide, *Journal of the American Ceramic Society*, 78 (1995) 41–48

197. Shimada, S., Inagaki, M., Matsui, T., Oxidation kinetics of hafnium carbide in the temperature range of 480° to 600°C, *Journal of the American Ceramic Society* 75 (1992) 2671-2678

198. Shimada, S., Inagaki, M., A kinetic study on oxidation of niobium carbide, *Solid State Ionics* 63-65 (1993) 312-317

199. Zhang, L., Koka, R.V., A Study on the oxidation and carbon diffusion of TiC in alumina-titanium carbide ceramics using XPS and Raman spectroscopy, *Materials Chemistry and Physics* 57 (1998) 23-32

200.Mosser, A., Guemmaz, M., Raiser, D.,Boudoukha, L. Grob, J.J., Sens, J.C., Ion beam synthesis of non-stoichiometric titanium carbide: Composition structure and nanoindentation studies, *Nuclear Instruments and Methods in Physics Research Section B: Beam Interactions with Materials and Atoms* 111 (3) (1996) 263-270

201. Vleugels, J., Basu, B., Hari Kumar, K.C., Vitchev, R.G., Van Der Biest, O., Unlubricated fretting wear of TiB_2-containing composites against bearing steel, *Metallurgical and Materials Transactions A* 33A (2002) 3847-3859

202. Massalki, T.B., (Editor-In-Chief), *Binary Alloy Phase Diagrams 2nd Edition, Volume 1, Ac-Ag To Ca-Zn*, ASM International, Materials Park, Ohio, pp. 480-483, 498-500, 510-512

203. Giménez, S., Van der Biest, O., Vleugels, J., The role of chemical wear in machining iron based materials by PCD and PCBN super-hard tool materials, *Diamond & Related Materials* 16 (2007) 435–445

204. Reed-Hill, R.E., Abbaschian, R., *Physical Metallurgy Principles 3rd Edition*, PWS Kent, pp. 390-394

205. Paul, A., Elmrabet, S., Alves, L.C., Da Silva, M.F., Soares, J.C., Odriozola, J.A., Ion microprobe study of the scale formed during high temperature oxidation of high SI EN-1.4301 stainless steel, *Nuclear Instruments and Methods in Physics Research B* 181 (2001) 394-398

206. Pérez, F.J., Cristóbal, M.J., Hierro, M.P., Pedraza, F., The influence of implanted Si on the cyclic oxidation behavior of 2 different stainless steels; *Surface and Coatings Technology* 120–121 (1999) 442–447

207. Dunning, J.S., Alman, D.E., Rawers, J.C., Influence of silicon and aluminium additions on the oxidation resistance of a lean-chromium stainless steel, *Oxidation of Metals* 57 (5-6) (2002) 409-425

208. Huntz, A.M., Bague, V., Beauplé, G., Haut, C., Sévérac, C., Lecour, P., Longaygue, X., Ropital, F., Effect of silicon on the oxidation resistance of 9 % Cr steels, *Applied Surface Science* 207 (2003) 55-275

209. Grabke, H.J., Meier, G.H., Accelerated oxidation, internal oxidation, intergranular oxidation, and pesting of intermetallic compounds, *Oxidation of Metals* 44 (1-2) (1995) 147-176

210. Subramanian, S.V., Andrei, C., Botton, G., Characterization of interfacial layer at tool-chip contact in metal cutting with CBN tool 2nd annual report, Element Six Report, July 15, 2006

211. Shimada, S., A thermoanalytical study of oxidation of TiC by simultaneous TGA-DTA-MS analysis, *Journal of Materials Science* 31 (3) (1996) 673-677

212. Lee, D.B., Lee, Y.C., Kim, D.J., The oxidation of TiB_2 ceramics containing Cr and Fe, *Oxidation of Metals*, 56 (1-2) (2001) 177-189

213. ACerS-NIST, Phase Equilibria Diagrams, CD-ROM Database, Version 1, *National Institute of Standards and Technology, The American Ceramic Society*, 2004-2005

214. Ban'kovskaya, I.B., Oxidation Processes in Glass-Ceramic Composites Based on Titanium Boride, *Glass Physics and Chemistry* 33 (1) (2007) 80–85

215. Frage, N., Interaction between nonstochiometric titanium carbide and Fe-C alloys, *Metallurgical and Materials Transaction B* 30 (5) (1999) 857-863

216. Porter, D.A., Easterling, K.E., *Phase Transformations in Metals and Alloys*, CRC Press Taylor & Francis Group, USA, 2004, pp. 44-47